Cranfield UNIVERSITY

CRANFIELD UNIVERSITY

OMID GOHARDANI

THE INFLUENCE OF EROSION AND WEAR ON THE ACCRETION AND ADHESION OF ICE FOR NANO REINFORCED POLYMERIC COMPOSITES USED IN AERONAUTICS

School of Engineering
Department of Power and Propulsion

Ph.D. Thesis
Academic Years: 2009-2011

Supervisor: Dr. David W. Hammond

December 2011

Cranfield UNIVERSITY

CRANFIELD UNIVERSITY

School of Engineering
Department of Power and Propulsion

Ph.D. Thesis
Academic Years: 2009 – 2011

OMID GOHARDANI

THE INFLUENCE OF EROSION AND WEAR ON THE ACCRETION AND ADHESION OF ICE FOR NANO REINFORCED POLYMERIC COMPOSITES USED IN AERONAUTICS

Supervisor: Dr. DAVID W. HAMMOND
December 2011

This thesis is submitted in partial fulfillment of the requirements for the degree of
Doctor of Philosophy.

Dedication

This doctoral dissertation is dedicated to my beloved mother and father for their infinite love, guidance, support and stature as my ideal role models, for their invaluable decision of living life in freedom, and their everlasting fountain of inspiration. This dissertation is further dedicated to my beloved brothers Avid, Navid and Amir Shahram, with whom I am fortunate to share an eternal bond on a path beyond description in mere words. The true inspiration to this dissertation has been the sparks of encouragement and dreams I have witnessed come true through the work of my dear father as an aeronautical/aerospace engineer. This dissertation is further dedicated to the memory of my late grandmothers and grandfathers. In particular, the words of this dissertation is dedicated to the late Colonel Gohardani, my first inspirational source to science and true manners, who holds an eternal and special place in my heart and mind.

Omid Gohardani
Cranfield, United Kingdom

Acknowledgments

The author gratefully acknowledges Dr. David W. Hammond for his supervision, insightful discussions and suggestions during the course of this project and for his introduction to the wonderful world of material sciences. The author's deepest gratitude is extended to Prof. Pericles Pilidis for his invaluable support, help and encouragement. Prof. Marin Guenov, Prof. David Mba and Dr. Joao Amaral Teixeira are further greatly acknowledged for serving as committee members. Prof. Max F. Platzer, Naval Postgraduate School, Monterey, United States, is greatly acknowledged for his immensely useful suggestions in the historical review of the erosion topic in aviation and for his inspiration as a scientist. Prof. Kyla Macario, University of Arizona, United States, Prof. Lesley Wright, Baylor University, United States, and Prof. Luca Caracoglia, Northeastern University, United States are greatly acknowledged for their support and encouragement. The author further greatly acknowledges the assistance of the following individuals: Dr. David M. Williamson at Cavendish Laboratory, Cambridge University, United Kingdom for fruitful discussions and assistance in carrying out the experimental liquid erosion experiments at Cavendish Laboratory, Dr. Richard Purvis, University of East Anglia, United Kingdom, for carrying out the numerical computations of the droplet impact phenomenon, Dr. Maialen Chapartegui, Ms. Aroa Iriarte and Dr. Cristina Elizetxea, Tecnalia, Spain for specimen preparation and information regarding the materials, Mr. Oliver Ashworth, Vapormatt Ltd, United Kingdom for wet blasting of the specimens, Mr. Brian Stapleton for his invaluable help with the laboratory equipment and exceptional machine shop skills, Mr. Gary Muir and Mr. Jim Hurley for their help with the specimen cutting, Mr. Jafar Alzaili, for his assistance with the dynamic wettability experiments, Mrs. Marie-Laure Pervier for her assistance with the sound speed experiments, and Mr. Eduardo Piles Moncholi for his assistance with the ice adhesion tests. Finally, the author gratefully acknowledges the European Commission under its 7th Framework Programme, Theme 7: Transport (including aeronautics), for complete funding in support of the author's doctoral studies.

Nomenclature

Greek symbols

α	= The inner angle subtended by the surface and left edge of the corona jet
	= Constant
	= Angle of attack
α^*	= The outer angle subtended by the surface and left edge of the corona jet
β	= The outer angle subtended by the surface and right edge of the corona jet
	= Scaling factor or Vickers angle
β^*	= The inner angle subtended by the surface and right edge of the corona jet
χ	= Generic function
δ	= Scaling factor or spatial increment
δ_1	= Displacement thickness
δ_2	= Momentum thickness
δ_3	= Energy thickness
δ_{99}	= Boundary layer thickness
ε	= Percentage error
φ	= Incident angle of droplet
φ_L	= The angle at the left position of a rivulet moving along the surface
φ_R	= The angle at the right position of a rivulet moving along the surface
γ	= Surface tension
η^*	= Complex viscosity
λ	= The wave length of the water film
$\breve{\lambda}$	= Material independent coefficient
ν	= Poisson's ratio
	= Degree of freedom
θ	= The angle at the movement path of the droplet with the normal plane
$\widetilde{\theta}$	= Static contact angle
θ_L	= The angle at the left position of a moving bead along the surface

θ_R = The angle at the right position of a moving bead along the surface
θ_F = Hysteresis value of the frame
ρ = Density
σ = Standard deviation
σ^2 = Variance
τ = Time constant (duration)
= Pressure release time
τ^* = Water-hammer pressure termination time
τ_{ice} = Ice adhesion strength
τ_w = Wall shear stress
ω = Angular frequency
ξ = Width of a rivulet
ζ = Height of a rivulet
Φ = Generic function
Λ = Empirical constant
Ω = Generic height function
Ξ = Generic width function
Ψ = Constant

Latin characters

c_L = Velocity of the longitudinal wave
c_R = Velocity of the Rayleigh-wave
c_T = Transverse wave velocity
c = Speed of sound
c_f = Skin friction coefficient
d = Diameter
d_m = Mean diameter
f_d = Droplet frequency
g = 9.80665 $\mathrm{m \cdot s^{-2}}$, gravitational constant
gf = Load for hardness testing
h = Height of bead, rivulet or structure
h_{ice} = Thickness of ice
h_S = Thickness of the specimen
i = Integer
j = Integer
k = Integer
ℓ = Total length in the field of view
m = Mass
= Mass of the erodent
$\dot{m}$ = Mass flow

n = Number, number of impacts
$\breve{n}$ = Node
n_b = Number of beads in a frame
n_c = Number of coronas in a frame
n_r = Number of rivulets in a frame
$n_{t,b}$ = Total number of beads in all considered frames
$n_{t,c}$ = Total number of coronas in all considered frames
$n_{t,r}$ = Total number of rivulets in all considered frames
p_i = Point i
n_f = Total number of frames
n_s = Total number of splashing structures
p = Pressure
$\widetilde{r}$ = Radius of fracture commencing flaw
r_d = Radius of droplet
$r_{\min}$ = Inner damage annulus
$r_{\max}$ = Outer damage annulus
s = Standard deviation
t = Time
= Specimen thickness
v = Aerial speed of the erodent
$v_{\widehat{D}}$ = Equivalent speed for a 2 mm droplet
v_{MIJA} = Multiple Impact Jet Apparatus speed
w = Width of bead, rivulet or structure
x = Coordinate
y = Coordinate
z_c = Confidence level
A = Area
= Amplitude of the water film
$\mathcal{A}$ = Two-dimensional area of the corona structure
$\widetilde{A}$ = Sample area
$\overline{B}(x)$ = Representative bead structure
$\breve{C}$ = Shock wave velocity
$C(x, y)$ = Centroid position
Ca = Capillary number
D = Droplet diameter
$\widehat{D}$ = Droplet diameter, $D \equiv 2$ mm
F = Force
F_D = Dynamic driving force
E = Young's modulus
$\dot{E}$ = Erosion rate

$\widetilde{E}_C$ = Entropy within the photograph of a two-dimensional slice of the corona
$\widetilde{E}_F$ = Entropy within the frame of the image sequence
H = Height
= Height of corona
H_V = Vickers Hardness value
$\breve{I}$ = Current capacity
K_{Ic} = Fracture toughness
L = Length
N = Number
= Total number of droplets for a given frame
N_i = Number of impacts
$N_{\widehat{D}}$ = Number of total droplets
Oh = Ohnsorge number
P = Load
P_B = Bernoulli stagnation pressure
P_c = Pressure at the center of impact
P_s = Threshold pressure
P_w = Water-hammer pressure
R_a = Surface roughness
Re = Reynolds number
$\overline{R}_j$ = Averaged number of droplets within a sequence of images in a given zone
S = Spreading coefficient
= Material strength
S_n = Specimen number n
T = Temperature
V = Volume
V_L = Volumetric erosion loss
U_∞ = Free stream velocity
W = Width
We = Weber number
$\overline{W}(x)$ = Idealized water film
W_1 = Base width of corona
W_2 = Top width of corona
Z = Acoustic impedance
Z_L = Impedance of the liquid
Z_S = Impedance of the solid

Abbreviations

CL = Confidence level
CNT = Carbon nanotubes
CSMT = Corona splashing measurement tool
DTV = Damage threshold velocity
EASA = European aviation safety agency
FAA = Federal aviation administration
FSSP = Forward scattering spectrometer probe
HMEM = High mechanical energy mixer
HSM = High shear mixer
JAA = Joint airworthiness authorities
LAYSA = Multifunctional layers for safer aircraft
LWC = Liquid water concentration
LWCM = Liquid water concentration module
MIJA = Multiple impact jet apparatus
MWCNT = Multi-walled carbon nanotubes
NASA = National aeronautics and space administration
NWP = Numerical weather prediction
OAT = Outside air temperature
OAP = Optical array probe
SEM = Scanning electron microscope
SLD = Super-cooled large droplets
SWCNT = Single-walled carbon nanotubes
TAT = Total air temperature
TEM = Transmission electron microscopy
UAV = Unmanned air vehicle
VOF = Volume of fluid

Subscripts

0 = Initial state
max = Maximum
min = Minimum

Superscripts

e = Eroded state
p = Pristine state

Symbols

$^\circ$	= Degrees
®	= Registered trademark
$\propto$	= Proportional to
$\in$	= In the range of
∞	= Infinity
$\equiv$	= Identically equal to
$\Delta(\ldots)$	= Difference of
$\mathcal{O}$	= Order of
$\overline{(\ldots)}$	= Mean value
$\widetilde{(\ldots)}$	= Constant
$(\ldots)^*$	= Non-dimensionalized quantity
$(\ldots)^\star$	= Non-dimensionalized quantity with ℓ

Abstract

The usage of polymeric matrix composites in aerospace applications has been significantly prevalent based on their desired material characteristics, which include higher strength, lower weight and heat resistance. With current advancements in nanotechnology, carbon nanotube reinforced polymeric matrix composites may enhance the operational usage of these advanced materials even further. In this study, a set of novel aerospace material candidates are characterized based on their mechanical properties, resilience to liquid erosion, wettability and ice adhesion. The experimental evaluations presented, allow for a preliminary ranking of the polymeric matrix composites and assessment of the influence of reinforcing carbon nanotubes. The role of erosion in particular is highlighted from both a historical viewpoint and based on empirical results for static and dynamic wettability and ice adhesion. Discussion of different ranking systems and fractography arising as a consequence of liquid impact are further addressed in this study. It is found that the candidate samples exhibit different physical parameters but nominally similar erosion resilience despite the presence of the reinforcing carbon nanotubes. The wettability of the experimental materials and their ice adhesion characteristics are further shown to be influenced by the presence of carbon nanotubes and largely dependent upon degradation of the material surfaces.

Table of Contents

List of Figures

List of Tables

Chapter 1

Introduction

The usage of polymeric matrix composites within aerospace sciences has evolved widely due to the desirable properties of these materials. When an aircraft traverses the atmosphere, it may be subjected to numerous hazards stemming from atmospheric conditions, such as wind gust, lightning, precipitation, and other weather related phenomenon. Due to freezing temperatures at cruise altitudes for commercial aircraft and climb to this altitude, the aircraft icing phenomenon may arise as a consequence of flight through clouds and impact of droplets with the airframe. In particular forward facing surfaces of the aircraft are potential targets of such encounters. The consequences of the impacts are in large influenced by the local temperatures, the impact speed and the properties of the airframe materials. Hence, the impacts may result in droplet splashing, ice adhesion and in some instances erosion. This study is devoted to the possible implementation of candidate materials in aeronautical applications and their behavior when subjected to wetting conditions, erosion and ice adhesion. In particular, the role of carbon nanotubes on the aforemen-

tioned phenomenon is examined and each effect considered separately. The analysis can further enable conclusions of a synergistic view in which the role of erosion on wettability and ice adhesion is highlighted.

1.1 Research objectives

The objectives of this research is to establish a framework for the usefulness of a set of polymeric matrix composites reinforced with carbon nanotubes for usage in flight conditions on a commercial airliner. This framework hence encapsulates establishment of the mechanical properties of these specimens and aspects of wettability, erosion and adhesion of ice onto the aforementioned materials. The objective of this investigation is to examine the influence of carbon nanotubes on a set of candidate aerospace materials and whether resins reinforced with these advanced materials have an implementation potential within the aerospace industry.

This Ph.D. study is a part of the project, multifunctional layers for safer aircraft composite structures (LAYSA), initiated by the European Commission under the 7th Framework Programme, Theme 7: Transport (including Aeronautics). Established on the basis of demand for increased security and safety systems related to aircraft composite materials, the main objective of the LAYSA project consists of "*development of a new multifunctional layer with ice/fire protection and health monitoring capacity to be integrated into composite structures*" (European Commission, 2008). LAYSA is a research effort with 12 participating European members including five companies: Aernnova,

Advanced Composite Group, Aries Complex, Huntsman and INASCO. Moreover, three research centers: Centre de la Recherche Paul Pascal-Transform, Swerea SICOMP AB and Tecnalia as well as four universities: Cranfield University, University of Patras, Ecole Nationale Supérieure de Chimie de Lille, and Université de Pau et des Pays de l'Adour, participate in the LAYSA project. The project has an initial budget of € 3 million.

The objective of this project is to employ the desirable attributes of nanomaterials in conjunction with the epoxy resin matrices in order to study wettability, ice adhesion and erosion threshold characteristics for the different supplied materials and observe their influence thereof. The composite structures were supplied by the European Commission and Tecnalia (former INSAMET), a collaborating LAYSA partner, based in Spain. The long term objectives of the European project further involve the study of electrical or thermal heating, conductivity and proper dispersion of the nanomaterials. Moreover, the alignment and pre-treatment of the nanomaterials are to be established.

1.2 Dissertation structure

In Chapter 1 the research objectives of this dissertation are outlined. The literature review presented in Chapter 2 establishes the framework of previous studies carried out related to this research where in particular the connection between aircraft icing, erosion and wettability is described. Chapter 3, describes the basic mechanical properties of the supplied specimens as found empirically in this study. The uniformity, hardness and acoustic impedance of the supplied material are thereupon utilized in Chapter 4, to explain the obtained results for the encountered damage threshold velocities and coating stress levels obtained by means of two different multi-layered models. The wet blasting procedure described in this chapter, further highlights the intricate safety aspects related to handling these materials as described in Chapter 2 and further serves as a useful basis for determining the effect of surface roughness on static and dynamic wettability described in Chapter 5 and ice adhesion testing described in Chapter 6. Due to the scarcity of wettability procedures that would couple the static and dynamic wettability, Chapter 5 introduces the Dynamic and Static Wettability Scheme for Advanced Materials (DSWSAM) which is utilized to provide numerical results for the differences in wetting character between the supplied specimens. This scheme in conjunction with the ice adhesion properties of the specimens in Chapter 6, convey further specimen properties in addition to the ones presented in Chapter 3 and Chapter 4. Chapter 5, also makes use of a numerical approach to the droplet impact scenario at different incident angles and water layer depths by means of a volume of fluid (VOF) approach and a discussion

related to the numerical results. CHAPTER 7, describes the conclusions based on the findings of the empirical, numerical and methodologies described in CHAPTER 3 and CHAPTERS $4-6$. As a suggestion for an aeronautical application, CHAPTER 7 features a proposed platform under which a selection of the considered materials can be utilized on Unmanned Air Vehicles (UAVs) and the specific UAV that would serve as an adequate test bed for such an approach. Suggestions of future work are further described in CHAPTER 8.

Chapter 2

Literature review

2.1 Introduction

In this chapter, the literature review related to assessment of the candidate materials is presented. Initially, aircraft icing and its relation to the proposed testing methodology of the novel materials is outlined. The wettability, material properties and erosion resilience of the candidate materials are further discussed in light of relevant literature and methods suitable for empirical and analytical evaluation of the materials.

2.2 Aircraft icing

Aircraft icing occurs fundamentally as a range of conditions are fulfilled simultaneously. The main factors to icing are liquid water content, the temperature and the droplet size (Politovich, 2003). For certification purposes of aircraft the mentioned properties are utilized by the FAA in accordance with Figure

2.1 and recently proposed to become expanded by an Appendix O (Federal Aviation Administration, 2010), covering only supercooled large drop (SLD) icing conditions.

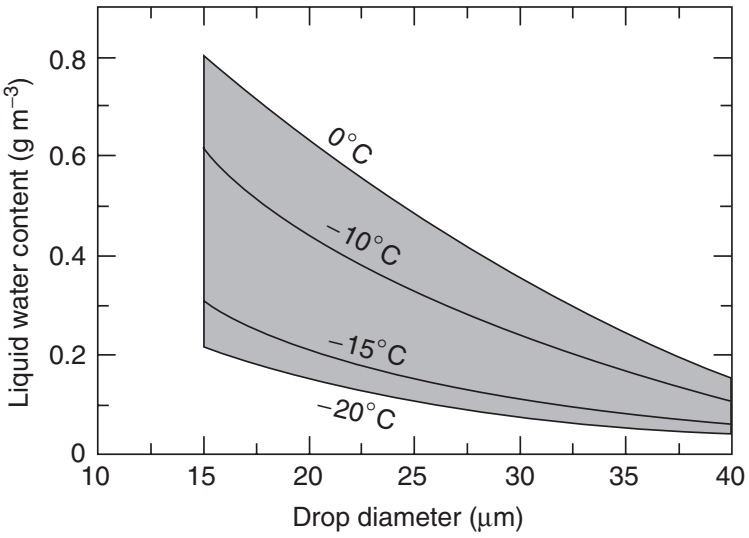

Figure 2.1. Aircraft icing envelopes showing liquid water content, droplet diameter and outside temperature. The icing envelope limits are shown as the shaded area. An aircraft must operate in these conditions safely, in order to get certified for aircraft icing conditions. *Source:* (FAA Federal Aviation Regulations 14 CFR Part 25, Appendix C; Politovich, 2003)

Aircraft icing develops upon existence of water droplets below freezing temperatures in the atmosphere that impinge on the surfaces of an aircraft during flight (Amendola and Mingione, 2001). The nature of the icing that occurs is dependent upon the density of liquid water per unit cubic meter, or the liquid water content, droplet size and temperature. For temperatures of -40 °C or lower, water droplets freeze instantly and ice crystals are formed. However, clouds may consist of a mixture of ice crystals and water droplets, or each separately. Icing usually has an inclination to occur for temperatures $T \in [0, -20]$

°C (Amendola and Mingione, 2001), with the full icing risk temperature range extending to −40 °C (Steuernagle et al., 2008). This observation can be utilized in order to prescribe an indicative temperature range for the ice adhesion testing on the supplied materials in this study.

A large number of droplets with different sizes and other particulates may be present in the atmosphere, as shown in Figure 2.2.

Figure 2.2. Schematic rendering of how aircraft icing may unfold, upon contact of super-cooled liquid droplets with the airframe. The droplet sizes have been exaggerated in the figure for visualization purposes. *Source:* (Gohardani, 2009) adapted from Donald McCann, National Weather Service Aviation Forecast Center.

The encounter of these droplets and particulates with the airframe can present several possible scenarios. A simplistic view of these outcomes implies that the droplets can either freeze immediately upon impact on the fuselage, splash

upon the airframe followed by freezing or erode the impact location. This simple example illustrates the conceptual intention of this research where wettability, erosion and ice adhesion can all occur upon the impact of one droplet. The schematic correlation between these occurrences are depicted in Figure 2.3.

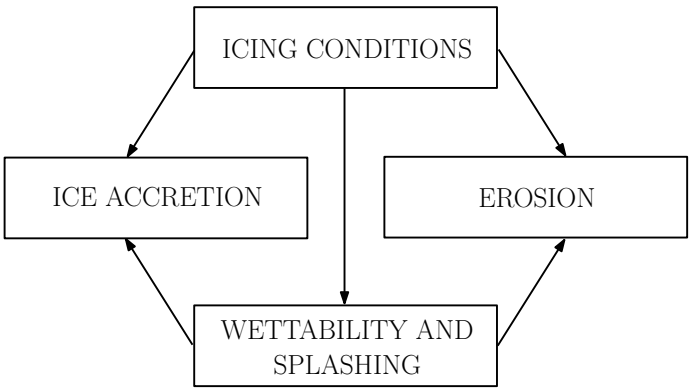

Figure 2.3. Relationship between the different phenomenon that may occur due to icing conditions. *Source:* (Gohardani, 2009)

The adverse effects of aircraft icing on fixed-wing aircraft are reduction of lift, stall angle of attack and an increase in profile drag (Gent et al., 2000). Ice accretion on wing and tail surfaces during take-off can result in control and stability problems. Additionally, accretion on propulsion system components can result in reduced propulsion efficiency and increased drag (Gent et al., 2000). Due to the mentioned adverse characteristics of aircraft icing, the best method to avoid aircraft icing is by prediction of weather conditions, commonly carried out by numerical weather prediction (NWP) models. Although these models often are computationally expensive and previously had larger

spatial and temporal limitations (Hoffmann, 1994), present methods in particular for aircraft icing applications such as the current icing potential (CIP) algorithm (Bernstein et al., 2005) and forecast icing potential (FIP) are able to outline icing potentials with a detailed diagnosis readily available (Government Accountability Office, 2010b) on the website of National Oceanic and Atmospheric Administration (NOAA).

2.2.1 Atmospheric aerosols

When an aircraft flies through the atmosphere, its external surfaces are subject to impact by a wide range of different particles. These particles are present in the atmosphere with different compositions, sizes and impact velocities. While it is difficult to delineate between all present atmospheric particles, some particles have a reoccurring tendency to appear. In particular, water and ice particles, contrails, dust, soot, volcanic ash and different pollutants make up most of the particles present in the atmosphere (Cger, 1999).

In order to estimate the range of impact particles that needs to be considered for the experimental erosion test on the novel material candidates of this study, the different particles and their physical sizes are assessed in this section. The typical atmospheric particle sizes are shown in Table 2.1.

Particle Name	Particle Size, d_m	Source
Atmospheric dust	$0.001 - 40$ μm	(Johnston, 1997)
Ice (Contrails)	$0.3 - 1$ μm	(Bond et al., 2002)
Rain droplet	$0 - 6$ mm	(Marshall and Palmer, 1948)
Soot	$50 - 100$ μm	(Petzold et al., 2003)
Volcanic Ash	< 2 mm	(Johnston, 1997)

Table 2.1. A set of particles and their mean diameter, $d_m \in [d_{\min}, d_{\max}]$ as given by the sources respectively.

2.2.2 Ice adhesion

In aircraft icing, the understanding of accretion and adhesion of ice on the body of the aircraft is crucial as it adversely alters the flight characteristics. It is therefore important to consider the long term effect of ice accretion on the surfaces of an aircraft which in essence depends on the outside air temperature (OAT), the temperature of the surface, liquid water concentration and geometrical size of the body (Gent et al., 2000). For the candidate materials it can therefore be appropriate to conduct ice accretion experiments at two different temperatures within the icing hazard range, that are feasible to attain and replicable with the experimental facility. As the accretion process is actualized by impact icing on the specimens, these can be indicative of a forward facing aircraft surface, for instance a leading edge. With reference to the inclination temperatures of aircraft icing, mentioned earlier in this section, the temperatures for the ice adhesion tests are chosen as $T = -5$ °C and $T = -10$ °C. Temperatures below these require a substantial cooling of the icing tunnel in which the tests are performed and will require a longer time to achieve. Such temperatures would further structurally rupture parts of the

ice adhesion test rig, which are limiting factors for the repeatability of the experiments. Gent et al. (2000), point out that accretion is influenced by the surface finish, another aspect that is examined in this study by ice adhesion testing on deliberately degraded candidate materials by means of wet blasting.

One of the early studies of the adhesion strength of ice to both metals and polymeric materials were conducted by (Raraty and Tabor, 1958). Since then many studies have been undertaken to examine the effect of ice adhesion on low energy surfaces (Croutch and Hartley, 1992), metals (Petrenko and Peng, 2003; Petrenko and Qi, 1999), plastics (Landy and Freiberger, 1967), lubricated surfaces (Baker et al., 1962) and super-hydrophobic surfaces (Kulinich and Farzaneh, 2009; Kulinich et al., 2011). In particular the work of Kulinich et al. (2011) conveys that superhydrophobic surfaces are not always able to repel ice, constraining their role as potential ice-repellents.

2.2.3 Ice prevention systems

In particular two different means are utilized in order to protect the aircraft from ice formation on its surfaces. In an anti-icing approach the accretion of ice is obstructed. A de-icing approach however, removes the ice in the aftermath of accretion on the surface. Three main concepts are devised in order to limit ice accretion on a surface (FAA, 2006):

- Thermal ice protection systems
- Chemical ice protection systems
- Mechanical ice protection systems

Thermal ice protection systems utilize heat to either remove accreted ice from a surface or to prevent ice from accretion on the surface. A chemical system utilizes lowering of the freezing point of water, in order to inhibit the water from freezing upon contact with the surface or by reduction of the bond strength of the accreted ice to the surface. The mechanical systems however, shed the ice from the surface. The required continuous engagement of thermal and chemical ice protection system often implies that these systems are more expensive to operate than for instance mechanical systems. The negative environmental aspects of utilizing special fluids and sacrificial coatings have further resulted in the search for icephobic coatings (Meuler et al., 2010). Figure 2.4, shows a number of ice protection systems on an aircraft.

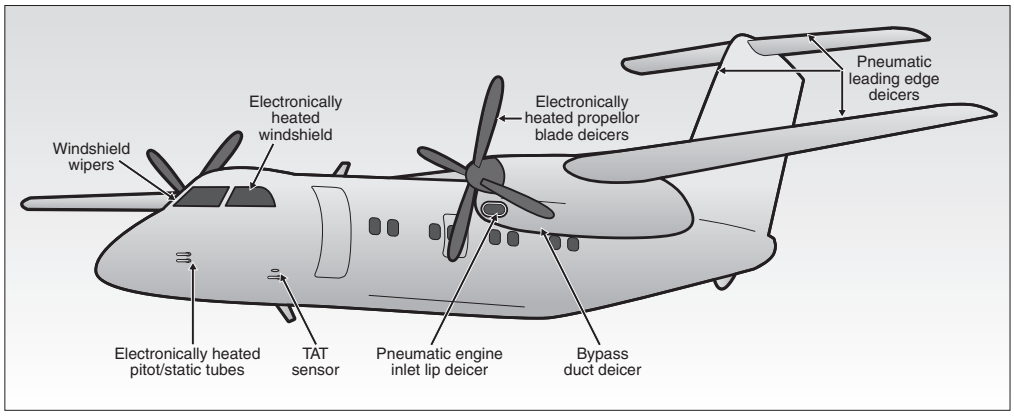

Figure 2.4. Examples of aircraft icing protection systems. *Source:* (Government Accountability Office, 2010a).

For aircraft icing, FAA and NASA's ARS database have during the period of 1998−2007, reported 828 incidents related to large commercial airliners and 989 related to noncommercial or general aviation aircraft (Government Accountability Office, 2010b). In light of this discussion, it can be established that despite the existing prediction tools and aircraft icing protection systems, icing is indeed a safety concern in aviation (Government Accountability Office, 2010a), which further serves as a motivation for further aircraft icing research.

2.3 Wettability

The intended usage of the candidate materials on an aircraft for instance in a leading edge application, entails that the airframe can be subjected to a barrage of droplets present in clouds and by precipitation. Hence, the wettability of the candidate materials is of interest in order to delineate between their wettability characters and expose their differences in wetting related to surface finish, uniformness and carbon nanotube presence. Figure 2.5, depicts a sessile drop on the surface of a specimen.

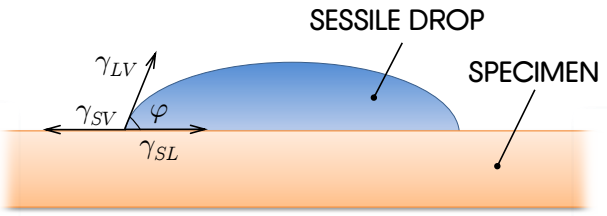

Figure 2.5. Contact angle, φ, of a sessile drop on a specimen surface. *Source:* Gohardani (2009) adapted from Kumar and Prabhu (2007).

The subscripts utilized in the figure are S for solid, V for vapor and L for liquid. For an ideal, non reacting surface the dynamic driving force, F_D as a function of time, is given by (Kumar and Prabhu, 2007)

$$F_D = \gamma_{SV} - \gamma_{SL} - \gamma_{LV}\cos(\varphi) \tag{2.1}$$

where γ is the tension at the interface between the two different phases. If there is no wetting driving force then, $F_D \equiv 0$, which corresponds to Young's formula (Young, 1805):

$$\cos(\varphi) = \frac{\gamma_{SV} - \gamma_{SL}}{\gamma_{LV}} \tag{2.2}$$

which is not defined for $\cos(\varphi) = 0$. Therefore, Adamson and Gast (1997) defined the spreading coefficient, S, as a means for analyzing the spread when this condition is fulfilled with S defined as

$$S = \gamma_{LV}\{\cos(\varphi) - 1\} = \gamma_{SV} - \gamma_{SL} - \gamma_{LV} \tag{2.3}$$

Kumar and Prabhu (2007) have identified seven different types of contact angles in their work. Table 2.2 refers to intrinsic contact angles, which in effect are static.

Contact angle, φ	$\cos(\varphi)$	Type of wetting
0	$+1$	Complete
$\pi/4$	$+1/\sqrt{2}$	Partial
$\pi/2$	0	$\varphi_{SV} = \varphi_{SL}$
$3\pi/4$	$-1/\sqrt{2}$	Partial non-wetting
π	-1	Non-wetting

Table 2.2. Different types of wetting based on the value of the contact angle, φ. *Source:* (Gohardani, 2009) adapted from (Kumar and Prabhu, 2007)

Conceptually, a dynamic contact angle is a time dependent contact angle that

occurs upon a moving contact line. In particular, the advancing contact angle, defined upon advancement toward the vapor phase and a receding contact angle, obtained as the contact angle is receding away from the vapor phase are of interest. The difference between the advancing and receding contact angles where the advancing angle is greater than the receding one is called the hysteresis (de Gennes et al., 2004).

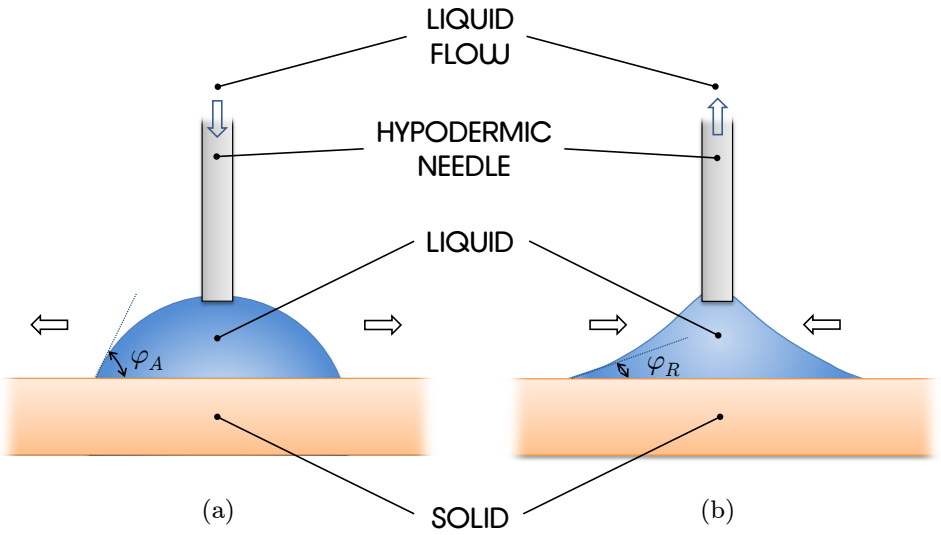

Figure 2.6. Schematic view of (a) the advancing contact angle, φ_A and (b) the receding contact angle, φ_R.

Factors that affect surface wetting are surface roughness, heterogeneity of the surface, temperature, the experimental conditions and the properties of the liquid (Kumar and Prabhu, 2007). In the terminology of surface wetting, hydrophobicity refers to the non-wetting characteristics of a surface. Hydrophilicity conversely, is the nature of a surface that easily becomes wet. These two properties can be observed by contact angle measurements (Bregg,

2006) as described in the previous section. The hydrophilic or hydrophobic nature of a surface can be described based on the value of the static contact angle, $\widetilde{\theta}$. For a hydrophilic surface, $\widetilde{\theta} < 90°$. A hydrophobic surface however has $\widetilde{\theta} > 90°$ (Bhushan and Jung, 2007). More recently a profound interest has been devoted to super hydrophobic surfaces with $\widetilde{\theta} \in [150°, 180°]$.

2.4 Erosion

Erosion is often referred to as a process at which a surface experiences damage upon contact with droplets or particulates. In nature, erosion is encountered in instances where the flow of a fluid is observed. Erosion may hence occur by for instance wind, water, ice and gravity (Gifford, 2005). In this description, it is important to distinguish between impingement and erosion. For rain erosion in particular Adler (1999), points out that impingement does not always result in erosion. However, it is observed that impingement is of necessity for erosion to occur. Impingement is merely the impact of the droplet or particulate on the target. Erosive wear is a collective name for a number of erosive mechanisms as shown in Figure 2.7.

The mechanisms differ based on the relative impact velocity, orientation, size and properties of the impacting droplets or particles (Stachowiak and Batchelor, 2006). For this experimental study, relatively high velocities approaching the same orders of magnitude as the velocity of commercial airliners are of interest. Hence, the erosive wear that will be encountered correspond to (c), (d) and (e) in Figure 2.7.

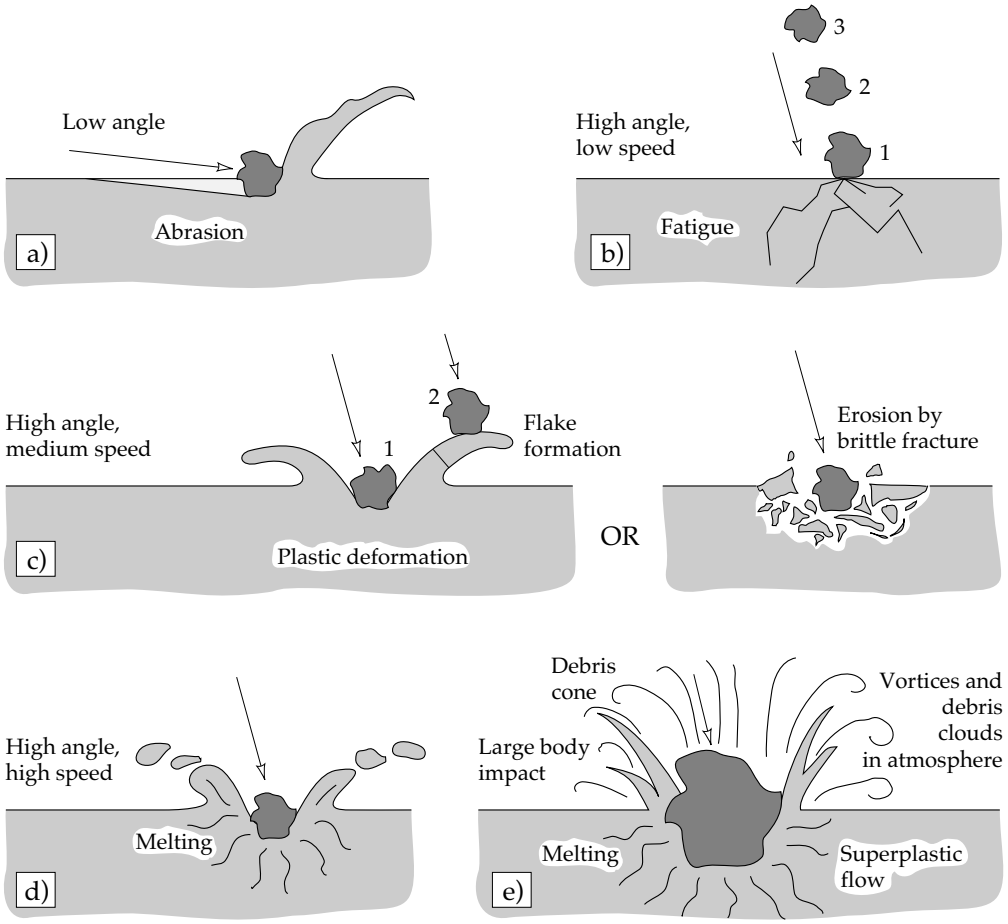

Figure 2.7. Erosive wear based on impact velocity and incident angle. *Source:* Adapted from (Stachowiak and Batchelor, 2006)

2.4.1 Classification of damage mechanisms

A number of different deformation mechanisms have in particular been identified for different solids subjected to liquid impact. The specification by Bowden and Brunton (1961) identifies the following deformations:

(*i*) circumferential fracture on the surface
(*ii*) subsurface fractures
(*iii*) plastic deformation in a large scale
(*iv*) deformation due to shear in the vicinity of the impact zone periphery
(*v*) fracture arising from the reflection and interference of stress waves

A brief description of these damage mechanisms is outlined in this section based on the complete discussion regarding these deformations by Bowden and Brunton (1958, 1961).

(i) Circumferential fracture on the surface

This type of deformation occurs upon impact, as a result of the distribution of pressure over the impact area. Following the lateral jetting, the stress distribution on the surface of the solid is such that radial tensions arise across the periphery of the impact site and its proximity. The circumferential fractures occur when these tensions exceed the breaking strength of the solid. However, no fracture within the area under pressure takes place, due to the compressive nature of the stresses within this region.

(ii) Subsurface fracture

This failure mechanism stems from a plastic flow, located at the vertical axis through the impact site where the maximum shear stress occurs. The time dependent pressure distribution dictates the location of the point of plastic flow below the surface. Fracture arises along the flow lines as a consequence of the short intense pulse over this region, upon which the solid is unable to

relieve the stress and deform rapidly.

(iii) Plastic deformation in a large scale

Similar to subsurface fracture this deformation initiates and spreads until the entire region yields. This type of deformation has mainly been observed in metals.

(iv) Deformation due to shear in the vicinity of the impact zone periphery

A normal impact of the liquid in essence produces suitable sites for shear failure. Pre-existing flaws on the surface, will additionally shear under tangential flow of the liquid, regardless of the normal forces.

(v) Fracture arising from the reflection and interference of stress waves

This type of fracture emanates from the interaction of the reflected compression pulse with the free boundaries of the specimen and the damage extending well beyond the impact zone. (Bowden and Field, 1964) examined this effect in particular for thin plates where the interaction of the Rayleigh-wave gave rise to a number of reinforcement scenarios described in further detail in Section 4.2.

According to Evans (1979), two distinct damage extremes related to impact fracture damage can be delineated. The first one concerns, impact by highly deformable projectiles on relatively hard targets. This type of impact primarily results in short circumferential cracks and surface chipping in particular for liquid projectiles. The formed cracks are located outside an undamaged

zone with the crack density, depth and length initially increasing to a maximum with the distance away from the impact site and approaching zero at the outer annulus of the damaged zone. The second damage extreme arises upon impact with relatively hard projectiles. The three distinct cracks identified in this context are radial cracks, lateral cracks and conical cracks. Observations by Knight et al. (1977) and Evans (1979), indicate that radial and conical cracks are initially formed and confined to existing fractures within the material, followed by the lateral cracks in the unloading phase, often leading to material removal. A spectrum of other possibilities, between the aforementioned damage extremes can also be responsible for fracture damage. A schematic of a radial crack and a conical crack is shown in Figure 2.8.

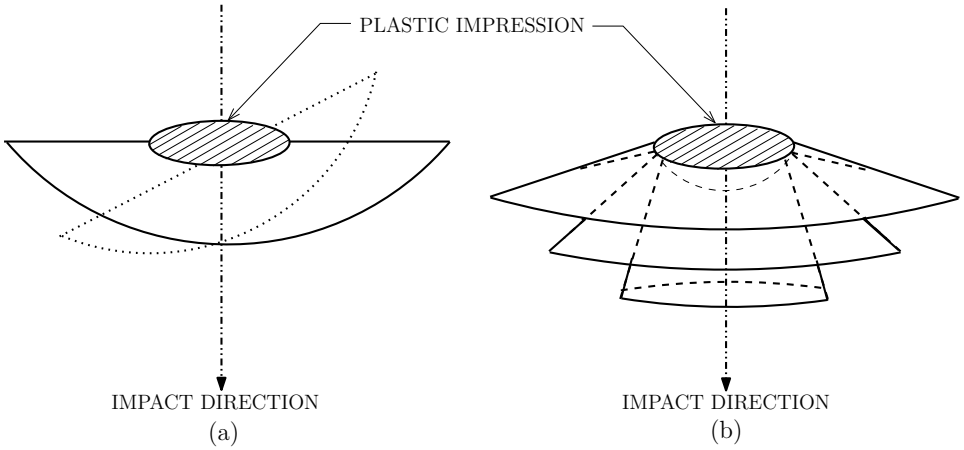

Figure 2.8. A schematic diagram of the morphology of (a) A radial crack and (b) A conical crack. Adapted from Evans (1979).

Hertzian cone cracks

Hertz (1881, 1882) initially studied the formation of cone cracks in brittle materials by the use of spherical indenters. In accordance with the contact

equations of Hertz, the maximum tensile stress occurs at the edge of the contact circle. This stress on the specimen surface is responsible for the formation of Hertzian cone cracks following an impact. The cracks initiate normal to the specimen surface and extend downwards into the material prior to full widening into a fully developed cone (Fischer-Cripps, 2007). Upon sufficient intersections of the formed cone and ring cracks, chunks of material breaks out, resulting in a mass loss. As a consequence, radial cracking occurs and the material degrades (Schmitt Jr., 1980).

Erosion rate in brittle materials

The volumetric erosion loss per impact V_L, in a brittle and homogeneous material can based on the elastic plastic theory be written as (Evans, 1981)

$$V_L = \frac{\breve{\lambda}(v^2 m)^{\frac{7}{6}}}{K_{Ic} H^{\frac{1}{6}}} \left(\frac{E}{H}\right)^{\frac{4}{5}} \tag{2.4}$$

In Equation (2.4), $\breve{\lambda}$ is a material independent coefficient, v is the aerial speed of the erodent, m is the mass of the erodent, K_{Ic} is the fracture toughness, and E and H are the Young's modulus and hardness of the target, respectively. The erosion rate is proportional to the volumetric erosion loss, $\dot{E} \propto V_L$.

2.4.2 Erosion in Aviation

Erosion of materials has for a long time been recognized by researchers within the aerospace industry as it can influence the useful life of the structure and in extreme cases the air-worthiness of the aircraft. A recent review by Gohardani (2011) identifies that in-flight testing has been used for a number of different

aircraft in order to characterize the performance of various materials as shown in Figure 2.9 and Table 2.3.

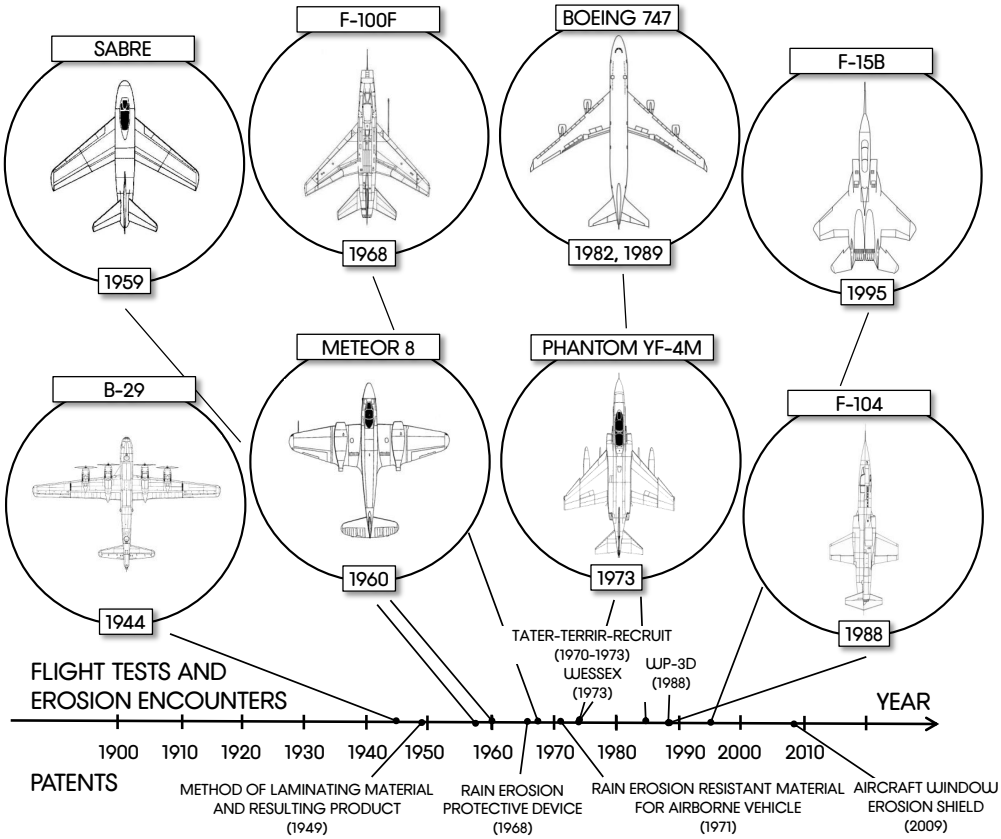

Figure 2.9. A timeline of instances related to in-flight erosion encounters or experiments on various aircraft. *Source:* (Gohardani, 2011).

According to Gohardani (2011) erosion is observed by a weight or optical transmission loss, decrease in mean volume or increase in cracks and their respective sizes, with regards to the structure of the air vehicle. The review also identifies that military aircraft are more frequently exposed to erosion due to higher cruise speeds, take-off and severe landing conditions from unconventional runways (Gohardani, 2011). In light of the mentioned observations, the

Year	Test aircraft	Test samples	Observations
1944	B-29	N/A	• Severe damage to leading edges and radome at moderate rainfall rates
1960	Meteor VT 150	Perspex	• Similar erosion results as whirling arms • Risky conditions for the pilots • $\approx$ 0.60 Mach • Altitude $\approx 1,000$ ft
1968	F-100F	Nickel Polyurethanes Neoprene Nitrile rubber Graphite Carbon Phenolic	• No indication of erosion observed on the nickel and polyurethane coatings • Significant erosion observed on neoprene and nitrile coatings
1970-1973	Tater-Terrier-Recruit†	Silica Phenolic Glass Phenolic Tungsten Rubber Phenolic	• Hydrometeor impact on ablative materials utilized as heatshields and nosetips of vehicles during reentry • 7.94 Mach − 9.41 Mach • Altitude $\in [10\ 000, 14\ 000]$ ft
1973	Wessex Helicopter	N/A	• Roughened rotor blades to simulate erosion • Premature rise in power, dependent on roughness
1975	Phantom YF-4M†	Perspex Araldite 1020/1180 Araldite 1180 Sierracin Fluorosil Viton Titanium Aluminum	• Flight tests carried out for the Concorde aircraft • $\alpha \in [5°30', 45°]$ • $I_R \in [5, 52]$ mm $\cdot$ h^{-1} • 0.76 Mach − 1.23 Mach
1988	F-104, WP-3D	AFRSI RCC Advanced TPS tile LI900 tiles LI2200 tiles	• Tests in low-altitude cumulus/high-cirrus clouds • Tile damage threshold defined as surface pitting • USAF KC-135 dropped from tests due to inadequate replication of the rain conditions • Flight tests in natural rain resulted in damage and erosion of the TPS tiles • 1.5 Mach • $\alpha = \{0°, 15°, 30°, 60°, 90°\}$
1995	F-15B	SHTPS Preoxidized Inconel 617 THS	• Conducted at NASA Dryden for the X-33 RLV • A fixture for 8 rows of TPS samples was used • $\alpha = \{0°, 10°, 20°\}$ • 0.76 Mach

Table 2.3. Examples of in-flight rain erosion tests. The following abbreviations have been utilized in the table: Advanced Flexible Reusable Surface Insulation (AFRSI), Super alloy Honeycomb TPS (SHTPS), Titanium Honeycomb Sandwich (THS), and Reinforced Carbon Carbon (RCC). N/A refers to instances where no specific materials are mentioned. † = Only selected materials are shown due to the large number of materials considered during the flight tests. *Source:* Adapted from Gohardani (2011).

modeling of erosion is identified as complex, in particular for advanced materials such as the considered materials in this study due to the different modeling regimes that might emerge from nano- to a macro-scale modeling. Erosion of the candidate materials in this study is essential in order to demonstrate their fitness of use on a commercial airliner. Figure 2.10, outlines a number of factors that may reduce erosion in aviation.

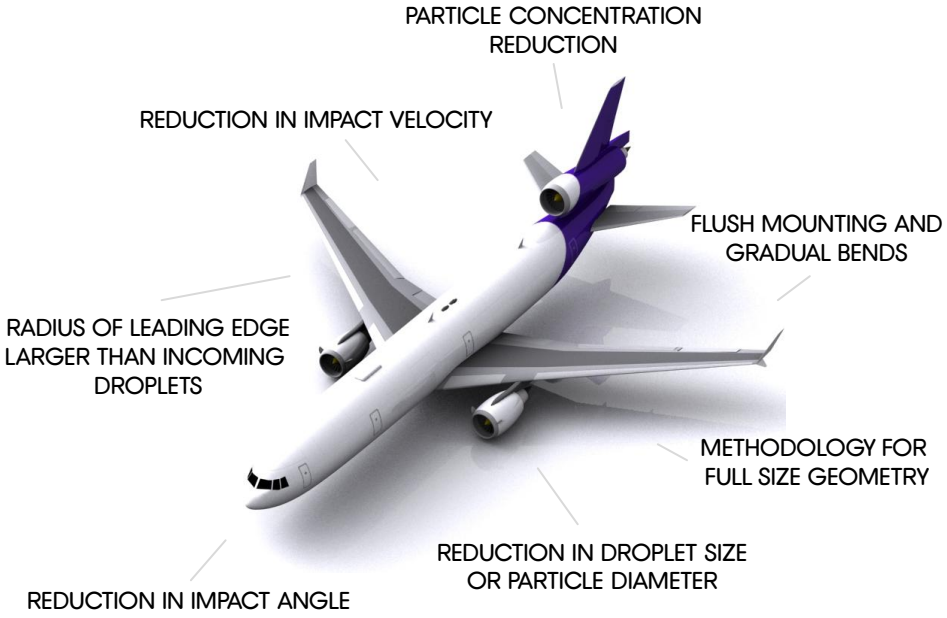

Figure 2.10. An overview of the factors that may reduce erosion in aviation. *Source:* Gohardani (2011).

2.4.3 Liquid-Solid Impact

As the usage of the candidate materials on an aircraft entails that they would become subjected to precipitation and in order to comprehend the unfolding

of erosion, the physical effects caused by impingement of liquid droplets on a specimen surface are considered. For the instance where a water droplet impinges the surface at a normal angle, two wave fronts are created with the longitudinal wave preceding the transverse wave, as shown in Figure 2.11.

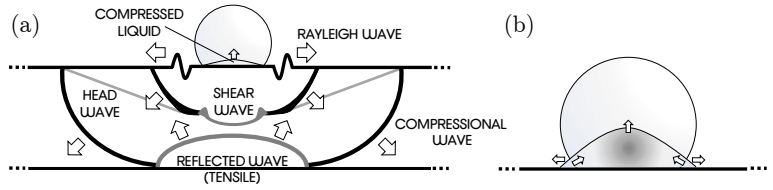

Figure 2.11. Schematic view of a shock wave propagation occurring upon impact of a spherical drop on a solid surface. (a) depicts the three waves that emanate following the impact and (b) shows the radial jetting upon movement of the contact periphery ahead of the shock wave in the drop initiating a release wave. *Source*: Adapted from Woods (1968); Coad and Field (1997).

According to Achenbach (1987), the speed of the longitudinal wave velocity is given by

$$c_L = \left\{ \frac{E}{\rho(1+\nu)} \left(\frac{\nu}{1-2\nu} + 1 \right) \right\}^{\frac{1}{2}} \tag{2.5}$$

The transverse wave velocity is further given by

$$c_T = \left(\frac{E}{\rho(2+2\nu)} \right)^{\frac{1}{2}} \tag{2.6}$$

The impact gives rise to another wave, called the Rayleigh wave which is confined to the surface of the specimen and is responsible for $\cong 2/3$ of the collision energy (Harris, 1999). The velocity of the Rayleigh-wave progression in a solid is given by

$$c_R = \left(\frac{0.862 + 1.14\nu}{1+\nu}\right)\left(\frac{E}{2(1+\nu)\rho}\right)^{\frac{1}{2}} \tag{2.7}$$

where ν, denotes the Poisson's ratio, ρ, is the density of the specimen and E is the Young's modulus. Hence, by knowing these three material properties, theoretical values of the Rayleigh wave velocity c_R, longitudinal wave velocity c_L, and transverse wave velocity c_T, can be determined.

Following a liquid-solid impact, a compressible stage and an incompressible stage can be identified. The pressure that arises during the compressible stage is often referred to as the water hammer pressure and has a magnitude of

$$P_w = v\left(\frac{\Pi_{i=1}^{2}\rho_i C_i}{\Sigma_{i=1}^{2}\rho_i C_i}\right) \tag{2.8}$$

This pressure is often approximated by

$$P_c \approx \rho_1 c_1 v \tag{2.9}$$

at the center or the impact site, where v denotes the impact velocity, ρ is the density, C is the shock velocity, indices 1 and 2 refer to the liquid and solid respectively, and c_1 is the shock speed in water. It is also notable that for a droplet curvature diameter of $\widehat{D}$ upon a contact diameter of $d_c = \widehat{D}v/c_1$, higher pressures than the water hammer pressure occur, but these are neglected due to their relative short duration (Lesser, 1981). The pressure release occurs after a time period

$$\tau = \frac{\widehat{D}v}{4c_1^2} \tag{2.10}$$

Following the compressible stage the pressure approaches the Bernoulli pressure

$$P_B = \frac{\rho_1 v^2}{2} \tag{2.11}$$

after a time elapse of (Field, 1999)

$$\tau^* = \frac{3\widehat{D}v}{4c_1^2} \tag{2.12}$$

For brittle materials, the strength S and fracture toughness K_{Ic}, are related to the radius of the fracture commencing flaw $\tilde{r}$, as (Chantikul et al., 1981; Hertzberg, 1989; Mecholsky, 1991)

$$\tilde{r} = \left(\frac{K_{Ic}}{1.24 \cdot S}\right)^2 \tag{2.13}$$

This entails that the decrease in strength of a brittle material $S \propto \tilde{r}^{-\frac{1}{2}}$.

2.5 Polymer Matrix Composite Resins

The usage of polymer composites has expanded considerably since their introduction half a century ago. Polymer composites are now utilized in a wide range of applications in the aeronautical industry, for space exploration, in medical equipment and robotic arms, in submarines, in the oil industry and manufacturing of sporting goods and electronic devices (Shalin, 1995). Particularly in commercial aircraft, there has been a significant increase in the total structural weight percentage attributed to composites, as shown in Figure 2.12, a trend which is anticipated to growth in the future. For this purpose,

polymeric composites reinforced with carbon nanotubes, serve as appropriate candidate materials for the purpose of future implementation on a commercial airliner, and hence are the subject of the present study.

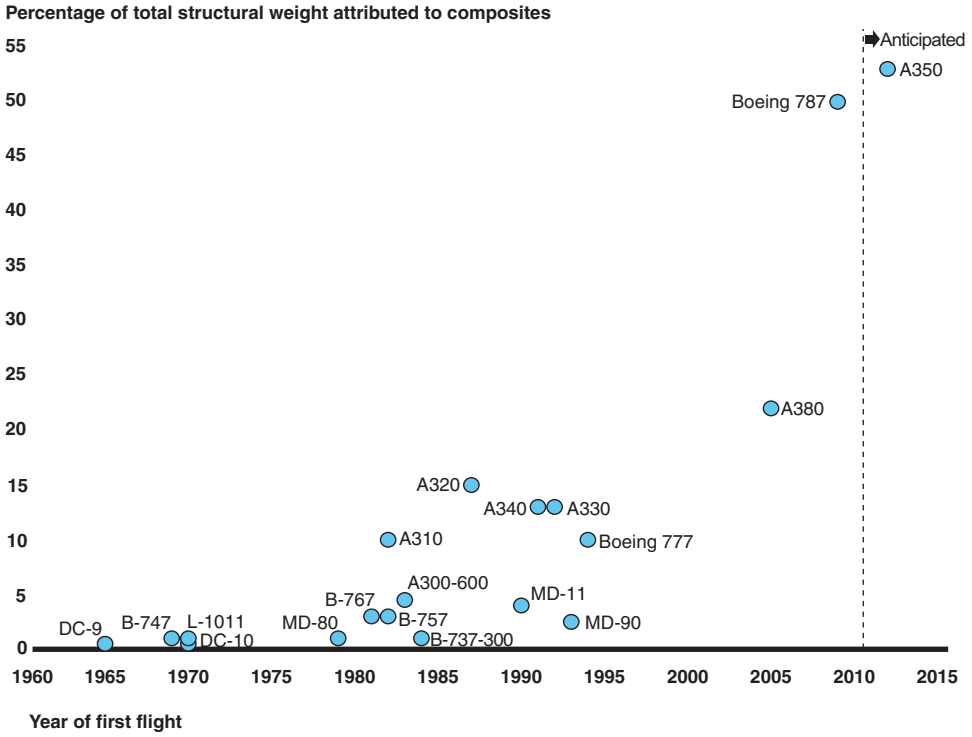

Figure 2.12. Commerical aircraft maiden flight versus total structural weight percentage attributed to composites. *Source:* Government Accountability Office (2011).

2.5.1 Polymer nanocomposites

With advancements in material science, polymer nanocomposites are becoming very attractive candidates in particular within the aerospace industry. These materials are essentially composites of polymers, reinforced with nanoparticles similar to the candidate materials in the present study. The reason for

considering polymer nanocomposites stems from their potential to achieve superior mechanical, thermal, physical, electrical and chemical properties. Theoretically, enhancing the performance of the pure resin is obtainable upon implementation of nanoparticles into the composite (Jordan et al., 2005). Nonetheless, due to numerous factors, some of the theoretical improvements have still not been achieved. In a review paper regarding polymer nanocomposites reinforced with carbon nanotubes, Moniruzzaman and Winey (2006) outline the numerous factors that may contribute to lack of performance despite the presence of the nanoparticles. These factors include the type of carbon nanotubes, their purity, defect density and dimensions, their loading, dispersion state, alignment in the polymer matrix, and the interfacial adhesion between the polymer matrix and carbon nanotubes. In particular, Moniruzzaman and Winey (2006) emphasize on the difficulties associated with carbon nanotube dispersion and refer to its method of quantification as a challenge.

Carbon Nanotubes

Since the introduction of carbon nanotubes (Ijima and Ichihashi, 1993), these allotropes of carbon, have been attractive because of their electrical and mechanical properties in a wide range of applications (Sclater and Chironis, 2007). The tensile Young's modulus and tensile strength of single-walled carbon nanotubes (SWCNT) and multi-walled carbon nanotubes (MWCNT) in comparison to Kevlar, is approximately 17 times higher and 41 times higher, respectively (Endo et al., 2008).

Some physical properties of carbon nanotubes and comparison to other reference materials, are outlined in Table 2.4.

Property	SWCNT	Comparison Material
Size	$d_{\text{SWCNT}} \approx 1.6 - 1.8$ nm	$d_{\text{MWCNT}} \approx 15 - 20$ nm
Density	$\rho_{\text{SWCNT}} \approx 1.33 - 1.40$ g/cm^3	$\rho_{\text{Al}} \approx 2.7$ g/cm^3
Tensile strength	$\sigma_{\text{UTS}} \approx 45$ GPa	$\sigma^{\star}_{\text{UTS}} \approx 2$ GPa
Current capacity	$\breve{I} \approx 1 \cdot 10^9$ A/cm^2	$\breve{I}_{\text{Cu}} \approx 1 \cdot 10^6$ A/cm^2
Temperature stability	$\breve{T} \approx 1000$ °C	$\breve{T}_{\text{metal}} < 600 - 1000$ °C
Young's modulus	$E_{\text{SWCNT}} \approx 1$ TPa	$E_{\text{MWCNT}} \approx 1.28$ TPa

Table 2.4. Physical properties of carbon nanotubes and comparison to other reference materials. In the table, the symbol ($\star$) denotes high-strength steel alloys. *Source:* (Collins and Avouris, 2000)

Despite the superior properties of carbon nanotubes in comparison to carbon fibers, one of the recognized problems is encountered related to the interface between the polymer matrix and the individual nanotubes under loading conditions (Endo et al., 2008; Schadler et al., 1998; Ajayan et al., 2000). This complexity is a result of two factors: Firstly, their aggregate nature entails that they behave differently than individual nanotubes. Moreover, an imperfect manufacturing or mixing can further weaken the interface between the polymer matrix and the carbon nanotubes, resulting in a poor load transfer (Ajayan et al., 2000). In the literature (Buschow et al., 2001) there is often a distinction between single walled carbon nanotubes (SWCNT) and multi-walled carbon nanotubes (MWCNT). In effect, Reich et al. (2004) merely describe SWCNT as hollow cylinders made of a single layer of graphite. Similarly, MWCNT are described as a number of concentric cylinders. Both SWCNT and MWCNT have similar length dimensions $\sim \mathcal{O}(\mu\text{m})$, but the diameters of MWCNT exceed that of SWCNT, $d_{\text{MWCNT}} > d_{\text{SWCNT}}$ (Reich et al., 2004).

Figure 2.13 shows a multi-walled carbon nanotube.

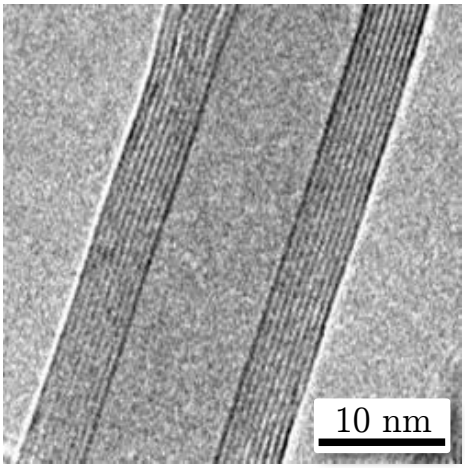

Figure 2.13. A Transmission Electron Microscope (TEM) photograph of a multi-walled carbon nanotube. The concentric walls surround a channel which is shown in the center of the photograph. Adapted and reprinted with the kind permission of NanoLab Inc. (2011)

Toxicity

One of the important factors when handling carbon nanotubes is the toxicity of these materials. It is therefore imperative that the impact of these materials on human health is determined. This task however, is proven to be rather intricate, due to the wide range of usage applications associated with carbon nanotubes, as outlined by Fiorito (2008). A number of studies have been undertaken by researchers in order to examine the effect on CNT on cells (Porter et al., 2007; Donaldson et al., 2006). The research about the toxicity is still ongoing but it indicates that carbon nanotubes may affect the human health adversely (Ralph and Hodson, 2009; Lam et al., 2006).

Safety

As the specimen loaded with carbon nanotubes will be utilized in a laboratory setting at Cranfield University, United Kingdom, some precautions regarding the safety has been undertaken. An extract of a sample Control of Substances Hazardous to Health Regulations (COSHH) form, for one of the specimens in this study is shown in Appendix J.

2.6 Conclusions

The literature survey related to the present study extends into several different disciplines which include but are not limited to material science, fluid mechanics and solid mechanics. The challenge of this project is to interlink aspects of these disciplines in order to fulfill the sought project objectives. Equally, it is established that the obtained results are applicable in all the aforementioned disciplines. It can be inferred by the literature survey that a paucity of reported investigations are carried out in the context of aircraft icing, where in particular the influence of carbon nanotubes is examined in the open literature. This limitation might be related to the complex manufacturing of resins with a well dispersed body of embedded carbon nanotubes and safety consideration.

It is also evident from the literature review that despite the promising properties of carbon nanotubes, studies indicate that simply mixing carbon nanotubes in a polymer matrix resin, does not automatically imply that a higher load transfer can be obtained. This indication has to be taken into consider-

ation and examined upon erosion of the candidate material which indeed are polymer matrix composites with carbon nanotube reinforcement. The erosion tests serve as a good indicator to confirm whether a better mixing of the carbon nanotubes is of necessity. Further it is recognized that a simplified model is beneficial in order to describe the surface behavior upon wetting and for differentiation between surfaces. As such a model is not encountered in the literature survey, it is recommended that such a model is developed. Another concrete conclusion based on the literature review is that the thickness of the specimens may have a large influence on the liquid erosion results.

In this chapter, the temperatures for the ice adhesion tests based on the literature review have been determined. It can also be stated that the conducted literature survey does not specifically determine the properties of the candidate materials within this study, due to their novel manufacturing and lack of existing material data for these materials. Therefore, it is identified that specific attributes related to these materials are to be established in this study.

Chapter 3

Physical Properties

3.1 Introduction

The physical properties of the substrate materials are in large determined by the manufacturing and preparation of the materials based on the usage of reinforcement, curing temperature and duration, as well as by the glass transition temperature, the dispersion of carbon nanotubes and the nature of the materials. In this study, once a set of specimens were manufactured, they were exposed to various tests determining their physical properties such as density, hardness and stiffness for instance represented by the acoustic impedance. Furthermore, an assessment was carried out based on non-uniformities of the aforementioned properties. Upon utilizing this approach, the specimens could be optimized based on a set of desired properties, and re-manufactured with knowledge of previous inherent physical properties. Hence, a loop between specimen preparation, physical property assessment and non-uniformity assessment was formed which was optimized for desired specimen properties, as

shown in Figure 3.1. The application of this approach within the framework of the supplied specimens was limited due to the large number of tests performed on each specimen, but may be applicable for future research efforts with the utilized specimens.

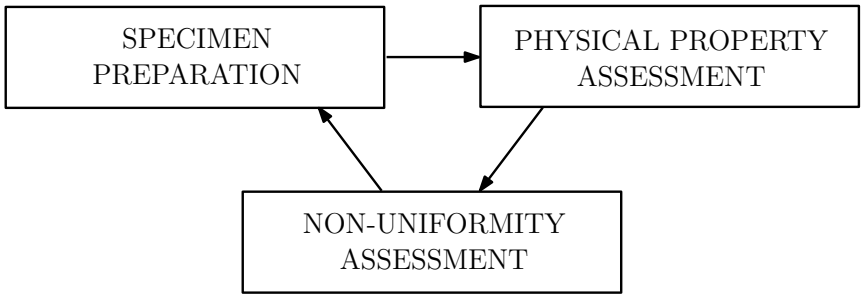

Figure 3.1. The relation between specimen preparation, physical property assessment and non-uniformity assessment which can result in optimization of the desired specimen properties.

3.2 Experimental specimens

A total number of 10 different materials referred to hereafter with a specimen number S_n were utilized in this study in two different prescribed conditions; as supplied and in an eroded condition, with $n = \{1, 2, \ldots, 10\}$. The majority of these materials were established epoxy resins commonly used within the aerospace industry with the addition of carbon nanotubes as a reinforcing agent. The set of candidate materials, feature 4 materials with pure resins, 3 resins with carbon nanotube reinforcement, 1 resin with aluminum nitride nanoparticle reinforcement and 2 multi-layered materials, as shown in Table 3.1. More explicitly, specimens S_1 (LY564) and S_2 (LY564 + 0.5% MWCNT)

were both combinations of Araldite® LY564/Aradur® 2954 with the exception that specimen S_2 also featured multi-walled carbon nanotubes (MWCNT) with 0.5% wt. Graphistrength® C100. Specimen S_3 (32_MINAS1_06), S_4 (32_A05_CANBIO1_06), S_5 (32_MINAS1_07), S_6 (32_A05_CANBIO1_07) were Araldite® MY0510/Aradur 976-1 combinations, with S_4 and S_6 having 0.5% wt. MWCNT as a reinforcement. Specimen S_7 (Araldite DBF) was an Araldite® DBF/Aradur® HY956EN base resin with 10% wt. aluminium nitride nanoparticles. Specimen S_8 (SW404 + XB5173) was a gelcoat consisting of a SW404/XB5173 combination. In contrast, to specimens $S_1, \ldots, S_8$ which were resins without any additional layers, specimens S_9 (LAYSA_ICE_01) and S_{10} (SICOMP_NA_ICE1) were multi-layered specimens consisting of several different materials. In order to facilitate the reference to the specimen names, the nomenclature of S_n, with $n = \{1, 2, \ldots, 10\}$ was utilized. Adopting this nomenclature specimens S_2, S_4, S_6 and S_{10} were reinforced with carbon nanotubes. The layered structures of the S_9 and S_{10} specimens are shown in Figure 3.2.

No.	Specimen Name	L [mm]	W [mm]	t [mm]	A [mm^2]	CNT
S_1	LY564	90	70	1	6300	N/A
S_2	LY564 + 0.5% MWCNT	90	56	3	5040	0.5
S_3	32_MINAS1_06	100	22	5	2200	N/A
S_4	32_A05_CANBIO1_06	100	22	6	2200	0.5
S_5	32_MINAS1_07	124	56	$3-5$	6944	N/A
S_6	32_A05_CANBIO1_07	120	56	5	6720	0.5
S_7	Araldite DBF	70	51	9	3570	N/A
S_8	SW404 + XB5173	80	47	4	3760	N/A
S_9	LAYSA_ICE	105	50	$4-5$	5250	B†
S_{10}	SICOMP_NA_ICE	100	33	$4-5$	3300	5.5
	Averaged properties	$\overline{L} \cong 98$	$\overline{W} \cong 46$	$\overline{t} \cong 4.6$	$\overline{A} \cong 4528$	

Table 3.1. Geometrical properties for the specimens. The averaged properties are given by the last row in the table. A given range for the thickness, exhibits a non-uniform thickness of the specimen. The weight percentage of carbon nanotubes are given in the CNT column and the symbol B† refers to Buckypaper.

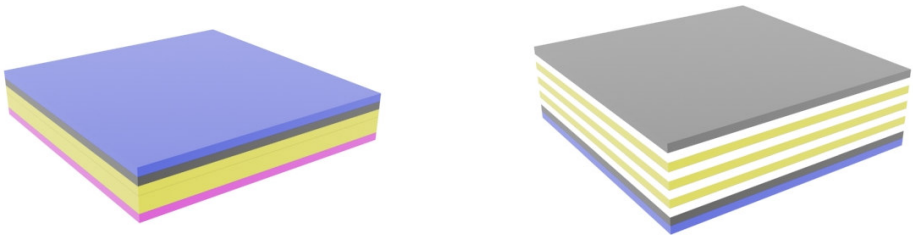

Figure 3.2. A schematic view of the provided multi-layered materials S_9 (left) and S_{10} (right). The schematic is not drawn to scale, and all layers have the same thickness for illustration purposes only.

The supplied materials were obtained from Tecnalia, Spain in cured form. Initially, a number of trial materials were manufactured in order to improve the manufacturing process, prior to consideration of the supplied candidate materials. The reasoning for the trial manufacturing is recognized in the literature (Endo et al., 2008), highlighting the processing of epoxy polymers filled with carbon nanotubes even at low weight percentage (< 5 % wt.) of carbon nanotubes as complicated, due to the high increase of viscosity. In the pristine state, no morphological treatment to the specimen surface were applied. This condition represents instances where no material degradation has been observed upon implementation of the material on an aircraft during flight. The second state was an eroded state of the material, attained upon its wet blasting by alumina. The choice of this abrasive stemmed from the need to obtain a fine degradation of the material without a catastrophic failure. Although, an eroded state of the material results from an accelerated testing technique, it does allow for establishment of surface morphology modifications on the resulting wetting characteristics of the materials. The average values of the surface roughness pre-erosion R_a^p, surface roughness post-erosion R_a^e and percentage change in surface roughness ΔR_a are shown in Table 4.5. The following section describes the specimen preparation for the given specimens in this study. Specimens 32_MINAS1_06 (S_3) and 32_A05_CANBIO1_06 (S_4) were prepared similarly to 32_MINAS1_07 (S_5) and 32_A05_CANBIO1_07 (S_6), respectively, with the exception that the former pair were the early prototypes of the materials.

LY564 (S_1)

The LY564 supplied by Huntsman had the epoxy component, Araldite® LY564 and hardener Aradur® 2954 both in liquid form, without any nanofillers. The epoxy was mixed with the hardener by mechanical stirring at 20 rpm for a period of 15 minutes. A 1 hour 80 °C and 8 hours 140 °C curing cycle was employed for preparation of this specimen.

LY564 + 0.5 % MWCNT (S_2)

The LY564 + 0.5 % MWCNT sample was the nanocomposite of the LY564, consisting of the epoxy component Araldite® LY564 and hardener Aradur® 2954 in liquid form. The nanofiller in this material was 0.5% of weight of MWCNT, Graphistrength® C100, from Arkema. The length of the MWCNT was $0.1 - 10$ μm, with the outer mean diameter $10 - 15$ nm and mean agglomerate size $\sim 200 - 500$ μm. Initially, a masterbatch consisting of a 3.45 wt.% MWCNT was prepared by means of a Heidolph RGL stirrer and a Cowles disk operated at 5 000 rpm for 15 minutes. Upon dilution of the masterbatch with the neat epoxy, an EXAKT 80E three-roll mill was employed for processing of the mixture by calendering. The used feed roll, center roll and apron roll were set to 17 rpm, 50 rpm and 150 rpm, respectively. Upon feeding the mixture into the three-roll mill and shearing for 2 minutes prior to collection, the entire collected volume was passed-through the mill at progressively smaller gap settings between the rolls. The collected epoxy and carbon nanotube dispersion was thereafter mixed with Aradur® 2954 by mechanical stirring at 20 rpm. The employed curing cycle for this specimen was similar to that of the

pure resin.

The obtained level of carbon nanotube dispersion by means of a scanning electron microscope (SEM) for the LY564 + 0.5 % MWCNT (S_2) specimen, is shown in Figure 3.3, with (a) showing generally uniform rich domains of the carbon nanotubes within the specimen at 5 000 × magnification and (b) acquired at 15 000 × magnification, aggregated carbon nanotubes in micron-size bundles.

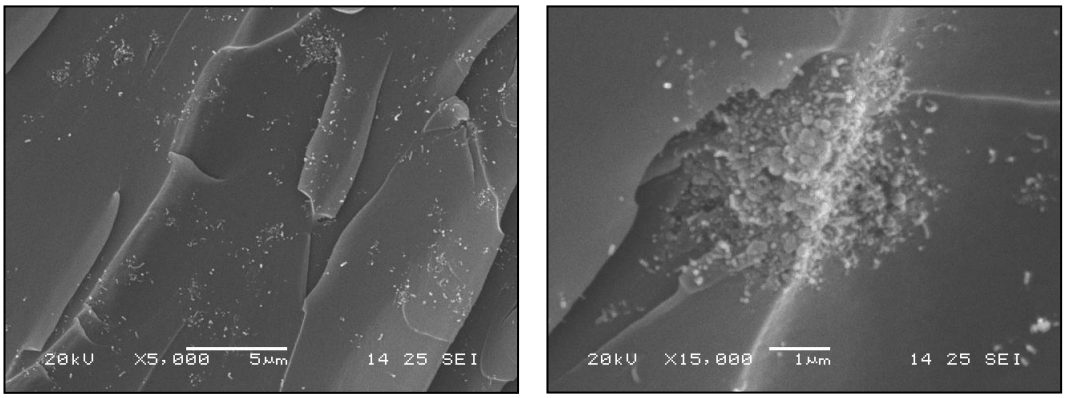

Figure 3.3. SEM photograph of the LY564 + 0.5 % MWCNT (S_2) specimen, containing 0.5 wt. % carbon nanotubes at (a) 5 000 × magnification and (b) 15 000 × magnification.

32_MINAS1_07 (S_5)

This bi-component epoxy resin system, consisted of an Araldite® MY0510 epoxy in liquid form and an Aradur® 976−1 hardener in powder form, without a nanofiller. The mixing of the components were carried out in accordance

with 100 parts A and 62 parts B based on weight mix-ratio, followed by mechanical stirring under vacuum during 30 minutes at 20 rpm. Upon casting in a metallic mould, a curing process in an oven was executed in two 30 minute cycles at 80 °C and 100 °C, followed by two 90 minute cycles at 120 °C and 150 °C, and a final 120 minute cycle at 177 °C.

32_A05_CANBIO1_07 ($S_{\mathbf{6}}$)

Similar to the pure resin, this specimen consisted of an epoxy component Araldite® MY0510, in liquid form and a hardener Aradur® $976-1$, in powder form, with 0.5 wt.% MWCNT Graphistrength® C100, supplied by Arkema. The dispersion process for the master batch consisted of an intial mixture of the epoxy and 2% wt. carbon nanotubes. Homogenization of the mixture was achieved by using a high shear mixer (HSM) at 6000 rpm and a duration of 30 minutes and a subsequent dispersion improvement using a high mechanical energy mixer (HMEM). In the sampling step, the duration of HMEM employment was optimized with respect to mechanical energy and mixing time. The masterbatch was then diluted by processing in a three roll mill. The Araldite® MY0510 and MWCNT dispersion was collected from the mill and the hardner was added under mechanical stirring at $600-2000$ rpm. Upon degassing and casting in a metallic mould, a similar curing cycle employed for the pure resin was executed.

For the 32_A05_CANBIO1_07 (S_6) specimen, the filler dispersion within the epoxy resin was evaluated by utilizing a grindometer and a Bresser LCD digital microscope with $40\times-1600\times$ capability. The rheological behavior was

furthermore evaluated by an Anton Paar MCR301 viscoelasticimeter equipped with a Peltier system and oven, as heating devices. By visual inspection, the aggregate size of the carbon nanotubes in the resin using HSM were $\sim$ 80 μm, as shown in Figure 3.4 (a). The aggregate size level became $\sim$ 30 μm following 10 minutes HMEM and $\sim 5-10$ μm, following two 30 minute mixing using HSM and HMEM, as shown in Figures 3.4 (b) and (c), respectively. The indicated aggregate sizes were consistent with those obtained with the grindometer. The acquired dispersion level is also shown in Figure 3.5 by rheology, upon increasing complex viscosity η^*, for the neat resin MY0510 at 25 °C.

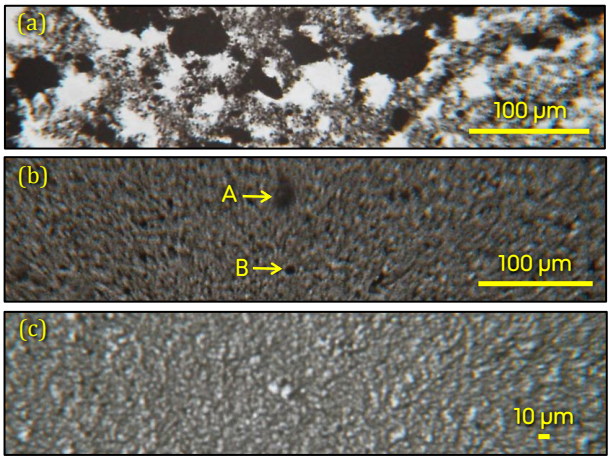

Figure 3.4. The aggregate size of the carbon nanotubes: (a) after 30 minutes (HSM $\sim$ 80 μm), (b) after 10 minutes (HMEM $\sim$ 30 μm), with 'A' and 'B' having sizes $\sim$ 30 μm and $\sim$ 8 μm respectively, and (c) after 30 minutes of HSM, followed by 30 minutes of HMEM $\sim$ 10 μm.

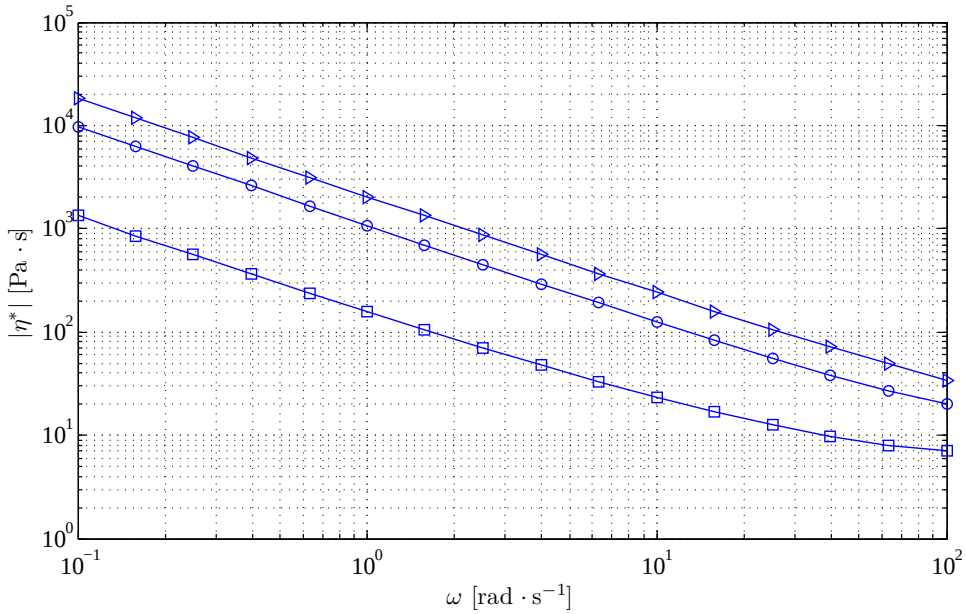

Figure 3.5. Complex viscosity $|\eta^*|$, of the nanotube masterbatch at 25 °C. The following symbols are used for: 30 minutes HSM (□), 10 minutes HMEM (○) and 30 minutes of HSM, followed by 30 minutes of HMEM (◁).

Araldite DBF (S_7)

This nanocomposite consisted of an Araldite® DBF and Aradur® HY956 EN base resin with 10% on weight aluminium nitride nanoparticles, supplied by PlasmaChem. The curing cycle used for this specimen was a 4 hour cycle at 25 °C followed by a 6 hour cycle at 60 °C.

SW404 + XB5173 (S_8)

This epoxy resin system, consisted of a SW404 gelcoat and a hardener in liquid form, without a nanofiller. The mixing of the components were carried out in accordance with 100 parts A and 9 parts B mix-ratio by weight. The cure schedule consisted of a 8 hour cycle at 60 °C, followed by four 2 hour cycles carried out at 80 °C, 100 °C, 120 °C, and 140 °C.

LAYSA_ICE ($S_{\mathbf{9}}$)

As one of the two multi-layered materials in this study, specimen S_9 featured 6 different layers, with the outer layer on top, to the inner layer on bottom described by SW404 gelcoat, MY0510, 3 layers of MY0510 + 5.5% MMT on top of a MTM44 − 1 FR substrate. This specimen featured Buckypaper infiltrated with an epoxy resin based solution.

LAYSA_ICE ($S_{\mathbf{10}}$)

The second multi-layered specimen, S_{10} consisted of the following layers stacked on top of the MTM44 − 1 substrate: 3 layers of glass fiber fabric and MY0510 +5.5% MMT, glass fiber fabric and MY0510 +5.5% CNT and SW404. This specimen featured an epoxy film with 5.5% of CNT.

3.3 Material Subdivision

Ten different materials were supplied in cured form by the European Consortium with the dimensions of the bulk materials shown in Table 3.1. The surface area range, $A \in [2200, 6944]$ mm^2, where the minimum area, $A_{\min} = 2200$ mm^2 served as a guideline for the subdivision of the surface specimens. The need for numerous experiments on the same material coupon, directed the study towards subdivision of the specimen surface into $4-5$ subareas, depending on the original size of the specimen.

The cutting of the specimens were carried out on a Felder saw equipped with a 52/60 diamond grit blade. The specimens were dry cut with a spindle speed

of 2500 rpm. During the cutting process the specimens were not subjected to any solvents or specific contaminants. Two different subdivision schemes were considered in order to allow for a consistent approach for future specimens. In effect, large specimens where $L \cong W$ were subdivided into 5 subareas, while smaller specimens where $L \ll W$ were divided into 4 subareas. The two different subdivision schemes are presented in further detail in Appendix C.

3.4 Density Measurements

In order to determine the density of each material, the density of the subdivided material coupons was determined by volume measurements and weight measurements by a Pioneer$^{\text{TM}}$ electronic balance, with an accuracy of ± 0.02. For each specimen the length L, width W, and height H, were measured five times for statistical purposes. Upon completion of all measurements the following data points were determined: $(L_1, L_2, \ldots, L_5)$, $(W_1, W_2, \ldots, W_5)$, $(H_1, H_2, \ldots, H_5)$ and $(m_1, m_2, \ldots, m_5)$. Based on these, the overall mean value for each dimension was estimated as shown in Table 3.2.

Length, L	Width, W	Height, H	Mass, m	Density, ρ
L_1	W_1	H_1	m_1	ρ_1
L_2	W_2	H_2	m_2	ρ_2
$\vdots$	$\vdots$	$\vdots$	$\vdots$	$\vdots$
L_N	W_N	H_N	m_N	ρ_N
$\bar{L}$	$\bar{W}$	$\bar{H}$	$\bar{m}$	$\bar{\rho}$

Table 3.2. Averaged properties of each specimen subarea.

The averaged quantity $\bar{\Phi}$ is then given by

$$\bar{\Phi} = \frac{1}{N}\sum_{i=1}^{N}\Phi_i \tag{3.1}$$

where Φ is given by

$$\Phi = (L, W, H, m, \rho) \tag{3.2}$$

and length L, width W, height H, mass m and density ρ are the quantities for each subarea. A complete set of the measurements are shown in Appendix A. For each specimen the average density was calculated based on the ratio of the mean mass and the mean volume of the sub-divisional areas, as

$$\bar{\rho} = \frac{\sum_{i=1}^{\widetilde{N}} m_{A_i}}{\sum_{i=1}^{\widetilde{N}} V_{A_i}} \tag{3.3}$$

where $\widetilde{N} \in [1, 5]$. Based on this mean density value $\bar{\rho}$, the variance of the density is calculated by

$$\sigma_\rho^2 = \frac{1}{N}\sum_{i=1}^{N}(\rho_i - \overline{\rho})^2 \tag{3.4}$$

where $N \in [1, 25]$. The standard deviation for the density, s_ρ is finally given by

$$s_\rho = \sqrt{\sigma_\rho^2} \tag{3.5}$$

Since the sample size $n < 30$, the confidence limits for the population's means can be determined using a $t-$distribution (Spiegel et al., 2009)

$$\bar{\rho} \pm t_c\Big(\frac{s_\rho}{\sqrt{n-1}}\Big) \tag{3.6}$$

where n denotes the sample size, and c for a degree of freedom $\nu = n - 1$ is given from Student's $t-$distribution. For 95%, 97.5% and 99% confidence limits and a sample size of $n = 25$ with the degrees of freedom $\nu = 24$ the corresponding $t-$ values are given by $t_{95\%} = 2.06$, $t_{97.5\%} = 2.49$ and $t_{99\%} = 2.80$.

In order to further assess the variations within the parameters $\Phi = (L, W, H, m, \rho)$, a visual inspection of each specimen area was carried out where distinct features such as bubbles, uneven surface properties and other properties that can be identified merely by the naked eye were noted. The range of measurements obtained can hence be accounted for as different initial properties are contained within the specimens and further explain these properties in greater detail. The density of the different specimens, their variance and standard deviation from the overall mean density value are shown in Table 3.3. The S_2 specimen has the lowest density and S_8 the highest density within the analyzed specimens.

Specimen No.	$\bar{\rho}$ [g/cm^3]	σ^2	σ
S_1	1.1102	0.0017	0.0407
S_2	1.0902	0.0020	0.0445
S_3	1.2588	0.0007	0.0256
S_4	1.2617	0.0003	0.0159
S_5	1.2465	0.0176	0.1327
S_6	1.3003	0.0010	0.0309
S_7	1.2446	0.0013	0.0367
S_8	1.7911	0.0019	0.0129
S_9	1.4493	0.0047	0.0689
S_{10}	1.5345	0.0019	0.0434

Table 3.3. The density ρ, variance σ^2 and standard deviation σ, for the given specimens.

The distribution of the densities are further shown in Figure 3.6.

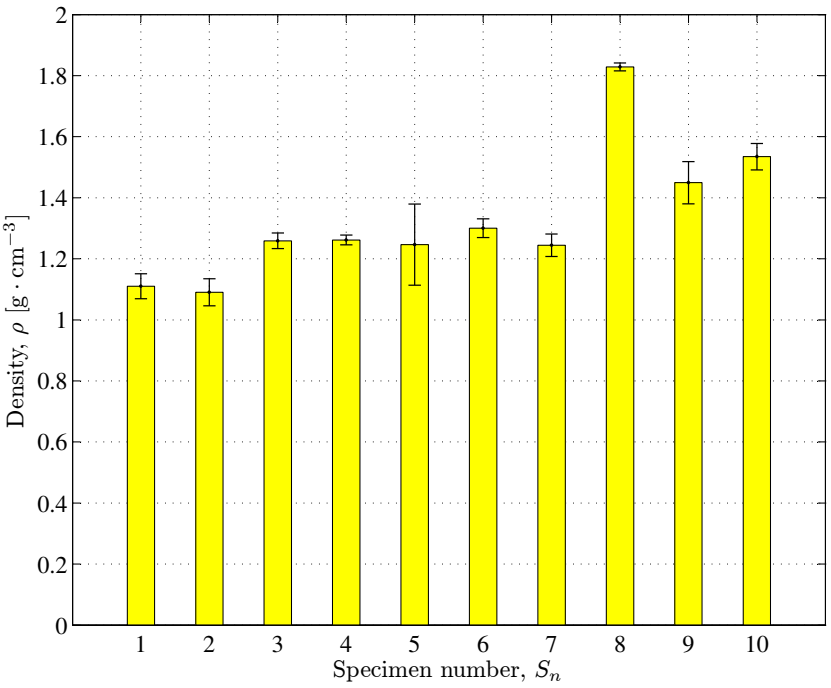

Figure 3.6. The densities of the supplied specimens S_n, with $n = \{1, 2, \ldots, 10\}$. The error bars denote the standard deviation of each density measurement.

3.5 Microhardness Testing

The microhardness indentation apparatus utilized for the experiments was a Shimadzu Micro Hardness Tester Type M, equipped with a Vickers indenter and automatic loading system (Shimadzu Corporation, 1977). The microhardness tests for each sample were initiated by visual inspection of the surface finish. All samples with exception of the S_1 (LY564) sample were subjected to hardness testing in their virgin states. The surface structure of S_1 made

distinction of Vickers indentation on its surface, extremely intricate to measure. For this purpose this sample was polished to a glossy surface finish using silicon carbide paper FEPA 800. The specimen thickness for specimen S_1, changed from 1 mm, to 0.7 mm as a result of the polishing.

The indentation process was carried out by adjusting the illumination and focusing of the low and high power objectives of the microhardness indenter, in order to clearly visualize the indentation location. Upon placement of the load $P = 1$ kg, the location of the specific indentation was indexed. The indexing of each indentation site was crucial since the diagonals would be measured utilizing a different microscope. The test duration of $\tau = 15$ seconds was then chosen for all the specimens. Once a suitable indentation location was identified, the load was applied and the locus of resulting depression documented. For each specimen, the surface was subdivided into 8 equally sized zones as shown in Figure 3.7.

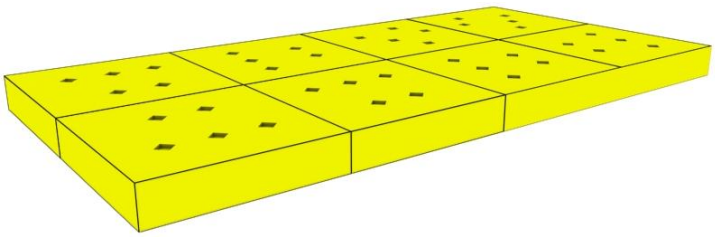

Figure 3.7. A schematic view of the 8 equally sized regions for the microhardness tests, with each region featuring 5 indentation sites. The size of the indents in the figure has been exaggerated for illustration purposes. *Source:* (Gohardani, 2010)

For each zone, 5 indentations were imaged where the distance between the indents was at least $4\overline{d}$, where $\overline{d}$, is the mean diagonal of the indents. Indentations were also avoided in the vicinity of the specimen edges. As the surface morphology of the different specimens could only be magnified up to 400× with the higher magnification ocular, the diagonals of the indentations were difficult to measure for certain specimens. Therefore a methodology was established where the actual measurement of the diagonal was no longer carried out on the microhardness indenter but on a micrograph produced of the indentation. The microscope that was utilized for this purpose was an Olympus BH series microscope, which had to be adapted to house a Nikon D5000 Digital SLR Camera. This was accomplished by utilizing a NFK 2.5× lens and a distance piece. The microscope was further equipped with a MSPlan10 (IC10) objective. The field of view of the camera was streamed in real-time to the monitor prior to the acquisition of the micrograph. With a known index of each indentation the micrographs were acquired by triggering of the camera utilizing a remote control, in order to avoid blurriness. The length of the diagonals arising from the indentation were measured digitally on a computer. The experimental setup for the microhardness tests is shown in Figure 3.8.

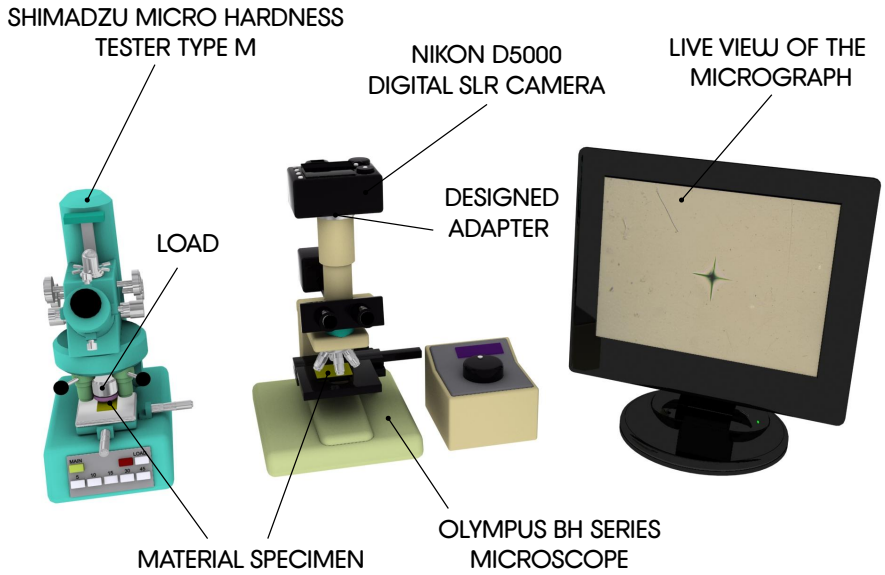

Figure 3.8. The experimental setup for the microhardness tests. Upon indentation with the microhardness tester the indentation is photographed utilizing the digital SLR camera.

In order to establish a physical scale, a diamond ruled stage micrometer with a specified spacing between the lines was also photographed. This allowed for measuring the length of the diagonals and assignment of a correct physical scale to their magnitude. The actual measurement of the diagonals on the photograph was carried out by utilizing ImageJ[†]. A Find edge filter which essentially applies a Sobel edge detector (Ferreira and Rasband, 2011) was used in order to find the edges of the indentation. Figure 3.9, shows an indent prior to and after application of the Find edge filter. Each indentation site featured two diagonals intersecting at the point of depression by the Vickers indenter.

[†]ImageJ is a public domain JAVA image processing program.

The Vickers hardness value is given by (Shimadzu Corporation, 1977; Sharpe, 2008)

$$HV = 1.854\left(\frac{P}{\bar{d}^2}\right) \tag{3.7}$$

with P [kg] as the load and $\bar{d}$ [mm] is mean diameter prescribed by

$$\bar{d} = \frac{d_1 + d_2}{2} \tag{3.8}$$

where d_1 and d_2, denote the length of the first and second diagonal of the same indentation respectively.

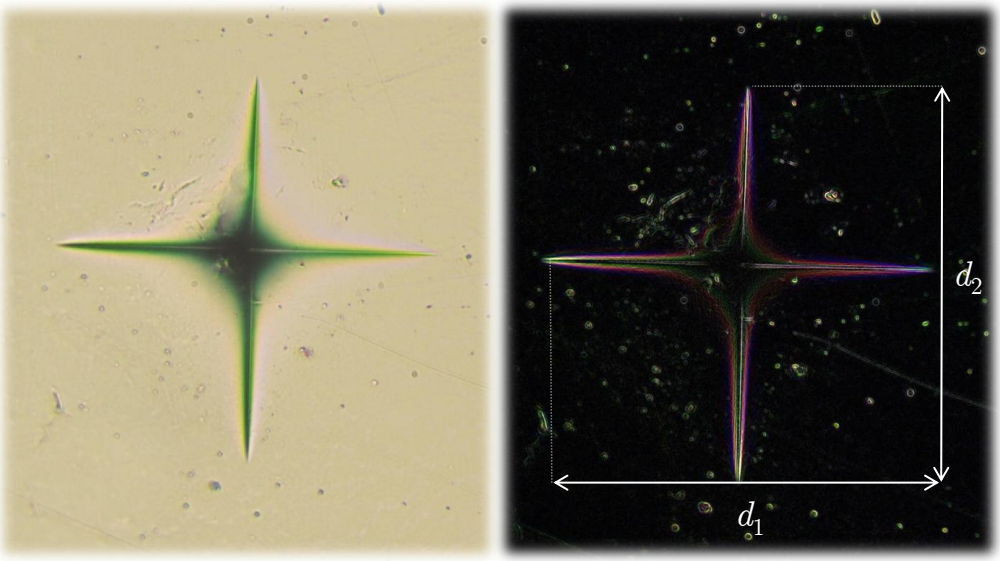

(a) (b)

Figure 3.9. (a) A representative Vickers indentation on the S_2 specimen. (b) The same indentation with applied Find edges filter in ImageJ. The filter defines the edges of the indentation for accurate measurement of the diagonals, d_1 and d_2, resulting in a mean diameter, $\bar{d} = (d_1 + d_2)/2$.

It is apparent from Figure 3.9 that no corner cracks are observed upon Vickers indentation at a load of $P = 1$ kg. Corner cracks usually emanate in brittle materials and are a measure of fracture toughness of the material (Ogilvy et al., 1977; Palmqvist, 1963). It is therefore not applicable to utilize the microhardness testing for estimation of the fracture toughness for the given specimens. The Vickers hardness test does however enable ranking of the specimens based on their hardness values and exhibit local hardness value differences between the specimens.

The mean local hardness value for each region, $H_{V,R}$, as shown in Figure 3.7 is given by

$$H_{V,R} = \sum_{i=1}^{5} \frac{HV_i}{5} \tag{3.9}$$

where i denotes the indentation index, and $R = 1,\ 2, \ldots, 8$. The mean overall hardness value for the entire specimen is hence given by

$$H_V = \sum_{R=1}^{8} \frac{HV_R}{8} \tag{3.10}$$

The confidence levels for a sample size $n \geq 30$, and normal population can be written as (Spiegel et al., 2009)

$$H_V \pm z_c\left(\frac{\sigma}{\sqrt{n}}\right) \tag{3.11}$$

where z_c it the confidence level, n is the sample size and σ is the standard deviation. For confidence levels 95%, 98% and 99% the corresponding values

are given by $z_{95\%} = 1.96$, $z_{98\%} = 2.33$ and $z_{99\%} = 2.58$. The averaged Vickers hardness values for the given specimens are shown in Table 3.4. The S_9 and S_{10} has been excluded from Table 3.4, due to their multi-layered nature.

S_n	H_V	σ	$CL = 0.95$	$CL = 0.98$	$CL = 0.99$	$\bar{d}$ [μm]	t [mm]
S_1	48.01	23.97	7.43	8.83	9.78	196.53	$0.7^{\dagger}$
S_2	39.67	4.30	1.33	1.59	1.76	216.20	3
S_3	62.18	11.10	3.44	4.09	4.52	172.70	5
S_4	64.89	19.21	5.95	7.08	7.84	169.05	6
S_5	57.28	5.18	1.61	1.91	2.11	179.92	$3-5$
S_6	54.27	2.93	0.91	1.08	1.20	184.86	5
S_7	40.10	8.37	2.59	3.08	3.11	215.06	9
S_8	73.13	6.16	1.91	2.27	2.51	15.24	4

Table 3.4. The Vickers hardness values (H_V), standard deviation σ, confidence levels (CL), mean diagonal $\bar{d}$ and the thickness value t for specimens S_n. The columns with CL represent the confidence intervals $z_c\sigma \cdot n^{-\frac{1}{2}}$, where z_c is the predefined critical value based on the desired confidence level. The symbol (†), refers to the post polished thickness value.

In Table 3.4, CL defines the confidence level in percent, for each corresponding accuracy of the Vickers hardness value. The confidence limits of a particular measurement is hence given by $HV \pm (z_c\sigma \cdot n^{-\frac{1}{2}})$, where the terms in brackets are displayed in Table 3.4.

It can be observed that S_8 (SW404 + XB5173) has the highest Vickers hardness value and S_2 (LY564 + 0.5% MWCNT) has the lowest hardness value. The most consistent specimen based on the lowest standard error in measurement, for a confidence level of 99% is the S_6 with only a deviation of 2.21%, while the highest standard error in the measurements is obtained for the S_1 specimen with 20.3%. It can be observed that the S_1 specimen has smallest thickness among all given specimens and the only specimen subjected to

surface grinding before the microhardness tests. Figure 3.10, shows different Vickers indentations on the supplied specimens.

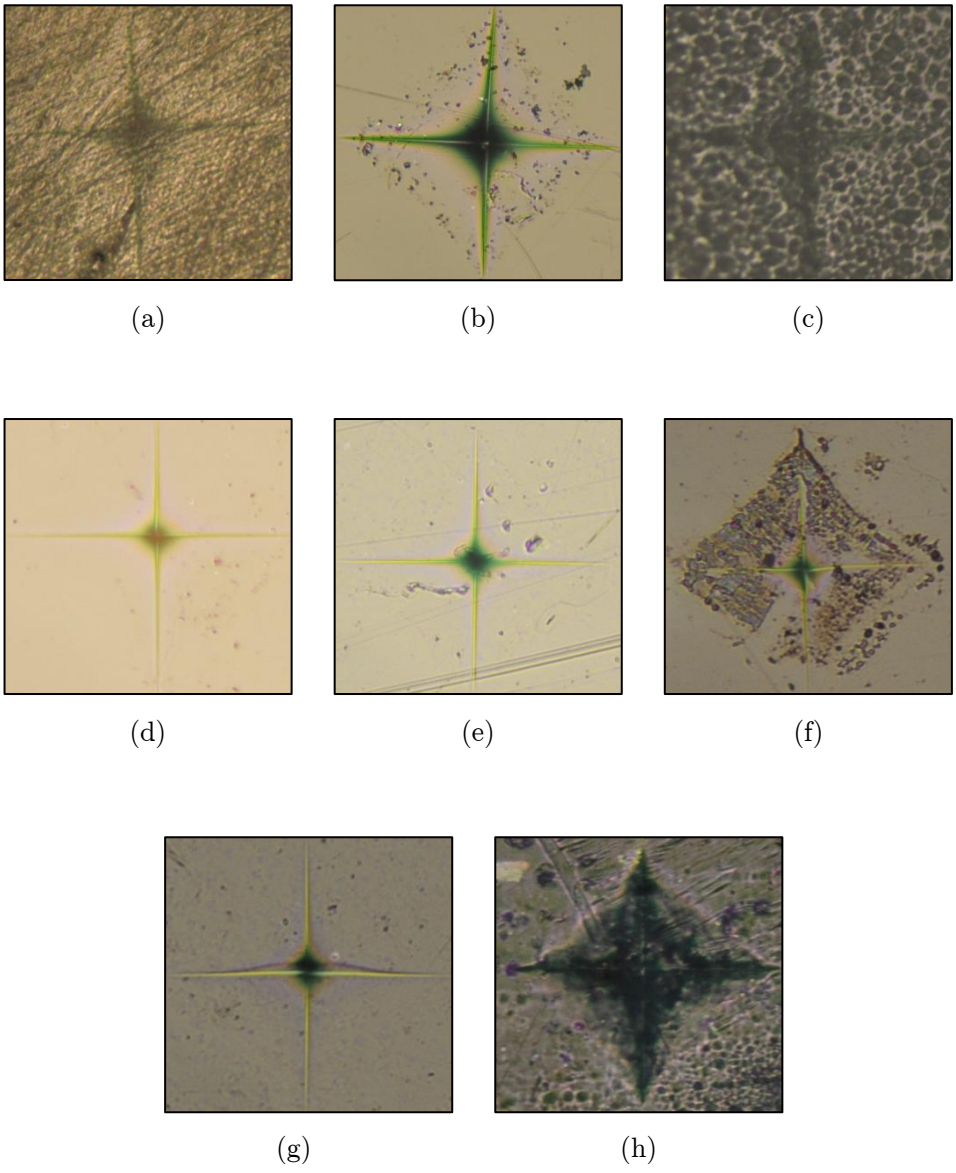

Figure 3.10. Vickers indentation on the different specimens. Vickers indentation on the different specimens (a) S_1, (b) S_2, (c) S_4, (d) S_3, (e) S_6, (f) S_5, (g) S_7, and (h) S_8.

The hardness topography shown for each specimen provides an indication about the distribution of the hardness on the specimen surface. In general the hardness values within a small spatial region are consistent. Nonetheless, different hardness values may be apparent due to numerous factors. These factors may for instance include the presence of bubbles and material flaws such as micro cracks or ensue from inconsistencies of mixing between the resin and hardener, or as a consequence of the dispersion process of the carbon nanotube reinforcement into the resin. The motivation for analyzing each specimen surface in different regions has thus been to assess how consistent the materials can be manufactured, from a hardness standpoint. Vickers hardness value distributions over the specimen surfaces for the different specimens are shown in Figures 3.11 − 3.18. It is notable to point out the interpolated values serve as indicators of a possible hardness value distribution on the specimen surfaces. Individual hardness values along the contour lines and the color coding therefore, do not necessarily restrict the hardness values to the specified values. The reasoning behind presentation of the interpolated data is solely to provide an inference about the distribution of hardness values based on the discrete hardness values within each region.

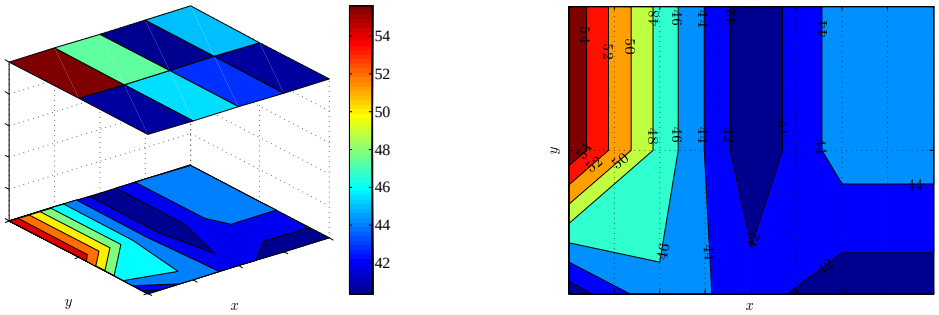

Figure 3.11. The regional Vickers hardness (HV) topography on the S_1 specimen and interpolated values based on the regional values.

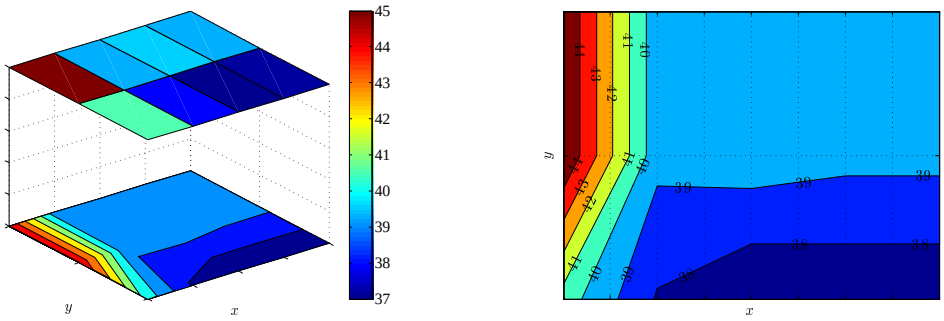

Figure 3.12. The regional Vickers hardness (HV) topography on the S_2 specimen and interpolated values based on the regional values.

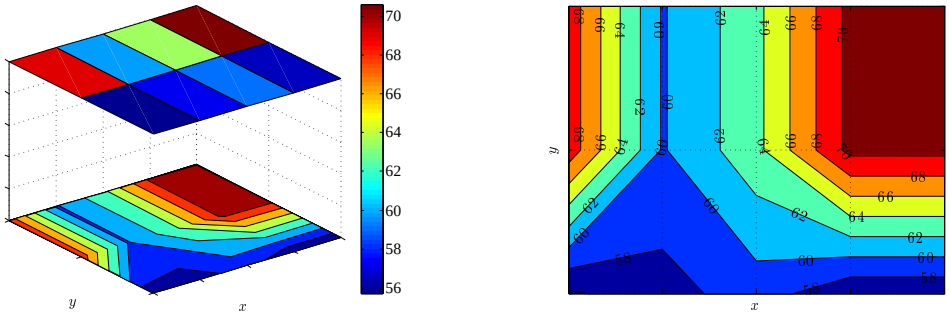

Figure 3.13. The regional Vickers hardness (HV) topography on S_3 and its interpolated hardness values.

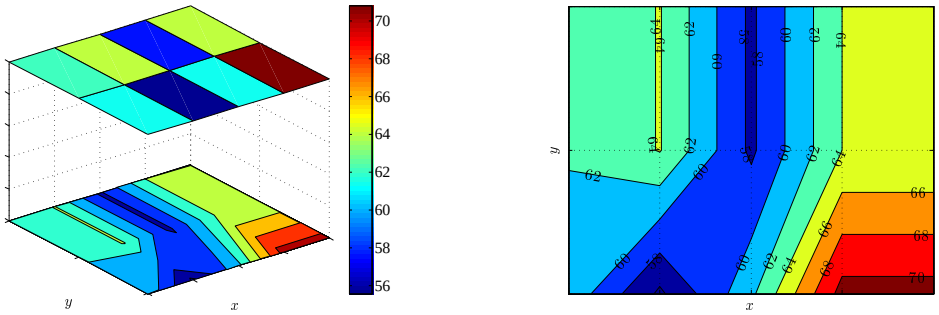

Figure 3.14. The regional Vickers hardness (HV) topography on S_4 and its interpolated hardness values.

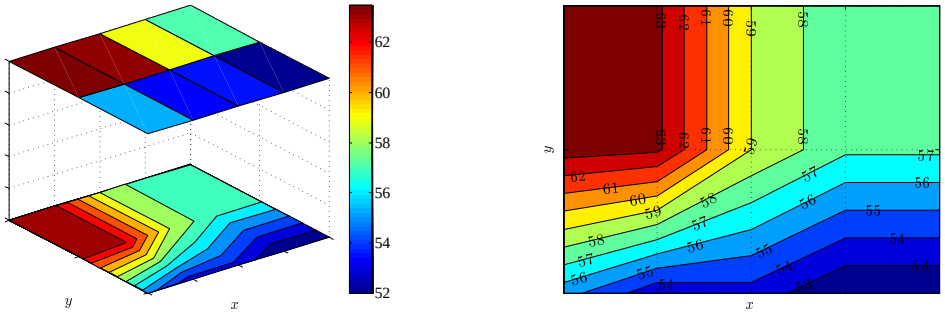

Figure 3.15. The regional Vickers hardness (HV) topography on the S_5 specimen and interpolated values based on the regional values.

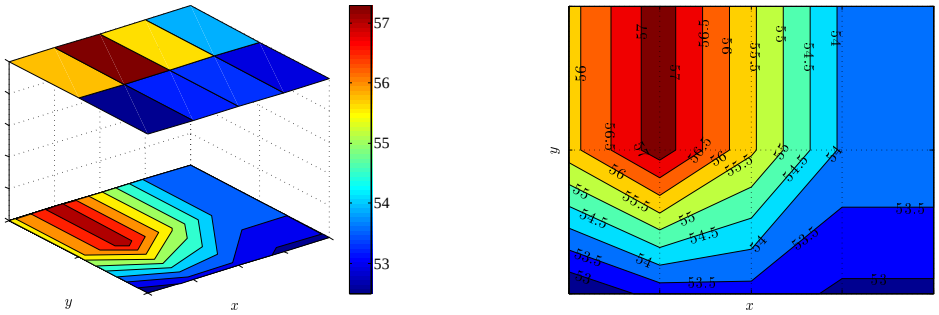

Figure 3.16. The regional Vickers hardness (HV) topography on S_6 and its interpolated hardness values.

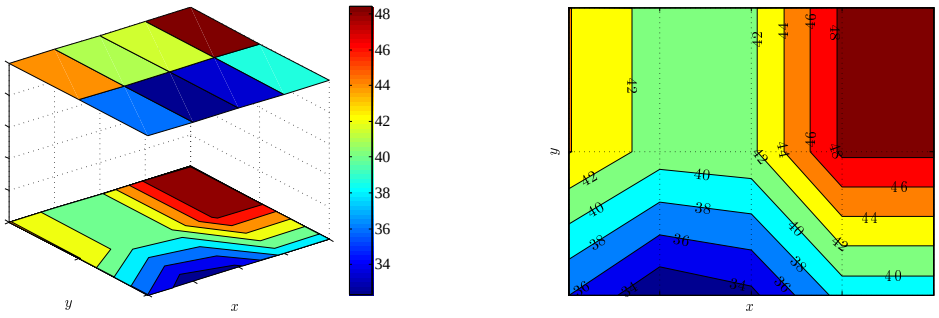

Figure 3.17. The regional Vickers hardness (HV) topography on the S_7 specimen and interpolated values based on the regional values.

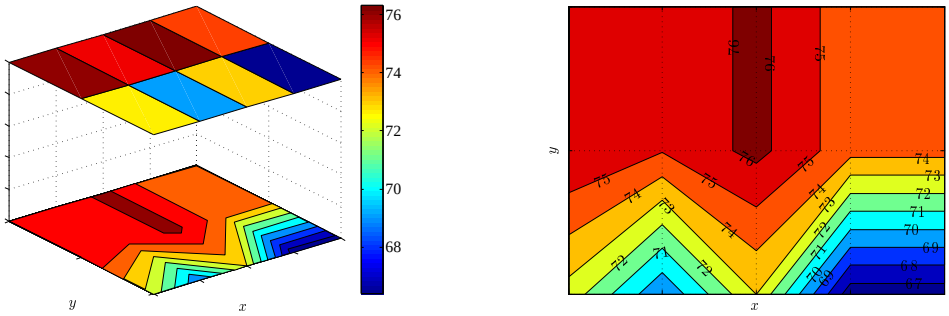

Figure 3.18. The regional Vickers hardness (HV) topography on S_8 and its interpolated hardness values.

Sources of errors

The errors associated with the micro indentation test can be divided into the following categories (Mott, 1956):

1. Human factor errors
2. Environmental induced errors
3. Instrumentation errors
4. Measurement errors

Human factor errors: For a proper calibrated hardness tester, the actual measurement can strongly be influenced by the judgment of the researcher. In order to avoid human errors all testing procedure and measurements have been carried out by utilizing a methodological scheme and followed thoroughly for each single experiment. The duration of the experimental runs have been kept constant and no experimental runs extending beyond three hours have been actualized. The main reason for this approach has been the elimination of possible human errors in measuring the indentation diameters from the micro-hardness micrographs, and minimization of the effects of astigmatism. Furthermore, the location of the microhardness tester during the course of the experiments has been kept constant. Prior to the experiments, the microhardness apparatus was calibrated by using a specimen piece with a known hardness value.

Environmental induced errors: Although minimization of human errors during the experimental runs is crucial, it is as important to account for possi-

ble environmental factors that might affect the results from the indentation tests. These factors mainly stem from vibrations of small amplitudes which are not observed during the experimental runs, or sudden changes in ambient conditions. As the experiments are conduced in the Icing Tunnel Facility at Cranfield University, United Kingdom, they have been avoided during the course of a running Icing Tunnel and the changes in airflow and temperature that a running tunnel imposes. In order to reduce the presence of possible vibrations, the micro-hardness tester was placed upon a damping absorbent optical table.

Instrumentation errors: The microhardness apparatus on its own is responsible for a number of errors that might alter the obtained hardness values considerably. Perhaps one of the most difficult sources of error to detect for a Vickers hardness value, is a deviation from the $\beta = 136°$, which is the standard angle for the Vickers pyramid indenter (Sharpe, 2008). This deviation might be a result of wear due to extended usage of the indenter and will directly influence the hardness value as the Vickers hardness value is based on the mean diagonal of the indentation. The effect of an incorrect apex angle $\beta \neq 136°$, can be investigated by considering a range of deviated apex angles of $\Delta\beta \in [0, -10°]$ resulting in a range of apex angles, $\beta + \Delta\beta$. However, in conducting such a study, the maximum deviation from the true Vickers hardness value was found to be approximately 4%, which is modest. The resulting percentage errors for the remaining angle deviations are shown in Appendix E. In order to ensure that the indenter had not changed shape significantly, an indent image was produced on a calibration specimen prior to the mi-

crohardness tests. After the tests, a final indentation was produced on the same calibration specimen used before the experiments. The error between the measurements prior and after the microhardness experiments was $\approx 1\%$, thus the effect of indentation shape alteration were considered to be negligible.

Measurement errors: As the actual measurements of the diagonals were carried out digitally, the errors that could arise from such measurement were mainly restricted to acquisition of photograph with adequate focus and well defined edges of the indentation. Using the experimental setup described in Figure 3.8, micrographs with a spatial resolution of 4288×2844 pixels with a 24-bit picture depth were acquired. ImageJ further enables measurements on the photograph to an accuracy within two significant figures, greatly reducing measurement errors. An error assessment was also carried out for the blurred boundary that arises upon employing the Find edges filter. As the maximum blurriness encountered in a single measurement never exceeded 10 pixels $\sim 5\%$ change in hardness value, the introduced error arising from this measurement tool, was considered to be negligble.

3.6 Speed of Sound Measurements

The sound speed measurements are carried out by employing a Sonatest Sitescan 120, with a capability of measuring velocities between $1000 - 9999\ \mathrm{m \cdot s^{-1}}$ (Sonatest PLC, 2000; Sonatest Limited, 2006). The ultrasonic thickness gauging is attained by employing a delay line contact transducer. A calibration block machined with parallel surfaces is utilized in order to calibrate the instrument prior to speed measurements. The calibration is executed upon adjusting the velocity within the material on the instrument, until a match between the actual thickness of the test material and the read out is obtained. The delay line contact transducer requires that the samples are clean and parallel on both the top surface and bottom surface, respectively (Sonatest PLC, 2000; Sonatest Limited, 2006). The multi echo mode is further employed in order to obtain the sound speed within the material, which measures the first and second return echoes following an interface echo. The obtained results are based on 5 averaged measurements with the probe positioned on the center location of each specimen surface. The acoustic impedance values, in Table 3.5 are solely based on the measured speed of sound in the transverse direction of the specimen surface. The thin nature of the supplied specimens, only allows for acoustic measurements in the mentioned direction. The speed of sound in each specimen is shown in Figure 3.19.

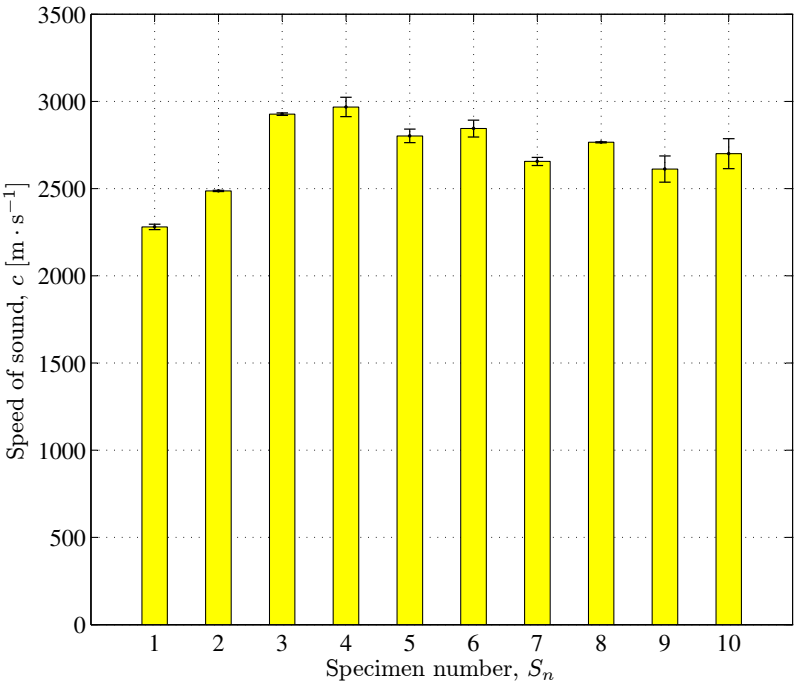

Figure 3.19. Speed of sound in the supplied specimens $S_1, \ldots S_{10}$. The error bars denote the standard deviation of each measurement.

The acoustic impedance values were acquired by using Equation (3.12)

$$Z = \rho \cdot c \tag{3.12}$$

with known values of ρ and c. An alternative representation of the acoustic impedance Z is given by Harris (1999).

$$Z = \sqrt{\frac{\rho E(1-\nu)}{(1-\nu)(1-2\nu)}} \tag{3.13}$$

where E is the Young's modulus, ν is the Poisson's ratio and ρ denotes the density.

The acoustic impedance Z, for the given specimens are shown in Table 3.5.

Specimen No.	Z $[\mathrm{g} \cdot \mathrm{cm}^{-2} \cdot \mathrm{s}^{-1}]$
S_1	253 150
S_2	271 110
S_3	368 450
S_4	374 440
S_5	349 260
S_6	369 810
S_7	330 520
S_8	505 690
S_9	378 550
S_{10}	414 350

Table 3.5. Characteristic acoustic impedance Z, for the given specimens.

3.7 Conclusions

The obtained results show that there are density differences between the supplied specimens. In particular these difference may arise from non-uniform dispersion of carbon nanotubes within the resins or other manufacturing defects. The Vickers hardness values of the reinforced materials with carbon nanotubes are not significantly different from those of the resins without a reinforcement and the addition of carbon nanotubes does not contribute to a higher Vickers hardness, with the opposite effect encountered for specimens S_2 and S_6. A range of Vickers hardness values is further encountered across the surfaces of the specimens which may be attributed to the dispersion uniformity of carbon nanotubes or other material defects arising from the manufacturing process. The added carbon nanotube reinforcement for specimens S_2, S_4 and S_6 in relation to the pure resins, results in nominally similar density and speed

of sound values. The establishment of empirical speed of sound measurements allow for a crucial flexibility to combine the density measurements with the sound speed results yielding empirically established acoustic impedance for each specimen. The impedance value may further be utilized in other material models, to characterize a measure of stiffness for the specimens. The reinforcement of pure resins with carbon nanotubes demonstrates that the reinforced resins S_2, S_4 and S_6 exhibit higher acoustic impedance in comparison to the pure resins without a reinforcement.

Chapter 4

Liquid Erosion

4.1 Experimental Setup

Only five of the 10 specimens were subjected to liquid erosion experiments. The reasoning behind the choice of these samples was related to an empirical study on the most recent manufactured base resins and the corresponding samples with embedded reinforcement. The choice of reinforcements was only confined to multi-walled carbon nanotubes at 0.5% wt. Based on this reasoning samples S_3, S_4, S_7, S_9 and S_{10} were excluded from the liquid erosion experiments. For the remaining samples, impact site number, coordinates and number of impacts were predefined, as shown in Figure 4.1.

The distance between two adjacent impact sites was kept at least 10 mm apart to avoid convolution arising from overlapping liquid impact jet damages. Moreover, a minimum distance $d_{\text{edge}} \approx 10$ mm was kept from the boundaries of the specimen surface. Deviations from the distance of bordering impact

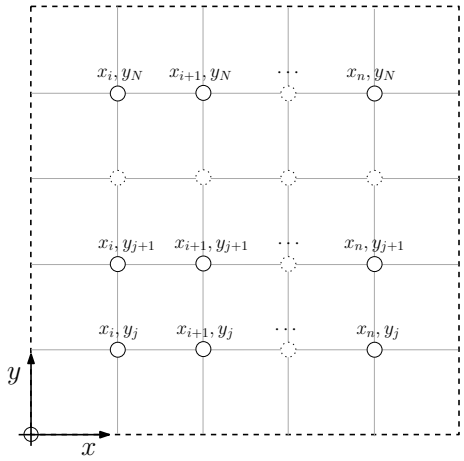

Figure 4.1. A schematic sample with a defined grid of impact sites. It is notable that a similar grid can be implemented on a non-square sample, where $n \neq N$. *Source:* (Gohardani, 2010)

sites arose when apparent material flaws were encountered. The utilized grid system for each sample is described further in Appendix B.

The liquid erosion tests were conducted at the Cavendish Laboratory, Cambridge University, United Kingdom. The impacting liquid droplets onto the specimen surface were produced upon using the Multiple Impact Jet Apparatus (MIJA). This apparatus is equipped with a pressure sensor, solenoids, a piston, a device for measuring velocity, nozzle and computer controlled $x - y$ specimen holder (Seward et al., 1990, 1992, 1994). The experimental cycle is initiated by the piston at rest. By increasing the pressure inside the vessel to a predetermined pressure value, a solenoid triggers the acceleration of the piston towards a titanium shaft. As the shaft is in connection with a water filled nozzle, discrete water jets are discharged from the nozzle of the orifice with the diameter, $d_{\mathrm{MIJA}} = 0.8$ mm. The cycle is finalized upon the return of the shaft and piston to their starting positions and blowing of air on the

remaining water on the specimen. The speed of the discrete water jets are measured by employing fiber optics. Figure 4.2 shows the schematic setup of MIJA at the Cavendish Laboratory, Cambridge University, United Kingdom.

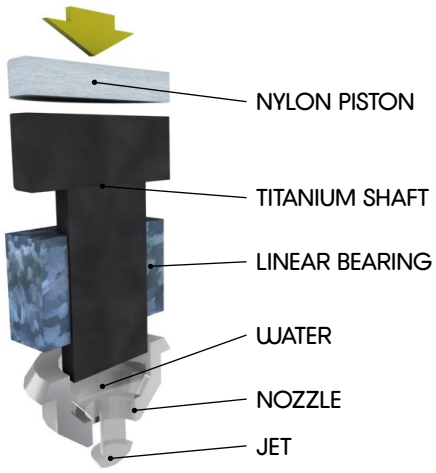

Figure 4.2. A schematic view of the Multiple Impact Jet Apparatus (MIJA).

Since the average rain droplet has a standardized diameter of $\widehat{D} = 2$ mm and $d_{\text{MIJA}} \neq \widehat{D}$, an equivalent speed, $v_{\widehat{D}}$ has been evaluated utilizing the empirical data of Hand et al. (1991), as given by Equation (4.1).

$$v_{\widehat{D}} = \widetilde{C}_0 + \widetilde{C}_1 \cdot v_{\text{MIJA}} + \widetilde{C}_2 \cdot v_{\text{MIJA}}^2 + \widetilde{C}_3 \cdot v_{\text{MIJA}}^3 \tag{4.1}$$

where

$$\begin{cases} \widetilde{C}_0 = 2.486 \\ \widetilde{C}_1 = 1.6676 \\ \widetilde{C}_2 = -0.0015467 \\ \widetilde{C}_3 = 8.9636 \cdot 10^{-7} \end{cases}$$

4.2 Damage Threshold Velocity

A crucial parameter in liquid erosion is the Damage Threshold Velocity (DTV). The DTV is essentially defined as the maximum velocity upon which a droplet can impact the material without causing any damage. A DTV curve is therefore produced by subjecting a material to a small number of impacts $\sim \mathcal{O}(1)$ at high impact velocities, moderate number of impacts $\sim \mathcal{O}(10)$ at moderate impact velocities and large number of impacts $\sim \mathcal{O}(300)$ at low velocities, as shown in Figure 4.3. Each location on the curve is visually inspected and designated as damaged or undamaged impact location, following the impact. The damage threshold curve is thereafter defined as the boundary between the damaged and undamaged sites. This entails that any impact velocity above the curve will result in damage on the material, as shown in Figure 4.3.

A theoretical Damage Threshold Velocity based on material properties is suggested by Evans et al. (1980)

$$v_{\mathrm{DT}}^{\mathrm{T}} \approx 1.41 \left(\frac{K_{Ic}^2 c_R}{\rho_1 c_1^2 d_1} \right)^{\frac{1}{3}} \tag{4.2}$$

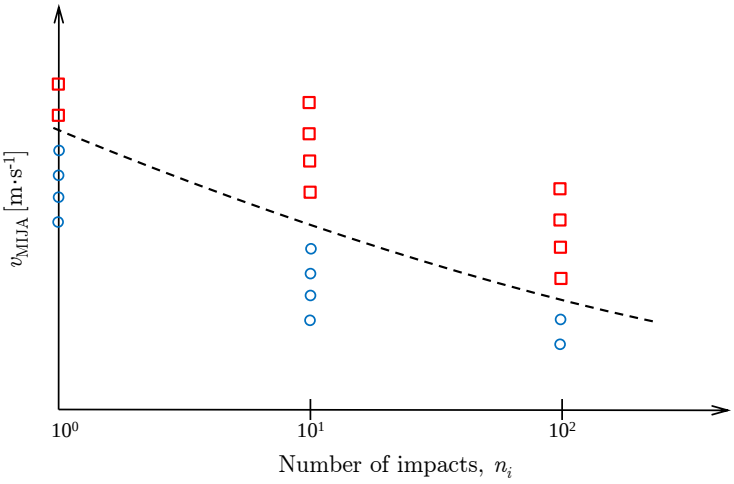

Figure 4.3. A general Damage Threshold Velocity curve. The damaged and undamaged sites for the material are denoted by symbols (□) and (○) respectively. The dashed line corresponds to the damage threshold curve.

where K_{Ic} is the fracture toughness, ρ_1 is the liquid density, c_1 is the compression wave speed in the liquid, d_1 is the liquid diameter and c_R is the Rayleigh-wave speed. The damage threshold velocity curves in this study are constructed by fitting a function obeying the relationship $\Lambda \cdot n^{-\beta}$ between the damaged and undamaged sites, where Λ and β are empirically determined constants.

In this study, MIJA speeds $v_{\mathrm{MIJA}} \in [61, 408]$ m $\cdot$ s^{-1} corresponding to an equivalent 2 mm droplet speed $v_{\hat{D}} \in [99, 486]$ m $\cdot$ s^{-1}, have been utilized in order to produce the Damage Threshold Velocity (DTV) curves. The distance between the impact sites has been chosen to be at least 5 mm. Larger spacings have been employed based on surface morphology, in order to avoid placement of impact sites near to material defects or close to the edges of the specimens. The micrographs used for assessment of the material damage have been ac-

quired using an Olympus BH-2 Microscope, and a 120 mm objective lens fitted with Olympus NeoSPlan 5× and 10× lenses. Reflected light is used for the micrographs, apart for the translucent samples where a transmitted light illumination is utilized. The variations in surface topography following droplet impacts are further highlighted by using a Normanski interference technique.

Dependence on the thickness of the specimen

For sufficiently thin specimens, the material damage may become further enhanced by the wave reflections within the solid following a liquid impact. The interaction of stress waves may in this context have a reinforcing effect on the damage. An analytical approach for a homogeneous material formulated by Springer (1976), allows for establishment of a threshold value for the thickness of the specimen, under which the wave reflections within the specimen approach negligible magnitudes, based on an impact with a droplet of diameter d. Two different time scales can be described for the impact of a liquid droplet onto a solid. The first one describing the duration of the incidence of the droplet at the interface of the specimen t_L, and the second one describing the duration of time period of the stress wave progression through a finite material thickness t_S. Equation (4.3) describes the mentioned phases respectively (Field et al., 1994).

$$\begin{cases} t_L = \frac{2d}{\hat{c}_L} \\ t_S = \frac{h_S}{\hat{c}_S} \end{cases} \tag{4.3}$$

where d is the droplet diameter, h_S is the thickness of the specimen and $\hat{c}_L$ is $\hat{c}_S$ are the speed of sound in the liquid and the solid respectively. In this context

the speed of the generated wave, $U_S \approx \hat{c}_S$ and negligible wave reflections in the specimen occur when $t_S > t_L$ resulting in

$$h_S > 2d \left(\frac{\hat{c}_S}{\hat{c}_L} \right) \tag{4.4}$$

Practically, it can be deduced that for a ratio between the actual specimen thickness H and the threshold thickness based on MIJA orifice $h_{s,\, d_{\mathrm{MIJA}}}$ greater than unity, i.e. $H/h_{s,\, d_{\mathrm{MIJA}}} > 1$, wave reflections within the specimen can be neglected.

The role of reflection and attenuation of stress waves in thin plates arising from liquid impacts has previously been examined by Bowden and Field (1964) and particularly in diamond (Field, 1999). As the three different waves shown in Figure 2.11, propagate through the solid following an impact by a liquid spheroid and $c_L > c_R$, a number of possible circular reinforcement regions will arise as depicted in Figure 4.4.

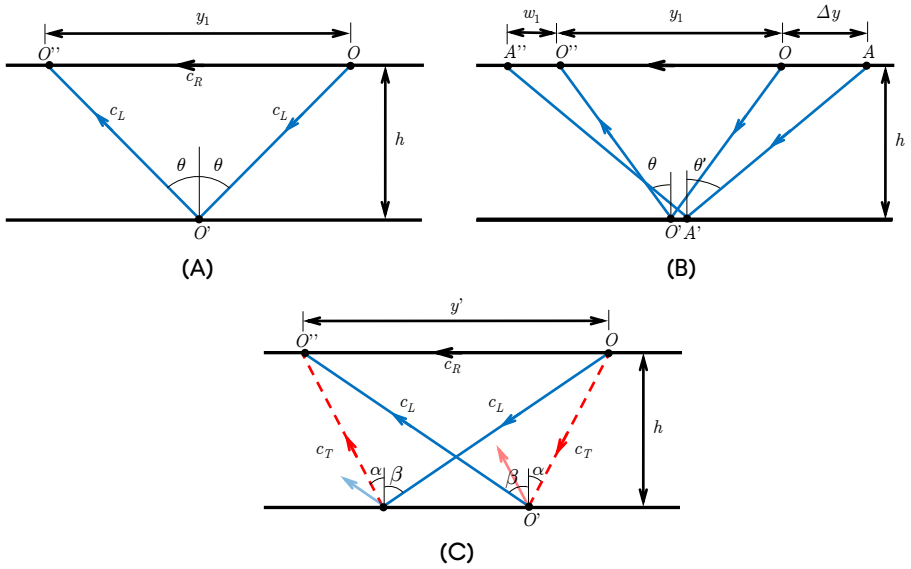

Figure 4.4. Possible wave reflections and reinforcements of stress waves in thin plates. (A) Impact from a point loading, (B) Impact over a region with diameter Δy and (C) Reinforcement upon return of the compressional wave as a tensile wave with the Rayleigh wave. Source: Adapted from Bowden and Field (1964).

For a finite thickness h on the specimen, the extent of the first fracture zone y_1 arising from a point loading at O is given by

$$y_1 = \frac{2h}{\left\{\left(\frac{c_L}{c_R}\right)^2 - 1\right\}^{\frac{1}{2}}} \tag{4.5}$$

as shown in Figure 4.4 (A). However, since the droplet produced by the multiple impact jet apparatus (MIJA), covers an area with diameter Δy instead of a point, a more representative formulation for the width of the zone as shown

in Figure 4.4 (B), is given by

$$w_1 = \frac{\Delta y}{\zeta^2 - 1} \tag{4.6}$$

where $\zeta = c_L/c_R$ and the path of the Rayleigh wave along the exposed surface of the contact area and all longitudinal waves are considered. Intense pulses, may result in apparent reflections due to the higher order bands (Bowden and Field, 1964) before reinforcement with the Rayleigh wave, where the n:th band may be expressed as $y_n = ny_1$. A band is in this context defined as a zone within the impact region. Bowden and Field (1964) also explain that a reinforcement with a surface wave may occur at a radius $y' \in [y_1, y_2]$ as shown in Figure 4.4 (C), where $y' = f(h, c_L, c_T, c_R)$. For a longitudinal wave with an incidence angle α, a reflected longitudinal wave with a similar angle and a reflected transverse wave with angle β is produced, where the relationship between the angles α and β is given by

$$c_T \sin(\alpha) = c_L \sin(\beta) \tag{4.7}$$

The discussion of reflection and reinforcement of stress waves by Bowden and Field (1964) generally concerns materials such as glass and Perspex, which in essence are isotropic, solid, elastic and brittle in nature. The considered materials, resins without fibers in this study are therefore subjected to the same theoretical consideration of wave reflection within the solids, as considered by Bowden and Field (1964). This approach can be extended to the S_1 material due to its known material properties such as Young's modulus, Poisson's ratio

and the speed of sound in the solid.

Reflection of waves at a solid-air boundary

Using an analytical approach the locations of intense stress levels following reflections within the solid can be described. Arenberg (1948), describes that for a compressional incident wave on a solid-air boundary

$$A \exp[ik(ax + y - \omega t)] \tag{4.8}$$

the two reflected components are given by

$$A_1 \exp[ik(-ax + y - \omega t)] \tag{4.9}$$

$$A_2 \exp[ik(-bx + y - \omega t)] \tag{4.10}$$

where $a = \cot(\alpha)$, $b^2 = a^2(2\xi + 2) + 2\xi + 1$ and

$$\xi = \frac{\nu}{1 - 2\nu} \tag{4.11}$$

The ratios between the amplitudes A, A_1 and B_1 are given by

$$\frac{A_1}{A} = \frac{a(2a^2\xi + 2a^2 + 2\xi + 1)^{\frac{1}{2}} - [\xi + (\xi + 1)a^2]^2}{a(2a^2\xi + 2a^2 + 2\xi + 1)^{\frac{1}{2}} + [\xi + (\xi + 1)a^2]^2} \tag{4.12}$$

$$\frac{B_1}{A} = \frac{a[2\xi + 2(\xi + 2)a^2]}{2(2a^2\xi + 2a^2 + 2\xi + 1)^{\frac{1}{2}} + [\xi + (\xi + 1)a^2]^2} \tag{4.13}$$

$$\frac{A_1}{B} = \frac{-2[\xi + (\xi+1)a^2] - [2a^2(\xi+1) + 2\xi + 1]^{\frac{1}{2}}}{[\xi + (\xi+1)a^2]^2 + a(2a^2\xi + 2a^2 + 2\xi + 1)^{\frac{1}{2}}} \tag{4.14}$$

where A and B denote the amplitudes of the longitudinal wave and transverse wave at angles α and β respectively and A_1 and B_1 describe the reflected component of the corresponding wave. For the transverse wave, the values of b that make $a \in \mathbb{R}$ can be used as other values imply a totally reflected transverse wave with phase shifts. The ratio of the amplitudes, incident and reflected angles for different Poisson's ratios are shown in Table 4.1 and Table 4.2.

Material	ν	$\frac{C_L}{C_T}$	$\frac{y_1}{x}$	$\frac{y'}{x}$	$\frac{y_2}{x}$	θ	α	β
Glass	0.24	1.71	4.71	7.36	9.42	32.7°	53.3°	28.9°
S_1 (LY564)	0.35	2.09	3.69	6.51	7.38	26.7°	53.5°	22.6°
Perspex	0.40	2.44	3.09	5.96	6.18	22.7°	52.1°	18.85°

Table 4.1. Angles θ, α, β, with acoustic and geometrical ratios for different values of Poisson's ratio.

Material	ν	ξ	θ	$-\frac{A_1^*}{A}$	$-\left(\frac{A_1}{A}\right)^3$	α	$-\frac{A_1}{A}$	$\frac{B_1}{A}$	β	$\frac{B_1}{B}$	$-\frac{A_1}{B}$
Glass	0.24	0.46	32.67°	0.55	0.17	55.3°	0.03	0.45	28.9°	0.03	0.41
S_1 (LY564)	0.35	1.17	26.67°	0.83	0.57	53.5°	0.52	0.42	22.6°	0.52	0.16
Perspex	0.40	2.00	22.73°	0.92	0.78	52.1°	0.72	0.34	18.9°	0.72	0.08

Table 4.2. Angles θ, α, β, and amplitudes A, B, A_1, A_1^* and B_1 for different Poisson's ratios, with A_1^* given for the y_1 zone.

The erosion resilience of the specimens in this study are presented as Damage Threshold Velocity curves. The accumulated damage on samples subjected to multiple droplet impact may be assumed to arise as a consequence of numerous impacts at moderate speeds, few impacts at higher speeds and initiation of fracture at the intermediate speed levels. Figures $4.5 - 4.9$, feature micrographs of each candidate specimen upon exposure to different number of

impacts at different velocities. The damage threshold velocities of the specimens S_1, S_2, S_5, S_6, and S_8, and a compilation of their behavior according to $f(n) = \Lambda \cdot n^{-\beta}$ are shown in Figures 4.10 $-$ 4.12. The empirical constants Λ and β for the examined specimens are shown in Table 4.3.

Specimen number S_n	Λ	β
1	517.14	0.208
2	505.72	0.239
5	430.01	0.243
6	506.68	0.258
8	513.94	0.229

Table 4.3. The empirical constants Λ and β for $f(n) = \Lambda \cdot n^{-\beta}$.

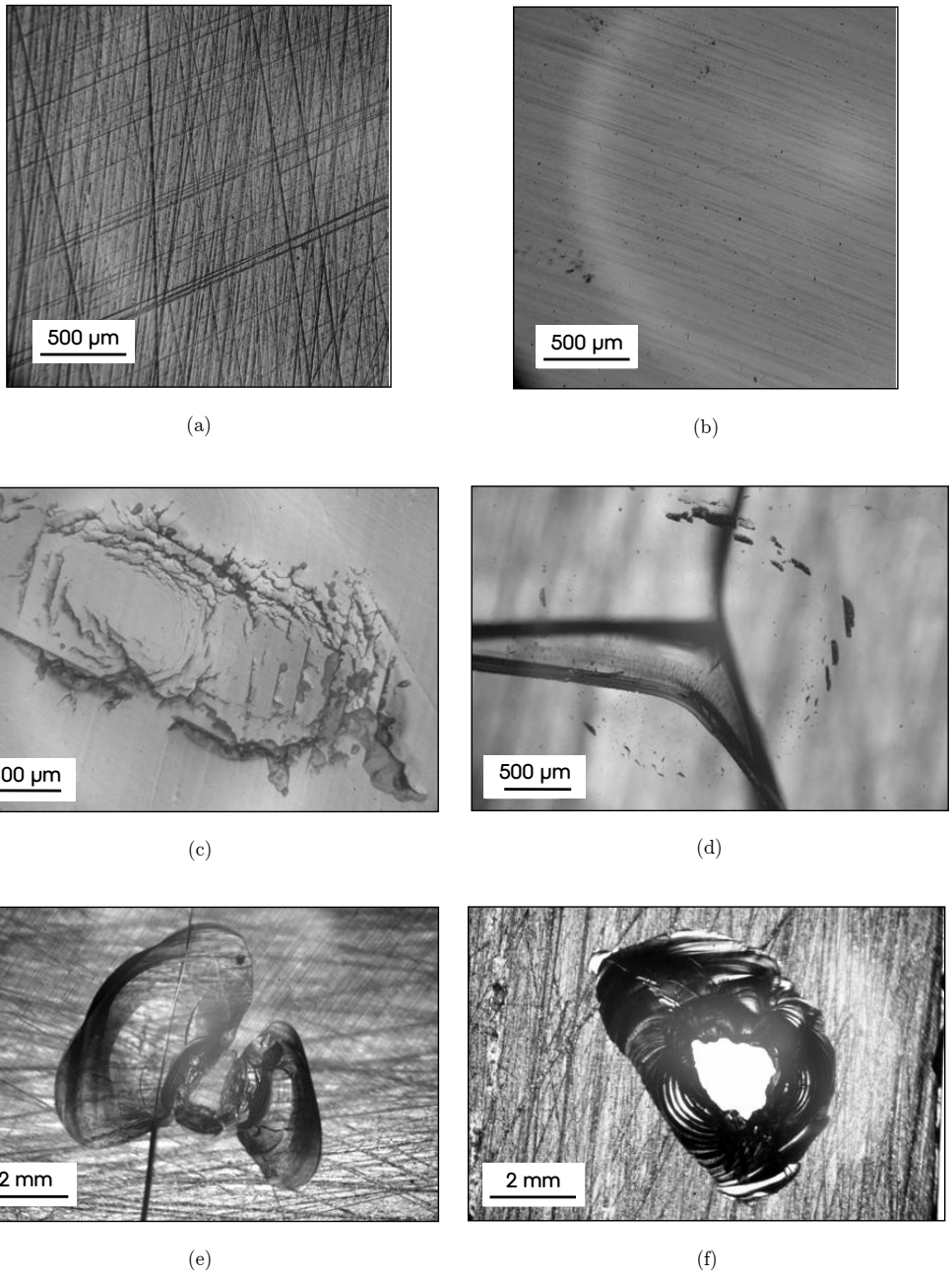

Figure 4.5. Micrographs of the S_1 sample: Prior to liquid impact: (a) Unpolished region in S_1, (b) Polished region in S_1. Post liquid impact micrographs: (c) $v_{\mathrm{MIJA}} \cong 110\ \mathrm{m \cdot s^{-1}}$ at 300 × impacts, (d) $v_{\mathrm{MIJA}} \cong 410\ \mathrm{m \cdot s^{-1}}$ at 1 × impact, (e) $v_{\mathrm{MIJA}} \cong 250\ \mathrm{m \cdot s^{-1}}$ on S_1 at 20 × impacts, and (f) $v_{\mathrm{MIJA}} \cong 250\ \mathrm{m \cdot s^{-1}}$ at 30 × impacts with transmitted light.

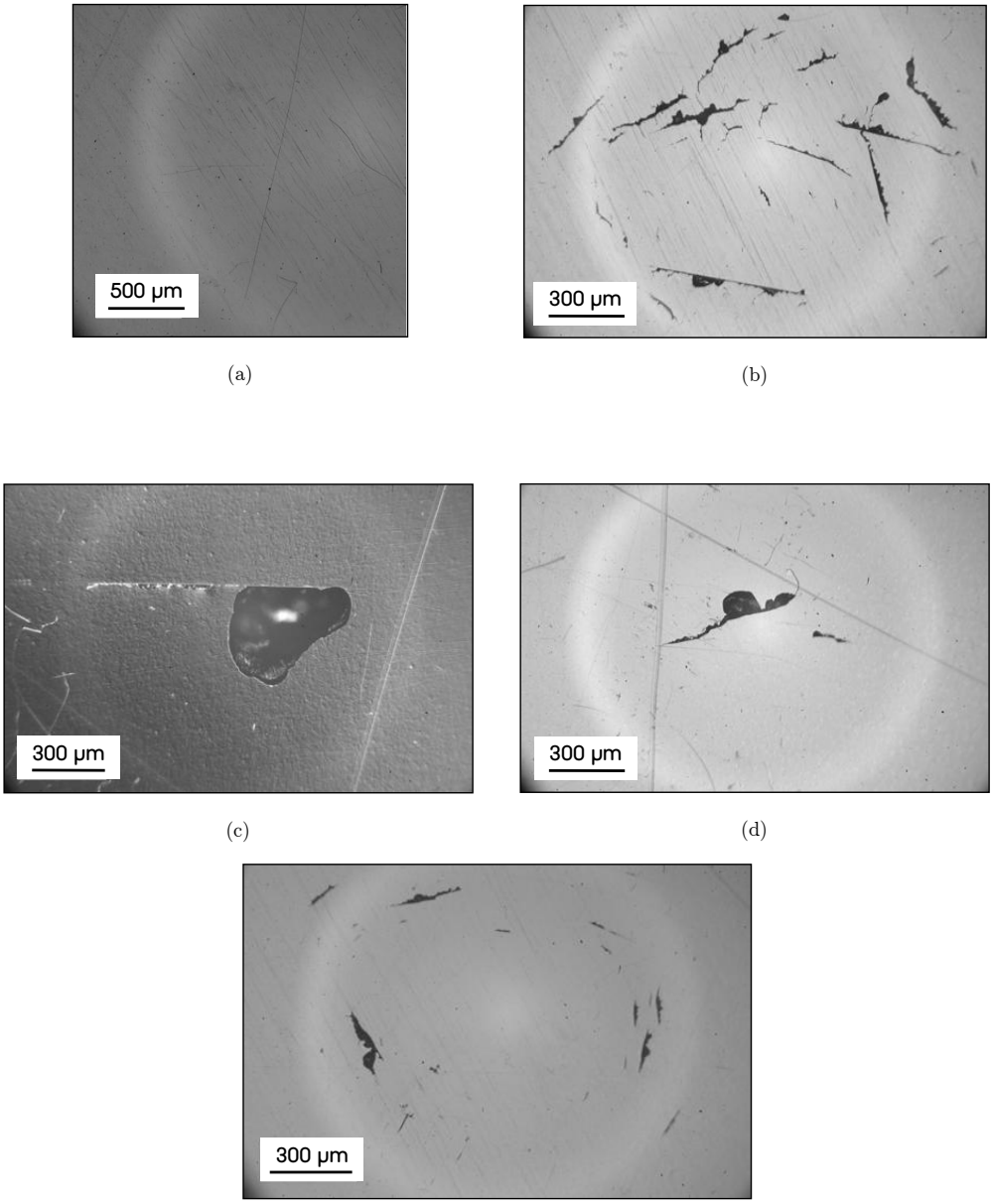

Figure 4.6. Micrographs of the S_2 sample: Prior to liquid impact: (a) Pristine surface. Post liquid impact micrographs: (b) $v_{\mathrm{MIJA}} \cong 110\ \mathrm{m \cdot s^{-1}}$ at 300 × impacts, (c) $v_{\mathrm{MIJA}} \cong 410\ \mathrm{m \cdot s^{-1}}$ at 1 × impact, (d) $v_{\mathrm{MIJA}} \cong 140\ \mathrm{m \cdot s^{-1}}$ on S_2 at 20 × impacts, and (e) $v_{\mathrm{MIJA}} \cong 140\ \mathrm{m \cdot s^{-1}}$ at 50 × impacts.

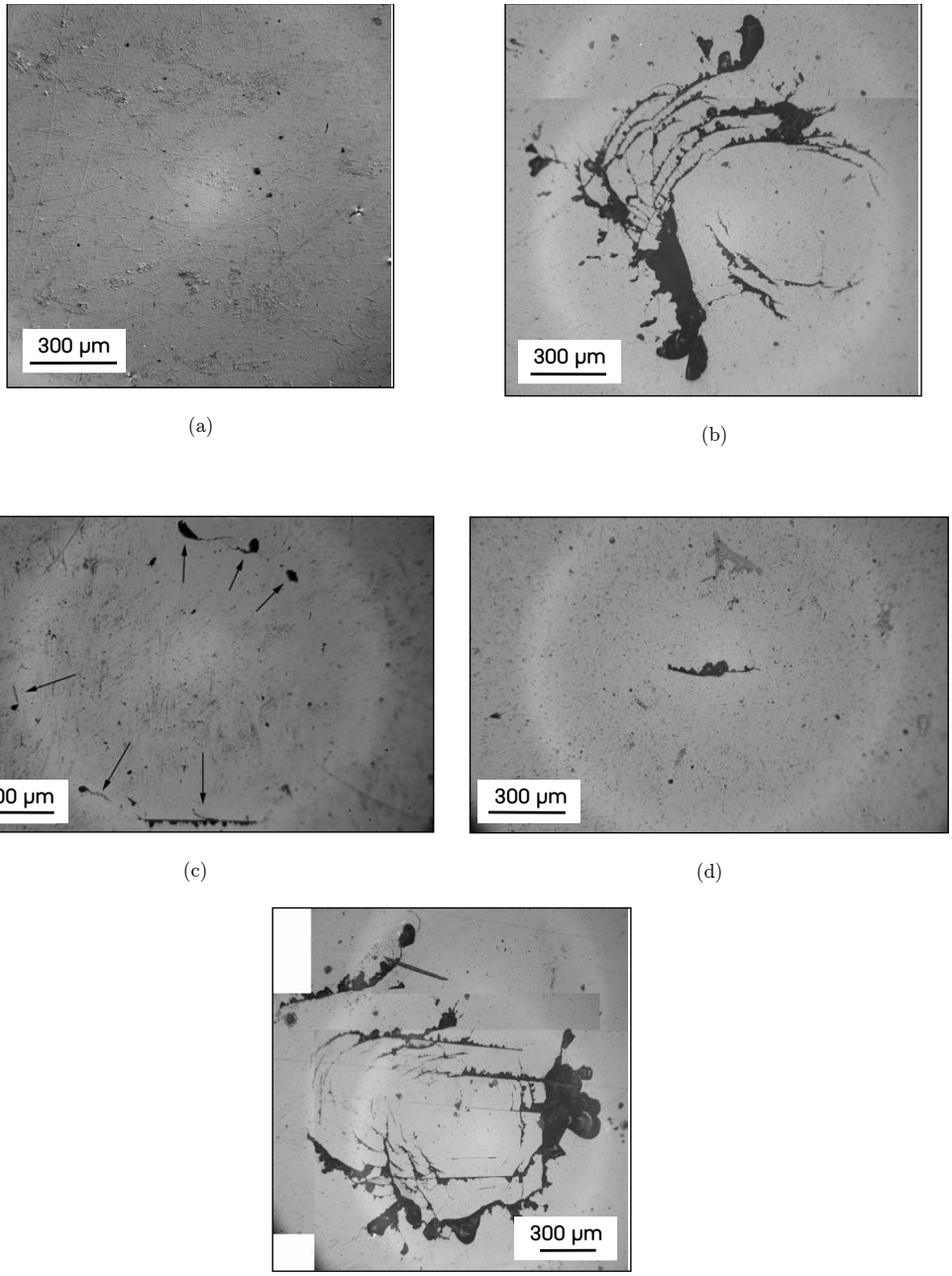

(a) (b) (c) (d) (e)

Figure 4.7. Micrographs of the S_5 sample: Prior to liquid impact: (a) Pristine surface. Post liquid impact micrographs: (b) $v_{\mathrm{MIJA}} \cong 110\ \mathrm{m \cdot s^{-1}}$ at 300 × impacts, (c). $v_{\mathrm{MIJA}} \cong 410\ \mathrm{m \cdot s^{-1}}$ at 2 × impacts, (d) $v_{\mathrm{MIJA}} \cong 150\ \mathrm{m \cdot s^{-1}}$ on S_5 at 20 × impacts, and (e) $v_{\mathrm{MIJA}} \cong 150\ \mathrm{m \cdot s^{-1}}$ at 100 × impacts.

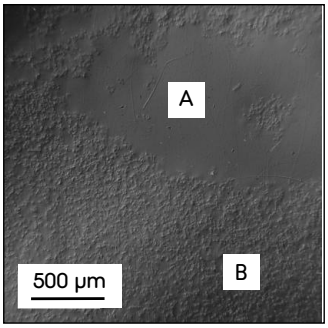

(a)

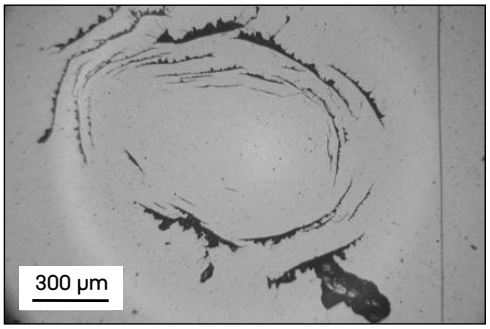

(b)

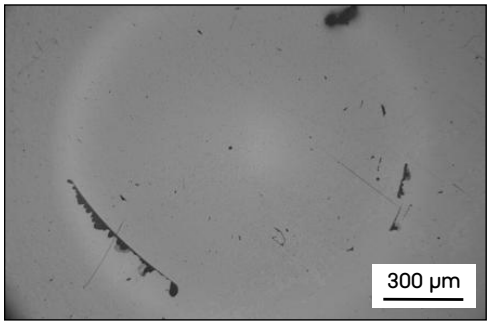

(c)

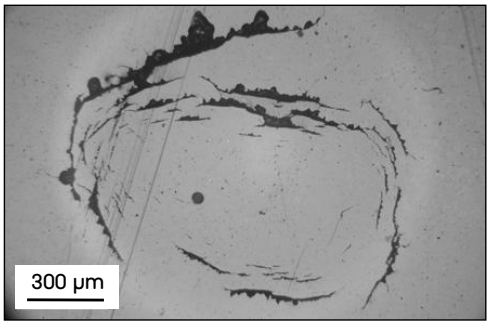

(d)

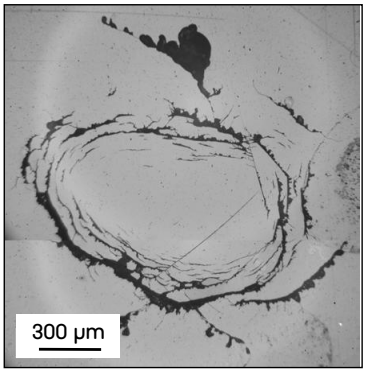

(e)

Figure 4.8. Micrographs of the S_6 sample: Prior to liquid impact: (a) Pristine surface with a different phase denoted by 'A' apparent within the matrix 'B'. Post liquid impact micrographs: (b) $v_{\mathrm{MIJA}} \cong 110\ \mathrm{m} \cdot \mathrm{s}^{-1}$ at 300 × impacts, (c) $v_{\mathrm{MIJA}} \cong 410$ at 2 × impacts, (d) $v_{\mathrm{MIJA}} \cong 150\ \mathrm{m} \cdot \mathrm{s}^{-1}$ on S_6 at 50 × impacts, and (e) $v_{\mathrm{MIJA}} \cong 150\ \mathrm{m} \cdot \mathrm{s}^{-1}$ at 100 × impacts.

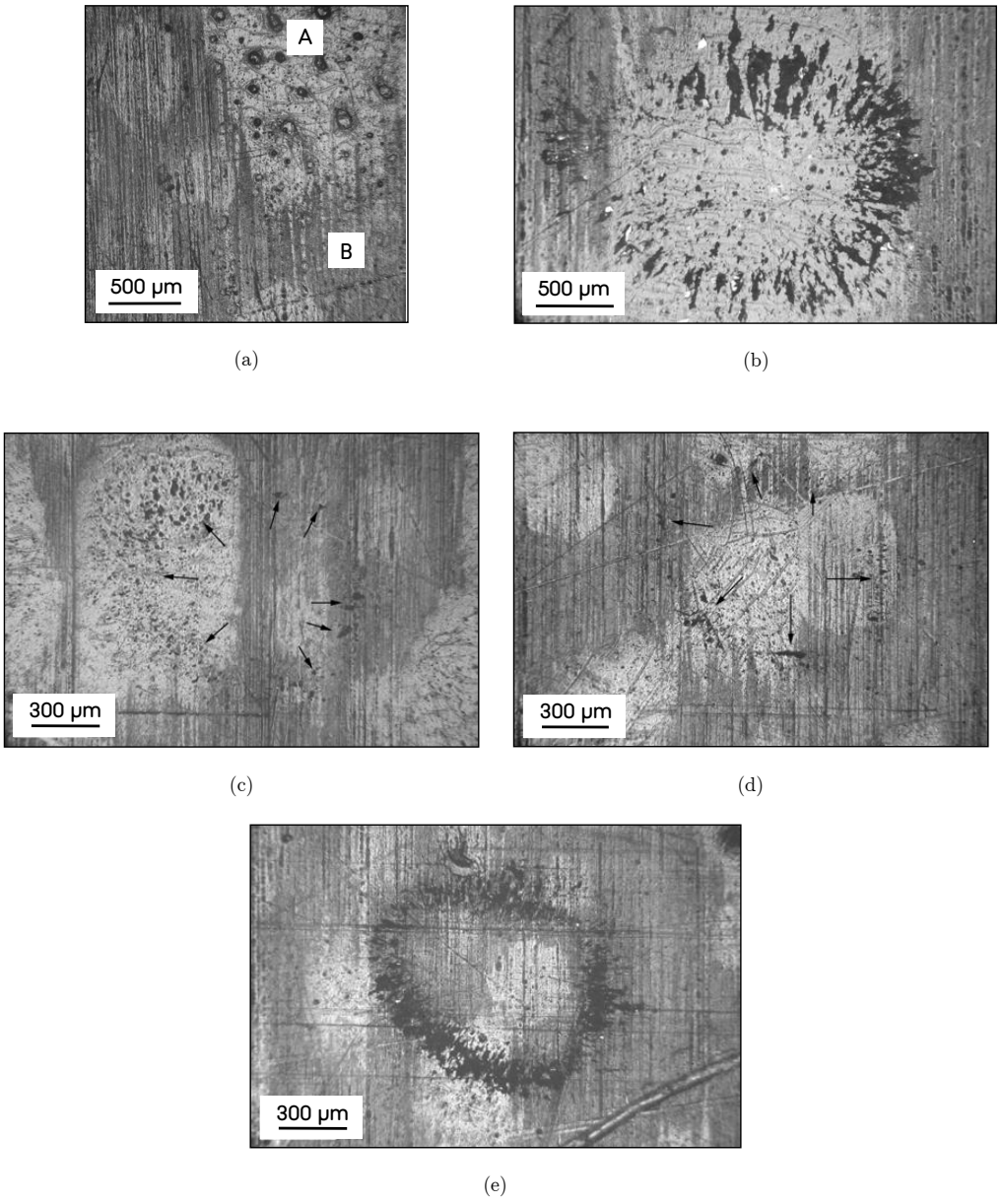

Figure 4.9. Micrographs of the S_8 sample: Prior to liquid impact: (a) Pristine surface with a different phase denoted by 'A' apparent within the matrix 'B'. Post liquid impact micrographs: (b) $v_{\mathrm{MIJA}} \cong 110\ \mathrm{m \cdot s^{-1}}$ at 300 × impacts, (c) $v_{\mathrm{MIJA}} \cong 410\ \mathrm{m \cdot s^{-1}}$ at 2 × impacts, (d) $v_{\mathrm{MIJA}} \cong 350\ \mathrm{m \cdot s^{-1}}$ on S_8 at 3 × impacts, and (e) $v_{\mathrm{MIJA}} \cong 350\ \mathrm{m \cdot s^{-1}}$ at 10 × impacts.

The water hammer pressure P_w, center of impact pressure P_c and Bernoulli stagnation pressure P_B, according to Equations (2.8), (2.9) and (2.11) for different impact speeds are shown in Figure 4.13 (a). Similarly, the time period before initiation of the pressure release τ and duration of the water hammer pressure τ^* versus the impact velocity calculated using Equations (2.10) and (2.12) are plotted in Figure 4.13 (b).

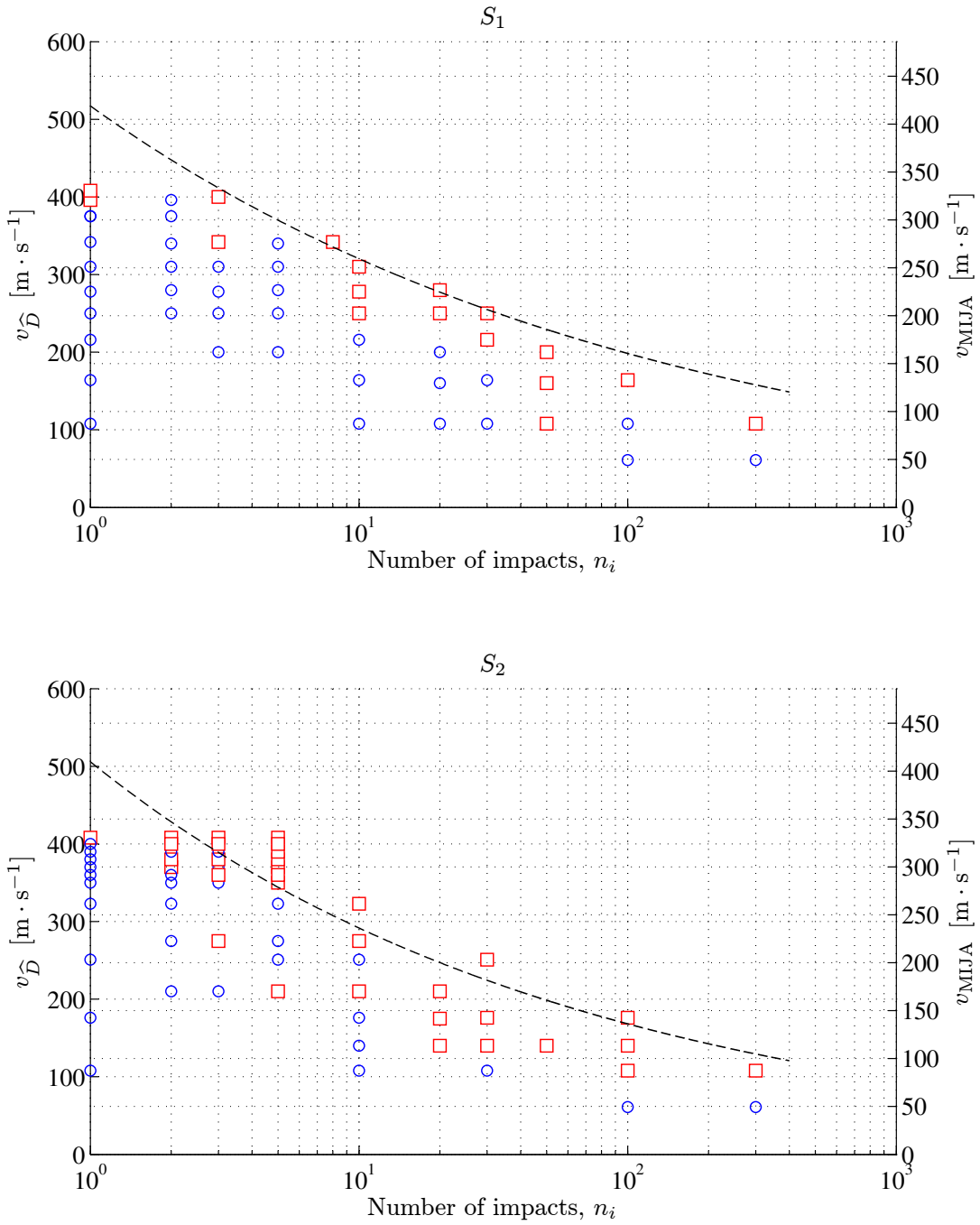

Figure 4.10. Damage Threshold Velocity curves for specimens S_1 and S_2. The undamaged sites are marked with blue circles (○) and the sites where damage was encountered with red squares (□).

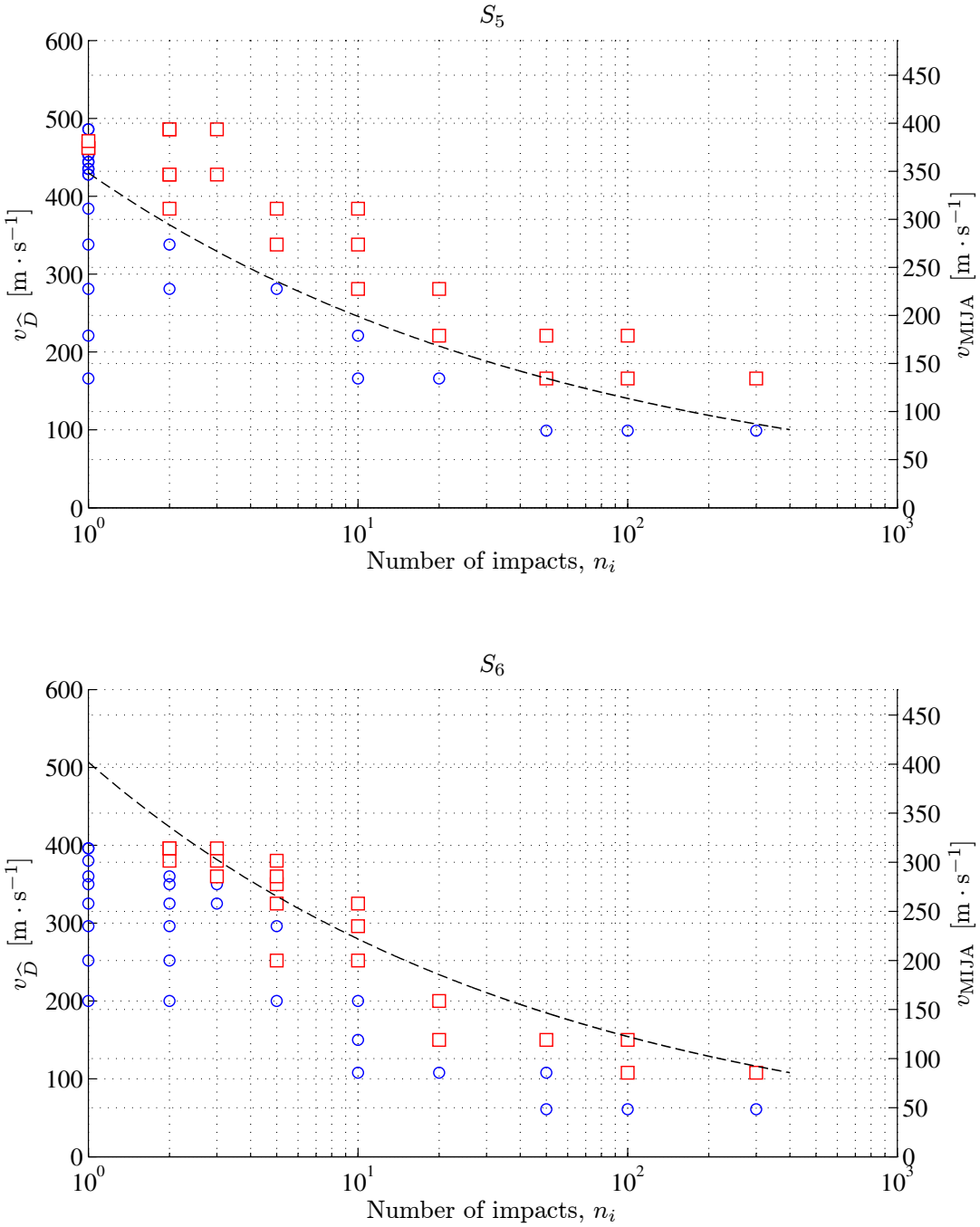

Figure 4.11. Damage Threshold Velocity curves for specimens S_5 and S_6. The undamaged sites are marked with blue circles (○) and the sites where damage was encountered with red squares (□).

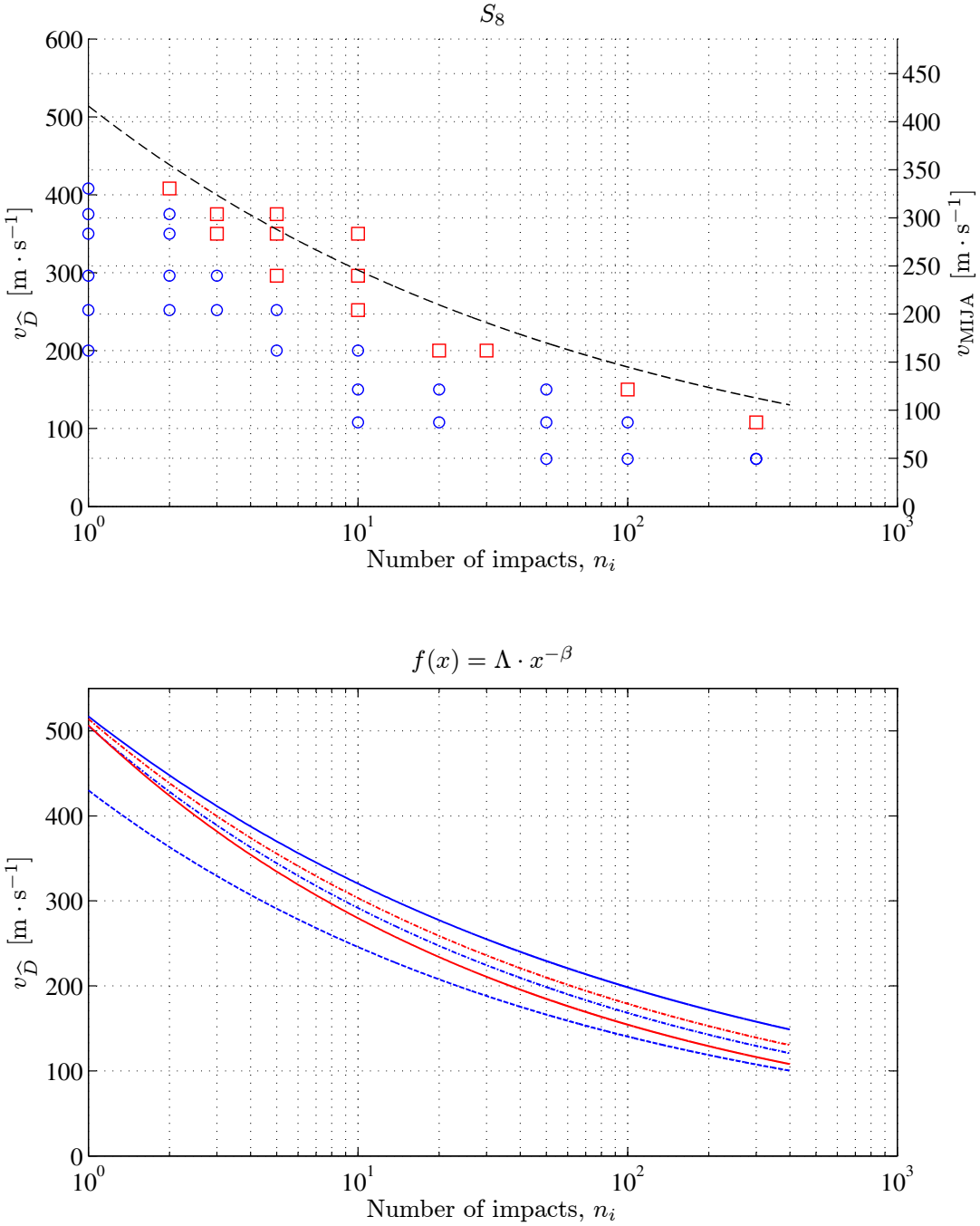

Figure 4.12. Damage Threshold Velocity curves for specimen S_8 (top) and functions $f(x) = \Lambda \cdot x^{-\beta}$ (bottom), with $x = n$ and $\Lambda \in [430.01, 517.14]$ and $\beta \in [0.208, 0.258]$. The S_1, S_2 and S_5 specimens are represented in blue with solid, dashed-dotted line, and dashed line respectively. The S_6 and S_8 specimens are further represented by a solid red and dashed-dotted red line. The order of the curves at $n = 300$ from highest erosion resilience to lowest: S_1, S_8, S_2, S_6, and S_5.

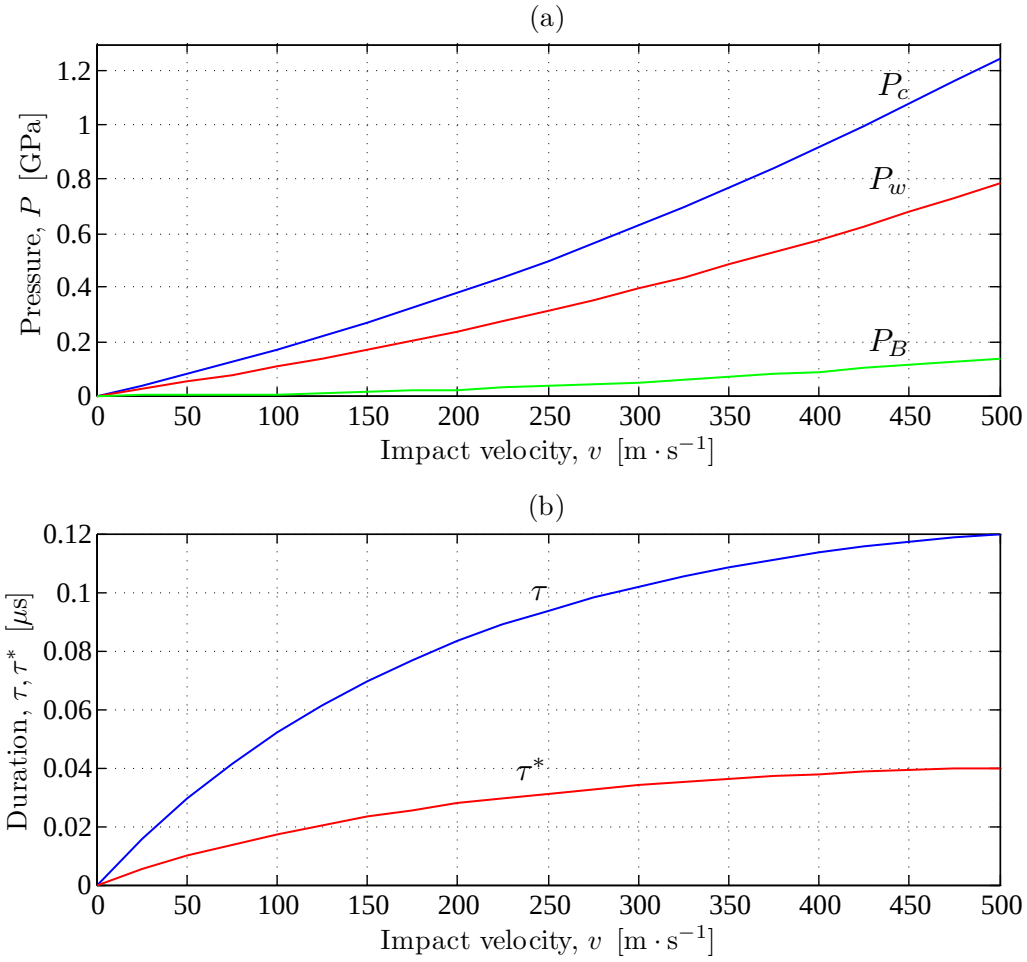

Figure 4.13. (a) The center of impact pressure P_c (in blue), water hammer pressure P_w (in red) and Bernoulli stagnation pressure P_B (in green) for different impact velocities. (b) The duration of pressure release τ (in blue) and water hammer pressure τ^* (in red), for different impact velocities.

The tested specimens exhibit nominally similar damage threshold velocities $v_{\widehat{D}} \cong 130 \pm 20$ m $\cdot$ s^{-1}, as addressed in further detail for each specimen and shown in Figure 4.12. For an equivalent 2 mm droplet velocity at the damage threshold velocity, the water hammer pressure $P_w \approx 0.14$ GPa, pressure at the center of the impact $P_c \approx 0.23$ GPa and the Bernoulli stagnation pressure $P_B \approx 9.4$ MPa, as calculated by Equations (2.8), (2.9) and (2.11). These values should be viewed against the tensile strength of the material which is ~ 80 MPa (Huntsman Advanced Materials, 2007). As the water hammer pressure and stagnation pressure are greater than the tensile strength of the material, substantial damage to the material is expected. The pressure release commences at $\tau \approx 0.02$ μs and the water-hammer pressure terminates at $\tau^* \approx 0.06$ μs with an estimated crater diameter at impact $d_c \approx 0.15$ mm.

Based on the damage threshold velocity results in Figure 4.12, sample S_1 (LY564) is most resilient to liquid impact and sample S_5 (32_MINAS1_07) stands out as most susceptible to liquid impact. The studied samples exhibit close related performance when subjected to liquid erosion. Based on the empirical results, the following ranking can be delineated in order of decreasing liquid erosion resilience: S_1 (LY564), S_8 (SW404 + XB5173), S_2 (LY564 + 0.5% MWCNT), S_6 (32_A05_CANBIO1_07) and finally S_5 (32_MINAS1_07), as shown in Figure 4.12. It is observed that despite an increase of Vickers hardness value in excess of 52% between S_1 (LY564) and S_8 (SW404 + XB5173), the S_1 specimen still demonstrates a higher erosion resilience. From the literature review, and particularly from Equation (2.4) it is shown that the erosion rate $\dot{E} \propto E^{n_1} H^{n_2} K_{Ic}^{n_3}$, where the constants n_1,

n_2 and n_3 are empirically determined. However, with unknown values of fracture toughness K_{Ic}, and Young's modulus E, for the considered materials in this study and the relationship between Vickers hardness and erosion resilience exhibiting a random nature, the erosion rate can not be determined as a function of Vickers hardness, Young's modulus and fracture toughness with corresponding empirical constants, for the materials of this study. A schematic micrograph of cracks in the proximity of an impact site and the corresponding crack lengths are shown in Figure 4.14 and Table 4.4 respectively. In Table 4.4, the average surface crack separation is defined as $\Delta r = \sum_{i=1}^{N} \frac{\delta_i}{N}$ where δ_i denotes the distance between the cracks along a radius extending from the impact location. The S_8 material has been omitted from this table due to its non-radial cracking.

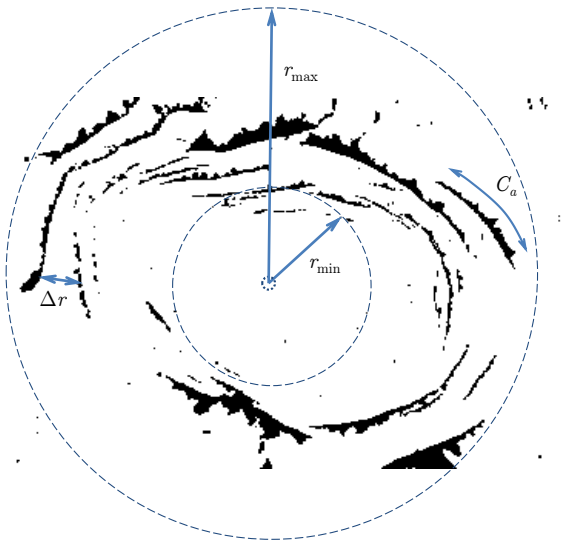

Figure 4.14. A schematic micrograph of Hertzian ring cracks in the vicinity of a liquid impact site. The crack length C_a, inner damage annulus $r_{\min}$, outer damage annulus $r_{\max}$ are depicted in the figure.

Specimen No.	$C_a^{\min}$ [μm]	$C_a^{\max}$ [μm]	$r_{\min}$ [μm]	$r_{\max}$ [μm]	Δr [μm]
S_1	58	836	157	861	91
S_2	43	643	329	942	233
S_5	57	911	280	1166	46
S_6	44	578	205	927	56

Table 4.4. Crack length C_a, inner damage annulus $r_{\min}$, outer damage annulus $r_{\max}$ and average surface crack separation Δr for the specimens at 300 impacts.

The resulting fracture from high speed liquid impact onto a solid can be related to different damage mechanisms as identified by Bowden and Brunton (1958, 1961). In their work they specify these deformations as:

(i) circumferential fracture on the surface
(ii) subsurface fractures
(iii) plastic deformation in a large scale
(iv) deformation due to shear in the vicinity of the impact zone periphery
(v) fracture arising from the reflection and interference of stress waves

The damage deformation nomenclature specified by Bowden and Brunton (1961) is adopted in this study, and referred to upon describing the failure classifications.

$\boldsymbol{S_1}$ (LY564)

This sample has visible surface scratches and is the only sample in the study with $H/h_{s,\,d_{\mathrm{MIJA}}} < 1$. Hence, it is clear that wave reflections within this specimen when subjected to an incoming droplet are not negligible. As S_1 is a material with established material properties (Huntsman Advanced Materials, 2007), these have been used to provide theoretical values for the wave

speeds within the material, radius of fracture initiating flaw and the damage threshold velocity. Under the assumption that specimen S_1 exhibits a brittle behavior, the radius of a flaw that initiates a crack can be estimated using Equation (2.13). The radius of critical flaw size based on the properties of LY564 is estimated as $\tilde{r} \approx 61.3\ \mu$m.

The theoretical value of the damage threshold velocity in accordance with Equation (4.2), $v_{\mathrm{DT}}^{\mathrm{T}} \approx 90\ \mathrm{m} \cdot \mathrm{s}^{-1}$. From Figure 4.10 however it can be deduced that Equation (4.2) underestimates the Damage Threshold Velocity as $v_{\mathrm{DT}}^{\mathrm{T}} < v_{\mathrm{DT}}^{\mathrm{Exp}}$. A poor correlation of Equation (4.2) with experimental data for other materials is however also confirmed in studies elsewhere (Adler, 1987, 1981). This limitation in the model, is due to the drop interactions with the local aerodynamic flow field not being considered. For a better correlation between the model and the experimental results, Adler (1987) suggests that more complete statistical and aerodynamic analyses are carried out. The theoretical values for wave speeds in the S_1 specimen are, $c_L \approx 4770\ \mathrm{m} \cdot \mathrm{s}^{-1}$, $c_T \approx 2291\ \mathrm{m} \cdot \mathrm{s}^{-1}$ and for the Rayleigh-wave $c_R \approx 2255\ \mathrm{m} \cdot \mathrm{s}^{-1}$. The result of the transverse wave velocity falls therefore within approximately 1% of the measured speed of sound in the specimen which indicates a good agreement between the experimental and theoretical value.

The S_1 specimen is the only specimen in the study that exhibits a Hertzian cone crack, as shown in Figure 4.5 (f). The occurrence of reflecting waves within the specimen and their interference with the Rayleigh-wave, can in part explain the resulting Hertzian cone crack. Theoretical values for the

width of first and second cracking zones, as well as the amplitudes for the incident angles in comparison to glass and Perspex is presented in Tables 4.1 and 4.2. Based on these results, a fracture zone is most likely to occur at radius y_1 where $-A_1/A$ is over 80%, and the second band at y_2 where $(-A_1/A)^3$ is quite large. The resulting fracture on this specimen is attributed in large to classification categories (i), (ii) and (v), as explained earlier in this section. As this sample features some polishing scratches, Rayleigh waves open and expand these defects. For scratches with a tangential placement to the impact circumference the radial jetting further exploits these defects and multiple nucleation points are evident along the length of the material flaw. The stripped material arising as a consequence of this phenomenon lies in a direction away from the center of the impact. The sub-surface gross cracking located at the impact site is of Hertzian cone crack nature. The conical fragment base, located on the rear side of the specimen detaches upon repeated impacts on the same location as shown in Figure 4.5 (f). In order to compare the obtained damage threshold velocity for the S_1 specimen, with other materials, a literature survey was carried out, in which the work of Seward et al. (1990) was chosen as means of comparison. Although the empirical work of Seward et al. (1990) has been carried out on IR-window materials and not polymeric matrix composites, the present study features the commonality of using the same experimental apparatus, which makes the comparison possible. The logarithm of fracture toughness of the S_1 (LY564) material as a function of damage threshold velocity is hence shown in Figure 4.15.

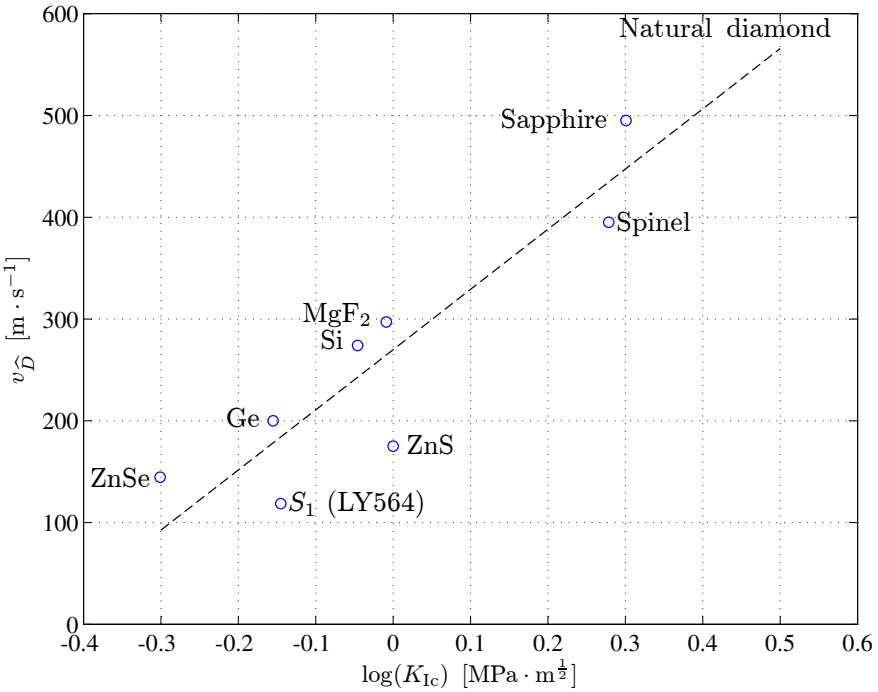

Figure 4.15. The logarithm of fracture toughness for a number of IR-window materials (Seward et al., 1990) and the S_1 (LY564) specimen versus the equivalent impact velocity for 300 impacts.

The S_1 features a low damage threshold velocity in comparison to the tested IR-window materials.

S_2 (LY564 + 0.5% WT. MWCNT)

This specimen has a glossy surface finish with $H/h_{s,\,d_{\mathrm{MIJA}}} > 1$. Therefore, wave reflections that would influence the DTV results are negligible within this specimen. The density is lower for this material in comparison to the pure resin. The sound speed within the specimen is however higher than for the non-reinforced matrix, as a consequence of carbon nanotube reinforcement. The category of fracture in this specimen is mainly by type (i) deformation where micro-cracks initiate at surface flaws as a result of the Rayleigh-waves and

radial jetting. The damaged and undamaged impact sites of the S_2 specimen are shown in Figure 4.10.

$\boldsymbol{S_5}$ (32_MINAS1_07)

Pre-existing surface flaws are apparent on this specimen, although it has not been subjected to a surface treatment, for instance polishing with $H/h_{s,\,d_{\mathrm{MIJA}}} > 1$. This matrix also exhibits type (i) deformation and is the thickest specimen in the study. The damage nucleation sites of this sample are evident upon the Rayleigh waves traversing the surface asperities. The resulting circumferential cracks are shown in Figures 4.7 (b) and (e). The damage threshold velocity curve for the S_5 material is shown in Figure 4.11.

$\boldsymbol{S_6}$ (32_A05_CANBIO1_07)

This sample does not feature any large surface defects and has a slightly higher density and speed of sound in comparison to the pure resin, with $H/h_{s,\,d_{\mathrm{MIJA}}} > 1$. The sample features almost circular Hertzian ring cracks due to the absence of large surface flaws. These cracks subsequently serve as steps in the surface so that radial jetting can further strip away material from the specimen. For the preceding samples the pre-existing surface flaws served as interaction points of the radial jetting. Figure 4.8 (c), shows the nucleation sites for damage on the S_6 sample.

$\boldsymbol{S_8}$ (SW404 + XB5173)

This sample surface is highly pitted with $H/h_{s,\,d_{\mathrm{MIJA}}} > 1$. This specimen was the only specimen in the study which did not exhibit Hertzian ring cracks.

The inherent pitted feature of this specimen made the distinction of damage identification from the natural texture of the specimen challenging. Nonetheless, damage is nucleated in sites where the radial jetting interacts with the surface pitting resulting in a mottled annulus in the vicinity of the impact site, as shown in Figures 4.9 (c) and (d). The damage threshold velocity curve for this material is shown in Figure 4.12.

4.3 Wet Blasting

In order to create a degraded surface finish, corresponding to an eroded state of the specimen several possible approaches could be considered. The most common approach in this regard would be to utilize solid erosion by means of Silicon carbide in order to obtain the desired surface finish. Nonetheless, for the aforementioned specimens this approach is hazardous as it would result in generation of dust and possible contamination of the testing equipment by carbon nanotubes. Another possible technique in obtaining an eroded surface finish, was to utilize a wet blasting approach in which an abrasive, which in this specific case is chosen as aluminum oxide and water is ejected from the nozzle of a blast gun by means of compressed air. The wet blasting process of the specimens, was actualized by using a standard Vapormatt "Vapormate" blast gun operated at a process air pressure of 2.5 bar. The aluminum oxide abrasive was of grade 100/120, measured in US mesh. The distance between the blast gun and each specimen surface was maintained at 100 mm, with the blast gun positioned perpendicular to the surface. The blast duration period for each specimen was further 30 seconds.

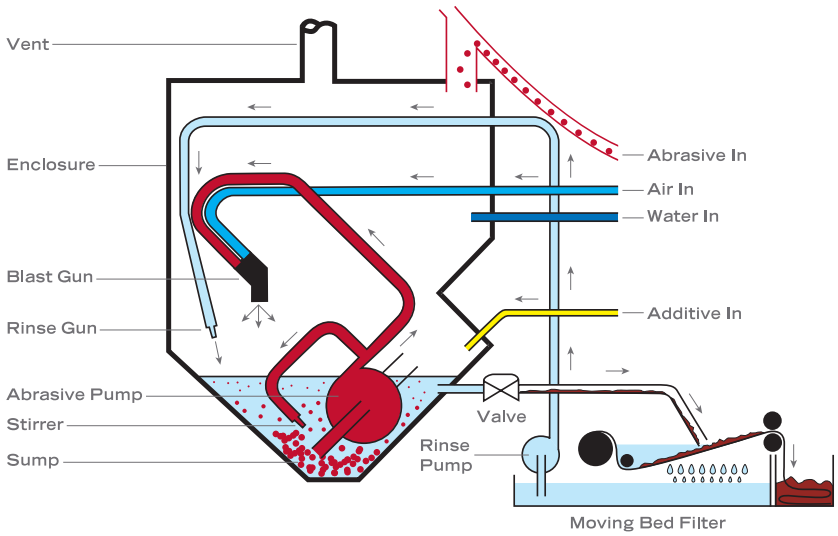

Figure 4.16. A schematic overview of the wet blasting technique. Reprinted with kind permission of Vapormatt, United Kingdom. *Source:* (Vapormatt, 2009).

Figure 4.16 provides an overview of the wet blasting process. As the system is contained and the abrasive recycled, dust or equipment contamination is not generated upon utilizing this approach. Hence, this technique was chosen in order to reduce the safety hazards and for obtaining an eroded state of the specimens utilizing a wet blasting machine. One of the challenges of using this approach was to hold the specimens in place during the wet blasting process. This was commonly achieved by shielding the left and right boundaries of the rectangular specimens. For certain specimens, it was possible to subject the surface to wet blasting without shielding the boundaries which results in an average surface roughness finish on the entire specimen area R_a^e. If the boundaries are to be shielded, two different surface finishes might appear on

the same specimen surface, R_a^p and R_a^e. However it should be noted that the boundaries with the R_a^p surface finish at most made up 20% of the entire specimen area. The averaged surface roughness prior and after wet blasting of the candidate materials was established by utilizing a Taylor Hobson Surtronic 3+, and employing a diamond stylus. The instrument features a minimum and maximum traverse length of 0.25 mm and 25.4 mm, respectively. The traverse speed is further 1 mm $\cdot$ s^{-1} at a resolution of 0.01 μm (Taylor Hobson Precision).

The surface roughness for the materials in the pristine state R_a^p and eroded state R_a^e are shown in Table 4.5.

S_n	R_a^p [μm]	R_a^e [μm]	$\Delta\overline{R}_a$
S_1	5	4.24	-0.2
S_2	0.74	4.4	4.9
S_3	0.20	3.98	18.9
S_4	0.8	3.74	3.7
S_5	0.20	4.06	19.3
S_6	1.2	3.92	2.3
S_7	0.8	2.32	1.9

Table 4.5. The pristine surface roughness R_a^p and eroded surface roughness R_a^e and the percentage increase or decrease in surface roughness defined by $\Delta\overline{R}_a \equiv (R_a^e - R_a^p)/R_a^e$.

For the majority of the specimens, the wet blasting process resulted in an averaged surface roughness $R_a^e \cong 4$ μm, implying in a higher surface roughness in relation to the pristine state. For the S_1 (LY564) specimen however, the wet blasting process resulted in a lower value of surface roughness. This feature stems from the initial surface characteristics of S_1, which was highly pitted and exhibit visible surface scratches. The highest and lowest percent-

age increases in surface roughness are according to Table 4.5 encountered for the S_5 and S_1 specimens respectively.

4.4 Stress Reduction on the Substrate by usage of A Coating Layer

Springer's model

An alternative approach in order to reduce the stress in the substrate and determine the suitability of the candidate materials for leading edge applications, was to supply the substrate material with a thin coating. For practical reasons the thickness of the coating should be $\sim \mathcal{O}(0.5)$ mm. The analytical model of Springer (1976), has in this chapter been utilized in order to assess the influence of coating and substrate choice on the stress factor, σ^*. By definition, a large value on the stress factor is preferred, as it indicates a larger stress reduction due to the presence of the coating on the substrate. For cases of $\sigma^* < 0$, the combination of coating and substrate are not desired as they instead of decreasing the stress in the substrate, imply that the stress within the substrate is increased due to the presence of the coating material. Hence, this analytical approach can be used to identify suitable coating and substrate combinations and their potential stress reduction on the substrate. The analytical model of Springer (1976) has the following underlying assumptions:

- The coating and substrate are homogeneous.
- The substrate extends semi-infinitely with its thickness $h_S > 2d(\frac{C_S}{C_L})$.

- The speed of the stress waves into the coating and the droplet is equal to the speed of sound.
- The material is unstressed prior to liquid impact.
- The stress wave is one-dimensional and propagates normal to the specimen. Further, stress waves parallel to the specimen surface are neglected.

This formulation examines the impact of a liquid droplet with diameter d, onto a two layered structure with the first layer formed by the coating and the second layer by the substrate, as shown in Figure 4.17. Upon impingement on the coating two different wave fronts travel into the liquid and coating respectively, denoted by C_l and C_c. The wavefront in the coating further advances towards the coating-substrate interface, where a portion of the stress wave is reflected back into the coating and the remaining part is transmitted to the substrate. Due to this reflection a new wave is now advancing in the coating with a different magnitude. Springer (1976) outlines a thorough derivation of mathematical expression in which the magnitude of the left traveling waves σ_L^*, with waves propagating towards the coating-liquid interface, and right traveling waves σ_R^*, with waves propagating towards the coating-substrate interface, are expressed as

$$\begin{cases} \sigma_L^* = \frac{1+\Psi_{sc}}{1+\Psi_{sc}\Psi_{ls}} \left[1 - (\Psi_{sc}\Psi_{lc})^k\right] \\ \sigma_R^* = \sigma_L^* - \Psi_{sc}(\Psi_{sc}\Psi_{lc})^{k-1} \end{cases} \tag{4.15}$$

where

$$\Psi_{sc} \equiv \frac{Z_s - Z_c}{Z_s + Z_c} \tag{4.16}$$

$$\Psi_{ls} \equiv \frac{Z_l - Z_c}{Z_l + Z_c} \tag{4.17}$$

with $\Psi_{sc}\Psi_{ls} < 1$. It can be shown (Springer, 1976) that the mean stress in the substrate is reduced if

$$\begin{cases} Z_l < Z_c > Z_s \\ Z_l > Z_c < Z_s \end{cases} \tag{4.18}$$

and that the mean stress in the substrate is enhanced when

$$\begin{cases} Z_l < Z_c < Z_s \\ Z_l > Z_c > Z_s \end{cases} \tag{4.19}$$

The number of reflections within the coating is further given by

$$\overline{k} = \begin{cases} k_e\gamma & \text{, when } t_l < t_e \\ k_e & \text{, when } t_l > t_e \end{cases} \tag{4.20}$$

where k_e denotes the maximum number of reflections after which the waves have negligible magnitudes. The non-dimensional parameter is defined as $\gamma \equiv \overline{k}/k_e$, and can be expressed as

$$\gamma = \frac{d}{h_c}\left\{\frac{C_c}{C_l}\frac{1+\frac{Z_l}{Z_s}}{1+\frac{Z_c}{Z_s}}\right\}\left\{\frac{2}{1+\frac{Z_l}{Z_c}}\right\} \tag{4.21}$$

The reduction stress at the substrate surface is further given by

$$\frac{\overline{\sigma^h}}{\sigma_\infty} = 1 - \Psi_{sc}\Psi_{ls}\left\{\frac{1-\exp(-\gamma)}{\gamma}\right\} \tag{4.22}$$

In Equation (4.22), $\overline{\sigma^h}$ describes the experienced stress without the presence of the coating and σ_∞, the stress with the present coating. The stress factor σ^*, is in the present study defined as

$$\sigma^* \equiv 1 - \left(\frac{\overline{\sigma^h}}{\sigma_\infty}\right) \tag{4.23}$$

The stress factor σ^*, hence defines the reduction of stress due to the presence of the coating layer on the substrate and is given in percent. Equally, for values of $\sigma^* < 0$, the presence of the coating increases the stress on the substrate in comparison to the case where the coating layer is absent. Using Equations (4.15) $-$ (4.22), two different approaches can be used to determine the suitability of the coatings on a substrate material, as shown in Figure 4.17.

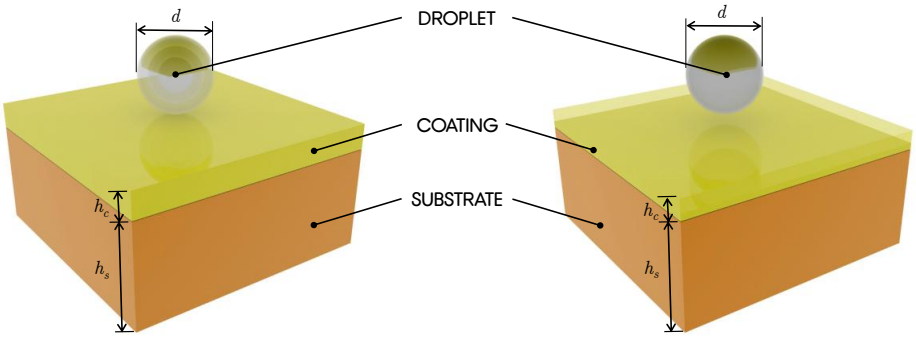

Figure 4.17. A schematic of the substrate and coating arrangement and possible influence of droplet size d (left) and coating thickness h_c (right), on the stress factor σ^*.

With the given set of candidate materials and their known basic material properties, the analytical formulation is able to provide the combination of substrate and coating material that results in the largest reduction of stress

on the substrate material. Hence, a sensitivity analysis was carried out with specimens $S_1 - S_{10}$, and a constant coating thickness $h_c^{\text{const.}} \equiv 0.3$ mm, and a constant droplet size $\widehat{D} = 2$ mm. The most suitable substrate and coating combination is established based on the percentage in reduced stress, $\left(\frac{\overline{\sigma^h}}{\sigma_\infty}\right)^* = 1 - \frac{\overline{\sigma^h}}{\sigma_\infty}$, and the number of coatings for which a given substrate yields $\left(\frac{\overline{\sigma^h}}{\sigma_\infty}\right)^* > 0$, denoted by $n_{\text{prot}}^{\text{coat}}$. For optical windows, an alternative approach that offers protection for the window, consists of a two-layered system, in which the cladding is placed on top of the optical window. A cladding is in general thicker than a coating, with a thickness $\sim \mathcal{O}(1)$ mm. In this system, also a compliant adhesive layer may be present between the interface of the window and cladding. The benefit of utilizing a compliant layer is that a large fraction of the impact energy is reflected back into the cladding (Harris, 1999). In essence, a similar approach can be implemented with the current candidate materials, in order to examine the potential role of the cladding on the substrate, here analogous to the optical window. The fraction of the reflected energy in the two-layered system can be written as (Gentilman, 1993)

$$\mathcal{F}_R = \frac{(Z_1 - Z_2)^2}{(Z_1 + Z_2)^2} \tag{4.24}$$

where the subscripts 1 and 2, designate the top and bottom layer respectively. Although, Equation (4.24) is a simplification and merely based upon the acoustic impedance of the involved materials, it is able to infer results regarding suitable substrate/cladding combinations. Figure 4.18, shows a schematic of the substrate material, the compliant layer and the cladding.

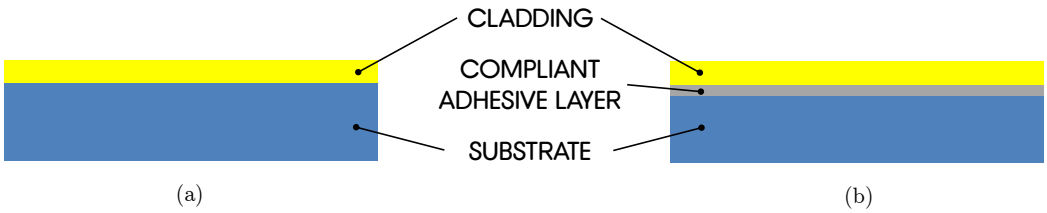

Figure 4.18. A schematic of (a) the substrate and the cladding, and (b) the substrate, the adhesive compliant layer and the cladding.

Stress mitigation results

The sensitivity analysis presented in Appendix G, examines the role of all specimens $S_1 - S_{10}$ as substrate candidates. The analysis is carried out for a fixed coating thickness $h_c \equiv 0.3$ mm and an impact droplet size of $d = 2$ mm, with the substrate described by one of the candidate material, and the different coatings by the remaining candidate materials. Table 4.6, exhibits the substrate that offers most protection based on the number of one layered coatings which can be placed upon it $n_{\text{prot}}^{\text{coat}}$, and the largest value of the reduction stress on the substrate denoted by $\sigma_{\max}^{*} = (1 - \overline{\sigma^h}/\sigma_\infty)_{\max}$.

Substrate	$\sigma_{\max}^{*}$ [%]	$n_{\text{prot}}^{\text{coat}}$
S_1	1.70	9
S_2	1.50	8
S_3	0.69	5
S_4	0.65	3
S_5	0.82	6
S_6	0.68	4
S_7	0.97	7
S_8	N/A	0
S_9	0.62	2
S_{10}	0.40	1

Table 4.6. The suitable substrate for the different coatings, $n_{\text{prot}}^{\text{coat}}$ and the largest value of reduced stress in the coatings, $\sigma_{\max}^{*} = (1 - \overline{\sigma^h}/\sigma_\infty)_{\max}$.

The results from the analysis indicate that the best substrate candidate within the set of considered materials is S_1 (LY564), since a material layer with a thickness of 0.3 mm made of all the remaining candidate materials placed on top of S_1 substrate, would result in a reduction of stress on the substrate material. The influence of the droplet size on the reduction stress for the S_1 (LY564) substrate, is shown in Figure 4.19.

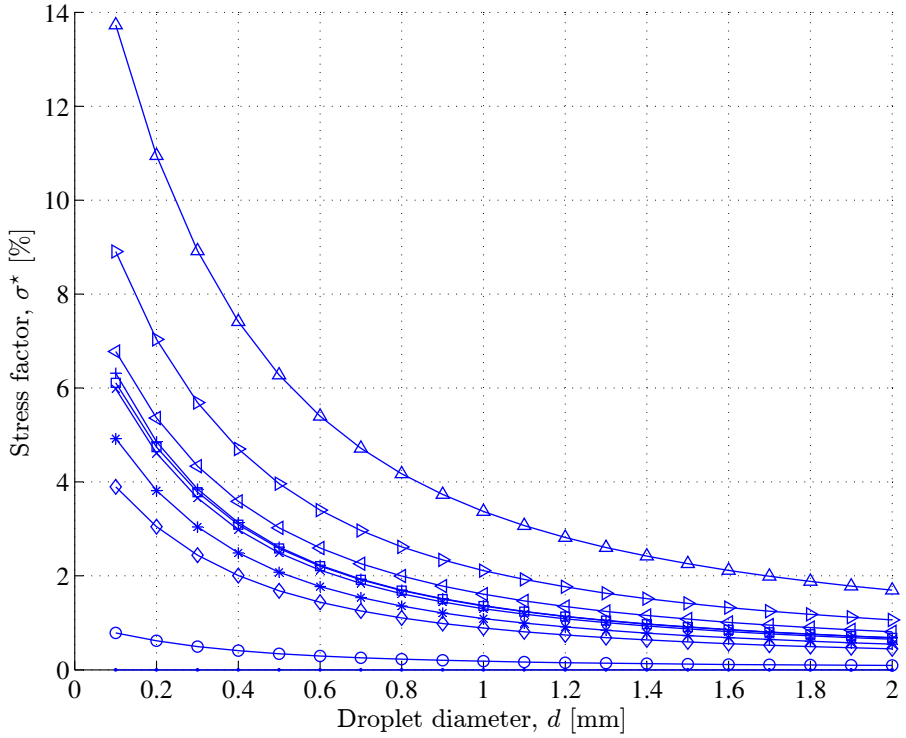

Figure 4.19. The influence of droplet diameter d, on the stress factor $\sigma^* = 1 - (\overline{\sigma^h}/\sigma_\infty)$, within the coating for a fixed specimen thickness of $h_c \equiv 0.3$ mm. The following symbols are utilized for each specimen: S_1 ($\cdot$), S_2 ($\circ$), S_3 ($\times$), S_4 ($+$), S_5 ($*$), S_6 ($\square$), S_7 ($\Diamond$), and S_8 ($\triangle$). The multi-layered specimens are denoted by S_9 ($\triangleright$) and S_{10} ($\triangleleft$) respectively.

Figure 4.19, indicates that the choice of the S_1 (LY564) as a substrate material results in stress reduction on the substrate when combined with all the other candidate materials $S_2 - S_{10}$. It can be deduced that S_8 (SW404 + XB5173) is the coating material that provides the largest protection for the substrate material with its largest level of protection $\sigma^* \approx 1.7\%$ for a standard rain droplet, with a droplet size of $d = 2$ mm. It is also observed that lowest level of protection is offered by the S_2 (LY564 + 0.5% MWCNT) coating, with $\sigma^* \approx 0.09\%$ at the same droplet size. Although the difference between the

largest and lowest level of protection is small at the level of a standard rain droplet, it increases for smaller droplet sizes. The properties of the multi-layered materials in this analysis, have been approximated upon using an average acoustic impedance across all layers and is therefore not based on each individual layer. The influence of coating thickness is examined for all considered materials for a fixed droplet size of 2 mm, as shown in Figure 4.20.

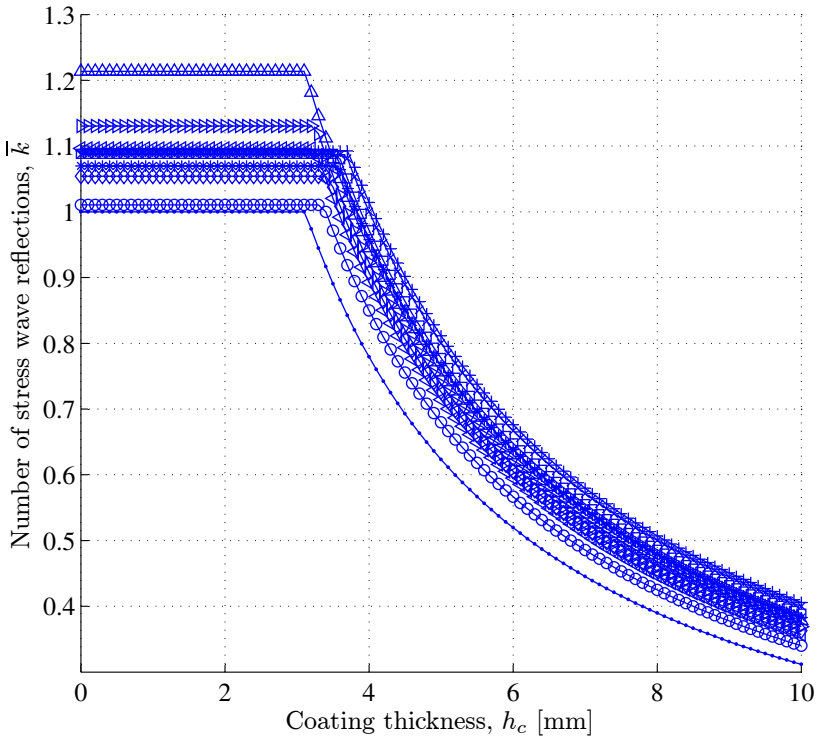

Figure 4.20. The influence of coating thickness h_c on the number of stress wave reflections during the time of impact $\overline{k}$, within for a fixed standard rain droplet size $d = 2$ mm. The following symbols are utilized for each specimen: S_1 ($\cdot$), S_2 ($\circ$), S_3 ($\times$), S_4 ($+$), S_5 ($*$), S_6 ($\square$), S_7 ($\Diamond$), and S_8 ($\triangle$). The multi-layered specimens are denoted by S_9 ($\triangleright$) and S_{10} ($\triangleleft$) respectively.

From Figure 4.20, it can be deduced that the number of stress wave reflection $\overline{k}$, is independent of the coating thickness h_c, for values of $h_c < 3$ mm. Although large values of a coating layer imply that $\overline{k} \to 0$, these values are not physically realistic and do not reduce the number of stress wave reflections considerably. The results also suggest that for the considered materials an added thickness of 1 mm may significantly reduce the number of stress reflections within the substrate, and that beyond a coating thickness $h_c > 4$ mm, no significant reduction in the number of stress waves within the coating is evident. In order to examine the influence of utilizing different substrate and coating materials, based on Equation (4.24), a number of combinations of the candidate materials were considered. Table 4.7, shows the specimen number S_n, with $n = \{1, 2, \ldots, 10\}$, the acoustic impedance Z, based on the findings of Section 3.6, and the reflected energy $\mathcal{F}_R$ for each substrate and cladding combination. In Table 4.7, the substrates are shown as rows and each corresponding reflected energy as a column, corresponding to case (a) in Figure 4.18. The specific column S_L^C, refers to implementation a compliant adhesive layer between the substrate and cladding, corresponding to case (b) in Figure 4.18. All results shown in Table 4.7 are in given in percent.

S_n	S_1^S	S_2^S	S_3^S	S_4^S	S_5^S	S_6^S	S_7^S	S_8^S	S_9^S	S_{10}^S	S_L^C
S_1^C	0.00	0.12	3.44	3.74	2.55	3.51	1.76	11.08	3.94	5.83	95.06
S_2^C	0.12	0.00	2.32	2.56	1.59	2.37	0.98	9.12	2.74	4.37	94.72
S_3^C	3.44	2.32	0.00	0.01	0.07	0.00	0.29	2.46	0.02	0.34	92.90
S_4^C	3.74	2.56	0.01	0.00	0.12	0.00	0.39	2.22	0.00	0.26	92.78
S_5^C	2.55	1.59	0.07	0.12	0.00	0.08	0.08	3.35	0.16	0.73	93.25
S_6^C	3.51	2.37	0.00	0.00	0.08	0.00	0.31	2.41	0.01	0.32	92.87
S_7^C	1.76	0.98	0.29	0.39	0.08	0.31	0.00	4.39	0.46	1.27	93.60
S_8^C	11.08	9.12	2.46	2.22	3.35	2.41	4.39	0.00	2.07	0.99	90.38
S_9^C	3.94	2.74	0.02	0.00	0.16	0.01	0.46	2.07	0.00	0.20	92.71
S_{10}^C	5.83	4.37	0.34	0.26	0.73	0.32	1.27	0.99	0.20	0.00	92.05

Table 4.7. Reflected energy for substrate and coating combinations of the candidate materials, with and without a compliant layer. In the table the subscripts S and C refers to a substrate and cladding respectively. The case with the compliant adhesive layer is denoted by S_L^C. All results given in the table are in percent.

From Table 4.7, it can be deduced that the highest fraction of the incident stress wave to be reflected back at the interface is for the substrate combination of specimens S_1 (LY564) and S_8 (SW404 + XB5173). For the adhesive compliant layer, an acoustic impedance of $Z = 940\,000\ \mathrm{kg \cdot m^{-2} \cdot s^{-1}}$, is chosen based on the literature (Harris, 1999). It is interesting that the identified combination of materials, that results in the highest fraction of impact energy reflected is the same combination, that was identified by Springer's model, explained earlier in this section. This observation is based on two different approaches, employing the acoustic impedance values estimated in Section 3.6. The values of the reflected energy due to the presence of an adhesive layer, are solely based on the acoustic impedance values of the cladding and the adhesive layer. A caveat with this approach is that it does not account for the layer thicknesses, nor the presence of the substrate material when the S_L^C is presented. Nonetheless, a significant change is observed upon employ-

ing a compliant adhesive layer in the fraction of impact energy that would be reflected back to the cladding. Hence, this approach infers that a multi-layered system can significantly enhance the performance of individual layers, if a correct combination of layers and compliant adhesive layers is employed.

4.5 Conclusions

Based on liquid impacts on the candidate materials, the damage threshold velocities of polymeric matrix composites with and without reinforcing carbon nanotubes have been established empirically. It is notable that the presence of carbon nanotubes does not infer that a higher erosion resilience is encountered. Despite the nominally similar damage threshold velocities the mathematical function $f(n) = \Lambda \cdot n^{-\beta}$, is able to provide a ranking consistent with the empirical observations. The experimental results also convey that the thickness of the specimen h_s has a significant role during the tests, if the specimen thickness is below a threshold thickness, $h_s > 2D(\frac{\hat{c}_S}{\hat{c}_L})$ as demonstrated with the Hertzian cone crack on S_1 material following the liquid impact. The exercised wet blasting technique on the specimens has been carried out without occurrence of a catastrophic failure of the materials and health hazards.

It has further been possible to deliberately erode the surfaces of the supplied candidate materials, in order to examine the influence of erosion on other parameters in this study, such as wettability and ice adhesion.

The presented analytical stress mitigation model on the substrate, referred

to as Springer's model, is despite its simplicity capable of determining suitable coating and substrate combinations. The stress factor which in effect is the measure of reduced stress on the substrate due to the presence of the coating, is found to be marginal for all considered cases, with $\sigma^* \sim 2\%$ at most, for a single droplet impact. Despite the simplicity of the analytical approach, the model identifies substrates S_1 (LY564) and coating S_8 (SW404 + XB5173) to provide most reduction in stress at the substrate surface. These specimens additionally exhibit the highest damage threshold values respectively, indicating their large erosion resilience. Based on this observation, it can be concluded that the influence of stress factor, is highly dependent upon the choice of the coating and the substrate. The limitation of the model is that it can not directly be linked to the erosion resilience of the coating and substrate in a two-layered system, as an incorrect choice of coating and substrate might still ensue in an increase in stress at the substrate.

The cladding and a compliant adhesive layer model, has further successfully been employed in order to find the suitable cladding and substrate combination. The two different employed stress mitigation models, have hence indicated the same substrate/coating combination, as the most suitable one in terms of stress reduction. The simplistic nature of the models, have despite their limitation exhibited that different levels of stress mitigation can be achieved upon combination of the specimens in a layered system.

Chapter 5

Wettability

5.1 Static Wettability

Contact angle measurements were carried out on the candidate materials, in order to obtain the advancing and receding angle for each specimen. This method conveys results about the surface energy using Young's equation (Young, 1805)

$$\gamma_{\mathrm{SG}} - \gamma_{\mathrm{SL}} - \gamma \cos(\varphi) = 0 \tag{5.1}$$

where γ is the energy and the subscripts SG and SL denote solid-gas and solid-liquid respectively. The drop is modified by either dispensing or retracting its volume, resulting in an advancing angle θ_A or a receding angle θ_R, measured by a protractor. This method allows for an assessment of the homogeneity of the specimen, as droplets can be deposited on different locations on the specimen surface. In this study an averaged value of five measurements placed on different locations on the surface are presented. Hysteresis ψ, can in this

context be defined as $\psi \equiv \theta_A - \theta_R$. The equilibrium Young contact angle θ_C can also be expressed in terms of the advancing and receding angles (Tadmor, 2004) as

$$\theta_C = \arccos\left\{\frac{\Gamma_A \cos(\theta_A) + \Gamma_R \cos(\theta_R)}{\Gamma_A + \Gamma_R}\right\} \tag{5.2}$$

where $\Gamma_{A,R} \equiv \{\sin^3(\theta_{A,R})/(2-3\cos(\theta_{A,R})+\cos^3(\theta_{A,R}))\}^{1/3}$. The static wetting of the specimens was assessed by employing contact angle measurements on both pristine and eroded specimen surfaces. The experimental setup for the contact angle measurements is shown in Figure 5.1.

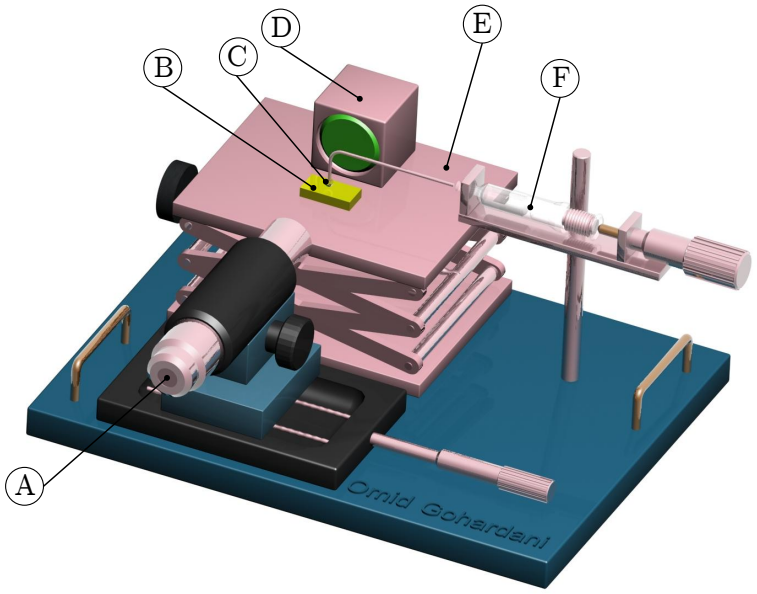

Figure 5.1. The experimental setup for the contact angle measurements, with notations: (A) Eye piece fitted with a protractor, (B) specimen, (C) generated droplet, (D) LED with diffuser, (E) vertical adjustable table, and (F) syringe and spring device fitted with a micrometer.

The specimen was positioned on a table with a vertical adjustment capability and illuminated by an LED light with a diffuser, which provided a uniform illumination of the droplet. The 5 cc syringe with a glass luer slip tip fitted

with a 6" needle and 90° blunt end produced the 2.04 mm drop of deionized water. The volume of fluid utilized for these measurements ranged between $10 - 90$ μl. The uncertainty of the measurements was mainly related to the manual goniometry readings of the back-lit droplet's advancing and receding angles. Since imperfections in surface uniformity and cleanness were present at the time of the readings, an error of $\sim 5°$ is expected for the contact angle measurements. Table 5.1, shows the advancing θ_A, receding θ_R, equilibrium Young contact angle θ_C, and their corresponding hysteresis ψ. Surface roughness on the specimens in the pre- and post-erosion state are given by R_a^p and R_a^e respectively. The percentage increase/decrease is further given by $\Delta R_a = (R_a^p - R_a^e)/R_a^p$.

S_n	R_a^p [μm]	R_a^e [μm]	ΔR_a	θ_A [°]		θ_R [°]		ψ [°]		θ_C [°]	
S_1	5	4.24	−0.152	110	75	22	11	88	64	22	11
S_2	0.74	4.4	4.946	93	90	33	6	60	84	35	6
S_3	0.2	3.98	3.675	87	80	28	10	58	70	30	10
S_4	0.8	3.74	4.946	80	90	17	10	64	80	18	10
S_5	0.2	4.06	19.30	90	68	28	13	62	55	30	14
S_6	1.2	3.92	2.267	93	70	32	8	62	62	33	8
S_7	0.8	2.32	1.90	82	110	32	22	50	88	34	22
S_8	0.6	2.98	3.967	117	90	60	8	57	82	63	8

Table 5.1. Surface roughness and contact angles on the specimens in the pre- and post-erosion states. For each contact angle, the left column shows the pristine and the right column the eroded value.

As both the S_9 and S_{10} specimens, have the SW404 + XB5173 material as the outermost layer, these specimens were excluded from wet blasting and Table 5.1. Nonetheless, in order to examine the potential influence of surface preparation on the resulting contact angles in multi-layered materials, the corresponding contact angles were measured on the outermost layer of these two

specimens. It was found that S_9 has $\theta_A = 108°$, $\theta_R = 63°$, $\theta_C = 60°$ and the hysteresis angle $\psi = 45°$. The corresponding angles for the S_{10} specimen are 103°, 28°, 75° and 31°. As $\theta_A < 150°$, for all considered candidate materials in this study, none of the materials exhibited a super-hydrophobic character. The advancing angle θ_A, is the maximum advancing angle and the receding angle θ_R the minimum receding angle. Observance of a range of metastable contact angles between θ_A and θ_R, similar to the present study is confirmed in other studies, for instance by Krishnan et al. (2005), who conclude that a single contact angle fails to adequately represent the wettability of a surface and that the maximum advancing and minimum receding angle, are essential for an adequate representation of the surface wetting. For this reason, the equilibrium Young contact angle being a function of both the advancing and receding angle, provides an additional level of representation of the surface wettability with $\theta_C^p > \theta_C^e$, for the studied samples. From Table 5.1, it can further be observed that the hysteresis values for the eroded candidate materials with carbon nanotube reinforcement is higher than the corresponding pristine values. As the foundational causes of the hysteresis value is still being examined, this interpretation can be attributed to for instance surface roughness, heterogeneity, molecular mobility, liquid penetration and surface wetting, as described by Lam et al. (2002).

5.2 Dynamic Wettability

5.2.1 Experimental facilities

The dynamic wettability experiments are carried out at the vertical droplet tunnel located at Cranfield University, United Kingdom. The tunnel is located next to the main Icing Tunnel, with the flow in both tunnels powered by a centrifugal backward curved suction fan, capable of producing flow rates, $\dot{m}_{\text{Fan}} \in [30, 100]$ kg·s^{-1}. The temperature range $T \in [-30, +30]$ °C is attained by the refrigeration plant which has a capacity of 400 kW. Upon generation of the flow, the air from the fan is directed through a duct into a heat exchanger for cooling and directed into a steering dish in the adjacent vertical tunnel where it gets accelerated toward the test section (Hammond et al., 2003). A droplet generator equipped with an interchangeable platinum nozzle orifice disk is placed on top of the steering dish. Upon entering the contraction section of the vertical droplet tunnel, the mono dispersed droplets are accelerated towards the test section, where the gentle contraction length of 5 meters, ensures that no aerodynamic breakup of the droplets occurs. The test section is situated on top of two control valves, capable of regulating the locus of the stagnation point (Luxford, 2005; Quero, 2006). The target specimen is placed on a designed target holder, that allows for vertical position adjustment of the specimen. This is essential in order to account for the range of different specimen thicknesses within the study.

The incident angle of the oncoming air in relation to the target is $\alpha = 70°$. Upon contact with the target area the flow is bifurcated and exits the tun-

nel through two control valves into the air inlet of the main Icing Tunnel, where it gets regenerated by the fan. The droplet diameter in this study has been confined to $d = 400$ μm, with three different free stream velocities $U_\infty \approx \{35, 50, 60\}$ m $\cdot$ s^{-1}, in accordance with expected number of splashing structures for statistical purposes. The mono dispersed droplets are ejected from the orifice of the droplet generator at a frequency of $f_d \approx 12$ kHz. Figure 5.2 shows a rendering of the experimental setup for the dynamic wettability experiments.

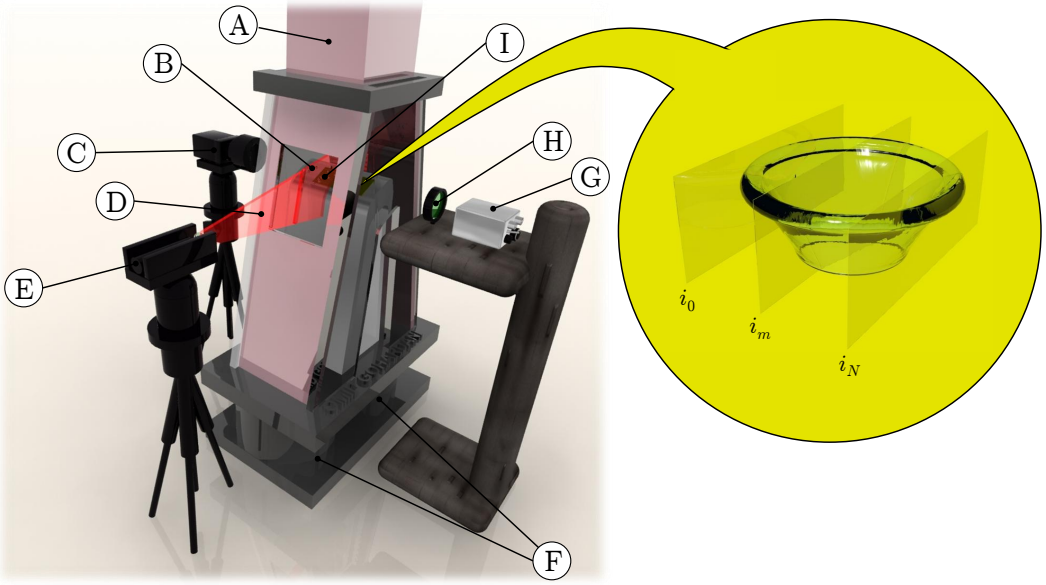

Figure 5.2. The experimental setup for the dynamic wettability experiments with notations: (A) Vertical droplet tunnel, (B) droplet cloud, (C) CCD camera, (D) laser sheet, (E) laser, (F) control valves, (G) LED strobing device, (H) collimating lens, and (I) specimen target. The right hand side image depicts a schematic corona structure with virtual planes $i_0, \ldots, i_N$, with i_m showing the mid-plane of the corona. *Source:* (Gohardani and Hammond, 2011)

The illumination of the target area is attained by directing the light from an LED through a collimating lens. The LED device is strobed with a pulse period $T = 40$ ms and pulse length $\tau = 5$ μs which results in approximately one strobe per acquired frame of the experiment. The image acquisition is actualized by employing a Sony XCD-SX90 camera operated at 30 FPS. The camera is equipped with a 50 mm lens and 13 mm extension. The distance between the camera and the wall of tunnel $d_W = 50$ mm, the LED and the collimating lens $d_C = 40$ mm, and further between the collimating lens and the wall of the tunnel, is $d_L = 100$ mm. The optical magnification of the image is hence 0.32. The experimental images are acquired upon utilizing a graphical user interface on a personal computer.

5.2.2 Illumination and imaging

As the light from the LED device is captured along the length of the specimen, splashing features are apparent in the volume of space along the width of each specimen. The image acquisition camera is focused on the mid-plane of the specimen surface as denoted by i_m in Figure 5.2. This entails that any structure appearing within this plane of sight will appear entirely in focus on the experimental photographs. Equally, a deviation from this plane will result in structures appearing not entirely in focus. However, as the employed illumination within the depth of field is adequate, even off-plane splashing features are distinguishable. This approach hence results in capturing of most splashing events, at the expense of them appearing simultaneously on similar locations along the width of the specimen which may result in distinction

of certain features becoming intricate. The different virtual slices along the width of the specimen with the focused slice on half-width of the specimen are shown in Figure 5.2. With this notation, the LED light travels through all virtual planes providing an integrated view upon image acquisition.

In order to estimate the local liquid water content on the specimen surface, a laser sheet with a 2 mm width as measured by image acquisition of the laser light, was used to illuminate the exact half-width of the specimen, where the camera was focused parallel to the oncoming droplets. Upon entering the laser sheet, the droplets were illuminated and visible as distinct features upon image acquisition. The finite thickness of the laser sheet further implied that very few unfocused droplets were observed. The visible droplets were then counted in each frame along the length of the specimen, resulting in a local liquid water content value for each frame. This value was thereafter averaged across the entire acquisition period of one experiment, resulting in an averaged liquid water content value for the experiment. This methodology was based on the fact that all drops have the same size, which is a highly valid assumption, as virtually no aerodynamic breakup of the droplets occurred within the framework of this study.

5.3 The DSWSAM Methodology

One of the challenges in analyzing the wetting characters of the candidate materials is establishment of a framework, under which the features of each material is examined on the same basis. For this purpose the Dynamic and

Static Wettability Scheme for Advanced Materials henceforth referred to as (DSWSAM) was developed in order to establish this frame of reference. This adopted methodology has been employed to provide insight into the similarity and differences between the wetting characters of the candidate materials. The methodology seeks to discriminate between different types of wetting on the surfaces of the candidate materials and their splashing features following liquid impacts. The inputs and outputs of the DWSAM are shown in Figure 5.3.

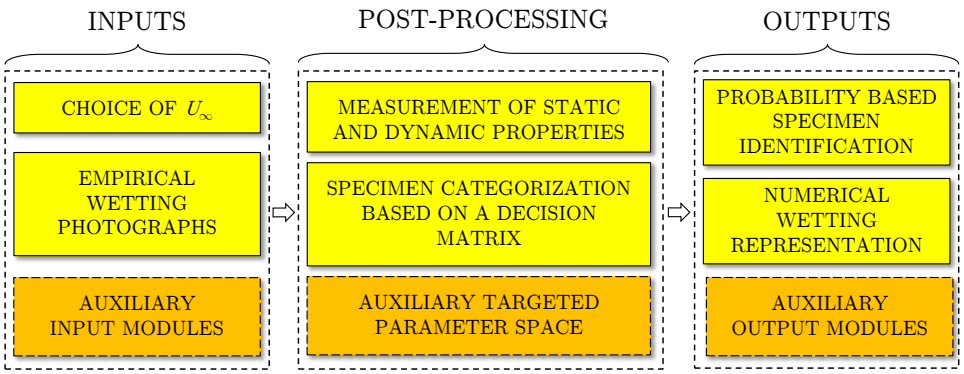

Figure 5.3. Flowchart of inputs, post-processing and data outputs of the DSWSAM methodology based on empirical results. Auxiliary modules can additionally target other parameter spaces and provide additional outputs than those described in this study.

Initially, a free stream velocity for the experiments was chosen on the basis of proximity to a reasonable flight speed within the range supported by the experimental facility, without the complexities of possible shock waves and aerodynamic shattering of the drops. Thus, the free stream velocities $U_\infty = \{35, 50, 60\}$ $\mathrm{m \cdot s^{-1}}$, were chosen for this purpose, as these velocities could easily be obtained in the Vertical Droplet Tunnel, and since they fulfilled the initial criteria.

Upon choice of the velocity, the liquid water concentration was obtained based on a numerical scheme that identifies the droplet cloud distribution from experimental photographs and provides an averaged histogram of the cloud spatial distribution on the target. The two Graphical User Interface tools developed in MATLAB®,†(The MathWorks Inc., 2011), are called the Liquid Water Content Module (LWCM) and the Corona Splashing Measurement Tool (CSMT), respectively. These modules are explained in further detail in

†MATLAB is a high-level computing language developed by MathWorks®.

Sections 5.3.1 − 5.3.3. The dynamic wetting photographs ascribed in the pre- and post-erosion state, are utilized as inputs to the DSWSAM methodology. In general the hydrophobic and hydrophilic nature on the specimen is determined by visual inspection of the specimen surface. For all analyzed images, initially the location of the specimen surface is located. For certain images the actual location of the surface might be obscured by the presence of a partial or continuous water film. Three different categories are therefore identified based on the waviness of the water film on the surface as show in Figure 5.4.

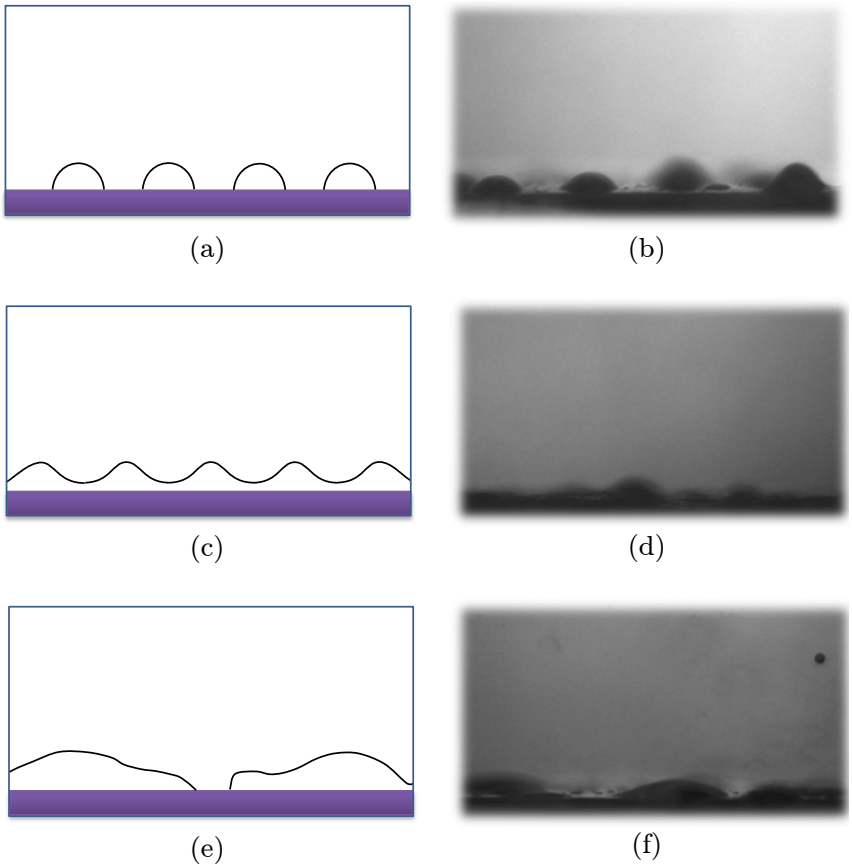

Figure 5.4. Idealized hydrophobic and hydrophilic wetting structures on a specimen surface along with a corresponding representative experimental photograph. A hydrophobic surface is shown in (a) and (b). A hydrophilic surface however is shown in (c) and (d). Figures (e) and (f) finally represent a hydrophobic/hydrophilic surface.

Three different categories are identified based on the waviness of the water film on the surface are: A hydrophobic, hydrophilic and hydrophobic/hydrophilic surface. The surface was classified as hydrophobic, if the specimen surface was partially visible and only obstructed by discrete ligaments of water, shown in Figure 5.4 (a)−(b). If a continuous water film water film layer was present on the specimen surface, it was categorized as a hydrophilic surface, as shown in Figure 5.4 (c)−(d). For instances where an intermediate water film layer with partial characteristics of a continuous water film was identified, the specimen was either classified as hydrophilic or hydrophobic, as shown Figure 5.4 (e)−(f).

For hydrophobic surfaces based on Figure 5.4 (a)−(b), and the corresponding description, the number of fluid ligaments along the surface of the specimen were counted. A larger number of ligaments in that respect represents a more hydrophobic surface.

For a hydrophilic surface, Figure 5.4 (c)−(d) and a surface where the hydrophobic or hydrophilic surface character are difficult to categorize Figure 5.4 (e)−(f), the averaged wave length of the structures are determined. As the interaction of droplets on the specimen surface with and without an existing wetting character during the experiments largely results in formation of coronas, the structure of a water splash corona is the only feature that can be compared across all considered specimens. For comparison purposes, the geometrical attributes of a corona structure consisting of the two angles that the jets subtend with the specimen surface, the width of the corona at base

and top respectively, as well as the height of the corona are of interest, as these features may serve as a probe to determine the surface character and discriminate between the different surfaces.

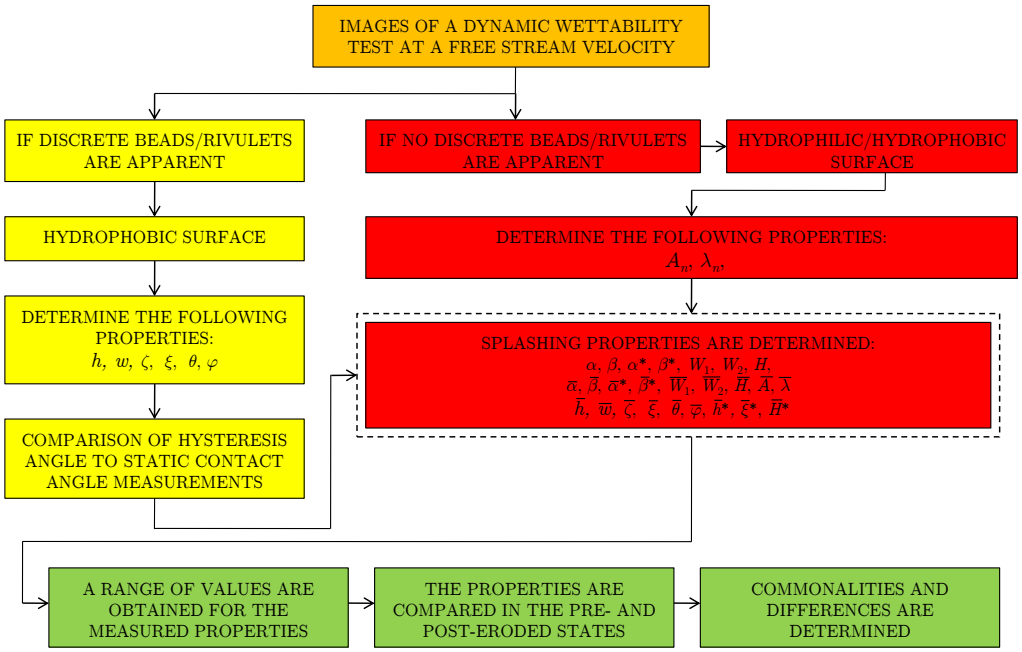

Figure 5.5. Methodology for dynamic wettability test analysis.

There are in particular three important modules that enable a comprehensive assessment of the wetting characteristics of the given specimens:

- The wetting conditions
- The wetting character of the surface
- The resulting fluid structures upon water droplet impact

The wetting conditions are largely determined by the droplet impact velocity, droplet size and air shear forces, as well as the local liquid water concentration at which the experiments are carried out. The resulting wetting character of the surface is described by either beads, rivulets or partial and complete water film layers. The encountered fluid structures in this study are in large coronas upon splashing on the surface of the specimens. For each of the aforementioned modules, a tool has been developed that enables a simplified assessment of the wetting characteristics of the considered specimen. In particular, the wetting condition is addressed by the Liquid Water Content Module (LWCM). The wetting character of the surface is actualized by usage of an idealized fluid structure categorization and a mathematical description of a representative water film layer. The resulting fluid structures ensuing upon water droplet impacts are analyzed by employing the Corona Splashing Measurement Tool (CSMT).

5.3.1 Wetting condition

The droplet size has in this study been confined to $d = 400$ μm, in order to provide adequate wetting conditions on the surface and a large number

of splashing structures. The wetting conditions of the surface is besides the aerodynamic forces on the target, surface character, and incident angles, determined by the number of droplets that impact the specimen surface, per unit time. The local liquid water concentration is hence of crucial importance to establish the likelihood of surface wetting and in order to compare the wettability of the different surfaces. In order to obtain the local liquid water content (LWC), experimental photographs from 10 experiments were considered. Each experiment consists of 347 images acquired under a sampling time $\tau \approx 10$ seconds at 30 FPS. The liquid water content module (LWCM) developed in MATLAB® reads in each experimental image separately. On the acquired photographs the droplets are visible as white streaks against a black background. Upon setting a normalized contrast level for all images, the droplet tracking scheme is employed in order to find the centroid positions of each droplet, while the off-plane droplets are neglected in accordance with Figure 5.6.

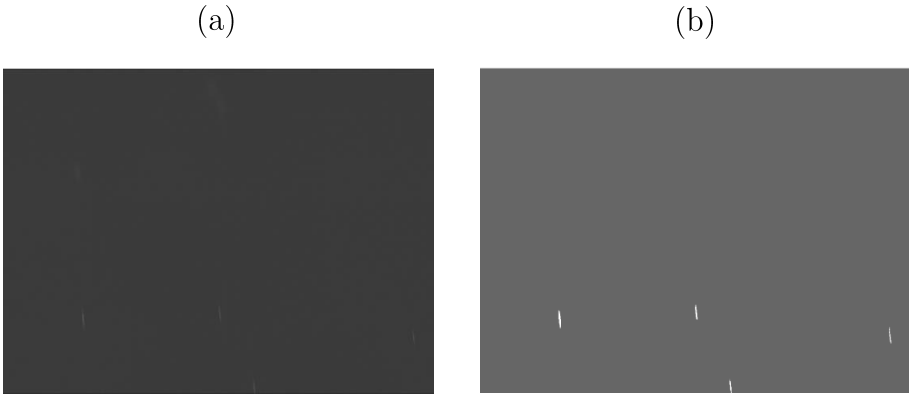

Figure 5.6. Droplet counting by the liquid water content module (LWCM). The original acquired experimental photograph is shown to the left (a) and the modified binary image to the right (b). The off-plane droplets are neglected as set by a threshold parameter in the module. The contrast and brightness levels of the images have been altered for visualization purposes.

The position of each centroid can be written as $\{C(x,y)\}_i$. For each image, the total number of centroids is hence identified, resulting in the total number of centroid positions for the droplets within each frame, described by

$$C_{\text{Total}} = \left[\sum_{i=1}^{N} \{C(x,y)\}_i\right]_j \tag{5.3}$$

In order to produce a histogram of the number of droplets within each frame a non-dimensional length $L^\star = \frac{x}{L}$ is introduced with $L^\star \in [0,1]$. The non-dimensional length along the specimen is further divided into 10 equally sized bins. The allocation of each centroid position i to each bin k is actualized by

$$\frac{nL^\star}{10} \leqq C(L^\star)_i < \frac{(n+1)L^\star}{10} \tag{5.4}$$

with $n = 0, 1, \ldots, 9$, $i = 1, 2, \ldots, N$ and $k = 1, 2, \ldots, 10$. For each centroid position fulfilling Equation (5.4), an increment is added to the total number of droplets within each bin m_k. The total number of droplets for a given frame is hence described by

$$N_j = \sum_{k=1}^{N} m_k \tag{5.5}$$

The averaged number of droplets within a sequence of images, in a given zone were further given by

$$\overline{R}_j = \frac{1}{n}\left\{\sum_{i=1}^{n} D_i\right\}_j \tag{5.6}$$

where $i = \{1, 2, \ldots, n\}$, $j = \{1, 2, \ldots, 10\}$ and n is the number of frames equal to 349. With known number of droplets, a similar approach for estimation of the local Liquid Water Content (LWC) as Ide (1999) was employed. This

method was used by Ide (1999), in order to establish the liquid water content in NASA Glenn's Icing Research Tunnel, based on a combined droplet distribution given by a forward scattering spectrometer probe (FSSP) and an optical array probe (OAP), from Particle Measuring System, Inc. For a constant droplet diameter, D and total sample area for the bins $\widetilde{A}$, the LWC can be expressed as

$$LWC \cong \frac{\rho \pi D^3}{6 \widetilde{A} U_\infty t} \sum_i R_j \tag{5.7}$$

where ρ is the water density, t is the sampling time, U_∞ is the free stream velocity, and the sum refers to the total number of droplets. The local liquid water content for free stream velocities $U_\infty \approx \{35, 50, 60\}$ m $\cdot$ s^{-1} was estimated to $LWC \cong \{0.38, 0.16, 0.02\}$ g $\cdot$ m^{-3}. Figure 5.7 shows the averaged number of droplets within 10 equally sized bins at three different free stream velocities for a sampling duration of 10 seconds. The lack of droplets between the first and last bin for free stream velocities above 35 m $\cdot$ s^{-1} indicates that lower local LWC values are observed with an increasing U_∞ and a change is observed in the cloud distribution. For statistical purposes $U_\infty \approx 35$ m $\cdot$ s^{-1} hence provides results across the entire specimen surface. For the remaining free stream velocities $U_\infty \approx \{50, 60\}$ m $\cdot$ s^{-1}, the entire population of the analyzed results are taken from the locations of the first and last bin, as shown in Figure 5.7, in order to account for a well chosen population.

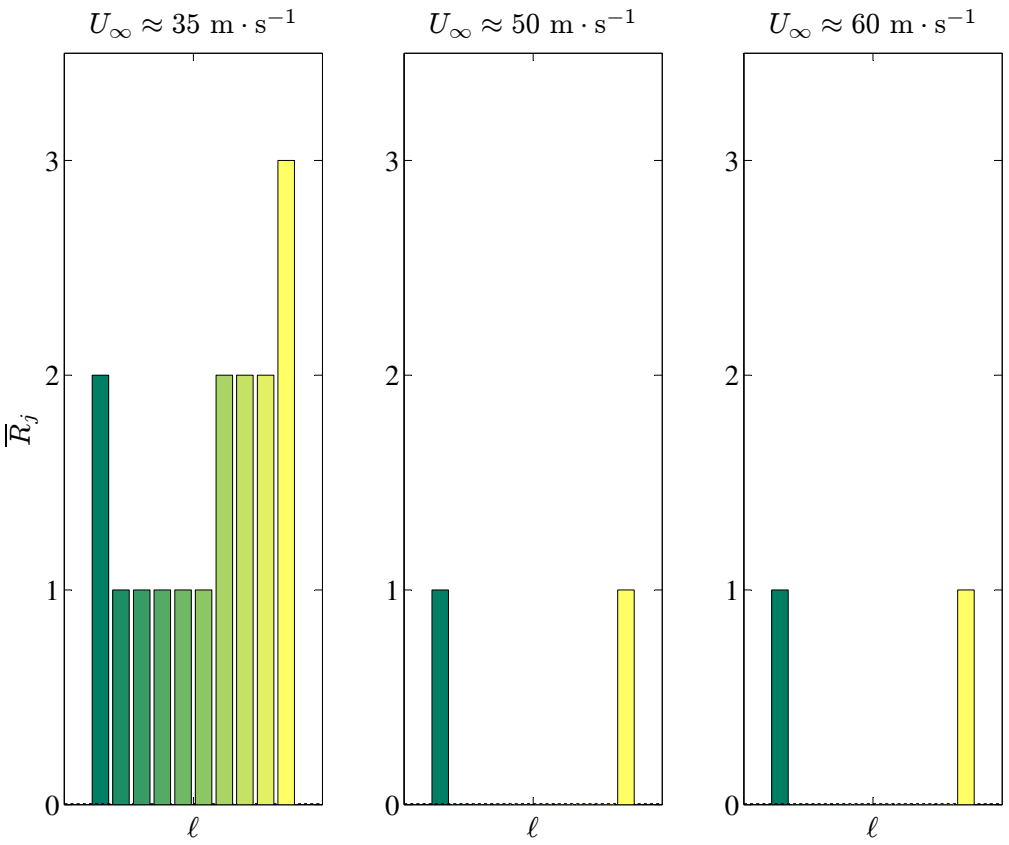

Figure 5.7. The number of averaged droplets within each bin $\overline{R}_j$, designated by a dark color for the first bin and a bright color for the last bin, for different free stream velocities U_∞ along the total length of the specimen within the field of view ℓ, during image acquisition.

Upon utilizing the LWCM it is possible to estimate the local liquid water content within each frame for the entire experiment. The local LWC for three representative experiments with $U_\infty \approx \{35, 50, 60\}\ \mathrm{m \cdot s^{-1}}$ are shown in Figure 5.8.

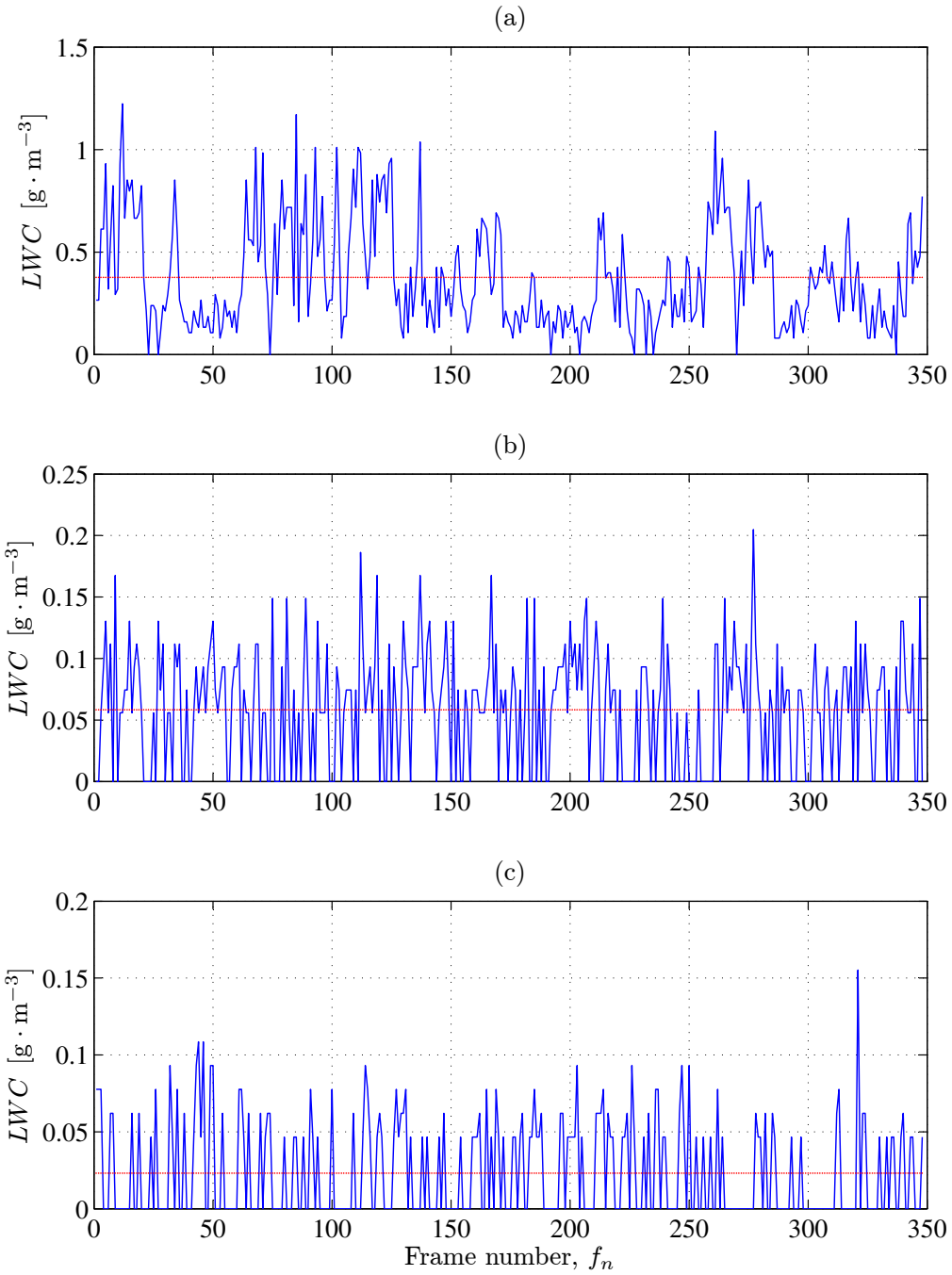

Figure 5.8. The local liquid water concentration LWC versus the frame number f_n, for representative free stream velocities (a) $U_\infty \approx 35\ \mathrm{m \cdot s^{-1}}$, (b) $U_\infty \approx 50\ \mathrm{m \cdot s^{-1}}$ and (c) $U_\infty \approx 60\ \mathrm{m \cdot s^{-1}}$. The dotted red line, indicates the average LWC value for each corresponding experiment.

5.3.2 Wetting character of the surface

In order to adopt a nomenclature that can easily be measured empirically and described analytically a number of different structures describing possible wetting features of the surface were defined based on visual inspection of the empirical image population, as shown in Figure 5.9.

CATEGORY	GEOMETRY	PARAMETERS	OUTPUTS
BEADS (I)	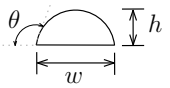	w, h, θ	$\overline{h}/\overline{w}$, $\overline{w}/\overline{h}$, $\overline{\theta}$, n_b, $n_{b,c}$
RIVULETS (II)	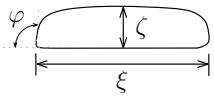	ξ, ζ, φ	$\overline{\xi}, \overline{\zeta}, \overline{\xi}/\overline{\zeta}, \overline{\zeta}/\overline{\xi}$, $\overline{\varphi}$, n_r, $n_{r,c}$
WATER FILM (III)	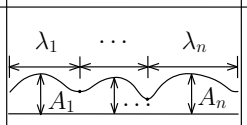	$A_1, \ldots, A_n$ $\lambda_1, \ldots, \lambda_n$	$\overline{A}, \overline{\lambda}$ $f_{wf,e}$
CORONA (IV)	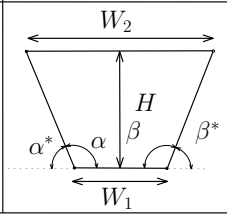	α, β, α^*, β^* W_1, W_2, H	h^*, ξ^*, H^* $\overline{W}_1$, $\overline{W}_2$, $\overline{H}$ $\overline{\alpha}/\overline{\beta}$, $\overline{\beta}/\overline{\alpha}$ $\overline{\alpha}^*/\overline{\beta}^*$, $\overline{\beta}^*/\overline{\alpha}^*$ $\overline{E}_C/\overline{E}_F$

Figure 5.9. Fluid structure categories with corresponding measured parameters and outputs upon employing the DSWSAM Methodology.

Four fluid structure classifications, Categories I – IV were identified within the population, to be present on the specimen surface, upon impact of the droplet stream onto the surface within the field of view of the camera. The parameters shown in Figure 5.9 refer to the measured parameters and the

output column to outputs from this module. Categories I and II, represent idealized bead and rivulet structures, respectively. As fluid structures of each presented category in Figure 5.9, on the experimental images feature different geometrical sizes, a representative fluid structure for each category was determined upon averaging over a large population of images with the considered structures.

The distinction between a bead (Category I) and a rivulet (Category II) is largely determined by $\xi \gg w$, for a rivulet, while $h \sim \zeta$. The distinction criterion employed hereby is that a structure is categorized as a rivulet if $\xi > \ell/2$, where ℓ is the length of the specimen within the field of view. This criterion, clearly distinguishes between beads and rivulets as a more moderate length restriction on ξ would make the distinction between beads and rivulets difficult. Due to the larger spatial extent of a rivulet, it can be stated that the number of beads often is greater than the number of rivulets, $n_b > n_r$. A large population of beads on the surface $n_b \gg 1$, further infers that the surface is hydrophobic.

A continuous water film (Category III) is present in the case where $\xi \to \infty$, with the amplitude of each wave $A_i > 0$. A partial water film is further apparent when $A_i > 0$ is followed by $A_{i+1} \to 0$ and $A_{i+2} > 0$, along the entire surface of the specimen, in a continuous manner. Hence, it can readily be established that Category II differs from Category III, as it has a more discrete character.

The ensuing fluid structure following the impact of an incoming droplet of size d, is a corona structure, Category IV. The employed nomenclature hence allows for determination of the corona structure parameters regardless of the initial formed surface fluid classification (Categories I − III). A set of parameters that address a comparison between the incoming and splashing structure are hence, $h^* \equiv H/(\overline{h}+d)$, $\zeta^* \equiv H/(\overline{\zeta}+d)$ and $A^* \equiv H/(d+\overline{A})$. The reasoning behind analyzing the geometrical parameters of the corona structures across all considered specimens is to provide a metric for wettability of each material. In particular this method is useful, upon analyzing the wetting character of the pre- and post eroded specimens, as it provides an insight into the influence of erosion on the wetting character of each specimen.

The defined structures in Figure 5.9, are idealized for simplicity, described merely by the shown geometrical properties. Although shape deviations from the idealized structures may exist in comparison to the encountered structures during the experimental runs, the defined geometrical structures in large, adequately capture the behavior of the fluid characters on the surface, and allow for simple measurements of the fluid features by utilizing a personal computer.

In order to analyze the experimental photographs, a baseline for the location of the top surface of the specimen is established utilizing the ImageJ[†] software (Ferreira and Rasband, 2011). All categories except Category IV are thereafter discretized by positioning of nodes $\breve{n}_i$, with $i = \{1, 2, \ldots, N\}$, using the multi-point tool in ImageJ. A schematic of the nodes of a continuous water

[†]ImageJ is a public domain JAVA image processing program.

film is shown in Figure 5.10.

Figure 5.10. A schematic of a discretized water film with corresponding nodes $\breve{n}_i$ and amplitudes A_i, with $i \in [1, N]$

.

The intermediate distance between the points, $\Omega_i = |x_{i+1} - x_i|$ hence represents different length scales where $\Omega_i = \lambda_i$ is the wave length of the water film, $\Omega_i = w_i$ is the width of a bead and $\Omega_i = \xi_i$ is the width of a rivulet, depending on the analyzed structure. The height of each structure $\Xi_i = |y_{\text{apex}} - y_i|$, is defined as the distance between the base and the apex of the structure, with $\Xi_i = A_i$ denoting the amplitude of the water film, $\Xi_i = h_i$ denoting the height of a bead and $\Xi_i = \zeta_i$ denoting the height of a rivulet. A surface covered with beads can in an idealized representation consist of n number of beads, each having a width w_n and height h_n placed adjacent to each other and described as

$$B_n(x) = \frac{h_n(-4x^2 + 8xH_n - 4H_n^2 + w_n^2)^{\frac{1}{2}}}{w_n} \tag{5.8}$$

where the horizontal distance of the apex location of each bead from the origin H_n, is defined as

$$H_n(x) \equiv \begin{cases} \frac{w_1}{2} & , n = 1 \\ w_1 + \frac{w_2}{2} & , n = 2 \\ H_{n-1} + w_{n-1} + w_n & , n > 2 \end{cases} \tag{5.9}$$

A representative bead structure can further be represented by

$$\overline{B}(x) = \frac{\overline{h}(-4x^2 + \overline{w})^2}{\overline{w}} \tag{5.10}$$

with $\overline{h} = \sum_{n=1}^{N} \frac{h_i}{n}$ and $\overline{w} = \sum_{n=1}^{N} \frac{w_i}{n}$ determined from the experiments. The idealized water film layer can similarly be expressed by

$$\overline{W}(x) = \overline{A}\sin(\omega x) + \widetilde{B} \tag{5.11}$$

where $\omega = 2\pi/|\overline{\lambda}|$, $\widetilde{B}$ is a constant and the parameters $\overline{A} = \sum_{n=1}^{N} \frac{A_i}{n}$ and $\overline{\lambda} = \sum_{n=1}^{N} \frac{\lambda_i}{n}$, are determined upon discretization using the empirical photographs. The water film layer is then confined between the function $\overline{W}(x)$ and $y = 0$, for $x \in [0, \infty)$.

5.3.3 Resulting fluid structures upon impact

A collision of a water droplet with a specimen surface may result in different scenarios in which bouncing, spreading and splashing may occur (Rein, 1993). For splashing structures, the nature that follows is largely dependent upon the depth of the water layer, the incident angle, droplet speed and the wettability of the target. Additionally at high velocities, growth of fingers and their consequent breakup into satellite droplets is apparent at the edge of the formed corona upon impact of a droplet onto a surface, similar to the observations of Aziz and Chandra (2000). This growth of fingers around the periphery of the droplet during spreading is according to Allen (1975) a result of the Rayleigh-Taylor Instability, which arises upon acceleration of the interface of

fluids with different densities. Empirically, the Rayleigh-Taylor instability has been studied for instance by utilizing a paramagnetic fluid combination (Gohardani, 2008; Gohardani et al., 2006, 2007; Gohardani and Jacobs, 2008). In their findings Gohardani et al. (2006, 2007) found that experiments with a flat initial interface between the two fluids with different densities, developed a random surface pattern with the dominant length scale well approximated by the fastest growing wavelength given by viscous linear stability theory. Due to the large number of simultaneous droplet impacts and the negligible influence of the satellite droplets on the core corona structures in this study, the resulting satellite droplets from the fingering phenomenon have been omitted from the analysis. For the chosen droplet size $D = 400$ μm, it was empirically observed that this droplet size resulted in a large number of impacts and splashing corona structures due to the local LWC and was capable of exposing the target area to adequate wetting, such that the nature of hydrophobic specimens by beads and rivulets and hydrophilic specimens with continuous layers of water films would be exposed. The wetting characteristics of the considered materials, can qualitatively or by mere observation of the naked eye be described for each material. However, since the corona structures are similar in nature a qualitative approach does not suffice for distinction purposes between the different materials. For this reason, a quantitative approach was developed that would describe the encountered corona characteristics numerically. One of the most fundamental parameters needed to be determined was the number of acquired images, required for the dynamic wettability experiments of each specimen. Based on the fact that a significant change in cloud distribution and liquid water content is observed at higher free stream velocities,

according Section 5.3.1, and in order to ensure that the results would be based upon an adequate statistical population, an initial analysis was carried out in which the number of images per candidate material was determined to 1,000 images. This number of acquired images would regardless of the local liquid water content, provide at least 100 useful images for further analysis. The number of useful images in this respect further increases for lower free stream velocities. As 8 candidate materials, with the exception of the multi-layered materials were considered for the dynamic wettability experiments in both a pristine and eroded state, the total number of required images for the dynamic wettability experiments was estimated to 16,000 images. The multi-layered materials were excluded from the dynamic wettability experiments, as they both had the S_8 (SW404 + XB5173) as the outermost layer. This layer was already one of the 8 considered candidate materials in the dynamic wettability tests. The large number of experimental photographs in this study signified the development of a measuring tool, in analyzing the empirical images. First and foremost, the consistency of applying the exact same measurement technique across the entire population was determined to be crucial. Additionally, a robust yet rapid measurement of the desired properties was essential. For this reason an new measurement module, namely the corona splashing measurement tool (CSMT) was developed in MATLAB®. Figure 5.11 shows the CSMT positioned on top of an empirical image of a corona structure.

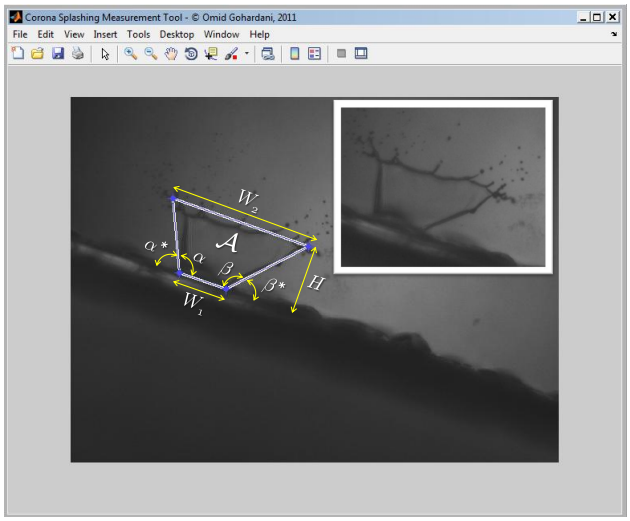

Figure 5.11. The Corona splashing measurement tool (CSMT), developed in MATLAB®.

The CSMT is based upon positioning of 4 vertices on the empirical image by the user, on top of the location of the corona structure. The resulting geometry consists of vectors $\mathbf{v} = \{\mathbf{v}_1, \mathbf{v}_2, \ldots, \mathbf{v}_4\}$ placed counter-clockwise on the initial position at the left upper corner of the corona structure. The geometrical parameters of the CSMT are shown in Figure 5.12.

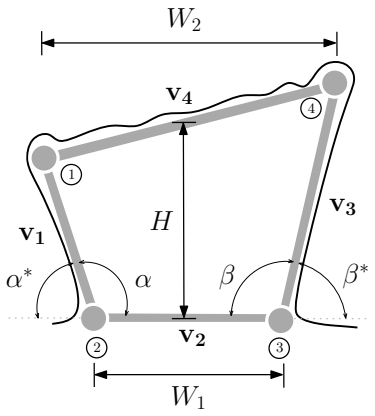

Figure 5.12. Geometrical parameters used in the corona splashing measurement tool.

The angle α, subtended by the structure is therefore described by

$$\alpha = \arccos\left(\frac{\mathbf{v}_1 \cdot \mathbf{v}_2}{\|\mathbf{v}_1\| \cdot \|\mathbf{v}_2\|}\right) \tag{5.12}$$

Similarly the angle β, is given by

$$\beta = \arccos\left(\frac{\mathbf{v}_2 \cdot \mathbf{v}_3}{\|\mathbf{v}_2\| \cdot \|\mathbf{v}_3\|}\right) \tag{5.13}$$

In addition, the angles fulfill the requirement of $\alpha + \alpha^* = 180°$ and $\beta + \beta^* = 180°$. The height of the corona H, is with the given nomenclature described by

$$H = \frac{\eta}{2(\|\mathbf{v}_4\| - \|\mathbf{v}_2\|)} \tag{5.14}$$

where

$$\eta = 4\sqrt{(s - \|\mathbf{v}_2\|)(s - \|\mathbf{v}_4\|)(s - \|\mathbf{v}_4\| - \|\mathbf{v}_3\|)(s - \|\mathbf{v}_4\| - \|\mathbf{v}_1\|)} \tag{5.15}$$

and s is given by

$$s = \frac{\|\mathbf{v}_1\| + \|\mathbf{v}_2\| + \|\mathbf{v}_3\| + \|\mathbf{v}_4\|}{2} \tag{5.16}$$

The two-dimensional area of the corona structure is hence given by

$$\mathcal{A} \approx \frac{H \cdot (\|\mathbf{v}_2\| + \|\mathbf{v}_4\|)}{2} \tag{5.17}$$

In order to estimate the amount of variability in pixel intensity within the region of interest subtended by the 4 vertices of the corona structure, the entropy within the region of the experimental photographs was computed.

The entropy for a grayscale image in MATLAB®, is defined as a measure of the randomness associated with the texture of the image (Gonzalez et al., 2009), and is computed according to

$$\widetilde{E} = -\sum p \cdot \log_2(p) \tag{5.18}$$

where p contains the count of the histogram. This approach was applied both to the entropy of the entire image resulting in the entropy of the frame, E_F and confined to only the corona, for which E_C was computed. This parameter provides an insight into the uniformity of the pixel intensity within the corona structure, as recorded on the experimental photograph. Smoother textures hence result in lower and rough textures in higher entropy values. The corona measurement splashing produces measurement of the corona structure given by the generic function

$$\Phi = f(\alpha, \beta, \alpha^*, \beta^*, W_1, W_2, H, \mathcal{A}, E_C, E_F) \tag{5.19}$$

The CSMT outputs the parameters given in Equation (5.19) for a given initial position of the vertices designated by $p_i(x_i, y_i)$ with $i = 1 \ldots 4$ implying in an output from the generic function Φ_p, as shown in Figure 5.13 (left). If the position of any of the i coordinates is altered resulting in $p_i'(x_i', y_i')$ with $i = 1 \ldots 4$, and $p \neq p'$, the software is capable of producing a new generic function $\Phi_{p'}$, shown in Figure 5.13 (right). The repositioning procedure can hence be carried out until all the vertices of the CSMT are places on top of the four edges of the corona structure on the empirical image, resulting in a

final generic function for the specific frame Φ_F, with $F \in [0, N]$ and N is an positive integer.

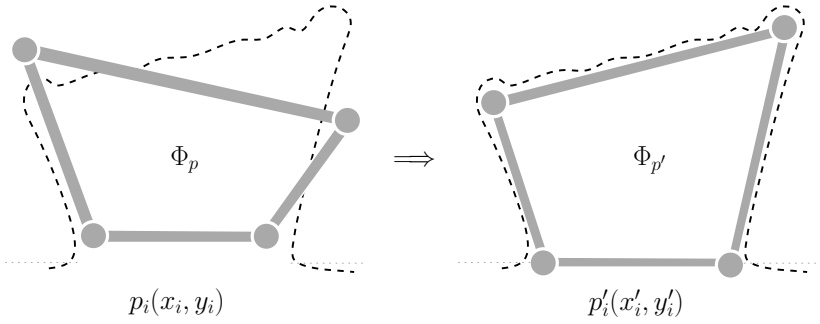

Figure 5.13. The repositioning of vertices in the corona splashing measurement tool (CSMT), from $p_i(x_i, y_i)$ to $p_i'(x_i', y_i')$. The dashed line indicates the location of the actual corona structure.

Based on the measured parameters, a range of non-dimensional factors are obtained for the splashing features. These properties are measured both in the pre- and post eroded states of the specimens respectively and their commonalities and differences are determined. Four different combinations of geometrical parameters are considered in order to establish the behavior of the corona structure. The initial one examines the skewness of the corona by examining the ratio $\frac{\alpha^*}{\beta^*}$. Three different cases can now unfold.

$$\frac{\alpha^*}{\beta^*} = \begin{cases} \text{Right} - \text{skewed corona} & > 1 \\ \text{Neutral corona} & = 1 \\ \text{Left} - \text{skewed corona} & < 1 \end{cases} \tag{5.20}$$

The second parameter of interest is

$$\frac{\overline{W}_2 - \overline{W}_1}{\overline{W}_1} \tag{5.21}$$

which describes the expansion of base width to the width at top of the corona, in percent. A value of $\frac{\overline{W}_2-\overline{W}_1}{\overline{W}_1} > 1$, hence implies an expansion and $\frac{\overline{W}_2-\overline{W}_1}{\overline{W}_1} < 1$, a reduction of the width in comparison to the base width of the corona. The aspect ratio of the corona is furthermore given by

$$\frac{\overline{W}_1 + \overline{W}_2}{2\overline{H}} \tag{5.22}$$

A value of $\frac{\overline{W}_1+\overline{W}_2}{2\overline{H}} = 1$, is indicative of a square shape of the corona, and $\frac{\overline{W}_1+\overline{W}_2}{2\overline{H}} > 1$, a rectangular shape. As an exemplary case of DSWSAM data extraction, from a continuous water film shown in Figure 5.14 (a), initially the datum line, corresponding to the location of the top surface of the specimen is identified on the experimental image, as shown by the dashed yellow line in Figure 5.14 (b). Thereafter, the water film is discretized with a finite number of nodes. The distance between each adjacent pair of nodes results in a wave length number. Similarly the apex point between these nodes is referred to as the amplitude of those node pairs. Upon identification of the wave lengths and amplitudes, for the entire water film, these values are averaged. Hence, an idealized, averaged and representative wave length and amplitude is defined for the continuous water film. The limitations of the DSWSAM, are referred to in Section 5.3.5. Representative photographs for specimens $S_1 - S_4$ and $S_5 - S_8$ in their pristine and eroded state respectively, are shown in Figures 5.15 and 5.16.

The general observation for the wetting characteristics of the considered materials is that specimens in the pre-eroded state are mainly hydrophobic as indicated by the formation of discrete water beads upon wetting. With mod-

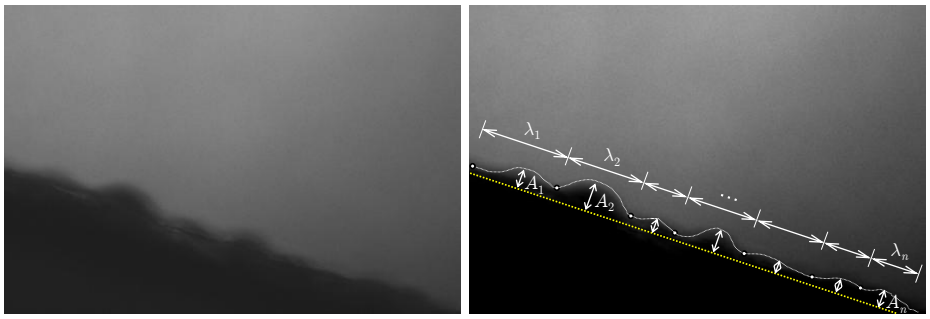

(a) (b)

Figure 5.14. (a) A continuous water film and (b) discretization of the same continuous water film in accordance with DSWSAM.

ifications to the surface morphology by erosion, a partial or complete water film is apparent on all considered specimens. The difference between the specimens in the post-eroded state is therefore, solely determined by the number of streams along the specimen surface. For the specimens exhibiting completely continuous water films, these streams merge to one coherent water film flowing along the specimen surface, where as specimens with partial wetting characteristics have a discrete number streams separated by non-wetted regions between them.

The idealized wetting structures on the different specimen surfaces represented by mathematical functions are shown in Tables 5.2 − 5.4, for a set of free stream velocities $U_\infty = \{35, 50, 60\}\ \mathrm{m \cdot s^{-1}}$. The results are shown in non-dimensional form in order to be comparable between the different cases. The utilized notation hence is established based on the total length of the specimen in the field of view ℓ, upon empirical image acquisition. For a bead the non-dimensional height and width are given by $h^\star = \frac{\overline{h}}{\ell}$ and $w^\star = \frac{\overline{w}}{\ell}$. The number of beads is further enumerated by n_{st}, with the number of spacings

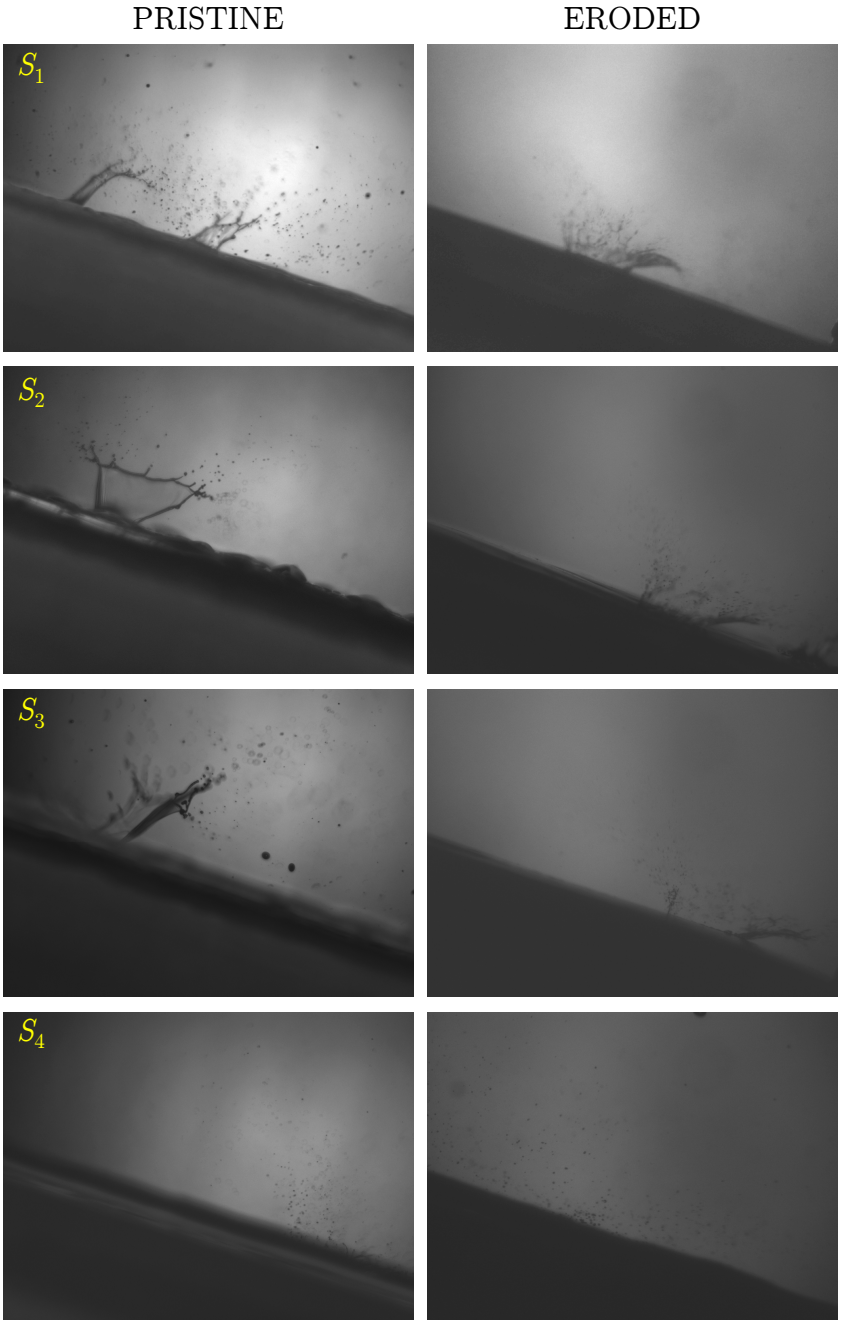

Figure 5.15. Pre- and post-erosion photographs of splashing structures on specimen $S_1 - S_4$. The brightness and contrast of the images have digitally been enhanced for visualization purposes.

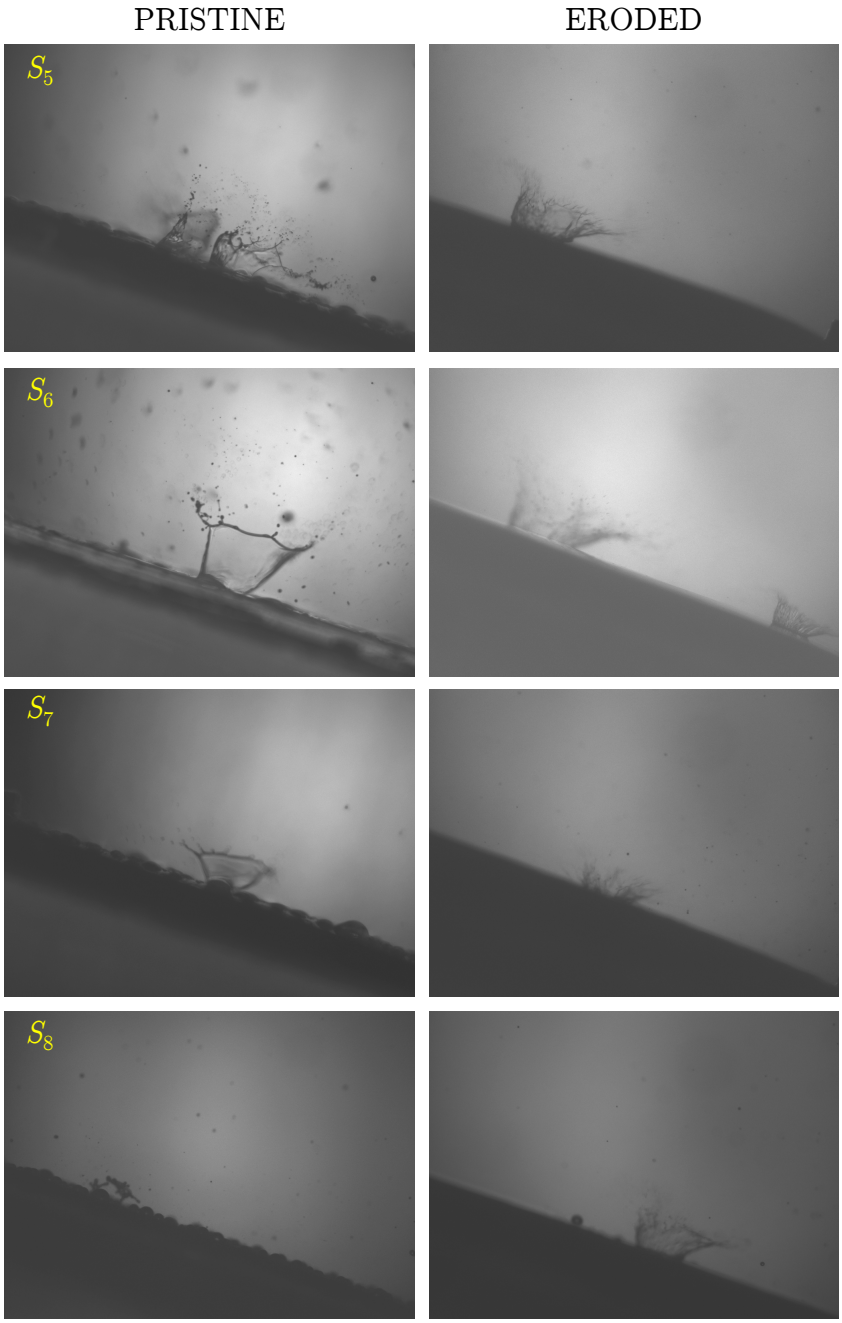

Figure 5.16. Pre- and post-erosion photographs of splashing structures on specimen $S_5 - S_8$. The brightness and contrast of the images have digitally been enhanced for visualization purposes.

between the beads given by n_{sp}. This notation hence implies that $n_{\text{st}} > n_{\text{sp}}$. The event where $n_{\text{st}} \gg n_{\text{sp}}$ is evident where upon a cluster of beads are encountered on the surface placed adjacent and in certain instances overlapping each other. Similarly for a rivulet, the height and width are denoted by $\zeta^{\star} = \frac{\overline{\zeta}}{\ell}$ and $\xi^{\star} = \frac{\overline{\xi}}{\ell}$. For rivulets the number of spacings is not considered allowing the plurality of rivulets to be represented by a single rivulet with the mean value of height and width established by the considered rivulets. Lastly, for a water film $A^{\star} = \frac{\overline{A}}{\ell}$, denotes the non-dimensional amplitude and $\lambda^{\star} = \frac{\overline{\lambda}}{\ell}$, the non-dimensional wave length of the water film.

Tables 5.2, 5.3 and 5.4 are presented with non-dimensional parameters, in order for the scale of the structures to be apparent. Idealized representations of the surface structures, shown in Figures 5.17 $-$ 5.22, only the number of bead structures n_{st} are considered.

$S_n^{p,e}$	$\overline{w}$ [μm]	$\overline{h}$ [μm]	$\overline{\xi}$ [μm]	$\overline{\zeta}$ [μm]	$\overline{\lambda}$ [μm]	$\overline{A}$ [μm]	n_{st}	n_{sp}
S_1^p	$\circ$	$\circ$	$\circ$	$\circ$	1276.9	231.20	$\circ$	$\circ$
S_1^e	$\circ$	$\circ$	$\circ$	$\circ$	1185.1	145.26	$\circ$	$\circ$
S_2^p	1398.2	314.14	$\circ$	$\circ$	$\circ$	$\circ$	6	5
S_2^e	$\circ$	$\circ$	$\circ$	$\circ$	1184.1	95.480	$\circ$	$\circ$
S_3^p	1118.8	330.40	$\circ$	$\circ$	$\circ$	$\circ$	10	8
S_3^e	$\circ$	$\circ$	$\circ$	$\circ$	1147.8	207.49	$\circ$	$\circ$
S_4^p	755.04	308.44	$\circ$	$\circ$	$\circ$	$\circ$	12	9
S_4^e	$\circ$	$\circ$	$\circ$	$\circ$	1156.7	188.96	$\circ$	$\circ$
S_5^p	$\circ$	$\circ$	$\circ$	$\circ$	1550.8	358.59	$\circ$	$\circ$
S_5^e	$\circ$	$\circ$	$\circ$	$\circ$	1194.4	120.05	$\circ$	$\circ$
S_6^p	1057.8	220.65	$\circ$	$\circ$	$\circ$	$\circ$	8	7
S_6^e	$\circ$	$\circ$	$\circ$	$\circ$	1246.3	253.22	$\circ$	$\circ$
S_7^p	$\circ$	$\circ$	5300.4	113.38	$\circ$	$\circ$	$\circ$	$\circ$
S_7^e	$\circ$	$\circ$	$\circ$	$\circ$	1023.0	234.73	$\circ$	$\circ$
S_8^p	653.12	316.95	$\circ$	$\circ$	$\circ$	$\circ$	21	14
S_8^e	$\circ$	$\circ$	$\circ$	$\circ$	1198.5	208.46	$\circ$	$\circ$

Table 5.2. Representative surface structures for specimens $S_1 - S_8$, at a free stream velocity $U_\infty \approx 35\ \mathrm{m \cdot s^{-1}}$. The symbol ($\circ$) refers to non applicable instances. The superscript p and e refer to pristine and eroded state of the specimen respectively. The number of bead structures is given by n_{st}, with the number of spacings between the beads given by n_{sp}.

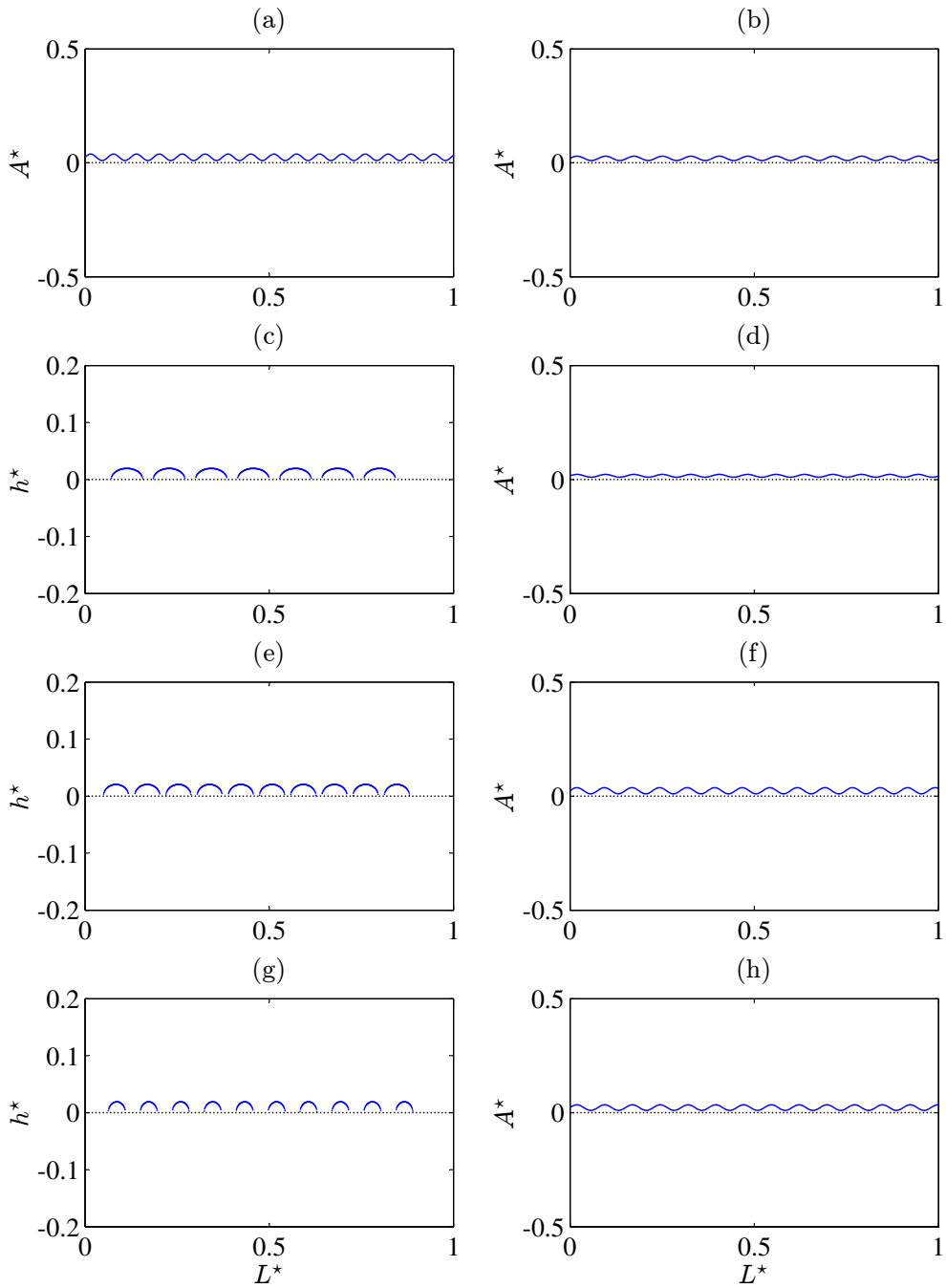

Figure 5.17. Representative surface structures at $U_\infty \approx 35\ \mathrm{m \cdot s^{-1}}$. The following notations are utilized: (a) S_1^p, (b) S_1^e, (c) S_2^p, (d) S_2^e, (e) S_3^p, (f) S_3^e, (g) S_4^p, and (h) S_4^e. The superscript p and e denote the pristine and eroded states of each specimen.

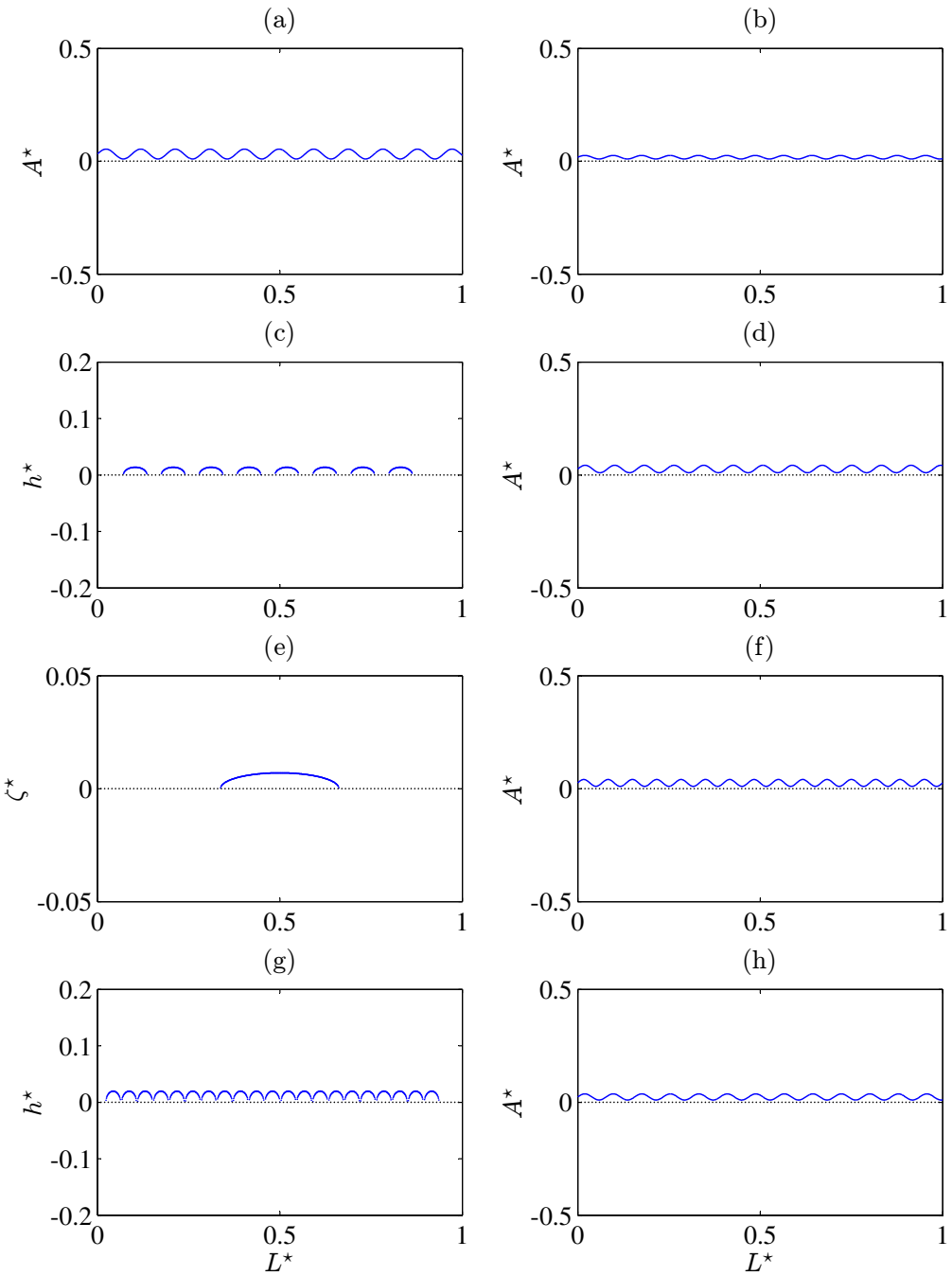

Figure 5.18. Representative surface structures at $U_\infty \approx 35\ \mathrm{m \cdot s^{-1}}$. The following notations are utilized: (a) S_5^p, (b) S_5^e, (c) S_6^p, (d) S_6^e, (e) S_7^p, (f) S_7^e, (g) S_8^p, and (h) S_8^e. The superscript p and e denote the pristine and eroded states of each specimen.

$S_n^{p,e}$	$\overline{w}$ [μm]	$\overline{h}$ [μm]	$\overline{\xi}$ [μm]	$\overline{\zeta}$ [μm]	$\overline{\lambda}$ [μm]	$\overline{A}$ [μm]	n_{st}	n_{sp}
S_1^p	$\circ$	$\circ$	$\circ$	$\circ$	1094.3	240.39	$\circ$	$\circ$
S_1^e	$\circ$	$\circ$	5779.2	55.100	$\circ$	$\circ$	$\circ$	$\circ$
S_2^p	830.61	294.30	$\circ$	$\circ$	$\circ$	$\circ$	8	7
S_2^e	$\circ$	$\circ$	$\circ$	$\circ$	1196.1	105.84	$\circ$	$\circ$
S_3^p	1128.4	379.63	$\circ$	$\circ$	$\circ$	$\circ$	9	6
S_3^e	$\circ$	$\circ$	$\circ$	$\circ$	1283.8	195.93	$\circ$	$\circ$
S_4^p	815.97	249.00	$\circ$	$\circ$	$\circ$	$\circ$	17	9
S_4^e	$\circ$	$\circ$	$\circ$	$\circ$	1078.3	234.12	$\circ$	$\circ$
S_5^p	$\circ$	$\circ$	$\circ$	$\circ$	1468.7	343.05	$\circ$	$\circ$
S_5^e	$\circ$	$\circ$	$\circ$	$\circ$	1085.5	178.67	$\circ$	$\circ$
S_6^p	$\circ$	$\circ$	$\circ$	$\circ$	1524.5	296.19	$\circ$	$\circ$
S_6^e	$\circ$	$\circ$	$\circ$	$\circ$	1172.9	206.80	$\circ$	$\circ$
S_7^p	$\circ$	$\circ$	5879.0	114.71	$\circ$	$\circ$	$\circ$	$\circ$
S_7^e	$\circ$	$\circ$	$\circ$	$\circ$	1245.1	220.60	$\circ$	$\circ$
S_8^p	506.40	182.05	$\circ$	$\circ$	$\circ$	$\circ$	16	12
S_8^e	$\circ$	$\circ$	$\circ$	$\circ$	1320.5	230.12	$\circ$	$\circ$

Table 5.3. Representative surface structures for specimens $S_1 - S_8$, at a free stream velocity $U_\infty \approx 50\ \mathrm{m \cdot s^{-1}}$. The symbol ($\circ$) refers to non applicable instances. The superscript p and e refer to pristine and eroded state of the specimen respectively. The number of bead structures is given by n_{st}, with the number of spacings between the beads given by n_{sp}.

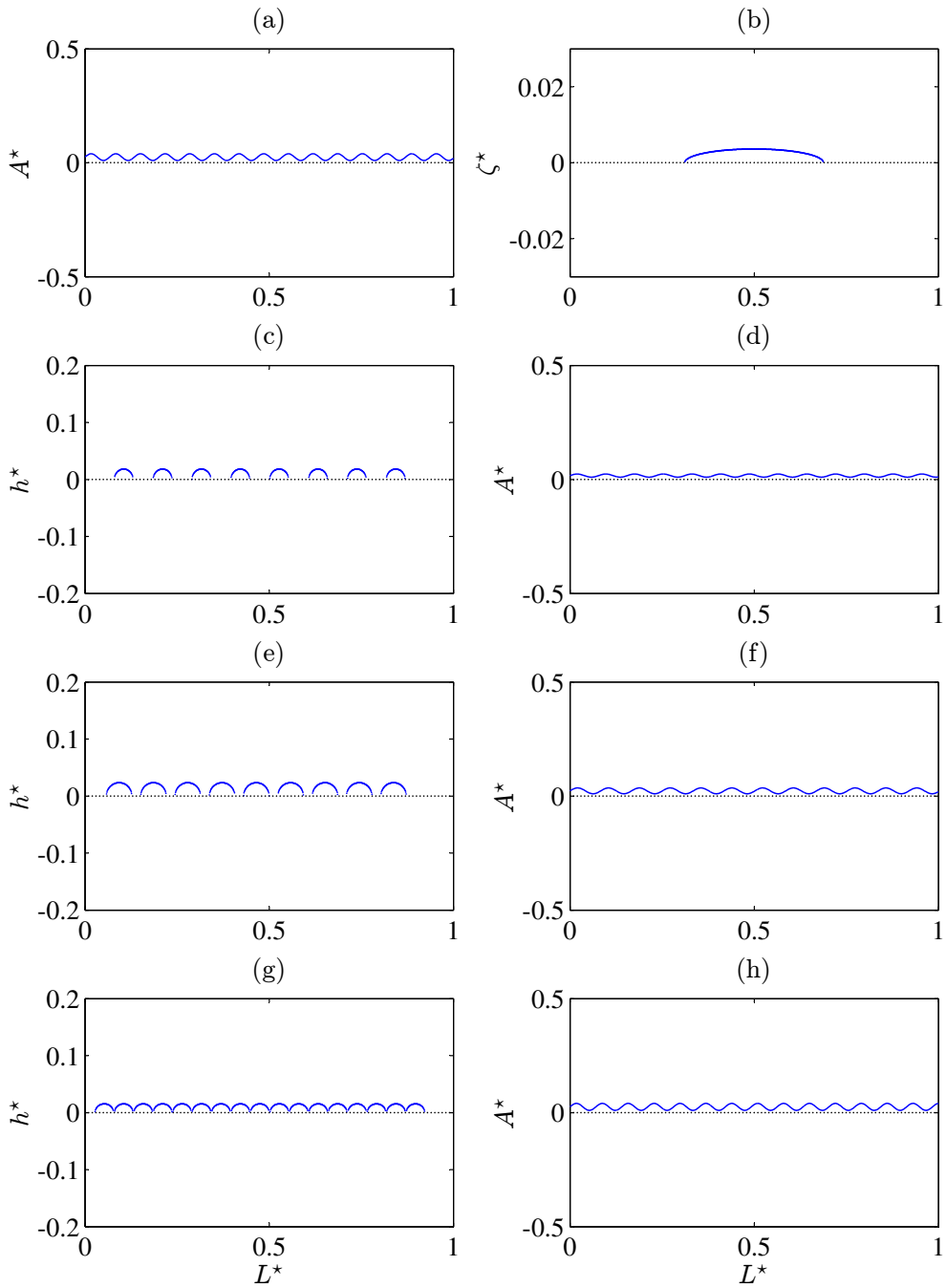

Figure 5.19. Representative surface structures at $U_\infty \approx 50\ \mathrm{m \cdot s^{-1}}$. The following notations are utilized i: (a) S_1^p, (b) S_1^e, (c) S_2^p, (d) S_2^e, (e) S_3^p, (f) S_3^e, (g) S_4^p, and (h) S_4^e. The superscript p and e denote the pristine and eroded states of each specimen.

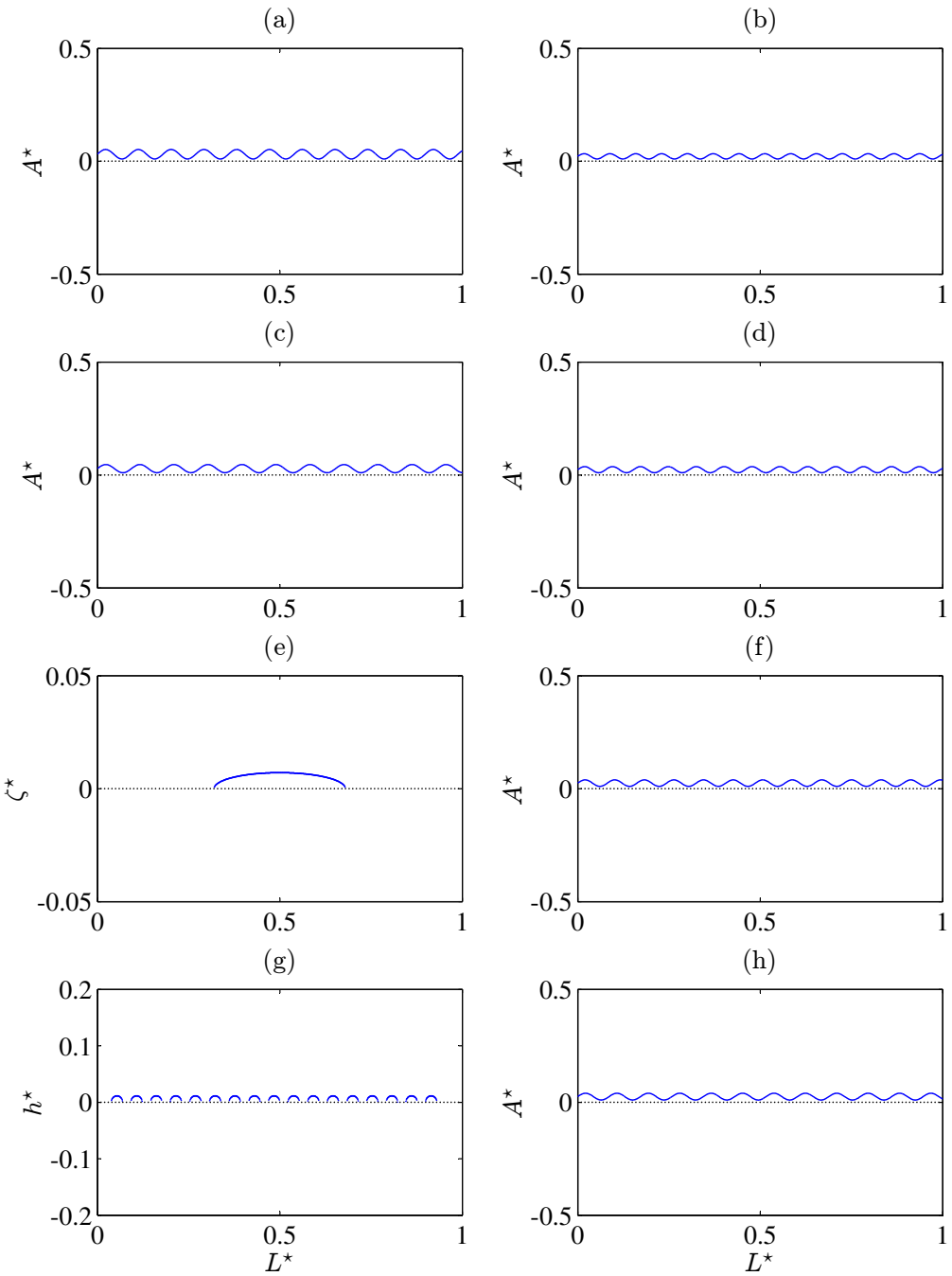

Figure 5.20. Representative surface structures at $U_\infty \approx 50\ \mathrm{m \cdot s^{-1}}$. The following notations are utilized i: (a) S_5^p, (b) S_5^e, (c) S_6^p, (d) S_6^e, (e) S_7^p, (f) S_7^e, (g) S_8^p, and (h) S_8^e. The superscript p and e denote the pristine and eroded states of each specimen.

$S_n^{p,e}$	$\overline{w}$ [μm]	$\overline{h}$ [μm]	$\overline{\xi}$ [μm]	$\overline{\zeta}$ [μm]	$\overline{\lambda}$ [μm]	$\overline{A}$ [μm]	n_{st}	n_{sp}
S_1^p	∘	∘	∘	∘	1015.44	284.73	∘	∘
S_1^e	∘	∘	5401.65	60.49	∘	∘	∘	∘
S_2^p	863.98	290.61	∘	∘	∘	∘	12	8
S_2^e	∘	∘	∘	∘	1347.60	198.55	∘	∘
S_3^p	829.18	299.64	∘	∘	∘	∘	10	7
S_3^e	∘	∘	∘	∘	1449.61	290.80	∘	∘
S_4^p	790.46	278.79	∘	∘	∘	∘	10	8
S_4^e	∘	∘	∘	∘	1304.00	307.18	∘	∘
S_5^p	∘	∘	∘	∘	1329.94	318.22	∘	∘
S_5^e	∘	∘	∘	∘	1335.80	194.30	∘	∘
S_6^p	756.47	310.94	∘	∘	∘	∘	13	8
S_6^e	∘	∘	∘	∘	1293.19	211.59	∘	∘
S_7^p	∘	∘	7248.04	129.17	∘	∘	∘	∘
S_7^e	∘	∘	∘	∘	1154.72	182.52	∘	∘
S_8^p	426.06	172.58	∘	∘	∘	∘	17	9
S_8^e	∘	∘	∘	∘	1324.60	233.59	∘	∘

Table 5.4. Representative surface structures for specimens $S_1 - S_8$, at a free stream velocity $U_\infty \approx 60\ \mathrm{m} \cdot \mathrm{s}^{-1}$. The symbol (∘) refers to non applicable instances. The superscript p and e refer to pristine and eroded state of the specimen respectively. The number of bead structures is given by n_{st}, with the number of spacings between the beads given by n_{sp}.

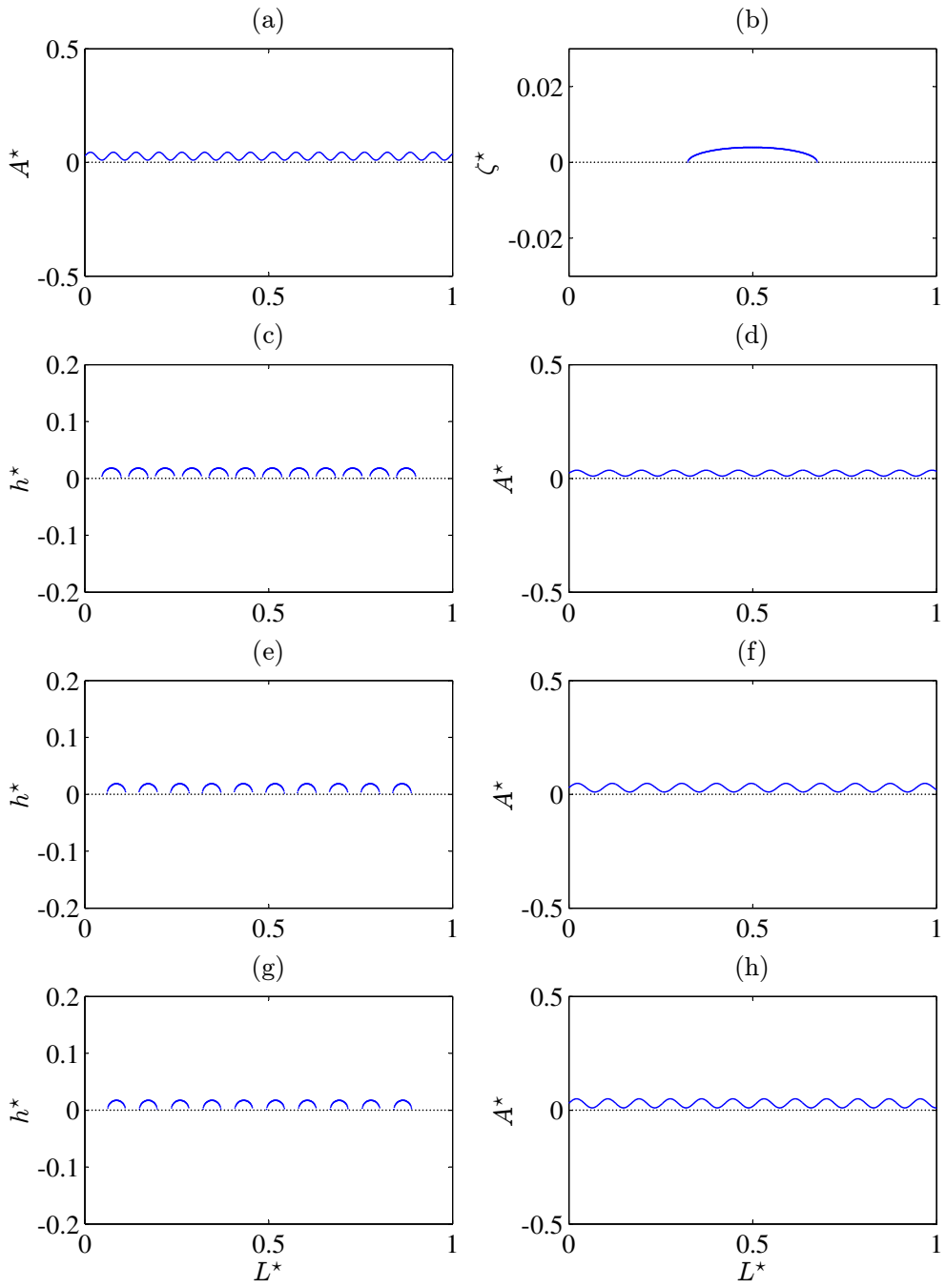

Figure 5.21. Representative surface structures at $U_\infty \approx 60$ m $\cdot$ s^{-1}. The following notations are utilized i: (a) S_1^p, (b) S_1^e, (c) S_2^p, (d) S_2^e, (e) S_3^p, (f) S_3^e, (g) S_4^p, and (h) S_4^e. The superscript p and e denote the pristine and eroded states of each specimen.

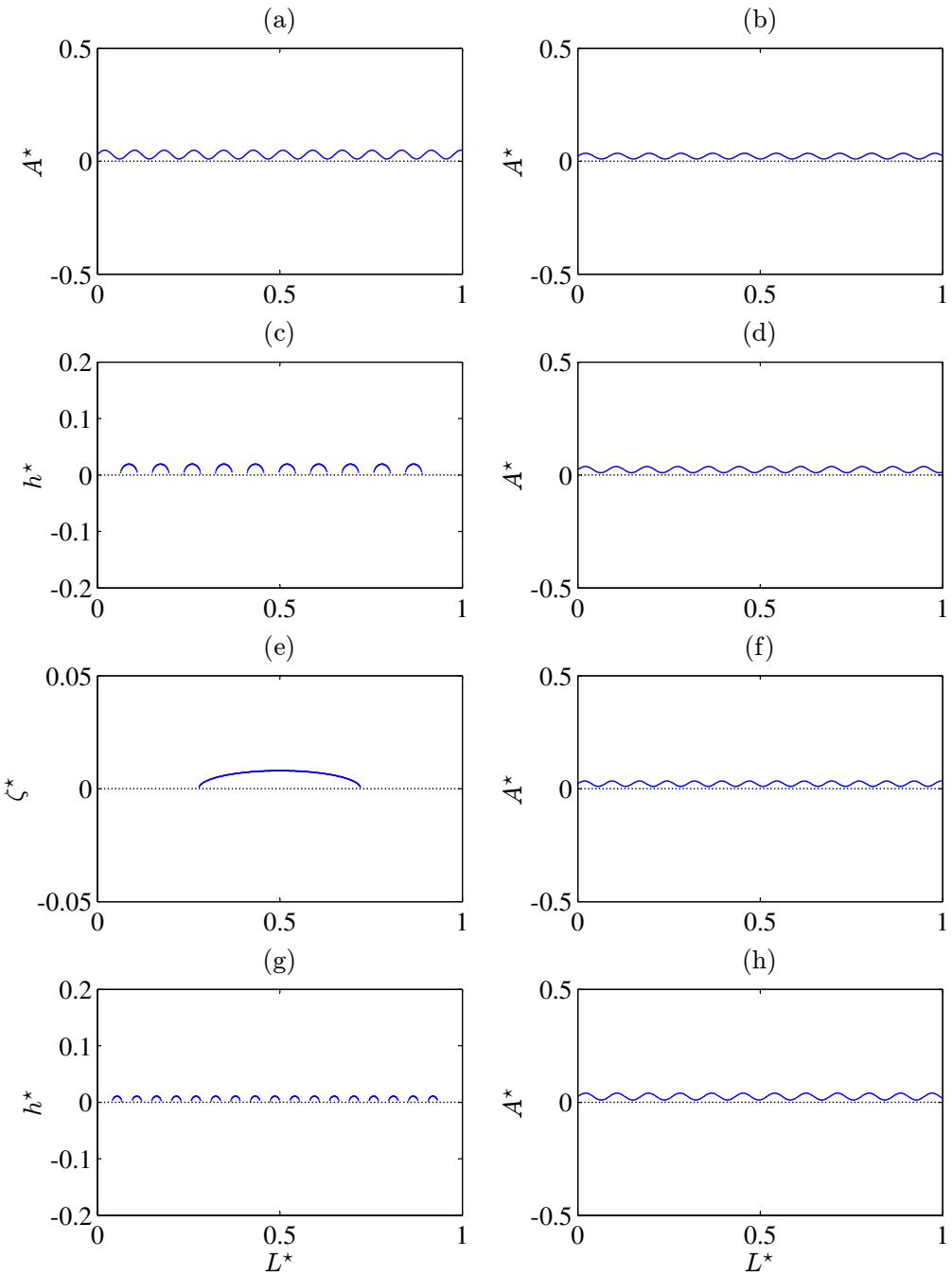

Figure 5.22. Representative surface structures at $U_\infty \approx 60$ m $\cdot$ s^{-1}. The following notations are utilized i: (a) S_5^p, (b) S_5^e, (c) S_6^p, (d) S_6^e, (e) S_7^p, (f) S_7^e, (g) S_8^p, and (h) S_8^e. The superscript p and e denote the pristine and eroded states of each specimen.

In order to characterize the corona structure, the generic function Φ establishes the value of at least ten parameters that geometrically describe the corona structure. For a generic parameter χ, chosen such that $\Phi = f(\chi)$, the CSMT further outputs the lower and upper bound of the parameter in the pristine and eroded settings respectively, i.e. $\chi \in [\chi_{\min}^{p,e}, \chi_{\max}^{p,e}]$. Figure 5.23 shows the minimum and maximum range of the parameters W_1, W_2, H and $\frac{E_C}{E_F}$ for a free stream velocity of $U_\infty \approx 35 \text{ m} \cdot \text{s}^{-1}$.

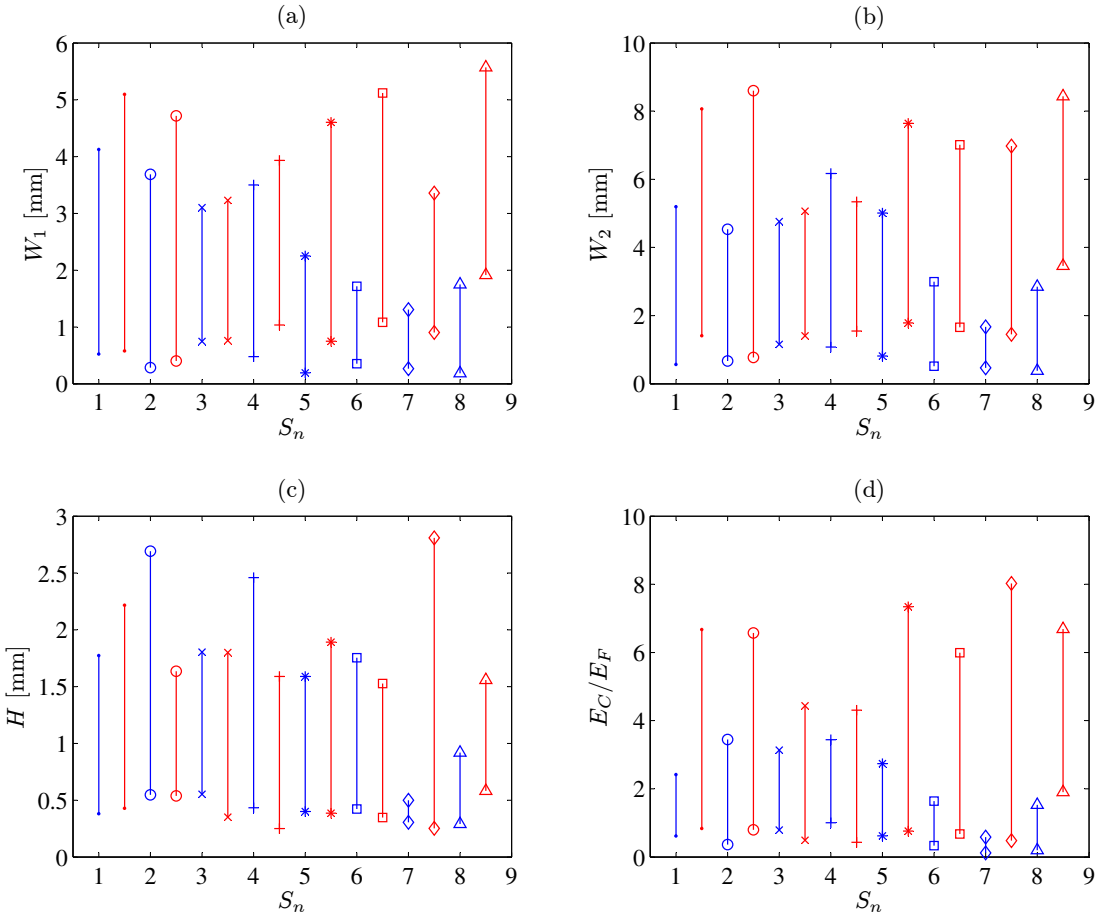

Figure 5.23. The width at base W_1 (a), width at top W_2 (b), height of corona H (c) and the ratio of the entropy of the corona in relation to the entire entropy of the frame (d) for specimens S_n, with $n = 1, 2, \ldots, 8$. The blue color refers to the pristine state and the red color to the eroded state of each specimen. The following symbols are utilized for each specimen: S_1 ($\cdot$), S_2 ($\circ$), S_3 ($\times$), S_4 ($+$), S_5 ($*$), S_6 ($\square$), S_7 ($\Diamond$), and S_8 ($\triangle$).

Similarly, Figure 5.24 shows the minimum and maximum range of the angles of the corona, namely α, β and the complimentary angles α^* and β^* for a free stream $U_\infty \approx 35\ \mathrm{m} \cdot \mathrm{s}^{-1}$.

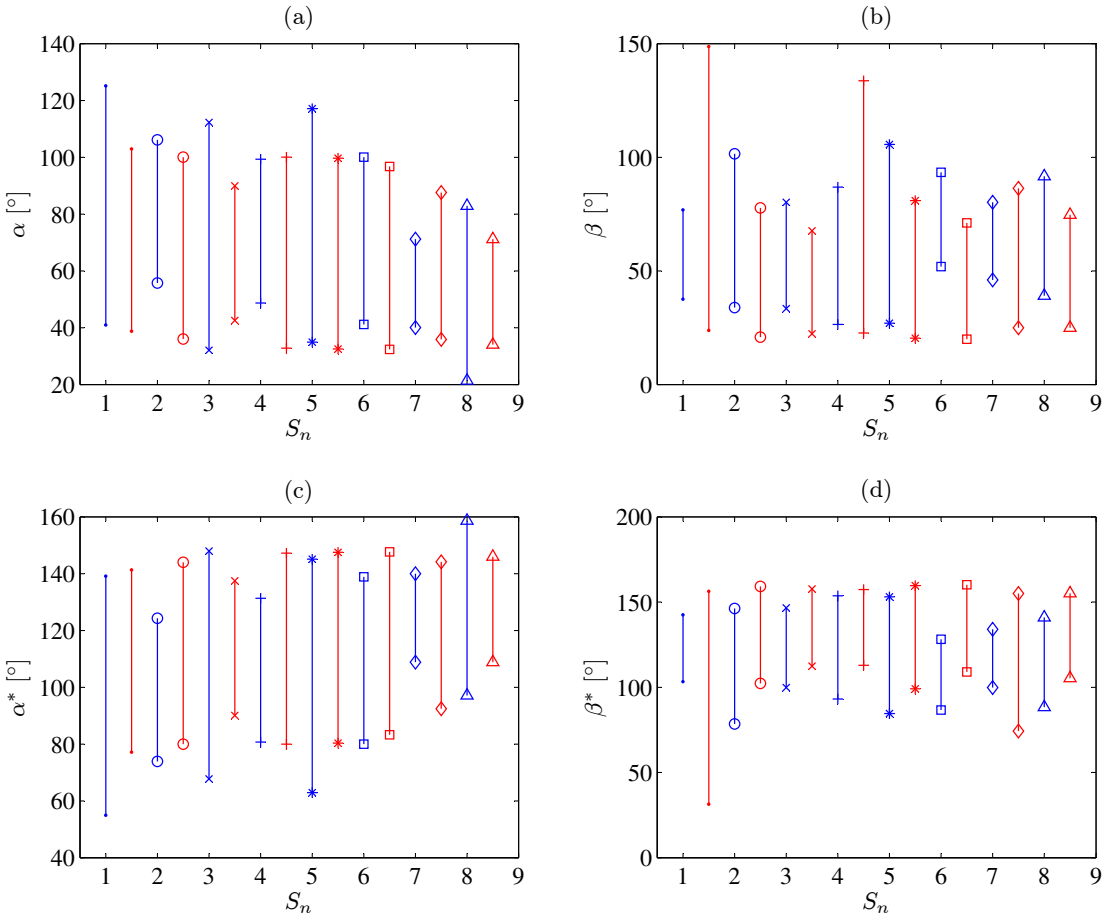

Figure 5.24. The angle α (a), angle β (b), α^* (c) and β^* (d) for specimens S_n, with $n = 1, 2, \ldots, 8$. The blue color refers to the pristine state and the red color to the eroded state of each specimen. The following symbols are utilized for each specimen: S_1 ($\cdot$), S_2 ($\circ$), S_3 ($\times$), S_4 ($+$), S_5 ($*$), S_6 ($\square$), S_7 ($\Diamond$), and S_8 ($\triangle$).

The geometrical properties presented in Figures 5.23 and 5.24 convey important behavior of the corona structure prior and after erosion of the surface. The first observation as that in general for all specimens the base of the corona

extends to a larger region. For the majority of the specimens this may arise from the fact that a more uniform surface finish is obtained allowing the water to spread more freely on the surface. It is also notable that the height of the corona is reduced for the eroded state of the specimen in comparison to the pristine state for the specimen reinforced with carbon nanotubes S_2, S_4 and S_6, which indicates that the hydrophobic nature of these specimens is reduced. This conjecture is indeed confirmed upon behavior of the fluid structures on the surfaces of these specimens shown in Figures 5.17 and 5.18, where erosion of the surface implies that a water film is obtained in contrast to the discrete number of beads formed on the surface in its virgin state. Due to the large number of parameters obtained, it is more fruitful to combine the parameters to infer general trends about their behavior. Figure 5.25 shows the behavior of the corona structure based on its skewness, expansion, aspect ratio and area.

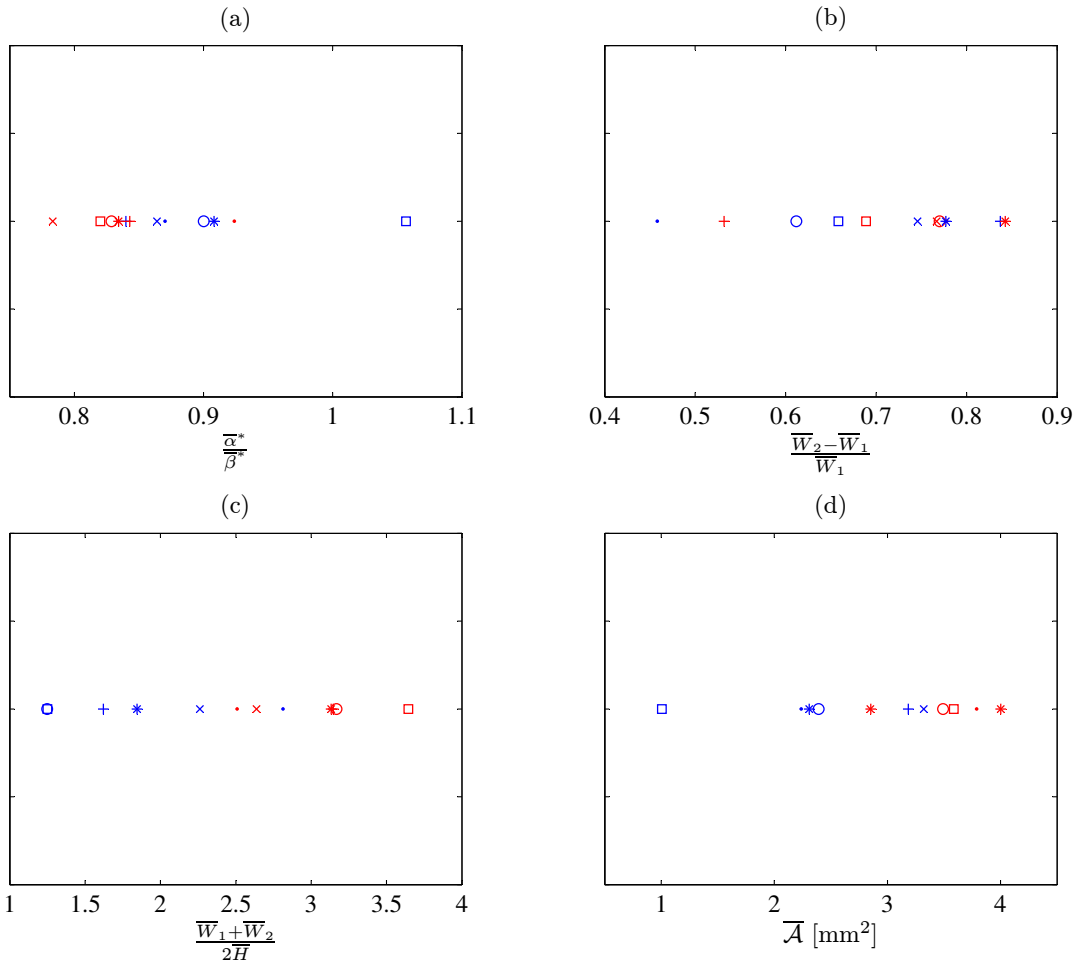

Figure 5.25. The skewness (a), expansion (b), aspect-ratio (c) and area of the corona (d) for specimens S_n, with $n = 1, 2, \ldots, 8$. The blue color refers to the pristine state and the red color to the eroded state of each specimen. The following symbols are utilized for each specimen: S_1 ($\cdot$), S_2 ($\circ$), S_3 ($\times$), S_4 ($+$), S_5 ($*$), S_6 ($\square$), S_7 ($\Diamond$), and S_8 ($\triangle$).

Figure 5.25 shows that majority of the coronas are skewed to the left in the pristine and eroded states respectively, apart from S_6 which is skewed to the right prior to erosion. The plurality of the formed corona structures further expand in the eroded state. The aspect ratio of the corona structures are further more rectangular shaped than square shaped. It is also notable that the two-dimensional area of the corona structure occupies a larger area in the

eroded state in comparison to the virgin state of the material. This may be a consequence of the continuous water film that is evident on most specimens in the aftermath of erosion, allowing for more fluid to become ejected from the surface upon impact.

For the free stream velocity of $U_\infty \approx 50\ \mathrm{m} \cdot \mathrm{s}^{-1}$, the minimum and maximum range of the parameters W_1, W_2, H and $\frac{E_C}{E_F}$ for a free stream velocity of $U_\infty \approx 50\ \mathrm{m} \cdot \mathrm{s}^{-1}$ are shown in Figure 5.26.

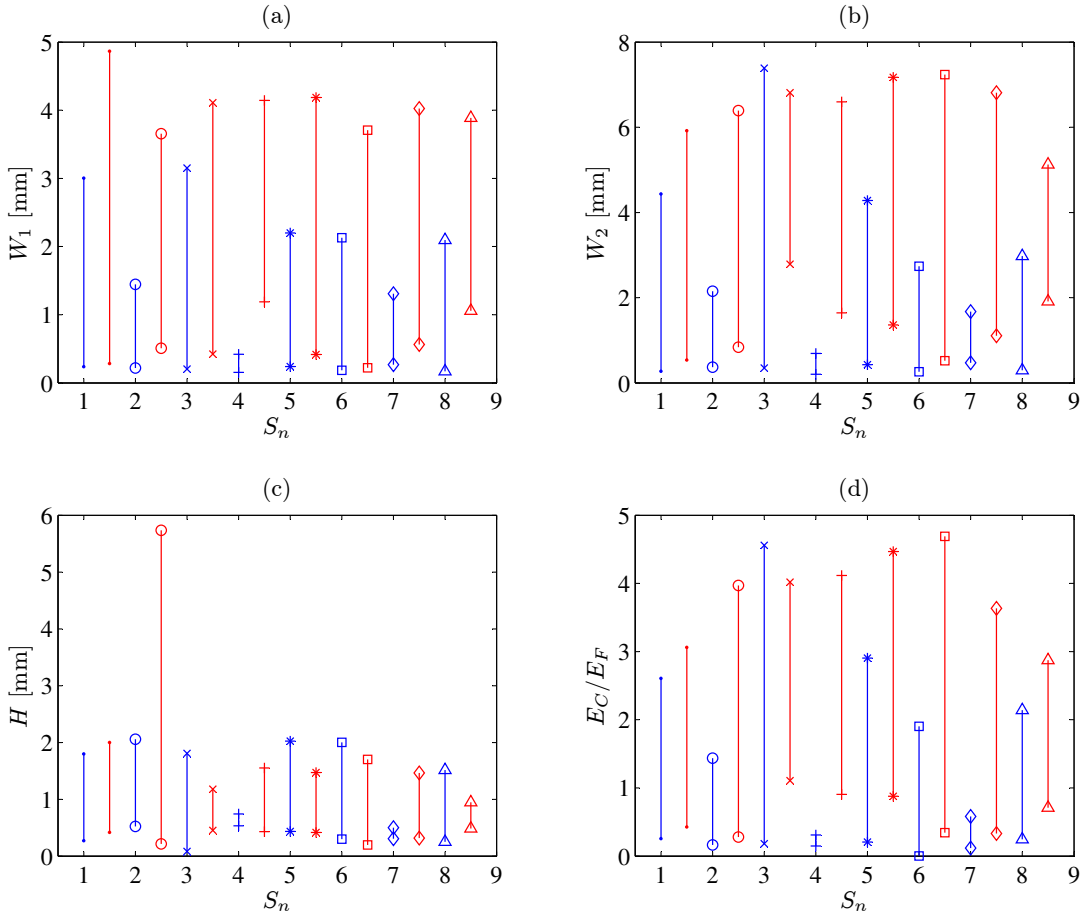

Figure 5.26. The width at base W_1 (a), width at top W_2 (b), height of corona H (c) and the ratio of the entropy of the corona in relation to the entire entropy of the frame (d) for specimens S_n, with $n = 1, 2, \ldots, 8$ and $U_\infty \approx 50\ \mathrm{m} \cdot \mathrm{s}^{-1}$. The blue color refers to the pristine state and the red color to the eroded state of each specimen. The following symbols are utilized for each specimen: S_1 ($\cdot$), S_2 ($\circ$), S_3 ($\times$), S_4 ($+$), S_5 ($*$), S_6 ($\square$), S_7 ($\Diamond$), and S_8 ($\triangle$).

Similarly, Figure 5.27 shows the minimum and maximum range of the angles of the corona, namely α, β and the complimentary angles α^* and β^* for a free stream $U_\infty \approx 50\ \mathrm{m} \cdot \mathrm{s}^{-1}$.

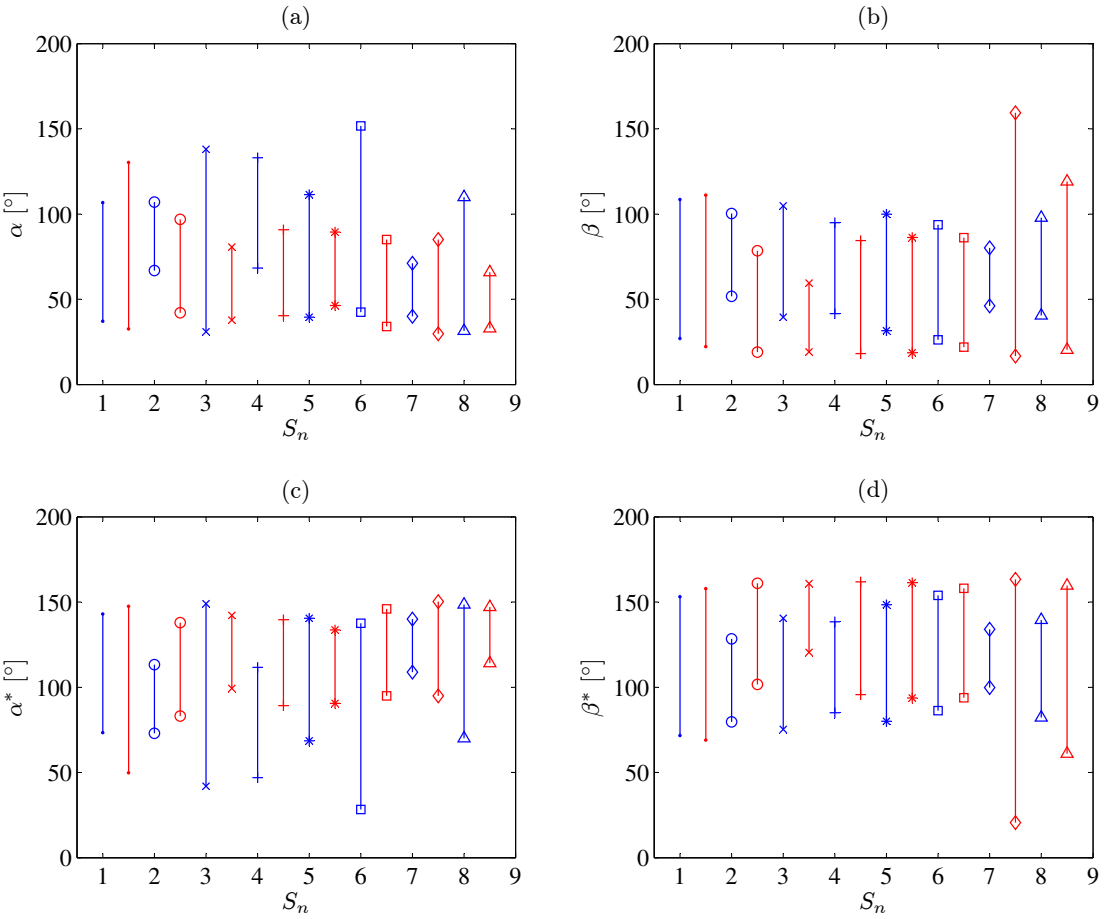

Figure 5.27. The angle α (a), angle β (b), α^* (c) and β^* (d) for specimens S_n, with $n = 1, 2, \ldots, 8$ and $U_\infty \approx 50\ \mathrm{m} \cdot \mathrm{s}^{-1}$. The blue color refers to the pristine state and the red color to the eroded state of each specimen. The following symbols are utilized for each specimen: S_1 ($\cdot$), S_2 ($\circ$), S_3 ($\times$), S_4 ($+$), S_5 ($*$), S_6 ($\square$), S_7 ($\Diamond$), and S_8 ($\triangle$).

The geometrical skewness, expansion of the base width, aspect-ratio of the corona and the two-dimensional area of the corona are shown in Figure 5.28 for a free stream $U_\infty \approx 50\ \mathrm{m} \cdot \mathrm{s}^{-1}$. It can be deduced that most coronas are left-skewed, however a few number are right-skewed. The aspect-ratio of most the corona structures is square shaped, but becomes more rectangular upon splashing on the eroded surfaces, which also features a higher area on these surfaces.

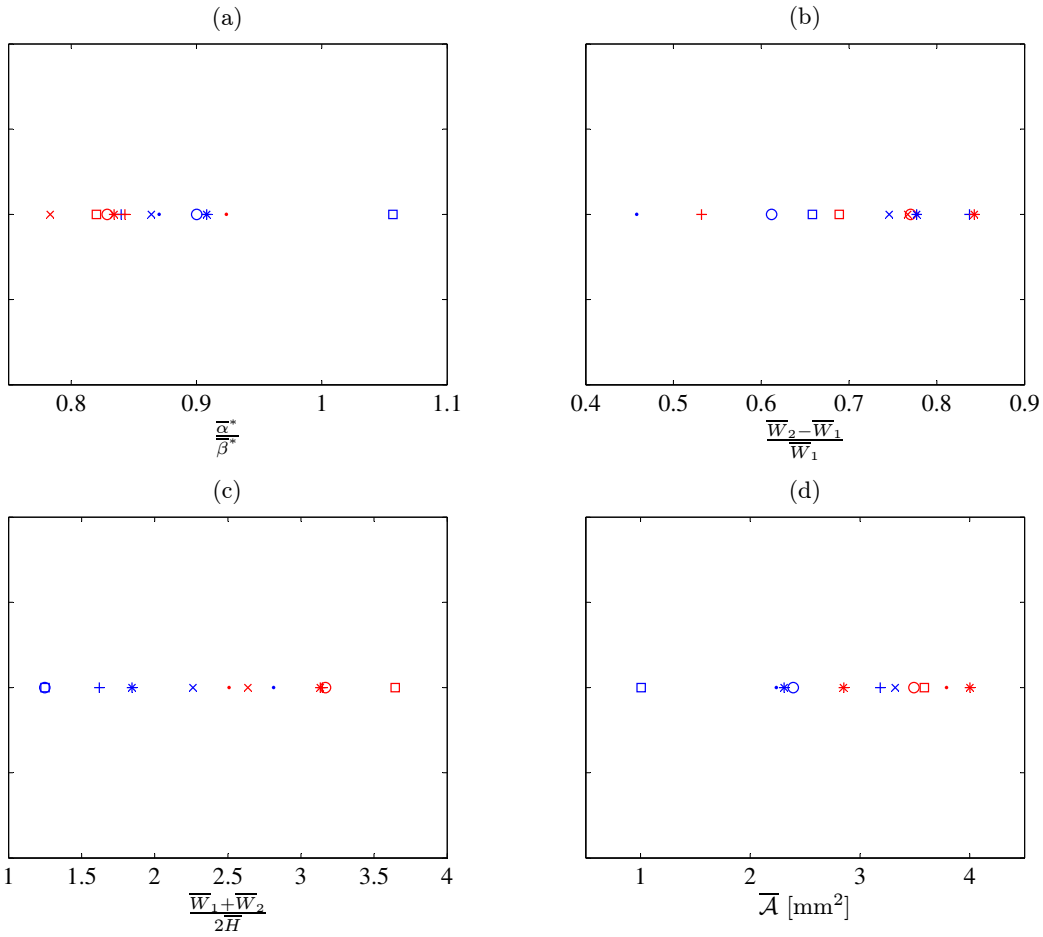

Figure 5.28. The skewness (a), expansion (b), aspect-ratio (c) and area of the corona (d) for specimens S_n, with $n = 1, 2, \ldots, 8$. The blue color refers to the pristine state and the red color to the eroded state of each specimen. The following symbols are utilized for each specimen: S_1 ($\cdot$), S_2 ($\circ$), S_3 ($\times$), S_4 ($+$), S_5 ($*$), S_6 ($\square$), S_7 ($\Diamond$), and S_8 ($\triangle$).

Figures 5.29 – 5.31, present the corresponding corona structure parameters for a free stream velocity of $U_\infty \approx 60\ \mathrm{m \cdot s^{-1}}$. Similar to the previous cases, an expansion of the width at the top of the corona is observed, with most coronas being left-skewed.

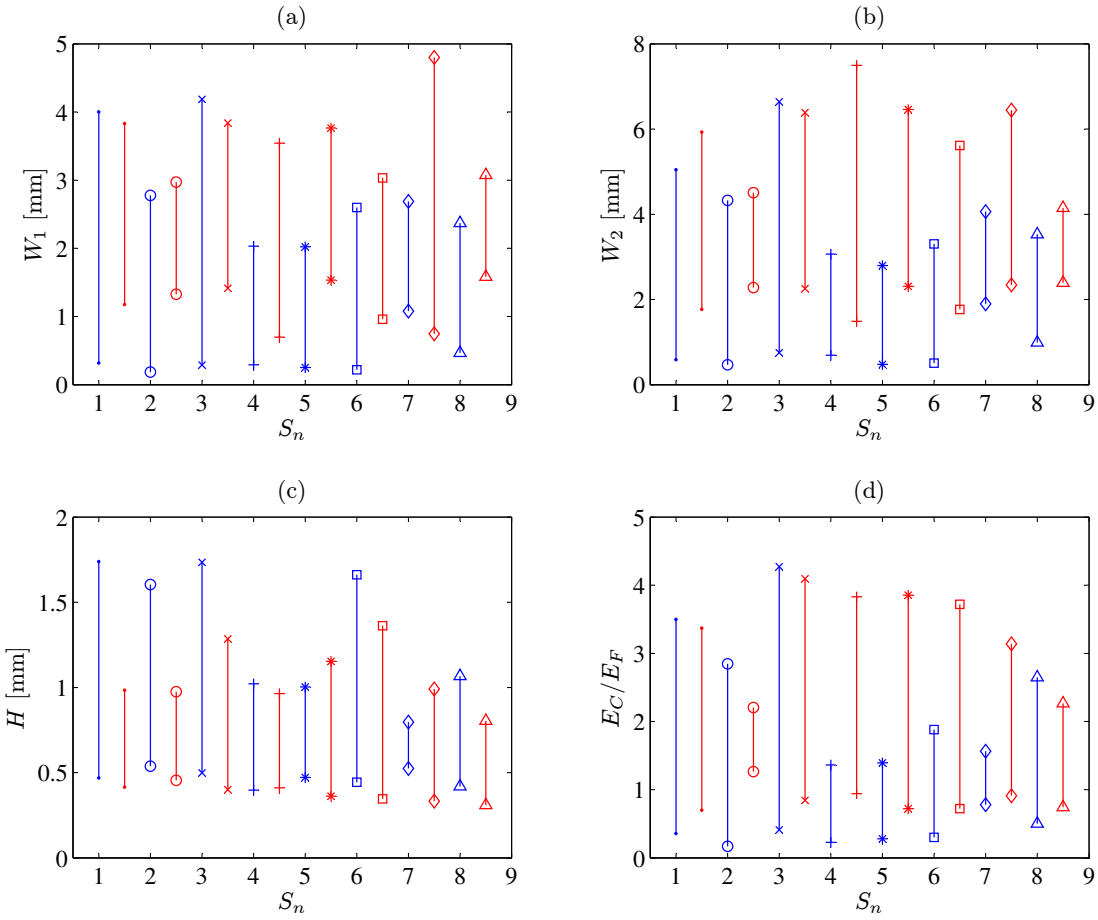

Figure 5.29. The width at base W_1 (a), width at top W_2 (b), height of corona H (c) and the ratio of the entropy of the corona in relation to the entire entropy of the frame (d) for specimens S_n, with $n = 1, 2, \ldots, 8$ and $U_\infty \approx 60\ \mathrm{m \cdot s^{-1}}$. The blue color refers to the pristine state and the red color to the eroded state of each specimen. The following symbols are utilized for each specimen: S_1 ($\cdot$), S_2 ($\circ$), S_3 ($\times$), S_4 ($+$), S_5 ($*$), S_6 ($\square$), S_7 ($\Diamond$), and S_8 ($\triangle$).

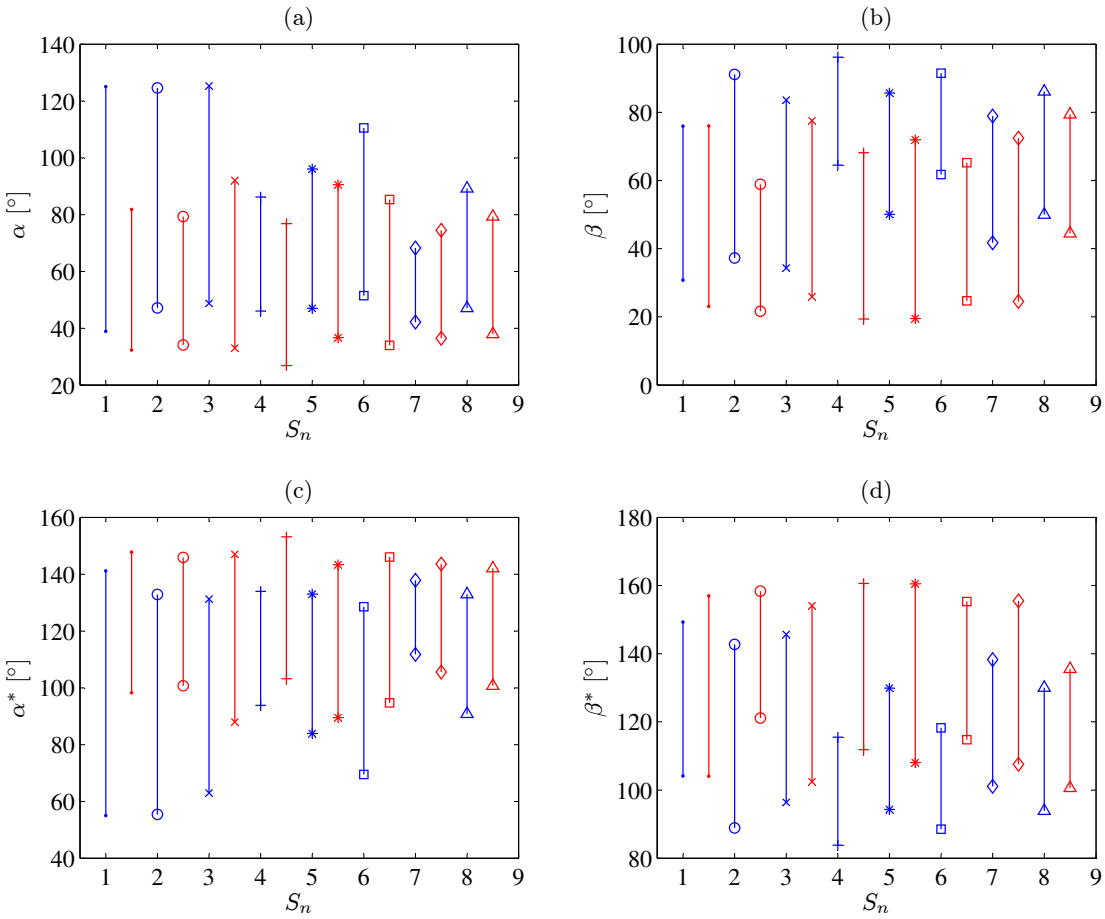

Figure 5.30. The angle α (a), angle β (b), α^* (c) and β^* (d) for specimens S_n, with $n = 1, 2, \ldots, 8$ and $U_\infty \approx 60$ m $\cdot$ s^{-1}. The blue color refers to the pristine state and the red color to the eroded state of each specimen. The following symbols are utilized for each specimen: S_1 ($\cdot$), S_2 ($\circ$), S_3 ($\times$), S_4 ($+$), S_5 ($*$), S_6 ($\square$), S_7 ($\Diamond$), and S_8 ($\triangle$).

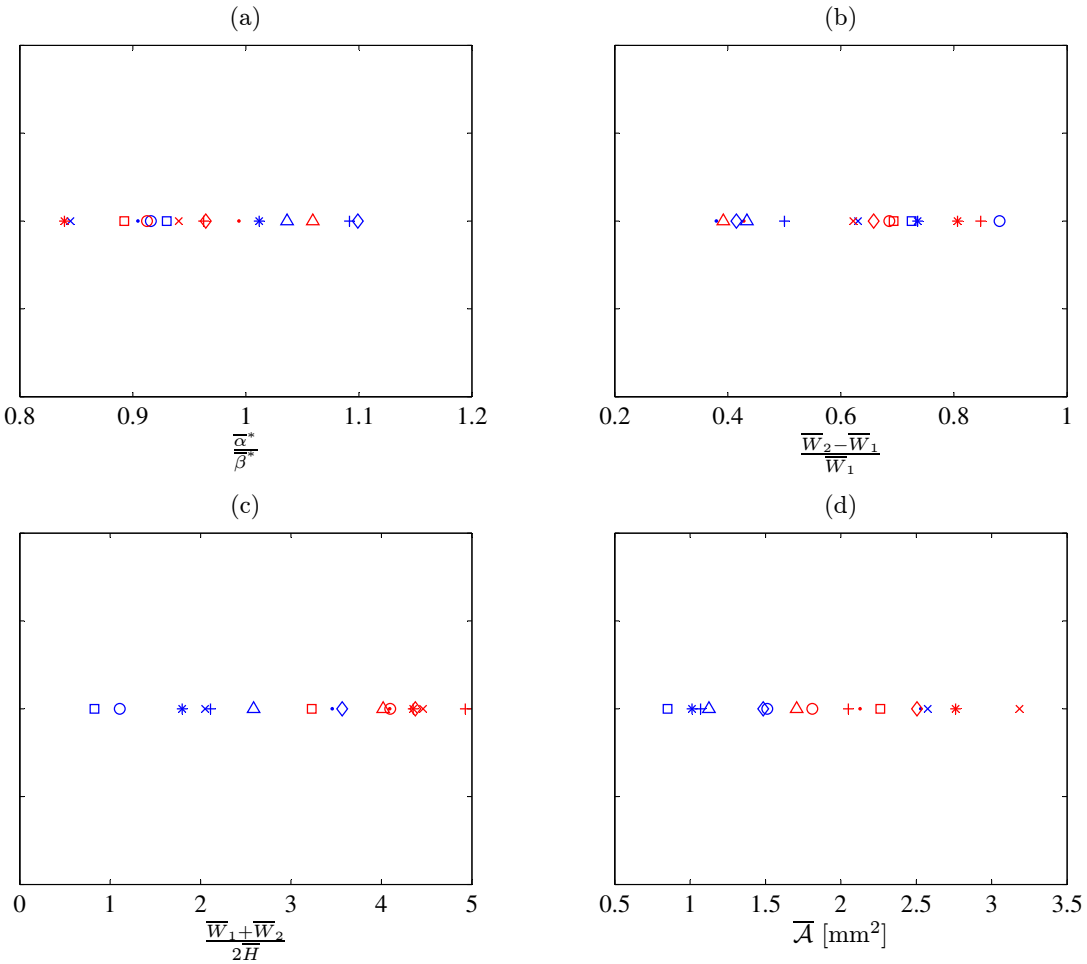

Figure 5.31. The skewness (a), expansion (b), aspect-ratio (c) and area of the corona (d) for specimens S_n, with $n = 1, 2, \ldots, 8$. The blue color refers to the pristine state and the red color to the eroded state of each specimen. The following symbols are utilized for each specimen: S_1 ($\cdot$), S_2 ($\circ$), S_3 ($\times$), S_4 ($+$), S_5 ($*$), S_6 ($\square$), S_7 ($\Diamond$), and S_8 ($\triangle$).

5.3.4 The size of the boundary layer

For obtaining an estimate of how the boundary layer might influence in the oncoming droplets to the target, a simplified approach can be taken into account for estimation of the size of the boundary layer thickness. Under the

assumption that the stagnation point is located at the leading edge of the specimen, the flow over the specimen surface can be approximated as the flow over a flat plate with an incident angle $\alpha = 0°$. For a finite length of the plate x, the inertial force $\rho u \frac{\partial u}{\partial x} \sim \rho \frac{U_\infty^2}{x}$. The friction force per unit volume is however given by $\frac{d\tau}{dy} \sim \mu \frac{U_\infty}{\delta^2}$. Equating the inertial and friction forces yields $\delta(x) \sim \{(\mu x)/(\rho U_\infty)\}^{\frac{1}{2}}$. If the position of the boundary layer thickness is determined when $u = 0.99U_\infty$, the boundary layer thickness can be defined as (Schlichting and Gersten, 2000)

$$\delta_{99} \approx 5.0\sqrt{\frac{\nu x}{U_\infty}} \tag{5.23}$$

The reduction of volume flux due to the action of viscosity or the displacement thickness δ_1, is described by (Schlichting and Gersten, 2000)

$$\delta_1 = \int_0^\infty \Big(1 - \frac{u}{U_\infty}\Big) dy \tag{5.24}$$

Similarly the momentum thickness δ_2, which represents the momentum in the boundary layer in relation to that in the outer flow can be defined as

$$\delta_2 = \int_0^\infty \frac{u}{U_\infty}\Big(1 - \frac{u}{U_\infty}\Big) dy \tag{5.25}$$

resulting in

$$\delta_2 = 0.34 \cdot \delta_{99} \tag{5.26}$$

The energy thickness δ_3, referring to the kinetic energy within the boundary layer in comparison to the inviscid outer layer is defined as (Schlichting and

Gersten, 2000)

$$\delta_3 = \int_0^\infty \frac{u}{U_\infty}\Big(1 - \frac{u^2}{U_\infty^2}\Big)dy \tag{5.27}$$

which yields

$$\delta_3 = 0.20 \cdot \delta_{99} \tag{5.28}$$

The wall shear stress can further be expressed as

$$\tau_w(x) \approx \sqrt{\frac{\rho\mu U_\infty^3}{x}} \tag{5.29}$$

and the skin-friction coefficient

$$c_f(x) \approx \frac{\tau_w(x)}{\frac{\rho U_\infty^2}{2}} \tag{5.30}$$

The splashing phenomenon is often related to different non-dimensional parameters such as the Reynolds number based on the diameter $Re_d \equiv (\rho U_\infty d)/\mu$, the Weber number $We_d \equiv (\rho U_\infty^2 d)/\sigma$, the Ohnsorge number $Oh \equiv \sqrt{We}/Re$, and the Capillary number $Ca \equiv We/Re$, where d is the droplet diameter, ρ defines the density, U_∞ is the free stream velocity, μ is the dynamic viscosity and σ denotes the surface tension. The spreading factor $\xi \equiv d_{\max}/d$, can further be expressed as (Pasandideh-Fard et al., 1996)

$$\xi = \sqrt{\frac{We + 12}{3\Big(1 - \cos(\theta_A) + \frac{4We}{\sqrt{Re}}\Big)}} \tag{5.31}$$

Table 5.5, shows the values of the boundary-layer thickness δ_{99}, displacement thickness δ_1, momentum thickness δ_2, and the energy thickness δ_3, wall shear

stress τ_w, and skin-friction coefficient c_f for different free stream velocities.

U_∞ $[\mathrm{m} \cdot \mathrm{s}^{-1}]$	δ_{99} $[\mu\mathrm{m}]$	δ_1 $[\mu\mathrm{m}]$	δ_2 $[\mu\mathrm{m}]$	δ_3 $[\mu\mathrm{m}]$	τ_w $[\mathrm{N} \cdot \mathrm{m}^{-2}]$	c_f
35	463	157	60.2	92.6	6.87	0.0093
50	387	132	50.3	77.5	11.7	0.0078
60	354	120	46.0	70.7	15.3	0.0071

Table 5.5. The boundary-layer thickness, displacement thickness, momentum thickness, energy thickness, wall shear stress and skin friction for different free stream velocities. All parameters are estimated for $x = L$, where L is the length of the specimen.

From Table 5.5, it is readily established that the approximate size of the boundary layer for a free stream velocity of 35 $\mathrm{m} \cdot \mathrm{s}^{-1}$ is approximately 463 μm, which should be viewed against the size of the incoming droplet $d =$ 400 μm. Therefore, a different structure behavior, such as distortion of the corona structure, observed in some of the empirical photographs, is expected at the interface between the boundary layer flow and the outer flow. These observations further validate the flat plate approximation for calculation of the boundary layer thickness. Table 5.6, shows the non-dimensional parameters for the considered free stream velocities.

U_∞ $[\mathrm{m} \cdot \mathrm{s}^{-1}]$	Re	We	K	Ca	ξ
35	12 271	6 725	49 856	0.55	$3.03 - 3.04$
50	17 530	13 725	101 747	0.78	3.32
60	21 035	19 764	146 567	0.94	3.47

Table 5.6. Non-dimensional parameters for different prescribed free stream velocities, U_∞.

It is notable that the influence of the advancing angle on the spreading factor ξ, is nominal for the considered cases as it influences the maximum spread diameter, $d_{\max}$ by less than 5%. From Table 5.6, it is evident that $d_{\max} \in$

$[1.2d-1.4d]$ where d is the initial diameter of the droplet. For corona structures where only the base has been visible in the experimental photographs, the spreading parameter underestimates the ensuing $d_{\max}$ since $W_1 \gg d_{\max}$, due to the presence of a partial and continuous water film on which the incoming droplet can more easily spread.

5.3.5 DSWSAM Methodology Discussion

Certain limitations are associated with the employed DSWSAM methodology, in this study. In particular, one of the limitations of DSWSAM is attributed to the time consuming approach in analyzing the experimental photographs. Nonetheless, despite a manual discretization process, the potential errors in discretization errors are considered to be very small. The reasoning behind this statement is that since an averaged property such as the wave length of the water film is presented, and the order of magnitude of the discrete values are approximately the same, potential errors in discretization will not have a great influence on the final results, as these are averaged out. Another limitation of DSWSAM, is that its empirical images, do not convey any geometrical information about the extent of surface roughness, and the exact location of the asperities. The analysis presented herein have been restricted to the four categories in DSWSAM.

In order to improve the DSWSAM methodology, the usage of a coherent backlight is recommended, that is confined to a limited volume of space, or thickness in which the interface of the fluid with the air becomes more distinct,

than the employed level within this study. Such an illumination approach paves the way for a more automatic image processing tool to be employed. One possible technique of interest for this purpose, may be the utilization of PLIF (Planar laser induced flourescence), but measures have to be taken into tunnel cleaning and that the fluid structures will not be altered by the fluorescent dye. The number of fluid categories, can be expanded from the present four categories and for instance include bouncing droplets, that follow upon impact on super hydrophobic surfaces. Additional categories can moreover, be added to the methodology by means of the auxiliary modules.

Despite the mentioned limitations of DSWSAM, it has provided a framework under which advanced materials are analyzed based on their wettability. This methodology has in this study successfully been implemented to differentiate between the wetting characters of advanced candidate materials for aerospace applications. For instance, the skewness of the corona structures is obviously a result of the incoming droplet incident angle, $\alpha = 70°$, which the DSWSAM methodology captures well, without any assumptions made regarding the incident angle of the droplets.

5.4 Impact Pressure and VOF Approach

As a complement to the experimental findings of this study, and in order to obtain an insight into conditions that are more difficult to actualize experimentally, a volume of fluid (VOF) approach was chosen particularly in order to determine the impact pressure following a liquid solid impact versus time.

Initially, a literature survey was carried out in order to outline the applicability of the mathematical formulations and their underlying assumptions for the peak pressure upon impact. Table 5.7, shows the different utilized equations in the literature, and their scope of applicability.

No.	Pressure	Description	Source
(i)	$P \approx \rho_1 C_1 v$	Water hammer pressure	Cook (1928)
(ii)	$P = \frac{\rho_1 v^2}{2}$	Dynamic pressure	Hammitt (1977)
(iii)	$P = \frac{\alpha}{2}(\rho_1 C_1 v)$	Modified water hammer pressure	Engel (1955)
(iv)	$P = v(\frac{\rho_1 C_1 \cdot \rho_2 C_2}{\rho_1 C_1 + \rho_2 C_2})$	Water hammer pressure with target elasticity	de Haller (1933)
(v)	$P = \rho_1 C_1 v_1 (1 + \frac{k v_1}{C_1})$	Modified water hammer pressure	Heymann (1968)
(vi)	$P = 0.7 \rho_1 C_1 v$	Pressure at the impact center	Rochester and Brunton (1974)
(vii)	$P = 3 \rho_1 C_1 v$	Pressure at contact edge	Heymann (1969)
$(viii)$	$P = p^* \rho_1 v^2$	VOF pressure	Purvis and Smith (2005)

Table 5.7. Different impact pressure expressions.

In Table 5.7, Equation (i) is often referred to as the water hammer pressure and represents the impact between a semi-infinite plane of liquid and solid respectively (Cook, 1928). This equation hence does not take the finite size of the droplet and target into account, nor does it account for the non-rigidity of the target (Hammitt, 1977). Equation (ii) describes the pressure that is expected in a steady state condition and is in general much smaller than the water hammer pressure. The impact of a spherical droplet with a rigid solid (Engel, 1955) is shown in Equation (iii). Equation (iv) represents the water hammer pressure upon considering the elasticity effect of a target which can be expected for finite sized targets (de Haller, 1933). Equation (v) is further a modified version of the water hammer pressure, where the shock wave velocity varies linearly with higher impact velocities (Heymann, 1968). The empirical expression of Equation (vi) obtained by Rochester and Brunton (1974), represents the impact pressure at the center of the impact. Equation (vii)

represents the analytical expression of pressure at the lateral edge of the jet (Heymann, 1969). It can be readily established from Table 5.7, that none of the provided equations are able to provide a time or space dependent value of the pressure, nor do these equations account for the existence of water film layer on the target. The pressure levels provided by Table 5.7, are therefore merely peak pressures. In order to gain insight into the liquid impact problem, a volume of fluid (VOF) approach is justified as it will provide a spatial and temporal dependent pressure profiles, with impact at different incident angles on different water layer depths.

The VOF approach, is based on a numerical scheme in which the governing equations are the Navier-Stokes equation in two-dimensions (Batchelor, 2000)

$$\rho\left(\frac{\partial u}{\partial x}+\frac{\partial v}{\partial y}\right)=0 \tag{5.32}$$

$$\rho\left(\frac{\partial u}{\partial t}+u\frac{\partial u}{\partial x}+v\frac{\partial u}{\partial y}\right)=-\frac{\partial p}{\partial x}+\mu\left(\frac{\partial^2 u}{\partial x^2}+\frac{\partial^2 u}{\partial y^2}\right) \tag{5.33}$$

$$\rho\left(\frac{\partial v}{\partial t}+u\frac{\partial v}{\partial x}+v\frac{\partial v}{\partial y}\right)=-\frac{\partial p}{\partial y}+\mu\left(\frac{\partial^2 v}{\partial x^2}+\frac{\partial^2 v}{\partial y^2}\right) \tag{5.34}$$

The duration of the compressible stage following a liquid droplet impact on a solid is small $\sim \mathcal{O}(\mu\text{s})$ and immediately followed by a an incompressible stage. The VOF approach has been studied by a number of researchers and compared to experiments (Quero et al., 2006; Purvis and Smith, 2004, 2005; Asadi and Passandideh-Fard, 2009; Asadi and Panahi, 2011). The findings

of these studies exhibit good agreements between the VOF methodology and the experimental results. An inviscid approach is often considered at early times (Josserand, 2002) of the impact, which are most important in terms of the pressure that occurs on the surface. For this purpose, an inviscid and incompressible approach is undertaken in this study. The benefits of utilizing the VOF approach in this study for resolving the pressure distribution in space and time and for different incident angles and water film layers depths, hence outweigh the inviscid and incompressible flow assumptions. The comparison of the VOF approach in this study, has further only been confined to the pressure distribution and not extended to the geometrical metrics of the corona structures of the experimental photographs, due to the conjecture that the target either has a completely absent water film layer, or that the existing water film is completely stationary without any surface perturbations and covers the surface without any dry patches or beads/rivulets. Since, the dynamic wettability experiments in large feature a water film in motion and beads/rivulets in combination with dry patches on the specimens surface, the VOF approach is not considered as a means of comparison for the corona metrics.

A volume of fluid (VOF) approach, is able to track the interface position and further handle topology changes. The interface position tracking is actualized by a step function F representing the fraction of the fluid within a grid

cell. In essence

$$F \equiv \begin{cases} 1, & \text{Full cell} \\ \\ 0, & \text{Empty cell} \end{cases} \tag{5.35}$$

and $F \in (0,1)$ contains a free surface. The time evolution of F is furthermore given by (Hirt and Nichols, 1981)

$$\frac{\partial F}{\partial t} + u\frac{\partial F}{\partial x} + v\frac{\partial F}{\partial y} = 0 \tag{5.36}$$

Using the aforementioned methodology the two different fluids are given by $F \equiv 0$ and $F \equiv 1$ respectively. The fundamental problem is in this setting ascribed by a spherical droplet with a diameter D impacting on a fluid layer with depth H_F at a non-dimensional velocity of $v^* = 1$ and times $t \sim \mathcal{O}(1)$ similar to the investigation of Purvis and Smith (2004, 2005); Quero et al. (2006). In their work (Purvis and Smith, 2004, 2005) analytically examined an inviscid model for the the droplet impact into a water layer and found good correspondence between the analysis, computations and experiments. A good agreement between the VOF approach and the experimental results was also observed by Quero et al. (2006). Following the impact, two jets are formed at a vertical position $y = 1.5H$. The utilized VOF method makes use of completely non-dimensional parameters, with the time $t^* = \frac{D}{V}$, pressure $p^* = \frac{p-p_\infty}{\rho U_\infty^2}$ and the spatial parameters $x^* = \frac{x}{D}$ and $y^* = \frac{y}{D}$. The depth of the water film layer is further given by $H^* = \widehat{\epsilon}D$, with $\widehat{\epsilon}$, defined as a fraction less than unity.

In the present study, three distinct levels of water film layer, $H^\star = \widehat{\epsilon}D$ have been subjected to impact with a single water droplet, with $\widehat{\epsilon} = \{0.0, 0.3, 0.5\}$,

where the specific case $H^* \equiv 0$, corresponds to the impact of a droplet on a non-existing water film layer. The incidence angle for the water droplet impact on each mentioned water layer depth has further been $\theta = \{20°, 45°, 70°, 90°\}$. Of particular interest, in utilizing the VOF approach in this study, was the ability to obtain the temporal and spatial change of the pressure following the impact of a sphere liquid onto a solid surface.

5.4.1 Results and Discussion

In light of this discussion, the pertinent equations that are comparable in this study are Equations (*ii*), (*iv*) and (*viii*) in Table 5.7. These equations are chosen to be representative of the considered impact problem, as they account for both the compressible stage and the incompressible state of the impact problem in consideration of the the rigidity of the target, which is a valid assumption. Equation (*iv*) considered for the incompressible stage of the droplet impact, is analogous to Equation (*ii*). Since Equation (*iv*), takes the rigidity of the target into account and is capable of providing a peak pressure it can be utilized to establish the effects of compressibility exerted on the surface. The limitation of the aforementioned equations in this section apart from Equation (*viii*), is that they provide a fixed upper-limit bound for the magnitude of the pressure at a normal incident angle. Therefore, the influence of incident angle, time dependency and existing water layer depth is not accounted for in these expressions. Equation (*viii*), however is provided on the basis that pressure is solved in the temporal and spatial extent based on the water depth layer, $p^* = f(x^*, t^*, H^*)$. The employed VOF method at

different water layer depths $H^* = \{0.0, 0.3, 0.5\}$ and incident angles, is shown in Figures $5.32 - 5.34$. The temporal evolution of the pressure is shown upon a decreasing pressure peak envelope, with the largest value representing the immediate instant after the impact and the final time step chosen such that the peak pressure $p^* \to 0$. Table 5.8, shows the peak pressure level, instant and location as well as the pressure impulse for the different water layer depths and angle of attacks. The pressure impulse $\widetilde{p}$, is given upon integration of the pressure during a finite time limit

$$\widetilde{p} = \int_0^{t^*_{\max}} p^* dt^* \tag{5.37}$$

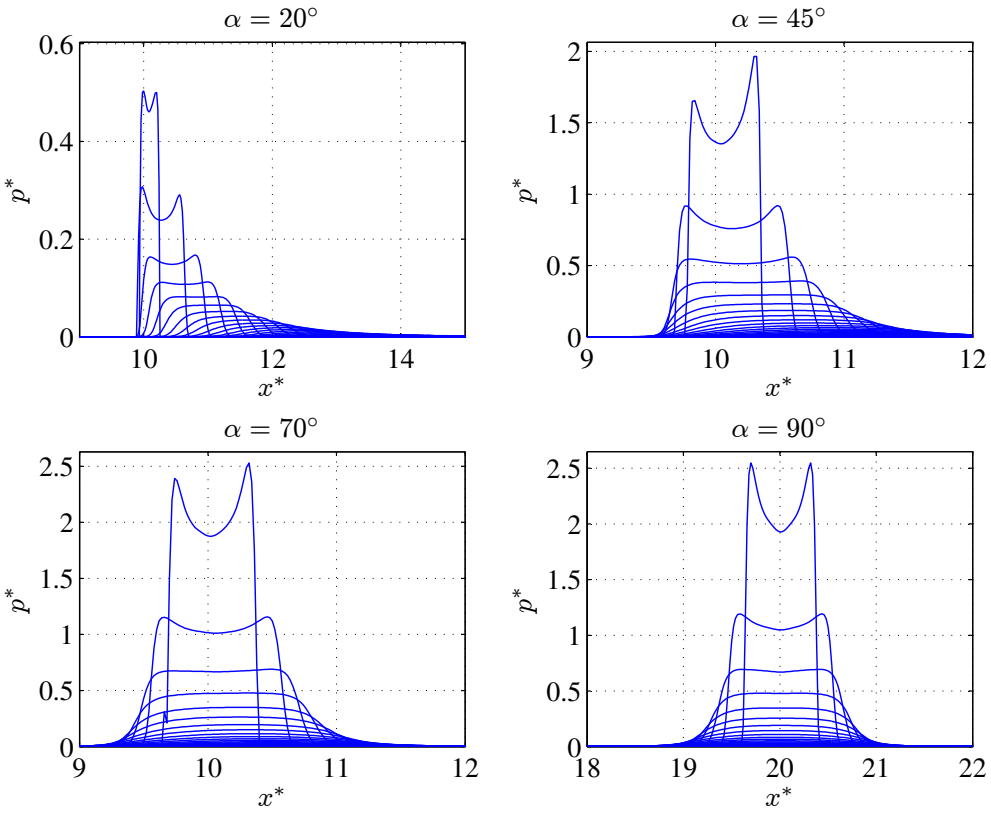

Figure 5.32. Non-dimensional pressure p^* versus distance x^*, for a fixed water layer depth $H^* = 0.0$, for impact angles $\alpha = \{20°, 45°, 70°, 90°\}$. The plot shows the time evolution of one droplet impact at different time steps, with $t^* = \frac{D}{V}$. For each incident angle, the impact location $x^*_{p,\max}$ and peak pressure $p^*_{\max}$, are shown in Table 5.8.

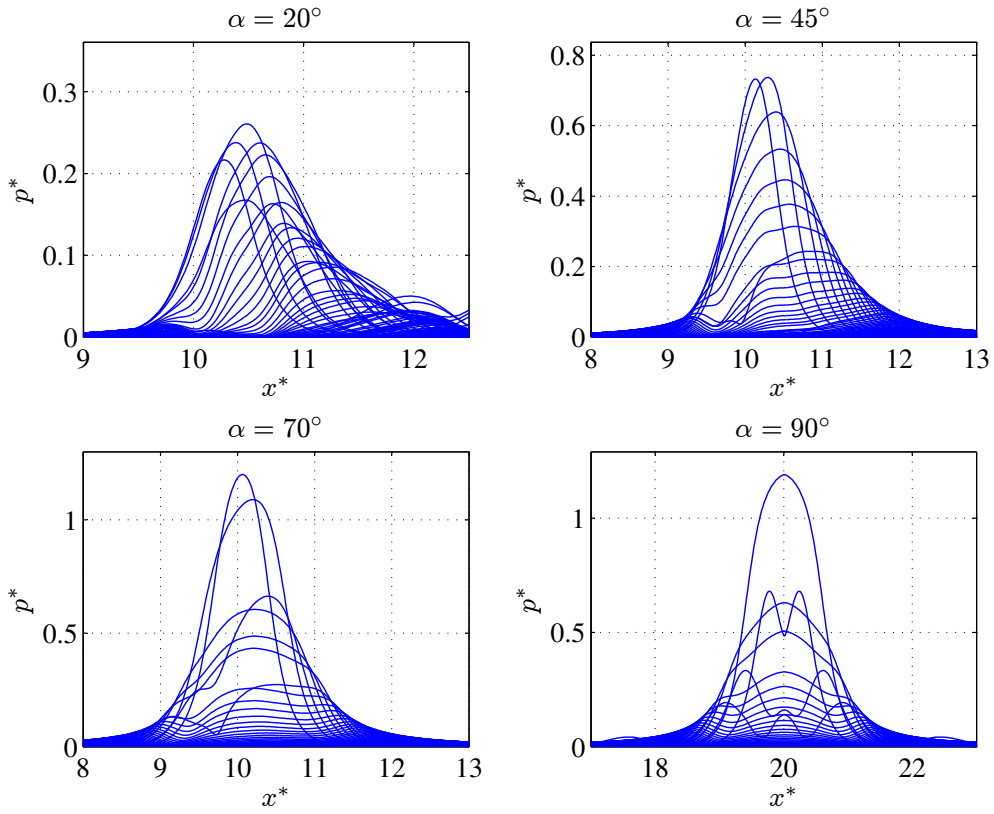

Figure 5.33. Non-dimensional pressure p^* versus distance x^*, for a fixed water layer depth $H^* = 0.3$, for impact angles $\alpha = \{20°, 45°, 70°, 90°\}$. The plot shows the time evolution of one droplet impact at different time steps, with $t^* = \frac{D}{V}$. For each incident angle, the impact location $x^*_{p,\max}$ and peak pressure $p^*_{\max}$, are shown in Table 5.8.

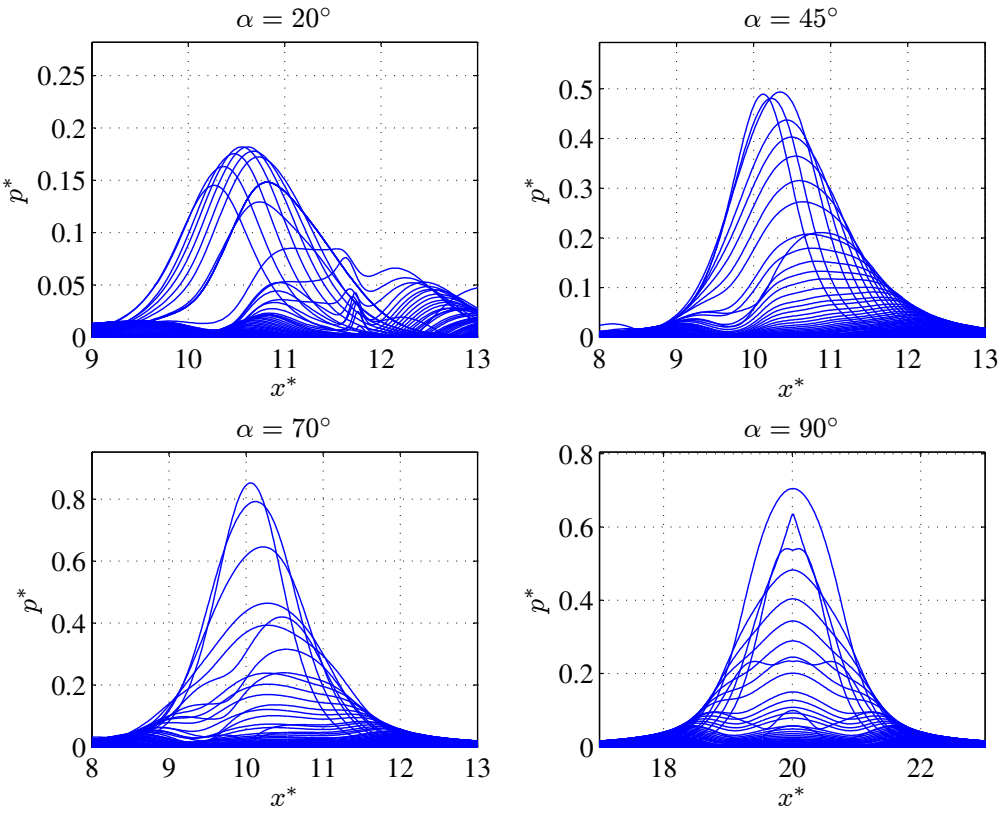

Figure 5.34. Non-dimensional pressure p^* versus distance x^*, for a fixed water layer depth $H^* = 0.5$, for impact angles $\alpha = \{20°, 45°, 70°, 90°\}$. The plot shows the time evolution of one droplet impact at different time steps, with $t^* = \frac{D}{V}$. For each incident angle, the impact location $x^*_{p,\max}$ and peak pressure $p^*_{\max}$, are shown in Table 5.8.

h^*	α [°]	$p^*_{\max}$	$t^*_{p,\max}$	$x^*_{p,\max}$	$\widetilde{p}$
0.0	20	0.5031	0.1	10.00	0.2887
	45	1.9647	0.1	10.32	0.6104
	70	2.5292	0.1	10.32	0.5637
	90	2.5467	0.1	19.70	0.5619
0.3	20	0.2607	0.4	10.48	0.3352
	45	0.7368	0.2	10.30	0.7958
	70	1.2008	0.1	10.06	0.8768
	90	1.1902	0.2	20.00	0.7299
0.5	20	0.1819	0.5	10.56	0.4256
	45	0.4936	0.3	10.34	0.6444
	70	0.8527	0.1	10.06	0.7501
	90	0.7050	0.3	20.00	0.6589

Table 5.8. The water depth layer H^*, incident angle α, peak pressure $p^*_{\max}$, location and instant of time where the peak pressure occurs denoted by $x^*_{p,\max}$ and $t^*_{p,\max}$ respectively. The non-dimensional impulse pressure is represented by $\widetilde{p}$.

Table 5.8 shows that the peak pressure level in general increases with a higher incident angle for the same water depth layer. The peak pressure level is further highest for the dry case ($H^* = 0.0$), and reduce in magnitude for the intermediate water layer depth ($H^* = 0.3$), and exhibits its lowest values for the thickest water film layer ($H^* = 0.5$). This observation infers that the water film layer indeed cushions the impact pressure. Additionally, it is observed that in particular incident angles $\alpha = 70°$ and $\alpha = 90°$, have nominally similar peak pressure values. At a normal incident angle, the peak pressure is however larger for the completely dry case, as opposed to the cases with a water film layer, in which it is slightly reduced. The pressure profiles for the dry case in particular agrees well with those of other researchers (Hammitt et al., 1978; Eggers et al., 2010), who found similar characteristic pressure peaks, slightly offset from the impact location. The additional contribution

of this study is that the effect of the incident angles has also been considered for $\alpha \in [0°, 90°]$. For incident angles $\alpha \neq 90°$ the peak pressures immediately after the impact are asymmetric. For the dry case this asymmetry is less pronounced and becomes more symmetric with as the peak is decreasing in magnitude. For the cases of $H^* = 0.3$ and $H^* = 0.5$, however, the asymmetry is more distinct. This observation is due to the presence of a water film layer in the latter cases and the absence of a water film layer for the dry case. In the dry case the two jets are not formed, and the influence of the impact is directly onto the solid without any other medium. For the cases of water film layer, the initial impact of the droplet not only affects the target, but also the water film layer and the two ejecting jets are formed. Hence, it is expected that the influence of the asymmetric nature of the pressure peak as a consequence of this phenomenon is more evident, as shown in Figures 5.33 and 5.34.

An alternative representation of the water hammer pressure equation accounting for elasticity, shown in Table 5.7 (iv), can be shown which accounts for the incident angle θ (Heymann, 1967)

$$P(\theta) = \frac{Z_L V \cos(\theta)}{1 + \frac{Z_L}{Z_S}} \tag{5.38}$$

where $Z_L = \rho_L C_L$ and $Z_S = \rho_S C_S$ denote the impedance of the liquid and solid respectively. In Equation (5.38), the angle θ refers to the angle subtended by the vertical normal plane and the line of movement of the droplet. It should also be observed that in the instance where $Z_S \gg Z_L$, the water-hammer

pressure equation is given by

$$P(\theta) = Z_L V \cos(\theta) \tag{5.39}$$

It can be deduced that the maximum pressure in Equations (5.38) and (5.39) occurs when $\theta = 90°$. Despite this observation, a number of studies (Kennedy and Field, 2000; Zhang, 2002; Shi and Field, 2004) have shown that the peak pressure does not necessarily occur at the center of impact, and can be slightly offset from the axis of symmetry for normal impacts. This observation, clearly explains the off-centered peaks in Figure 5.32.

5.5 Conclusions

It has been possible to implement DWSAM methodology in order to numerically describe the wetting behavior of advanced materials reinforced with carbon nanotubes in their pristine and eroded states respectively. Dynamic wettability of the considered materials exhibit seemingly similar wetting characteristics in the pristine state of the material, with the materials being largely hydrophobic. Upon erosion, the formation of water films on the specimen surfaces indicate a more hydrophilic behavior. Despite the complexities of image processing for different static and dynamic wettability arrangements, a methodology has been developed that discriminates between different empirical photographs of hydrophobic and hydrophilic specimens based on a numerical scheme. This scheme has thus far provided satisfactory results based on post-processing of the empirical photographs. The scheme can in future research be completed with additional modules to examine other fluid features.

The employed VOF method has further examined the effect of an existing water layer on the resulting pressure at different incident angles. The obtained results are consistent and infer physical properties of the different impact conditions.

Chapter 6

Ice adhesion

An important property in aircraft icing applications is the inherent ice adhesion characteristics of the materials utilized on the various surfaces of the aircraft. It is often desired that the utilized materials have low ice adhesion strength, enabling them to easily detach from the surfaces of the aircraft. Empirical studies of the ice adhesion strength for different materials are intricate due to the dynamic settings during which the ice accretion takes place. Hence, most researchers revert to static methods in which the ice is removed from the surface by means of pushing/pulling (Murase and Nanishi, 1985). In their experiments, Murase and Nanishi (1985) utilized a temperature regulated chamber. Specimens were mounted inside this chamber on a base turn-table in connection with a driving device able to generate push and pull forces connected to a load cell, process controller and recorder. Using this apparatus different stress and heating/cooling cycles could be generated. A more dynamic approach is to utilize the rotational system on which the shedding of the ice is attained by the outward pushing force of the apparatus

(Kulinich and Farzaneh, 2009). The experiments of (Kulinich and Farzaneh, 2009) make use of samples attached to aluminum beams spun in a centrifuge. A counter-weight placed on the opposite side of the beam, balances the beam in the centrifuge. The shear strength is in this configuration calculated based on the ratio of the centrifugal force over the deiced area. A more realistic approach however, is to utilize an icing tunnel in which the flight conditions are replicated and the accretion and adhesion of ice is natural. For this reason, the Cranfield Icing Tunnel was utilized for the ice adhesion tests on the candidate specimens in two different surface finish conditions. The pristine and eroded state of the material specimens, were used in order to examine the effect of erosion on the accretion and adhesion characteristics of the considered materials. In light of this discussion, the given specimens were subjected to ice shear tests. The ice adhesion unit, at Cranfield University, was originally developed by Pervier (2009) and prepared for use in the icing tunnel by Terzis (2009); Lou (2009), with further development by Gurrutxaga Lerma (2010) and Moncholi Piles (2011).

6.1 The Cranfield Icing Tunnel

The ice adhesion experiments were carried out in the Icing Tunnel at Cranfield University, United Kingdom. The chosen working section for these experiments was 760×760 mm^2, in which Mach numbers, $M \in [0.1, 0.5]$ can be achieved. The subzero temperatures in the tunnel are attained by the air with a refrigeration plant, able to extract heat from the air, placed adjacent to the tunnel. Using this plant and a water-spray system with provision for

99 spray nozzles a temperature range between $T \in [-30, +30]$ °C can be obtained (Hammond et al., 2003). The experimental conditions for this study were confined to a free stream velocity $U_\infty \approx 60$ m $\cdot$ s^{-1}, droplet Median Volume Diameter, $MVD \cong 20$ μm, with the air and water pressure for the tunnel $P_a \cong 26.5$ psi, and $P_w \cong 20$ psi, respectively. These conditions were based on the reproducibility of the experimental conditions. The liquid water concentration $LWC \cong 0.3$ g $\cdot$ m^{-3}, was used for both temperatures, $T = -5$ °C and $T = -10$ °C. A schematic rendering of the Cranfield Icing Tunnel is shown in Figure 6.1.

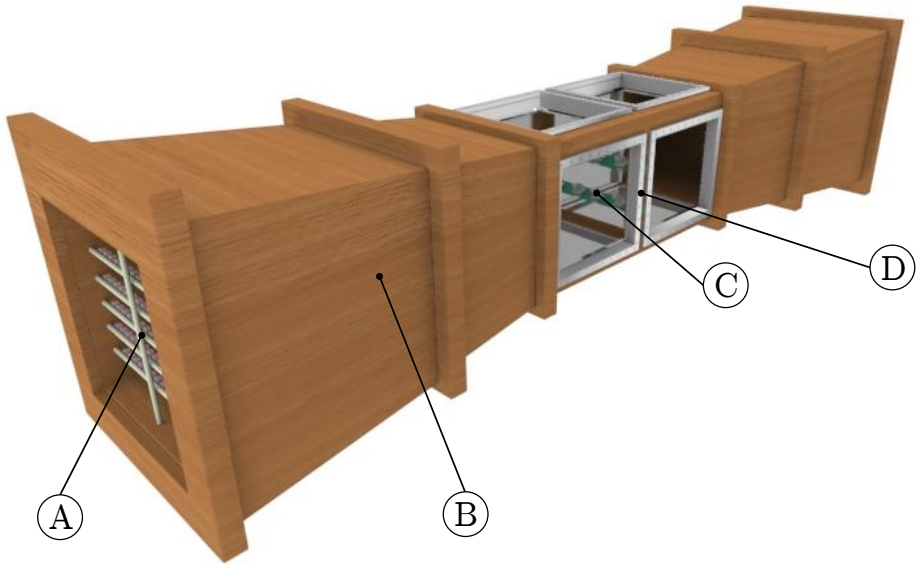

Figure 6.1. A schematic rendering of the Cranfield University Icing Tunnel. The following notations have been utilized in the figure: (A) Spray nozzles, (B) Cranfield Icing Tunnel, (C) Mounted ice adhesion bars with corresponding ice adhesion test units, and (D) Test section. The flow direction is from the spray nozzles towards the test section.

For ice adhesion testing, it is imperative that the produced cloud by the spray rakes is of uniform nature. Hence, an empirical calibration of the active water spray nozzles is a necessity in order to determine the nozzle configuration that results in the most uniform cloud over the target units. As the water spray nozzles are affixed to six different spray bars placed equidistantly away from each other in the vertical direction, placement of steel bars under certain nozzles distorts the flow and contributes to a more uniform droplet cloud inside the test section. The utilized spray nozzle configuration for this study is shown in Figure 6.2.

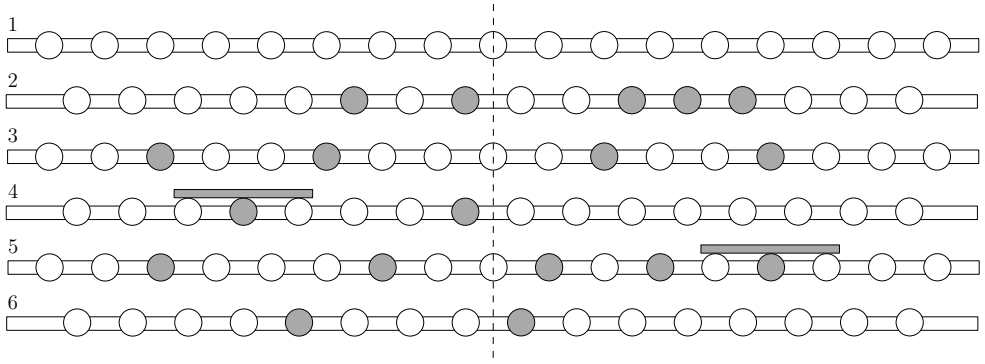

Figure 6.2. The utilized water spray nozzle configuration for the ice adhesion tests. The shaded areas denote the employed nozzles and bars, respectively.

6.1.1 Ice adhesion unit

The specimens are placed on an exchangeable shear test unit, comprising of a plunger and pressure tube arrangement as shown in Figure 6.3. The dimensions of the tests samples are $(L \times W \times H) = (20 \times 15 \times 4)$ mm^3. In order to accommodate specimens with $H \neq 4$ mm, the specimens are either grinded

or hoisted to the desired thickness for the shear test rig. In the present study 10 different materials are examined with and without reinforcing carbon nanotubes. The influence of surface morphology, ice adhesion and shear strength of 8 candidate materials were examined in both pristine and eroded states. The eroded state was obtained by wet blasting the specimens with alumina, with the resulting percentage increase and decrease of the surface roughness, ΔR_a shown in Table 4.5. Figure 6.3 shows the shear test unit prior to and after the impact ice shedding.

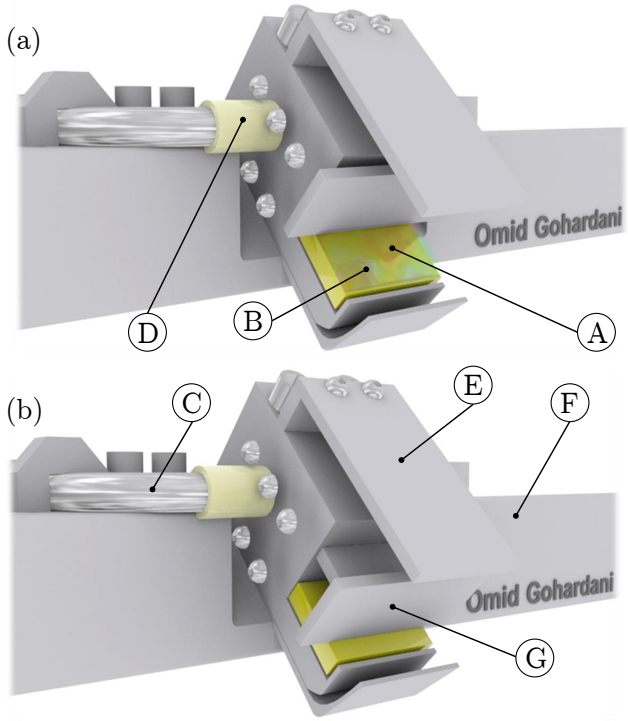

Figure 6.3. The employed ice shear strength unit at Cranfield University, United Kingdom, (a) prior to ice shedding, and (b) after engagement of the plunger. The following notations have been used in the figure: (A) Specimen, (B) Accreted ice on the specimen surface, (C) Air supply tube, (D) Inflatable rubber tube, (E) Specimen shield, (F) Specimen bar, and (G) Plunger. Unit design: Pervier (2009); Terzis (2009); Lou (2009); Gurrutxaga Lerma (2010), unit bar design: Moncholi Piles (2011), manufacturing: Hutchings, A., and digital rendering: Gohardani (2010).

6.1.2 Test procedure

The tests are carried out by an initial placement of the specimens in the shear test compartments. The test rig is capable of testing eight different units simultaneously. In effect, the choice of specimens in this setting have been such that the pristine and eroded samples are tested at the same conditions. The specimen surface is flush with the lower surface of the plunger as shown in Figure 6.3. Upon a nominal ice accretion $h_{\text{ice}} \cong 3$ mm on the specimen surface, the pressure is increased until a final peak pressure $\widehat{P}$, is identified for each specimen. Upon reaching the peak pressure, the ice sheds. Following the free movement of the plunger, a slight pressure drop is observed. For statistical purposes an averaged value of 4 different tests is utilized, resulting in an average peak pressure defined by

$$\overline{P} = \frac{1}{4}\sum_{i=1}^{4} \widehat{P}_i \tag{6.1}$$

The experimental procedure for the ice adhesion testing is carried out in accordance with a number of steps as shown in Figure 6.4. In order to undertake the ice adhesion experiments, the experimental samples have to conform to the dimensions $(L \times W \times H) = (20 \times 15 \times 4)$ mm^3. Accommodation of specimens with $H \neq 4$ mm, is actualized by the specimens either being grinded or hoisted to the desired thickness of the shear test rig units. This is crucial as a specimen thickness $H > 4$ mm, restrains the movement of the plunger, and a specimen thickness $H < 4$ mm, further ensues in the accretion of ice

below the plunger, which results in a shear test where the properties of the specimen are replaced by those of ice. Each specimen is positioned inside each shear test unit and the mobility of the plunger after placement of the specimen is inspected. Upon adequate sample preparation, the Icing Tunnel is prepared with a nozzle configuration that results in a uniform liquid water concentration (LWC). Upon choosing a desired temperature T, and free stream velocity U_∞ and mapping of the LWC, the shear tests units are placed on locations on the transversal bars where a uniform LWC is encountered. Upon an established nozzle configuration that results in a uniform cloud, the side window of the Icing Tunnel is removed and the specimens are cleaned with ethanol and paper towels without residues. The surface of the specimens upon initiation of the test must be completely dry and without any contamination or residues. Before removing the moist from the tunnel, the specimens are covered with paper towels and upon removal of the moist with blowing air, once again uncovered. A final check of the mobility of each plunger is carried out, assuring each plunger to move freely. Once, this assertion is completed, the side window of the icing tunnel is sealed into position. The nozzles are then engaged once the flow conditions are acclimatized to the desired temperature T, air pressure P_a and water pressure P_w. Upon engaging the nozzles ice accretion is observed on the surface of the specimens. Once the thickness of ice on top of the specimens surface $h_{\text{ice}} \approx 3$ mm, the ice adhesion shear test is commenced in accordance with the procedure in Figure 6.4.

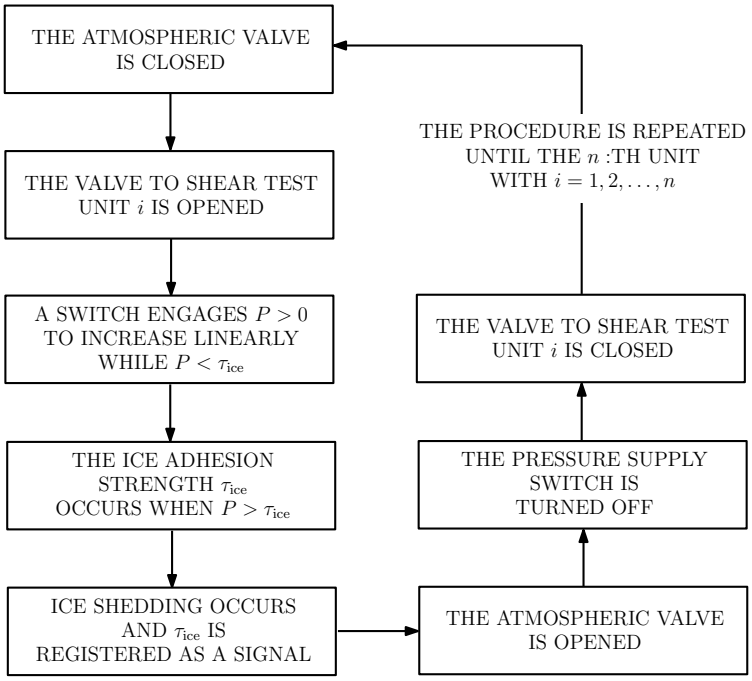

Figure 6.4. The ice adhesion test procedure.

Concurrently, 8 specimens can be subjected to ice shear tests depending on the number of shear test units employed. For each of these however, the following procedure must be undertaken. Initially, the atmospheric valve is closed where the overall pressure to the system is supplied from a gas cylinder with an adjustable pressure. The corresponding shear test unit valve is opened and a switch engaged in order to supply pressure to the test shear testing unit. Upon supplying pressure, the air is directed through the air supply via an elastic rubber tube placed behind the piston. As the end of the rubber tube is sealed, a continuous supply of pressure results in inflation of the rubber band inside the cavity of each shear test unit, while the threshold pressure, $P_{\text{s}} < \tau_{\text{ice}}$. Once $P_{\text{s}} > \tau_{\text{ice}}$, the accreted ice is shed from the shear test unit and the corresponding pressure value registered on an oscilloscope. The atmospheric

valve is at this point opened and the supply switch immediately turned off upon visual detection of the shedding. A delay in turning off the switch may result in the supplied pressure exceeding the fracture strength value of the rubber tube, which consequently may result in leakage and bursting of the rubber material. Finally, the corresponding valve for the shear test unit should be closed and this procedure repeated for the number of tested units.

6.2 Results and Discussion

The ice shear strength values of the considered materials are presented in Figure 6.5 prior to and post erosion, with the exception of specimen numbers $S_n = 9$ (LAYSA_ICE) and $S_n = 10$ (SICOMP_NA_ICE1). These specimens consist of multiple layers and are only supplied in a pristine state.

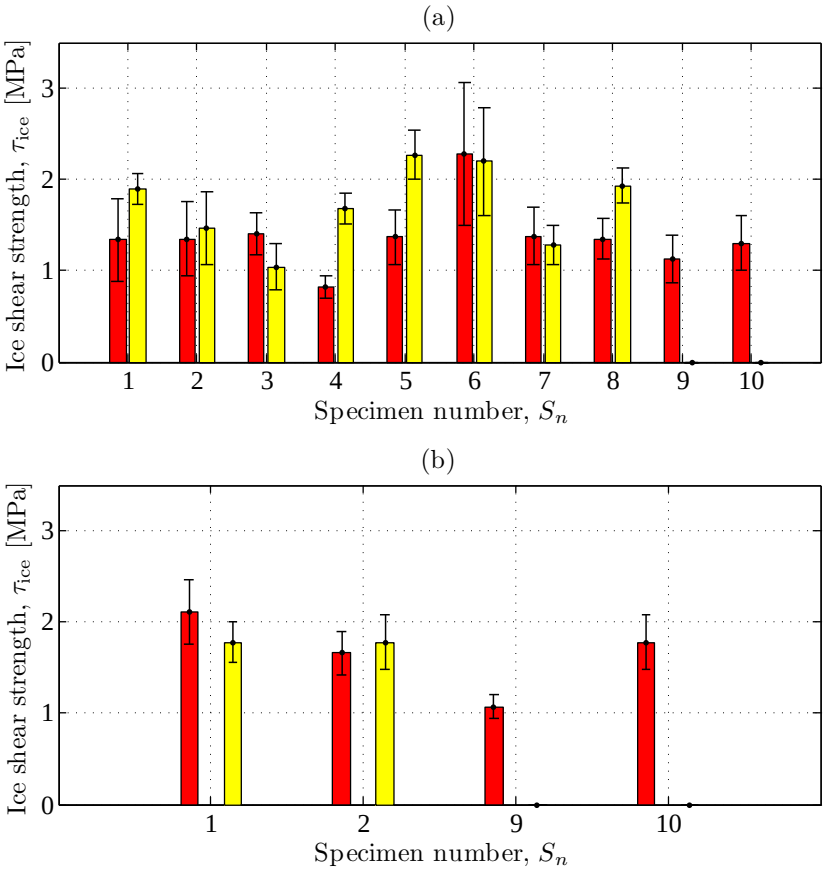

Figure 6.5. Ice shear strength τ_{ice}, for the tested specimens at temperatures (a) $T = -5°\mathrm{C}$ and (b) $T = -10°\mathrm{C}$, for a liquid water concentration, $LWC \cong 0.3$ $[\mathrm{g} \cdot \mathrm{m}^{-3}]$. The following notations are utilized for the specimen numbers, S_n: (1) LY564, (2) LY564 + 0.5% MWCNT, (3) 32_MINAS1_06, (4) 32_A05_CANBIO1_06, (5) 32_MINAS1_07, (6) 32_A05_CANBIO1_07, (7) Araldite DBF (8) SW404 + XB5173, (9) LAYSA_ICE_01, (10) SICOMP_NA_ICE1. The left column further describes the pristine and the right column the eroded state, respectively.

The general trend observed from Figure 6.5 indicates that the eroded samples in large exhibit higher ice adhesion strengths in comparison to the pristine counterparts. The higher values are associated with a higher pitting of the eroded surface, to which the formed impact ice may easily adhere hence requiring a higher shear force to detach the ice from the surface upon employing the shear test units. This observed trend is further encountered by other researchers (Zou et al., 2011). The lowest observed ice adhesion strength in comparison to the highest differ by a factor of two.

Influence of Temperature

In order to examine the role of temperature on the ice adhesion properties of the specimens, the S_1 and S_2 samples were selected and subjected to two different test temperatures $T = -5$ °C, and $T = -10$ °C, in both pristine and eroded states respectively. The liquid water content for both experimental sets were confined to $LWC \cong 0.3\ \mathrm{g} \cdot \mathrm{m}^{-3}$. The choice of these material samples stemmed from the establishment of carbon nanotube influence on the ice adhesion characteristics. The ice adhesion strength of the considered materials τ_{ice} at the aforementioned temperatures are shown in Figure 6.5.

The experimental results, suggest that the pristine state of the S_1 exhibits a lower ice adhesion strength than the eroded state at $T = -5$ °C. In contrast, the same specimen requires a higher ice adhesion strength at the pristine state than the eroded state at $T = -10$ °C. It should be noted that the pristine state of the specimen in fact has a higher average roughness value than the

eroded sample. Hence, a higher ice adhesion strength is expected for the pristine sample in comparison to the eroded one. This higher adhesion strength is encountered for the lower temperature, but not for the higher temperature for the S_1, which may be attributed to non-uniformities in the pristine specimen and the accretion thickness of ice on the specimen. Although the accretion thickness $h_{\text{ice}} \approx 3$ mm, for all the considered specimens, there might be instances where a deviation from this thickness may influence the acquired ice adhesion strength value. For S_2 (LY564 + 0.5% MWCNT), the eroded specimen exhibits a higher ice adhesion strength at both $T = -5$ °C and $T = -10$ °C, with an increase from the pristine values with 8.9% and 7.2% respectively. A higher ice shear strength value obtained at lower temperatures is also reported by Chu and Scavuzzo (1991) for impact ice shear strength, which in essence is consistent with the higher τ_{ice} value at $T = -10$ °C in comparison to $T = -5$ °C, for the S_1 specimen in its pristine state.

Influence of Surface Roughness

A compilation of the influence of the averaged surface roughness $R_a^{p,e}$ in the pristine and eroded states respectively and ice adhesion strength τ_{ice} are shown in Table 6.1.

S_n	τ_{ice}^p [MPa]	τ_{ice}^e [MPa]	R_a^p [μm]	R_a^e [μm]	$\Delta\tau_{\text{ice}}^*$
S_1	1.34	1.89	5	4.24	-2.70
S_2	1.35	1.47	0.74	4.4	0.02
S_3	1.40	1.04	0.20	3.98	-0.01
S_4	0.82	1.68	0.8	3.74	0.29
S_5	1.37	2.27	0.20	4.06	0.03
S_6	2.28	2.20	1.2	3.92	-0.01
S_7	1.38	1.28	0.8	2.32	-0.04
S_8	1.35	1.93	0.6	2.98	0.11

Table 6.1. The ice adhesion strength τ_{ice}, surface roughness R_a, and the non-dimensional change of adhesion strength per unit surface roughness $\Delta\tau_{\text{ice}}^* = \Delta\overline{\tau}_{\text{ice}}/\Delta\overline{R}_a$ for the given specimens, with $\Delta\overline{\tau}_{\text{ice}} \equiv (\tau_{\text{ice}}^e - \tau_{\text{ice}}^p)/\tau_{\text{ice}}^p$ and $\Delta\overline{R}_a \equiv (R_a^e - R_a^p)/R_a^e$. The superscripts e and p denote eroded and pristine state respectively.

From Table 6.1, it can be deduced that for the majority of the specimens an increase in surface roughness from the pristine state to the eroded state results in a higher ice adhesion strength. The reasoning behind this observation can mainly be attributed to the fact that a higher shear force is required to remove the ice from the surface due to the presence of surface grooves and pits to which ice can more easily adhere. It is however notable that exceptions are also observed where an increase in surface roughness results in a decrease in ice adhesion strength. This decrease however, is at most 26% less than the pristine sample. It should be emphasized that the single figure presented as the surface roughness value for each specimen in the pristine and eroded states, denotes an averaged estimate for the entire surface. Hence, local deviations from this surface roughness value are apparent, which easily can be observed by the visible surface flaws such as scratches and pits on the supplied specimen surfaces. These surface defects can in part explain the expected results at which an increase in surface roughness results in a decrease of ice adhesion

strength. In addition, the dispersion of carbon nanotubes within the resin, the interfacial bond between the matrix and the nanoparticles, aggolmeration of carbon nanotubes and other surface characteristics may contribute to the this inconsistency. In order to obtain an estimate of the relation of ice adhesion strength in the prisine and eroded states of the specimens in relation to their respective averaged surface roughness value, the non-dimensional change of adhesion strength per unit surface roughness $\Delta\tau^{*}_{\text{ice}}$ is introduced. From Table 6.1 it can be observed that $\Delta\tau^{*}_{\text{ice}}$ is nominally similar for the considered specimens and significantly different for specimens S_4 (32_A05_CANBIO1_06) and S_1 (LY564).

As expected, a comparatively higher value of the numerator of $\Delta\overline{\tau}_{\text{ice}}$ increases the value of $\Delta\tau^{*}_{\text{ice}}$. With exception of the S_1 (LY564) $\Delta\tau^{*}_{\text{ice}} < 0$ denotes the observation that the $\tau^{e}_{\text{ice}} < \tau^{p}_{\text{ice}}$. For S_1 however, this negative sign stems from the fact that $R^{p}_{a} > R^{e}_{a}$.

6.2.1 Sources of error

There are in effect a number of factors that may influence the outcome of the ice adhesion shear tests. In particular it is imperative that the surface of the specimen is entirely clean and free from any form of contamination or water droplets prior to the ice adhesion tests. As the same rubber tube may be employed for several ice adhesion tests, over time the elasticity of the rubber might be degraded resulting in leakage and improper seal of the applied pressure. The movement of the plunger may also during certain conditions be-

come restrained and slightly influence the outcome of the ice adhesion results. Perhaps one of the most difficult factors that may influence the ice adhesion results is to determine the instant at which the shear test procedure should be commenced. Although the same criterion $h_{\text{ice}} \approx 3$ mm, are to be utilized for all the specimens, this thickness may only be estimated by the naked eye, in which instances where $h_{\text{ice}} \neq 3$ mm may occur.

6.3 Conclusions

The utilized shear test units have provided consistent data upon exposing the set of specimen $S_1 - S_{10}$ to impact icing at a uniform liquid water concentration level. The ice accretion on the samples has therefore been natural and the effects of temperature and surface roughness have been evaluated in this study. The ice adhesion tests suggest that the pristine surfaces in general exhibit lower ice adhesion strength in comparison to the eroded specimens. The effect of erosion and wear is hence once again highlighted as a crucial element when discussing new advanced materials. Upon comparison of pristine samples with carbon nanotube reinforced samples the performance in terms of ice shear strength has nominally been similar. At a lower temperature for the S_1 however, a decrease in ice adhesion strength is observed for the pristine sample, while the eroded samples remain unaffected by the lower temperature.

Chapter 7

Conclusions

The implementation of carbon nanotubes and search for icephobic coatings in aerospace sciences is indeed a driving mechanism in search of advanced materials which can endure prolonged flight conditions and exposure to different wear mechanisms. The findings of this study highlight the crucial role of wear in terms of erosion on the performance of advanced aerospace materials reinforced with carbon nanotubes. One of the most fundamental elements of this study has been the characterization of the materials, in terms of uniformity. The performed density and microhardness results indicate that the materials reinforced with carbon nanotubes show evidence of non-uniformity which can be attributed to the dispersion of carbon nanotubes within the resins and manufacturing defects resulting in surface flaws.

The largest scatter of hardness values was found on the S_1 (LY564) specimen which can be attributed to its visible surface flaws and asperities. The lowest scatter of Vickers hardness value was found on the S_6 (32_A005_CANBIO1_07).

These variations should be considered when examining the different performance characteristics of the materials. In order to mimic the effect of wear and weathering, the materials were examined in two different states; pristine and eroded. This approach has hence provided the pristine state of the material to serve as a baseline for comparison between the two different states. The role of carbon nanotubes for the reinforced substrates S_2 (LY564 +0.5% MWCNT), S_4 (32_A005_CANBIO1_06) and S_6 (32_A005_CANBIO1_07) is that all of these materials demonstrate higher acoustic impedance values in comparison to the same matrix resins without the reinforcement.

In particular three different phenomena analogous to possible events during a flight scenario have been executed in order to characterize the materials in a ranking system. These events that might arise are a consequence of hydrometeors dynamically wetting or splashing on the surfaces of an aircraft upon the vehicle traversing a cloud system. The three considered empirical investigations has therefore been static and dynamic wetting, liquid erosion and ice adhesion.

Exposure to liquid erosion, in this study has established the damage threshold velocities of the candidate materials. The performance of all specimens, including those reinforced with carbon nanotubes have during these tests been nominally similar with $v_{\widehat{D}} \cong 130 \pm 20 \text{ m} \cdot \text{s}^{-1}$. Hence, carbon nanotubes at a weight percent of 0.5 utilized as reinforcement for the resins did not explicitly contribute to a lower or higher damage threshold velocity. The established damage threshold velocities of the considered materials limit their implemen-

tation in aeronautics to the flight speeds of Unmanned Air Vehicles, less than Mach 0.4.

The phenomena of wetting in a static and dynamic sense has been examined thoroughly for these materials upon employment of contact angle measurements and exposure of the materials to a barrage of droplets in a droplet tunnel with a gentle contraction in order to simulate a plausible dynamic wetting of the specimens. One of the greatest challenges of this study has been to describe the qualitative wetting observations of the materials quantitatively, without any pre-assumptions regarding the surface character, material and extent of hydrophobicity or hydrophilicity. For this purpose a new methodology, the Dynamic and Static Wettability Scheme for Advanced Materials (DSWSAM) has been developed that makes use of different modules and empirical results in order to describe idealized representations of the wetting nature of the different surfaces. The developed methodology is based on a defined category classification of the fluid structures and actualized upon employing a set of unique modules developed in MATLAB®. DSWSAM further enables other fluid categories to be implemented into the methodology and can further be tailored to target a special parameter space based on new auxiliary modules.

The implementation of the DSWSAM methodology has established a framework for the analysis of a large population of empirical images, which in this study has been 16,000. The developed Liquid Water Concentration Module (LWCM) and the Corona Measurement Splashing Tool (CMST) further

provide a consistent and unbiased analysis of the empirical data set for each experiment. In light of the findings of the DSWSAM methodology it can be established that erosion on the specimens in large contributes to a distinct change of the hydrophobic nature of the specimens. The reinforced specimens with carbon nanotubes all develop partial or continuous water films in the aftermath of erosion and other substrate materials without carbon nanotube reinforcement exhibit similar behavior upon erosion. The numerical scheme hence is able to capture this phenomenon that was observed qualitatively, by mere observation. This finding highlights an important aspect of the discussion of implementation of hydrophobic material in aerospace applications. Due to the relative high speeds at which most commercial airliners operate and the unavoidable encounters with weathering effects arising as a consequence of extended flight operations of the commercial fleet, the direct implementation of hydrophobic materials and their performance thereof will significantly depend upon the surface character. Hence, a pristine hydrophobic material may after a period of time exhibit a hydrophilic character under the assumptions that a similar dispersion process and weight percentage of carbon nanotube has been utilized. The change of surface character from a hydrophobic to a hydrophilic, is further highlighted by the larger base width of the coronas and two-dimensional areas of the corona structures that arise upon splashing on eroded surfaces.

The ice adhesion results accentuate the important role of surface character of the ice adhesion strength of the materials. This observation is further of immense importance as the ice accretion on the test materials ensues from im-

pact ice, with liquid water content levels similar to those experienced during flight conditions. The results largely infer that the ice adhesion strength of the eroded materials is higher than on the pristine samples at $T = -5°\text{C}$ and that this trend also holds for a lower temperature of $T = -10°\text{C}$.

It has also been shown that the employment of a multi-layered material combination can reduce the stresses on the surface of the outermost material, following a liquid impact. Conclusively, a multi-disciplinary approach has been undertaken into understanding the behavior of advanced materials reinforced with carbon nanotubes for implementation in aeronautics. This work has highlighted the role of surface effects on the ensuing wetting character, ice adhesion and material failure. The findings of this study should be considered within the applied weight percentage of carbon nanotube implementation and dispersion process, as higher weight percentage values, may alter the behavior of the materials considerably.

Based on the empirical and analytical assessment of the materials within the framework of this project a platform can be suggested on which the aforementioned materials may be utilized. One of the most crucial aspects on implementing the materials onto an aircraft has been determined by the damage threshold velocity (DTV) of each respective material. For a successful implementation of a material on the various surfaces of an aircraft the DTV has to be considerably higher than the maximum flight speed or cruise speed of the aircraft. In this context, it can be readily determined that the highest encountered DTV for a 2 mm droplet corresponds to a Mach number, $M \approx 0.4$.

A glance upon applicable cruise speeds for aircraft yields that this value is well below the cruise speeds of commercial airliners with $M \cong 0.8$, but well within the utilized cruise speeds of Unmanned Air Vehicles and micro air vehicles. For this purpose it is suggested that the platform on which these materials will be of most use is an unmanned air vehicle without an ice protection system. An example of one such aircraft is the conceptual Generic Unmanned Air Vehicle (GUAV) proposed by Gohardani and Gohardani (2012).

Chapter 8

Future work

The present study has established a framework for evaluation of empirical erosion results based on a mathematical formulation dependent on experimental parameters and employed a simplified 1−D analytical stress model consisting of a substrate/coating and a substrate/compliant layer and cladding. In particular, several aspects of this study may be subjected to an extended evaluation. One of the challenges as identified by the literature (Gohardani, 2011) that may contribute to further understanding of erosion of polymeric matrix composites reinforced with carbon nanotubes, is the level of erosion modeling that has to be exercised. Due to the different length scales involved, microscopic, mesoscopic and macroscopic approaches of the modeling process are possible. The challenge in this context would be to interlink these length scales such that the relevant erosion information is retrieved. A necessity for computational modeling of the erosion process is access to a large number of known material properties for the resins with the carbon nanotube reinforcement.

The other aspect of improvement related to the erosion process, is extension of the presented $1-D$ model to multi-layered materials and implementation of the carbon contributions within the analytical model.

In terms of dynamic wettability, the developed DSWSAM methodology can further be enhanced to an automated system, which determines the fluid structure categories without any user input. Incorporation of other fluid structure categories besides those mentioned in this study may further provide auxiliary information about the wetting characteristics of the considered surface.

For the ice adhesion strength tests, a more accurate method of estimating the accreted thickness of the ice can be considered, in order to minimize differences in test conditions, upon comparison of the test results.

Conclusively, characterization of the nature of future materials, in particular related to carbon nanotube dispersion and microstructure is of vital importance for a better insight into the understanding of the ice accretion, wettability and ice adhesion phenomena.

References

J. Achenbach. *Wave Propagation in Elastic Solids*. Number 0720403251. Elsevier Science, November 1987.

A.W. Adamson and A.P. Gast. *Physical Chemistry of Surfaces*. Wiley-Interscience, 1997.

W.F. Adler. Development of design data for rain impact damage in infrared-transmitting materials. *Proc SPIE*, 297:143–154, 1981.

W.F. Adler. Development of design data for rain impact damage in infrared-transmitting windows. *Opt Eng*, 26:143–151, 1987.

W.F. Adler. Rain impact retrospective and vision for the future. *Wear*, 233-235(0043-1648):25–38, December 1999.

P. M. Ajayan, L. S. Schadler, C. Giannaris, and A. Rubio. Single-walled carbon nanotube-polymer composites: Strength and weakness. *Adv. Mater.*, 12(10): 750–753, 2000.

RF Allen. The role of surface tension in splashing. *Journal of Colloid and Interface Science*, 51:350–351, 1975.

A. Amendola and G. Mingione. On the problem of icing for modern civil aircraft. *Air & Space Europe*, 3(3-4):214–217, 2001.

D.L. Arenberg. Ultrasonic Solid Delay Lines. *J Acoust Soc Am*, 20(1):1–26, 1948.

S. Asadi and H. Panahi. A Numerical Study of a Droplet Impingement on a Liquid Surface. *World Academy of Science, Engineering and Technology*, 79:720–724, 2011.

S. Asadi and M. Passandideh-Fard. A computational study on droplet impingement onto a thin liquid. *The Arabian Journal for Science and Engineering*, 34(2B):505–517, 2009.

S.D. Aziz and S. Chandra. Impact, recoil and splashing of molten metal droplets. *Int. J. Heat Mass Transfer*, 43:2841–2857, 2000.

H.R. Baker, W.D. Bascom, and C.R. Singleterry. The adhesion of ice to lubricated surfaces. *Journal of Colloid Science*, 17(5):477–491, 1962.

G.K. Batchelor. *An Introduction to Fluid Dynamics*. Cambridge Mathematical Library series, Cambridge University Press, 2000. ISBN 0-521-66396-2.

B. C. Bernstein, F. McDonough, M. K. Politovich, B. G. Brown, T. P. Ratvasky, D. R. Miller, C. A. Wolff, and G. Cunning. Current Icing Potential: Algorithm Description and Comparison with Aircraft Observations. *J. Appl. Meteor.*, 44:969–986, 2005.

B. Bhushan and Y.C. Jung. Wetting study of patterned surfaces for superhydrophobicity. *Ultramicroscopy*, 107:1033–1041, 2007.

T.C. Bond, D.S. Covert, J.C. Kramlich, T.V. Larson, and R.J. Charlson. Primary particle emissions from residential coal burning: Optical properties and size distributions. *J. Geophys. Res.*, 107:8347, 2002.

F.P. Bowden and J.H. Brunton. Damage to solids by liquid impact at supersonic speeds. *Nature*, 181:873–875, 1958.

F.P. Bowden and J.H. Brunton. The deformation of solids by liquid impact at supersonic speeds. *Proc Roy Soc A*, 263:433–450, 1961.

F.P. Bowden and J.E. Field. The brittle fracture of solids by liquid impact, by solid impact, and by shock. *Proc R Soc Lond A,*, 282:331–352, 1964.

R.K. Bregg. *New frontiers in polymer research*. Nova Publishers, Illustrated edition, 2006. ISBN 1594549567, 9781594549564.

K.H.J. Buschow, R.W. Cahn, B. Flemings, M.C.and Ilschner, E.J Kramer, and S. Mahajan. *Encyclopedia of Materials - Science and Technology, Volumes 1-11*. Elsevier, 2001. ISBN 978-0-08-043152-9.

Cger. *Atmospheric Effects of Aviation: A Review of NASA's Subsonic Assessment Project*. National Academies Press, 1999. ISBN 0309076609, 9780309076609.

P. Chantikul, G.R. Anstis, B.R. Lawn, and D.B. Marshall. A critical evaluation of indentation techniques for measuring fracture toughness: II, strength method. *J Am Ceram Soc*, 64:539–543, 1981.

MC Chu and RJ Scavuzzo. Adhesive shear strenth of impact ice. *AIAA Journal*, 29:1921–1926, 1991.

E.J. Coad and J.E. Field. The liquid impact resistance of CVD Diamond and other Infrared Materials. *Proc. SPIE*, 3060:169–180, 1997.

P.G. Collins and P. Avouris. Nanotubes for electronics. *Scientific American*, pages 62–69, December 2000.

S.S. Cook. Erosion by water hammer. *Proc. R. Soc. London, Ser. A*, 119: 481–488, 1928.

V.K. Croutch and R.A. Hartley. Adhesion of ice to coatings and the performance of ice release coatings. *J. of Coatings Technology*, 64(815):41–53, 1992.

P.G. de Gennes, F. Brochard-Wyart, and D. Quéré. *Capillarity and wetting phenomena: drops, bubbles, pearls, waves*. Springer, Illustrated edition, 2004. ISBN 0387005927, 9780387005928.

P. de Haller. Untersuchungen uber die durch kaviation hervorgerufenen korrosion. *Schweiz Bauzig*, 101:243, 1933.

K. Donaldson, R. Aitken, L. Tran, V. Stone, R. Duffin, G. Forrest, and A. Alexander. Carbon Nanotubes: A Review of Their Properties in Relation to Pulmonary Toxicology and Workplace Safety. *Toxicological Sciences*, 92(1):5–22, February 2006.

J. Eggers, M.A. Fontelos, C. Josserand, and S. Zaleski. Drop dynamics after impact on a solid wall: Theory and simulations. *Phys. Fluids*, 22(6), 2010. 062101.

M. Endo, M.S. Strano, and P.M. Ajayan. *Carbon nanotubes: Advanced topics in the synthesis, structure, properties and applications*, chapter Potential Applications of Carbon Nanotubes, pages 13–62. Springer, 2008.

O.G. Engel. Waterdrop collisions with solid surfaces. *J. Research National Bureau of Standards*, 54:281–298, 1955.

European Commission. LAYSA Project: Multifunctional LAYERS for SAfer Aircraft Composites Structures, 2008. URL `http://www.laysa.eu/`.

A.G. Evans. Impact Damage Mechanics: Solid Projectiles. In C. M. Preece, editor, *Treatise on materials science and technology*, volume 16. Academic Press, 1979.

A.G. Evans. Impact damage and erosion in infrared materials. In *Emerging optical materials*, pages 99–106, San Diego, CA; United States, 25-26 Aug 1981.

A.G. Evans, Y.M. Ito, and M. Rosenblatt. Impact Damage Threshold in Brittle Materials Impacted by Water Drops. *J Appl Phys*, 51:2473–2482, 1980.

FAA. Advisory circular no 20-73A, Aircraft Ice Protection. 2006.

FAA Federal Aviation Regulations 14 CFR Part 25, Appendix C. FAA. URL `www.faa.gov`.

Federal Aviation Administration. Airplane and Engine Certification Requirements in Supercooled Large Drop, Mixed Phase, and Ice Crystal Icing Conditions. 2010.

T.A. Ferreira and W. Rasband. *The ImageJ User Guide*, 1.45 edition, August 2011.

J.E. Field. ELSI conference: invited lecture: Liquid impact: theory, experiment, applications. *Wear*, 233-235:1–12, 1999.

J.E. Field, C.R. Seward, C.S.J. Pickles, E.J. Coad, and M. Watt. Studies of rain erosion mechanisms in a range of IR-transmitting ceramics - including coated sample. Technical Report SPC-92-4032, University of Cambridge, Cavendish Laboratory, 1994.

S. Fiorito. *Carbon nanotubes: angels or demons?* Pan Stanford Publishing, illustrated edition, 2008. ISBN 9814241016, 9789814241014.

A.C. Fischer-Cripps. *Introduction to contact mechanics*. Springer, 2007. ISBN 0387681876.

R. W. Gent, N. P. Dart, and J. T. Cansdale. Aircraft icing. *Philosophical Transactions: Mathematical, Physical and Engineering Sciences*, 358(1776): 2873–2911, 2000.

R. Gentilman. Preventing Rain Erosion Damage to ZnS and ZnSe Window with a Compliant Interlayer. *Proc. 5th DoD Electromagnetic Windows Symposium, Boulder, Colorado*, pages 203–210, 1993.

C. Gifford. *Weathering and Erosion*. Black Rabbit Books, 2005. ISBN 1583407316.

A.S. Gohardani and O. Gohardani. Ceramic engine considerations for future aerospace propulsion. *Aircraft Engineering and Aerospace Technology*, 84 (2), 2012.

O. Gohardani. Experimental investigation of Rayleigh-Taylor instability using a paramagnetic liquid combination. Master's thesis, University of Arizona, U.S.A., 2008.

O. Gohardani. The influence of erosion and wear on the accretion and adhesion of ice of polymeric composites loaded with nano particles - First Year Progress Report. Technical report, Cranfield University, 2009.

O. Gohardani. The influence of erosion and wear on the accretion and adhesion of ice for nano reinforced polymeric composites used in aeronautics - Second Year Progress Report. Technical report, Cranfield University, 2010.

O. Gohardani. Impact of erosion testing aspects on current and future flight conditions. *Progress in Aerospace Sciences*, 47(4):280–303, 2011.

O. Gohardani and D.W. Hammond. Droplet interaction and dynamic wettability of advanced materials used in aeronautics. In *6th Subrata Chakrabarti International Conference on Fluid Structure Interaction, Orlando, Florida, U.S.A.*, 9-11 May 2011.

O. Gohardani and J.W. Jacobs. Experimental investigation of the Rayleigh-Taylor instability using a paramagnetic liquid combination. In *11th International Workshop on the Physics of Compressible Turbulent Mixing (IWPCTM11), Santa Fe, New Mexico, U.S.A.*, July 13-18 2008.

O. Gohardani, R. Oemke, and J.W. Jacobs. PLIF flow visualization of magnetically stabilized Rayleigh-Taylor instability. In *Bulletin of the American Physical Society, 59th Annual Meeting of the APS Division of Fluid Dynamics,Tampa Bay, Florida, U.S.A.*, November 19-21 2006. BAPS.2006.DFD.LP.7.

O. Gohardani, R. Oemke, and J.W. Jacobs. Experimental study of Rayleigh-Taylor Instability utilizing a paramagnetic liquid combination. In *Bulletin of the American Physical Society, 60th Annual Meeting of the Divison of Fluid Dynamics, Salt Lake City, Utah, U.S.A.*, volume 52, November 18-20 2007. BAPS.2007.DFD.KM.6.

R.C. Gonzalez, R.E. Woods, and S.L. Eddins. *Digital Image Processing Using MATLAB*. Gatesmark Publishing, 2nd edition, 2009. ISBN 9780982085400.

Government Accountability Office. Aviation safety: Improved Planning Could Help FAA Address Challenges Related to Winter Weather Operations. Technical report, United States Government Accountability Office, 2010a. GAO-10-678.

Government Accountability Office. Aviation safety: Preliminary Information on Aircraft Icing and Winter Weather Operations. Technical report, United States Government Accountability Office, 2010b. GAO-10-441T.

Government Accountability Office. Aviation safety: Status of FAA's Actions to Oversee the Safety of Composite Airplanes. Technical report, United States Government Accountability Office, 2011. GAO-11-849.

B. Gurrutxaga Lerma. Refinement and stress analysis of an ice-to-substrate shear fracture test for use in the study of ice shedding on turbine components. Master's thesis, Cranfield University, 2010.

F.G. Hammitt. Liquid Jet and Droplet Impact (Chapter 6). Technical Report UMICH 014456-10-I, University of Michigan, March 24 1977.

F.G. Hammitt, J.B. Hwang, S.A. Barber, and M.K. De. Predictability of prototype machine liquid cavitation and droplet impact erosion from laboratory tests. *Wear*, 46:128–139, 1978.

D.W. Hammond, G. Luxford, and P. Ivey. The Cranfield University Icing Tunnel. In *41st AIAA Aerospace Sciences Meeting & Exhibit, Reno, NV; United States*, 6-9 Jan 2003.

R. Hand, J.E. Field, and D. Townsend. The use of liquid jets to simulate angle drop impact,. *J. Appl. Phys.*, 70:7111–7118, 1991.

D.C. Harris. *Materials for Infrared Windows and Domes*. SPIE - The International Society for Optical Engineering, 1999. ISBN 0-8194-3482-5.

H. Hertz. On the contact of elastic solids. *J. Reine Angew, Math.*, 92:156–171, 1881.

H. Hertz. On hardness. *Ver. Beförderung Gewerbe Fleisses*, 61:410, 1882.

R.W. Hertzberg. *Deformation and fracture mechanics of engineering materials*. Wiley, New York, 1989.

F. J. Heymann. On the shockwave velocity and impact pressure in high-speed liquid-solid impact. *J. Basic Eng., 90*, 90:400–402, 1968.

F. J. Heymann. High-speed impact between a liquid drop and a solid surface. *J. Appl. Phys.*, 40(13):5113–5122, 1969.

F.J. Heymann. A survey of clues to the relation between erosion rate and impact parameters. In *Second Rain Erosion Conference*, volume 2, 1967.

C.W. Hirt and B.D. Nichols. Volume of Fluid (VOF) Method for the Dynamics of Free Boundaries. *Journal of Computational Physics*, 39:201–225, 1981.

G.R. Hoffmann. *High-performance Computing and Networking: Networking and tools*. Springer, 1994. ISBN 3540579818, 9783540579816.

Huntsman Advanced Materials. Araldite LY564 - Aradur 2954, July 2007. URL `www.huntsman.com`.

R.F. Ide. Comparison of Liquid Water Content measurement techniques in an icing wind tunnel. Technical Report NASA/TM1999-209643, NASA, 1999.

S. Ijima and T. Ichihashi. Single-shell carbon nanotubes of 1-nm diameter. *Nature*, 363:603–605, 1993.

D.M. Johnston. Physical and social impacts of past and future volcanic eruptions in New Zealand. Ph.D. thesis, 1997.

J. Jordan, K.I. Jacob, R. Tannenbaum, M.A. Sharaf, and I. Jasiuk. Experimental trends in polymer nanocompositesa review. *Materials Science and Engineering: A*, 393(1-2):1–11, 2005.

C. Josserand. The Dynamics of Drop Impact. *ASME Conf. Proc.*, 689, 2002. doi:10.1115/FEDSM2002-31444.

C.F. Kennedy and J.E. Field. Damage threshold velocities for liquid impact. *J. Mater. Sci.*, 35:5331–5339, 2000.

C.G. Knight, M.V. Swain, and M.M. Chaudhri. Impact of small steel spheres on glass surfaces. *Journal of Material Science*, 12(8):1573–1586, 1977.

A. Krishnan, Y.-H. Liu, P. Cha, R. Woodward, D. Allara, E.A. Vogler, and A Contribution from the Hematology at Biomaterial Interfaces Research Group. An evaluation of methods for contact angle measurement. *Colloids and Surfaces B: Biointerfaces*, 43(2):95–98, 2005.

S. A. Kulinich, S. Farhadi, K. Nose, and X. W. Du. Superhydrophobic surfaces: Are they really ice-repellent? *Langmuir*, 27(1):25–29, 2011.

S.A. Kulinich and M. Farzaneh. Ice adhesion on super-hydrophobic surfaces. *Applied Surface Science*, 255(18):8153–8157, 2009.

G. Kumar and K.N. Prabhu. Review of non-reactive and reactive wetting of liquids on surfaces. *Advances in Celloid and Interface Science*, 133:61–89, June 2007.

C.N.C. Lam, R. Wu, D. Li, M.L. Hair, and A.W. Neumann. Study of the advancing and receding contact angles: liquid sorption as a cause of contact angle hysteresis. *Advances in Colloid and Interface Science*, 96(1-3):169–191, 2002.

C.W. Lam, J.T. James, R. McCluskey, S. Arepalli, and R.L. Hunter. A review of carbon nanotube toxicity and assessment of potential occupational and environmental health risks. *Crit. Rev. Toxicol.*, 36:189–217, 2006.

M. Landy and A. Freiberger. Studies of ice adhesion: I. Adhesion of ice to plastics. *Journal of Colloid and Interface Science*, 25(2):231–244, 1967.

M.B. Lesser. Analytic Solutions of Liquid-Drop Impact Problems. *Proc. R. Soc. Lond. A*, 377(1770):289–308, 1981.

D. Lou. The development production demonstration and analysis of the ice shear rig of the study of engine icing. Master's thesis, Cranfield University, 2009.

G. Luxford. *Experimental and modelling investigation of the deformation, drag and break-up of drizzle droplets subjected to strong aerodynamics forces in relation to SLD aircraft icing*. PhD thesis, Cranfield University, 2005.

J.S. Marshall and W.M. Palmer. The distribution of raindrops with size. *Journal of Meteorology*, 5:165–166, 1948.

J.J. Jr. Mecholsky. Quantitative fractography: An assessment. In V.D. Frechette and J. Varmer, editors, *Ceramic Transactions*, volume 17, 1991.

A.J. Meuler, J.D. Smith, K.K. Varanasi, J.M. Mabry, G.H. McKinley, and R.E. Cohen. Relationships between water wettability and ice adhesion. *ACS Appl Mater Interfaces*, 2(11):3100–10, 2010.

E. Moncholi Piles. Second Year Review of PhD Studies. Technical report, Cranfield University, 2011.

M. Moniruzzaman and K.I. Winey. Polymer Nanocomposites Containing Carbon Nanotubes. *Macromolecules*, 39:5194–5205, 2006.

B.W. Mott. *Micro-Indentation Hardness Testing*. Butterworths Scientific Publication, 1956.

H. Murase and K. Nanishi. On the relationship of thermodynamic properties of polymers with ice adhesion. *Annals of Glaciology*, 6:146–149, 1985.

NanoLab Inc., 2011. URL `www.nano-lab.com`.

I.M. Ogilvy, C.M. Perrott, and J.M. Suitter. On the indentation fracture of cemented carbide part 1 - Survey of operative fracture modes. *Wear*, 43: 239–252, 1977.

S. Palmqvist. *Jernkontorets Ann*, 147:107–10, 1963.

M. Pasandideh-Fard, Y.M. Qiao, S. Chandra, , and J. Mostaghimi. Capillary effects during droplet impact on a solid surface. *Phys Fluids*, 8(3):650–659, 1996.

M.L. Pervier. First Year Review of PhD Studies. Technical report, Cranfield University, 2009.

V.F. Petrenko and S. Peng. Reduction of ice adhesion to metal by using self-assembling monolayers (SAMs). *Canadian Journal of Physics*, 81(1-2): 387–393, 2003.

V.F. Petrenko and S. Qi. Reduction of ice adhesion to stainless steel by ice electrolysis. *J. Appl. Phys.*, 86(5450), 1999.

A. Petzold, C. Stein, S. Nyeki, M. Gysel, E. Weingartner, U. Baltensperger, H. Giebl, R. Hitzenberger, A. Döpelheuer, S. Vrchoticky, H. Puxbaum, M. Johnson, C.D. Hurley, R. Marsh, and C.W. Wilson. Properties of jet engine combustion particles during the PartEmis experiment: Microphysics and chemistry. *Geophys. Res. Lett.*, 30:1719, 2003.

M.K. Politovich. *Encyclopedia of Atmospheric Sciences, Volumes 1-6*. Elsevier, July 2003. ISBN 978-0-12-227090-1.

A.E. Porter, M. Gass, K. Muller, J.N. Skepper, P.A. Midgley, and M. Welland. Direct imaging of single-walled carbon nanotubes in cells. *Nature Nanotechnology*, 2:713–717, 2007.

R. Purvis and F.T. Smith. Large Droplet impact on water layers. In *42nd Aerospace sciences meeting and exhibit conference, Reno, NV, USA*, 2004. AIAA-2004-0414.

R. Purvis and F.T. Smith. Droplet impact on water layers: post-impact analysis and computations. *Phil. Trans. Roy. Soc. A*, 363:1209–1221, 2005.

M. Quero. *Analytical and experimental investigation into the thermal aspects of droplet impingement*. PhD thesis, Cranfied University, March 2006.

M. Quero, D.W. Hammond, Purvis R., and F.T. Smith. Analysis of supercooled water droplet impact on a thin water layer and ice growth. In *44th AIAA Aerospace Sciences Meeting and Exhibit, Reno NV, USA*, number AIAA-2006-466, 9-12 January 2006.

Z. Ralph and L. Hodson. Approaches to Safe Nanotechnology: Managing the Health and Safety Concerns Associated with Engineered Nanomaterials. Technical Report 2009-125, National Institute for Occupational Safety and Health, NIOSH (DHHS), March 2009.

L.E. Raraty and D. Tabor. The adhesion and strength properties of ice. *Proceedings of the Royal Society of London. Series A, Mathematical and Physical Sciences*, 245(1241):184–201, June 1958.

S. Reich, C. Thomsen, and J. Maultzsch. *Carbon nanotubes: basic concepts and physical properties*. Wiley-VCH, 2, illustrated edition, 2004. ISBN 3527403868, 9783527403868.

M. Rein. Phenomena of liquid drop impact on solid and liquid surfaces. *Fluid Dynamics Research*, 12(2):61–93, 1993.

M. C. Rochester and J. H. Brunton. *Influence of Physical Properties of the Liquid on the Erosion of Solids, Erosion, Wear, and Interfaces with Corrosion*, volume ASTM STP 567. American Society for Testing and Materials, 1974.

L.S. Schadler, S.C. Giannaris, and P.M. Ajayan. Load transfer in carbon nanotube epoxy composites. *Appl. Phys. Lett.*, 73(26):3842–3844, 1998.

H. Schlichting and K. Gersten. *Boundary-layer theory*. Springer, 2000. ISBN 3-540-66270-7.

G. Schmitt Jr. *Wear Control Handbook*, chapter Liquid and solid particle impact erosion, pages 231–282. American Society of Mechanical Engineers, 1980.

N. Sclater and N.P. Chironis. *Mechanisms and mechanical devices sourcebook*. McGraw-Hill Professional, 4, illustrated edition, 2007. ISBN 0071467610, 9780071467612.

C.R. Seward, E.J. Coad, C.S.J. Pickles, and J.E. Field. SPIE. *Proc. Window and Dome Technologies and Materials IV*, 2286:285, 1994.

C.R. Seward, C.S.J. Pickles, and J.E. Field. Single- and multiple-impact jet apparatus and results. *Proc. SPIE*, 1326:280–290, 1990.

C.R. Seward, C.S.J. Pickles, R. Marrah, and J.E. Field. SPIE. *Proc. Window and Dome Technologies and Materials III*, 1760, 1992.

R.E. Shalin. *Polymer matrix composites*. Springer, 1995. ISBN 0412613301.

W.N. Jr. Sharpe, editor. *Springer Handbook of Experimental Solid Mechanics*. Springer, 2008. ISBN 978-0-387-26883-5.

H. Shi and J.E. Field. Stress waves propagation in solids under high-speed liquid impact. *Science in China Ser. G Physics, Mechanics & Astronomy*, 47(6):752–766, 2004.

Shimadzu Corporation. Schimadzu Micro Hardness Tester Type M. Instruction's Manual CA227-905J, 1977.

Sonatest Limited. *Sitescan 250 Users Guide*. Sonatest Inc., 2006. Document Number: 147308.

Sonatest PLC. *Sonatest Sitescan 120 User's Manual*, 2000.

M.R. Spiegel, J.J. Schiller, and R. Alu Srinivasan. *Probability and Statistics*. McGraw-Hill, 2009. ISBN 978-0-07-154426-9.

G.S. Springer. *Erosion by liquid impact*. Number 0-470-15108-0. Scripta Publishing Company, 1976.

G.W. Stachowiak and A.W. Batchelor. *Engineering Tribology*. Elsevier Inc., 2006.

J. Steuernagle, K. Roy, and D. Wright. Aircraft icing. Technical report, Air Safety Foundation, 2008.

R. Tadmor. Line Energy and the Relation between Advancing, Receding, and Young Contact Angles. *Langmuir*, 20(18):7659–7664, 2004.

Taylor Hobson Precision. *Surtronic 3+*. Taylor Hobson Limited.

A. Terzis. Experimental evaluation of impact ice strength and design of a shear test rig for use in an icing tunnel. Master's thesis, Cranfield University, 2009.

The MathWorks Inc. *MATLAB® Getting Started Guide*, R2011b edition, 2011. URL `www.mathworks.com`.

Vapormatt. Vapormatt Manual Brochure, 2009.

R.D. Woods. Screening of surface waves in soils. *J Soil Mech*, 97:951–979, 1968.

T. Young. An Essay on the Cohesion of Fluids. *Philosophical Transactions of The Royal Society London*, 95:65–87, 1805.

Y.H. Zhang, D.and Xie. Study on nonlinear coupling wave model for liquid drop-solid impact. *Chinese Journal of Aeronautics*, 15(4):222–227, 2002.

M. Zou, S. Beckford, R. Wei, C. Ellis, G. Hatton, and M.A. Miller. Effects of surface roughness and energy on ice adhesion strength. *Applied Surface Science*, 257(8):3786–3792, 2011.

Appendix A

Density measurements

For each specimen the length L, width W and height H, were measured five times for statistical correctness. Upon completion of all measurements, the following data points were determined: $(L_1, L_2, \ldots, L_5)$, $(W_1, W_2, \ldots, W_5)$, $(H_1, H_2, \ldots, H_5)$ and $(m_1, m_2, \ldots, m_5)$. Based on these, the overall mean value of the each dimension were estimated as shown in Tables A.1−A.8.

S_1 (LY564)

Specimen Subarea, A_1						
No.	L (mm)	W (mm)	H (mm)	V (mm^3)	m (g)	ρ (g $\cdot$ cm^{-3})
1	24.39	15.73	1.744	669.09	0.71	1.0611
2	24.39	15.66	1.712	653.89	0.71	1.0858
3	24.43	15.70	1.735	665.46	0.71	1.0669
4	24.39	15.69	1.719	657.83	0.71	1.0793
5	24.39	15.69	1.724	659.74	0.71	1.0762
	$\bar{L} = 24.40$	$\bar{W} = 15.69$	$\bar{H} = 1.727$	$\bar{V} = 661.2$	$\bar{m} = 0.71$	$\bar{\rho} = 1.0738$
Specimen Subarea, A_2						
No.	L (mm)	W (mm)	H (mm)	V (mm^3)	m (g)	ρ (g $\cdot$ cm^{-3})
1	44.08	15.71	1.752	1213.3	1.29	1.0633
2	44.07	15.73	1.736	1203.4	1.28	1.0636
3	44.07	15.69	1.724	1192.1	1.28	1.0738
4	44.08	15.70	1.752	1212.5	1.29	1.0639
5	44.09	15.76	1.743	1211.1	1.28	1.0569
	$\bar{L} = 44.08$	$\bar{W} = 15.72$	$\bar{H} = 1.741$	$\bar{V} = 1206.5$	$\bar{m} = 1.28$	$\bar{\rho} = 1.0643$
Specimen Subarea, A_3						
No.	L (mm)	W (mm)	H (mm)	V (mm^3)	m (g)	ρ (g $\cdot$ cm^{-3})
1	70.15	55.56	1.512	5893.1	7.07	1.1997
2	70.11	55.95	1.608	6307.6	7.07	1.1209
3	70.16	55.56	1.623	6239.6	7.07	1.1175
4	70.12	55.93	1.591	6239.6	7.07	1.1331
5	70.17	55.58	1.637	6384.4	7.07	1.1058
	$\bar{L} = 70.14$	$\bar{W} = 55.72$	$\bar{H} = 1.594$	$\bar{V} = 6230.2$	$\bar{m} = 7.07$	$\bar{\rho} = 1.1345$
Specimen Subarea, A_4						
No.	L (mm)	W (mm)	H (mm)	V (mm^3)	m (g)	ρ (g $\cdot$ cm^{-3})
1	24.94	15.77	1.752	689.34	0.73	1.0590
2	24.44	15.91	1.752	681.25	0.73	1.0716
3	24.45	15.90	1.741	676.82	0.73	1.0786
4	24.44	15.71	1.752	672.68	0.73	1.0852
5	24.45	16.03	1.748	685.10	0.73	1.0655
	$\bar{L} = 24.55$	$\bar{W} = 15.86$	$\bar{H} = 1.749$	$\bar{V} = 681.06$	$\bar{m} = 0.73$	$\bar{\rho} = 1.0719$
Specimen Subarea, A_5						
No.	L (mm)	W (mm)	H (mm)	V (mm^3)	m (g)	ρ (g $\cdot$ cm^{-3})
1	44.08	15.95	1.723	1211.4	1.31	1.0814
2	44.06	16.00	1.735	1223.1	1.31	1.0710
3	44.05	16.07	1.747	1236.7	1.31	1.0593
4	44.01	16.03	1.726	1217.7	1.31	1.0758
5	44.05	16.06	1.720	1216.8	1.31	1.0766
	$\bar{L} = 44.05$	$\bar{W} = 16.02$	$\bar{H} = 1.730$	$\bar{V} = 1221.1$	$\bar{m} = 1.31$	$\bar{\rho} = 1.0728$

Table A.1. Density measurements on S_1 (LY564)

S_2 (LY564 + 0.5% MWCNT)

Specimen Subarea, A_1						
No.	L (mm)	W (mm)	H (mm)	V (mm^3)	m (g)	ρ (g $\cdot$ cm^{-3})
1	24.94	15.81	3.687	1453.79	1.60	1.1006
2	24.94	15.76	3.784	1487.32	1.61	1.0825
3	24.94	15.78	3.939	1550.21	1.61	1.0386
4	24.94	15.79	3.887	1530.71	1.60	1.0453
5	24.94	15.78	3.853	1516.36	1.61	1.0618
	$\bar{L} = 24.94$	$\bar{W} = 15.78$	$\bar{H} = 3.830$	$\bar{V} = 1507.69$	$\bar{m} = 1.606$	$\bar{\rho} = 1.0652$
Specimen Subarea, A_2						
No.	L (mm)	W (mm)	H (mm)	V (mm^3)	m (g)	ρ (g $\cdot$ cm^{-3})
1	30.41	15.73	3.946	1887.57	2.01	1.06486
2	30.42	15.71	3.709	1772.52	2.00	1.12833
3	30.40	15.72	3.660	1749.07	2.00	1.14346
4	30.36	15.71	3.968	1892.56	2.01	1.06205
5	30.35	15.74	3.884	1855.42	2.01	1.08331
	$\bar{L} = 30.39$	$\bar{W} = 15.72$	$\bar{H} = 3.833$	$\bar{V} = 1831.45$	$\bar{m} = 2.01$	$\bar{\rho} = 1.0953$
Specimen Subarea, A_3						
No.	L (mm)	W (mm)	H (mm)	V (mm^3)	m (g)	ρ (g $\cdot$ cm^{-3})
1	56.71	55.25	3.946	12363.7	13.32	1.07735
2	56.70	55.31	3.794	11898.3	13.32	1.11949
3	56.72	55.28	3.701	11604.4	13.33	1.14870
4	56.71	55.31	3.881	12173.3	13.33	1.09502
5	56.71	55.25	3.980	12470.2	13.32	1.06814
	$\bar{L} = 56.71$	$\bar{W} = 55.28$	$\bar{H} = 3.860$	$\bar{V} = 12102.1$	$\bar{m} = 13.32$	$\bar{\rho} = 1.1010$
Specimen Subarea, A_4						
No.	L (mm)	W (mm)	H (mm)	V (mm^3)	m (g)	ρ (g $\cdot$ cm^{-3})
1	24.91	15.66	3.274	1277.16	1.42	1.11184
2	24.91	15.74	3.704	1452.28	1.42	0.97777
3	24.92	15.70	3.192	1248.85	1.42	1.13705
4	24.90	15.67	3.180	1240.78	1.42	1.14444
5	24.92	15.66	3.449	1345.96	1.42	1.05501
	$\bar{L} = 24.91$	$\bar{W} = 15.69$	$\bar{H} = 3.360$	$\bar{V} = 1312.91$	$\bar{m} = 1.42$	$\bar{\rho} = 1.0816$
Specimen Subarea, A_5						
No.	L (mm)	W (mm)	H (mm)	V (mm^3)	m (g)	ρ (g $\cdot$ cm^{-3})
1	30.25	15.63	4.103	1939.93	1.96	1.01035
2	30.26	15.64	3.894	1842.90	1.96	1.06354
3	30.25	15.69	3.887	1844.86	1.97	1.06783
4	30.26	15.63	3.989	1886.65	1.96	1.03888
5	30.27	15.64	4.011	1898.90	1.96	1.03218
	$\bar{L} = 30.26$	$\bar{W} = 15.65$	$\bar{H} = 3.977$	$\bar{V} = 1882.68$	$\bar{m} = 1.96$	$\bar{\rho} = 1.0421$

Table A.2. Density measurements on S_2 (LY564 +0.5% MWCNT)

S_7 (Araldite DBF)

Specimen Subarea, A_1						
No.	L (mm)	W (mm)	H (mm)	V (mm^3)	m (g)	ρ (g $\cdot$ cm^{-3})
1	24.30	15.51	8.157	3074.3	3.86	1.2556
2	24.34	15.52	8.332	3147.5	3.86	1.2264
3	24.29	15.51	7.988	3009.3	3.86	1.2827
4	24.32	15.52	8.177	3086.4	3.85	1.2474
5	24.30	15.52	8.105	3056.7	3.87	1.2661
	$\bar{L} = 24.31$	$\bar{W} = 15.52$	$\bar{H} = 8.152$	$\bar{V} = 3074.8$	$\bar{m} = 3.86$	$\bar{\rho} = 1.2554$
Specimen Subarea, A_2						
No.	L (mm)	W (mm)	H (mm)	V (mm^3)	m (g)	ρ (g $\cdot$ cm^{-3})
1	24.85	15.48	7.901	3039.3	3.80	1.2503
2	24.87	15.48	7.937	3055.6	3.81	1.2469
3	24.86	15.5	7.841	3021.4	3.81	1.2610
4	24.87	15.48	8.741	3365.2	3.81	1.1322
5	24.95	15.49	7.806	3016.8	3.81	1.2629
	$\bar{L} = 24.88$	$\bar{W} = 15.49$	$\bar{H} = 8.045$	$\bar{V} = 3099.7$	$\bar{m} = 3.808$	$\bar{\rho} = 1.2285$
Specimen Subarea, A_3						
No.	L (mm)	W (mm)	H (mm)	V (mm^3)	m (g)	ρ (g $\cdot$ cm^{-3})
1	50.72	35.97	7.496	13675.7	17.89	1.3082
2	50.68	35.83	7.712	14003.9	17.89	1.2775
3	50.77	35.84	8.353	15199.1	17.89	1.1770
4	50.69	35.88	8.038	14619.2	17.89	1.2237
5	50.77	35.84	7.754	14109.2	17.89	1.2680
	$\bar{L} = 50.73$	$\bar{W} = 35.87$	$\bar{H} = 7.871$	$\bar{V} = 14321.7$	$\bar{m} = 17.89$	$\bar{\rho} = 1.2492$
Specimen Subarea, A_4						
No.	L (mm)	W (mm)	H (mm)	V (mm^3)	m (g)	ρ (g $\cdot$ cm^{-3})
1	24.76	15.52	8.473	3256.0	3.96	1.2162
2	24.77	15.52	8.187	3147.3	3.96	1.2582
3	24.76	15.53	8.467	3255.8	3.97	1.2194
4	24.80	15.53	8.247	3176.3	3.96	1.2467
5	24.75	15.52	8.313	3193.2	3.97	1.2433
	$\bar{L} = 24.77$	$\bar{W} = 15.52$	$\bar{H} = 8.33$	$\bar{V} = 3205.7$	$\bar{m} = 3.96$	$\bar{\rho} = 1.2365$
Specimen Subarea, A_5						
No.	L (mm)	W (mm)	H (mm)	V (mm^3)	m (g)	ρ (g $\cdot$ cm^{-3})
1	24.33	15.53	8.473	3201.1	4.04	1.2162
2	24.34	15.52	9.121	3445.5	4.04	1.1725
3	24.37	15.54	8.477	3210.3	4.04	1.2584
4	24.33	15.53	8.577	3240.8	4.04	1.2466
5	24.33	15.53	8.522	3220.0	4.04	1.2547
	$\bar{L} = 24.34$	$\bar{W} = 15.53$	$\bar{H} = 8.63$	$\bar{V} = 3263.6$	$\bar{m} = 4.04$	$\bar{\rho} = 1.2547$

Table A.3. Density measurements on S_7 (Araldite DBF)

S_3 (32_MINAS1_06)

Specimen Subarea, A_1						
No.	L (mm)	W (mm)	H (mm)	V (mm^3)	m (g)	ρ (g $\cdot$ cm^{-3})
1	22.16	15.64	5.406	1873.6	2.33	1.24358
2	22.16	15.66	5.221	1811.8	2.34	1.29152
3	22.13	15.65	5.413	1874.7	2.33	1.24286
4	22.10	15.66	5.484	1897.9	2.33	1.22765
5	22.16	15.58	5.382	1858.2	2.33	1.25393
	$\bar{L} = 22.14$	$\bar{W} = 15.64$	$\bar{H} = 5.381$	$\bar{V} = 1863.3$	$\bar{m} = 1.2516$	$\bar{\rho} = 1.2365$
Specimen Subarea, A_2						
No.	L (mm)	W (mm)	H (mm)	V (mm^3)	m (g)	ρ (g $\cdot$ cm^{-3})
1	22.11	15.60	5.201	1793.9	2.24	1.24867
2	22.10	15.60	5.204	1794.1	2.24	1.24852
3	22.10	15.63	5.356	1850.1	2.23	1.20535
4	22.12	15.48	5.076	1738.1	2.24	1.28875
5	22.12	15.66	5.260	1822.1	2.24	1.22938
	$\bar{L} = 22.11$	$\bar{W} = 15.59$	$\bar{H} = 3.662$	$\bar{V} = 1799.6$	$\bar{m} = 2.24$	$\bar{\rho} = 1.24364$
Specimen Subarea, A_3						
No.	L (mm)	W (mm)	H (mm)	V (mm^3)	m (g)	ρ (g $\cdot$ cm^{-3})
1	49.54	22.20	5.722	6293.0	7.88	1.25219
2	49.56	22.19	5.511	6060.7	7.87	1.29854
3	49.55	22.21	5.514	6068.2	7.87	1.29693
4	49.55	22.16	5.774	6340.0	7.87	1.24132
5	49.77	22.22	5.640	6237.2	7.87	1.26178
	$\bar{L} = 49.594$	$\bar{W} = 56.58$	$\bar{H} = 4.920$	$\bar{V} = 6199.9$	$\bar{m} = 7.87$	$\bar{\rho} = 1.2697$
Specimen Subarea, A_4						
No.	L (mm)	W (mm)	H (mm)	V (mm^3)	m (g)	ρ (g $\cdot$ cm^{-3})
1	22.41	15.53	5.971	2078.1	2.54	1.22229
2	22.30	15.52	5.940	2055.8	2.57	1.25012
3	22.42	15.49	5.784	2008.7	2.56	1.27446
4	22.25	15.51	6.005	2072.3	2.56	1.23534
5	22.31	15.50	5.935	2052.4	2.56	1.24735
	$\bar{L} = 22.34$	$\bar{W} = 15.51$	$\bar{H} = 5.927$	$\bar{V} = 2053.5$	$\bar{m} = 2.56$	$\bar{\rho} = 1.2457$

Table A.4. Density measurements on S_3 (32_MINAS1_06)

S_5 (32_MINAS1_07)

Specimen Subarea, A_1						
No.	L (mm)	W (mm)	H (mm)	V (mm^3)	m (g)	ρ (g $\cdot$ cm^{-3})
1	24.92	15.50	3.303	1275.8	1.63	1.27761
2	24.92	15.60	3.267	1270.1	1.62	1.27554
3	24.92	15.49	3.057	1180.0	1.62	1.37284
4	24.92	15.56	4.153	1610.4	1.62	1.00599
5	24.92	15.51	3.187	1231.8	1.63	1.32326
	$\bar{L} = 24.92$	$\bar{W} = 15.53$	$\bar{H} = 3.393$	$\bar{V} = 1995.0$	$\bar{m} = 1.62$	$\bar{\rho} = 1.2365$
Specimen Subarea, A_2						
No.	L (mm)	W (mm)	H (mm)	V (mm^3)	m (g)	ρ (g $\cdot$ cm^{-3})
1	30.36	15.43	3.535	1656.0	2.14	1.29228
2	30.35	15.44	4.372	2048.7	2.13	1.03967
3	30.30	15.41	3.606	1683.7	2.14	1.27099
4	30.30	15.44	3.451	1614.5	2.14	1.32550
5	30.31	15.42	3.346	1563.9	2.14	1.36841
	$\bar{L} = 30.32$	$\bar{W} = 15.43$	$\bar{H} = 3.662$	$\bar{V} = 1713.2$	$\bar{m} = 2.14$	$\bar{\rho} = 1.2479$
Specimen Subarea, A_3						
No.	L (mm)	W (mm)	H (mm)	V (mm^3)	m (g)	ρ (g $\cdot$ cm^{-3})
1	90.51	56.48	4.877	24931.2	31.53	1.26468
2	90.76	56.62	3.685	18936.6	31.53	1.66503
3	90.55	56.60	4.311	22094.4	31.52	1.42660
4	90.64	56.58	5.835	29924.3	31.52	1.05333
5	90.53	56.62	5.892	30201.3	31.52	1.04366
	$\bar{L} = 90.60$	$\bar{W} = 56.58$	$\bar{H} = 4.920$	$\bar{V} = 25220.1$	$\bar{m} = 31.52$	$\bar{\rho} = 1.2500$
Specimen Subarea, A_4						
No.	L (mm)	W (mm)	H (mm)	V (mm^3)	m (g)	ρ (g $\cdot$ cm^{-3})
1	24.81	15.40	6.445	2462.47	3.01	1.22235
2	24.71	15.60	6.394	2464.73	3.00	1.21717
3	24.73	15.34	6.517	2472.28	3.01	1.21750
4	24.71	15.33	6.512	2466.77	3.01	1.22022
5	24.72	15.49	6.472	2478.21	3.01	1.21459
	$\bar{L} = 24.74$	$\bar{W} = 15.43$	$\bar{H} = 6.468$	$\bar{V} = 2099.2$	$\bar{m} = 3.01$	$\bar{\rho} = 1.21831$
Specimen Subarea, A_5						
No.	L (mm)	W (mm)	H (mm)	V (mm^3)	m (g)	ρ (g $\cdot$ cm^{-3})
1	30.26	15.37	6.158	2864.06	3.62	1.26394
2	30.32	15.43	6.239	2918.84	3.62	1.24022
3	30.35	15.35	6.390	2976.93	3.63	1.21938
4	30.39	15.40	6.145	2875.90	3.63	1.26221
5	30.36	15.47	6.262	2941.07	3.63	1.23425
	$\bar{L} = 30.34$	$\bar{W} = 15.40$	$\bar{H} = 6.239$	$\bar{V} = 2915.36$	$\bar{m} = 3.63$	$\bar{\rho} = 1.24376$

Table A.5. Density measurements on S_5 (32_MINAS1_07)

S_4 (32_A05_CANBIO1_06)

Specimen Subarea, A_1						
No.	L (mm)	W (mm)	H (mm)	V (mm^3)	m (g)	ρ (g $\cdot$ cm^{-3})
1	22.27	15.57	6.326	2193.5	2.77	1.26282
2	22.25	15.56	6.328	2190.8	2.76	1.25980
3	22.25	15.57	6.257	2167.6	2.76	1.27328
4	22.25	15.38	6.336	2168.2	2.76	1.27294
5	22.25	15.57	6.312	2186.7	2.76	1.26219
	$\bar{L} = 22.25$	$\bar{W} = 15.53$	$\bar{H} = 6.312$	$\bar{V} = 2181.4$	$\bar{m} = 2.76$	$\bar{\rho} = 1.2662$
Specimen Subarea, A_2						
No.	L (mm)	W (mm)	H (mm)	V (mm^3)	m (g)	ρ (g $\cdot$ cm^{-3})
1	22.27	15.41	6.219	2134.2	2.69	1.26040
2	22.28	15.55	6.154	2132.1	2.70	1.26637
3	22.27	15.52	6.129	2118.4	2.70	1.27457
4	22.28	15.57	6.208	2153.6	2.69	1.24910
5	22.25	15.57	6.185	2142.7	2.70	1.26010
	$\bar{L} = 22.27$	$\bar{W} = 15.52$	$\bar{H} = 6.179$	$\bar{V} = 2136.2$	$\bar{m} = 2.70$	$\bar{\rho} = 1.2621$
Specimen Subarea, A_3						
No.	L (mm)	W (mm)	H (mm)	V (mm^3)	m (g)	ρ (g $\cdot$ cm^{-3})
1	49.52	22.21	6.136	6748.6	8.63	1.27878
2	49.50	22.19	6.320	6941.9	8.63	1.24317
3	49.51	22.23	6.221	6846.9	8.63	1.26043
4	49.50	22.20	6.297	6919.8	8.63	1.24715
5	49.51	22.25	6.048	6662.5	8.63	1.29532
	$\bar{L} = 49.594$	$\bar{W} = 22.22$	$\bar{H} = 6.204$	$\bar{V} = 6824.0$	$\bar{m} = 8.63$	$\bar{\rho} = 1.2647$
Specimen Subarea, A_4						
No.	L (mm)	W (mm)	H (mm)	V (mm^3)	m (g)	ρ (g $\cdot$ cm^{-3})
1	22.18	15.59	5.862	2027.0	2.55	1.25802
2	22.19	15.61	6.005	2080.1	2.55	1.22593
3	22.18	15.61	5.812	2012.3	2.56	1.27218
4	22.19	15.63	5.958	2066.4	2.55	1.23402
5	22.22	15.62	5.928	2057.5	2.56	1.24425
	$\bar{L} = 22.19$	$\bar{W} = 15.61$	$\bar{H} = 5.913$	$\bar{V} = 2048.6$	$\bar{m} = 2.55$	$\bar{\rho} = 1.24670$

Table A.6. Density measurements on S_4 (32_A05_CANBIO1_06)

S_6 (32_A05_CANBIO1_07)

Specimen Subarea, A_1						
No.	L (mm)	W (mm)	H (mm)	V (mm^3)	m (g)	ρ (g $\cdot$ cm^{-3})
1	24.89	15.54	5.165	1997.8	2.56	1.2814
2	24.90	15.61	5.125	1992.0	2.54	1.2751
3	24.89	15.58	5.182	2009.5	2.54	1.2640
4	24.89	15.63	5.108	1987.5	2.55	1.2832
5	24.90	15.55	5.136	1988.6	2.54	1.2773
	$\bar{L} = 24.89$	$\bar{W} = 15.58$	$\bar{H} = 5.143$	$\bar{V} = 1995.0$	$\bar{m} = 2.55$	$\bar{\rho} = 1.2762$
Specimen Subarea, A_2						
No.	L (mm)	W (mm)	H (mm)	V (mm^3)	m (g)	ρ (g $\cdot$ cm^{-3})
1	30.61	15.58	5.059	2412.7	3.03	1.2559
2	30.63	15.54	4.981	2370.9	3.03	1.2780
3	30.57	15.57	4.889	2327.0	3.02	1.2978
4	30.58	15.58	5.072	2416.5	3.03	1.2539
5	30.64	15.55	5.036	2399.4	3.03	1.2628
	$\bar{L} = 30.61$	$\bar{W} = 15.56$	$\bar{H} = 5.007$	$\bar{V} = 2385.3$	$\bar{m} = 3.03$	$\bar{\rho} = 1.2695$
Specimen Subarea, A_3						
No.	L (mm)	W (mm)	H (mm)	V (mm^3)	m (g)	ρ (g $\cdot$ cm^{-3})
1	85.17	56.86	5.401	26155.8	33.34	1.2747
2	85.17	56.87	5.097	24687.9	33.34	1.3505
3	85.17	56.89	5.181	25103.6	33.34	1.3281
4	85.18	56.88	5.261	25489.8	33.34	1.3080
5	85.19	56.86	5.321	25774.4	33.34	1.2935
	$\bar{L} = 85.18$	$\bar{W} = 56.87$	$\bar{H} = 5.252$	$\bar{V} = 25442.3$	$\bar{m} = 33.34$	$\bar{\rho} = 1.3104$
Specimen Subarea, A_4						
No.	L (mm)	W (mm)	H (mm)	V (mm^3)	m (g)	ρ (g $\cdot$ cm^{-3})
1	24.93	15.68	5.351	2091.7	2.65	1.2669
2	24.95	15.65	5.417	2115.2	2.65	1.2529
3	24.94	15.68	5.275	2062.8	2.64	1.2798
4	24.91	15.66	5.435	2120.1	2.64	1.2452
5	24.91	15.62	5.412	2105.8	2.65	1.2584
	$\bar{L} = 24.93$	$\bar{W} = 15.57$	$\bar{H} = 5.378$	$\bar{V} = 2099.2$	$\bar{m} = 2.646$	$\bar{\rho} = 1.2605$
Specimen Subarea, A_5						
No.	L (mm)	W (mm)	H (mm)	V (mm^3)	m (g)	ρ (g $\cdot$ cm^{-3})
1	30.58	15.65	5.417	2592.5	3.34	1.2884
2	30.58	15.62	5.452	2604.2	3.33	1.2787
3	30.59	15.54	5.432	2597.2	3.33	1.2822
4	30.59	15.53	5.476	2621.5	3.33	1.2702
5	30.59	15.53	5.432	2602.1	3.34	1.2836
	$\bar{L} = 30.59$	$\bar{W} = 15.64$	$\bar{H} = 5.442$	$\bar{V} = 2603.5$	$\bar{m} = 3.33$	$\bar{\rho} = 1.2806$

Table A.7. Density measurements on S_6 (32_A05_CANBIO1_07)

.

S_8 (SW404 + XB5173)

Specimen Subarea, A_1						
No.	L (mm)	W (mm)	H (mm)	V (mm^3)	m (g)	ρ (g $\cdot$ cm^{-3})
1	25.12	15.03	4.323	1632.2	2.98	1.8258
2	25.12	15.03	4.299	1623.1	2.98	1.8360
3	25.12	15.06	4.320	1634.3	2.98	1.8234
4	25.12	15.03	4.337	1637.5	2.98	1.8199
5	25.12	15.03	4.314	1628.8	2.98	1.8296
	$\bar{L} = 25.12$	$\bar{W} = 15.04$	$\bar{H} = 4.319$	$\bar{V} = 1631.2$	$\bar{m} = 2.98$	$\bar{\rho} = 1.8296$
Specimen Subarea, A_2						
No.	L (mm)	W (mm)	H (mm)	V (mm^3)	m (g)	ρ (g $\cdot$ cm^{-3})
1	25.12	15.53	4.346	1695.4	3.08	1.8166
2	25.12	15.54	4.337	1693.0	3.09	1.8252
3	25.13	15.53	4.354	1699.2	3.09	1.8185
4	25.12	15.53	4.362	1701.7	3.09	1.8159
5	25.13	15.53	4.378	1708.6	3.08	1.8027
	$\bar{L} = 25.12$	$\bar{W} = 15.53$	$\bar{H} = 4.355$	$\bar{V} = 1699.6$	$\bar{m} = 3.09$	$\bar{\rho} = 1.8157$
Specimen Subarea, A_3						
No.	L (mm)	W (mm)	H (mm)	V (mm^3)	m (g)	ρ (g $\cdot$ cm^{-3})
1	47.41	31.56	4.367	6534.2	11.34	1.7355
2	46.64	31.60	4.382	6458.3	11.34	1.7559
3	46.80	31.57	4.382	6537.8	11.34	1.7345
4	47.41	31.73	4.440	6679.2	11.35	1.6993
5	46.94	31.63	4.410	6547.6	11.36	1.7350
	$\bar{L} = 47.04$	$\bar{W} = 31.62$	$\bar{H} = 4.405$	$\bar{V} = 6551.3$	$\bar{m} = 11.35$	$\bar{\rho} = 1.7319$
Specimen Subarea, A_4						
No.	L (mm)	W (mm)	H (mm)	V (mm^3)	m (g)	ρ (g $\cdot$ cm^{-3})
1	80.06	10.10	4.381	3542.5	6.45	1.8208
2	80.05	10.12	4.376	3545.0	6.45	1.8195
3	80.04	10.10	4.344	3511.7	6.45	1.8367
4	80.05	10.12	4.325	3503.7	6.45	1.8409
5	80.09	10.10	4.297	3475.9	6.45	1.8556
	$\bar{L} = 80.06$	$\bar{W} = 10.11$	$\bar{H} = 4.345$	$\bar{V} = 3515.8$	$\bar{m} = 6.45$	$\bar{\rho} = 1.8346$
Specimen Subarea, A_5						
No.	L (mm)	W (mm)	H (mm)	V (mm^3)	m (g)	ρ (g $\cdot$ cm^{-3})
1	80.07	10.10	4.412	3568.0	6.47	1.8133
2	80.06	10.12	4.401	3565.7	6.47	1.8145
3	80.06	10.10	4.371	3534.4	6.48	1.8334
4	80.05	10.11	4.357	3526.1	6.47	1.8349
5	80.06	10.1	4.316	3489.9	6.46	1.8510
	$\bar{L} = 80.06$	$\bar{W} = 10.11$	$\bar{H} = 4.371$	$\bar{V} = 3536.8$	$\bar{m} = 6.47$	$\bar{\rho} = 1.8293$

Table A.8. Density measurements on S_8 (SW404 + XB5173)

Appendix B

Impact site coordinates

The following pages show the impact site locations, speeds and number of impacts, as well as the result from the impacts. The impact site locations are given by (x, y) [mm,mm], the speed of MIJA, (v_{MIJA}) [m/s] and the equivalent speed of a 2 mm droplet $(v_{\widehat{D}})$ [m/s]. Damage is indicated by (†) and no damage by $(-)$. Further, the following notations have been utilized for incipient $(\oplus)$, gross crack $(\otimes)$ and punctured through hole $(\odot)$.

S_1(LY564)

(x_i, y_i) [mm,mm]	v_{MIJA} [m/s]	$v_{\widehat{D}}$ [m/s]	N_i	Damage	Notation
$(10, 08)$	108	166	1	–	
$(50, 08)$	342	428	1	–	
$(50, 18)$	342	428	8	†	$\otimes$
$(10, 18)$	108	166	10	–	
$(10, 28)$	108	166	100	–	$\oplus$
$(10, 38)$	108	166	300	†	
$(30, 08)$	216	300	1	–	
$(30, 18)$	216	300	10	–	
$(60, 08)$	396	476	1	–	
$(60, 18)$	396	476	1	†	$\otimes$
$(20, 08)$	164	238	1	–	
$(20, 18)$	164	238	10	–	
$(20, 28)$	164	238	100	†	
$(40, 08)$	278	366	1	–	
$(40, 18)$	278	366	10	†	
$(50, 28)$	342	428	3	†	$\otimes$
$(40, 28)$	278	366	3	–	
$(60, 28)$	396	476	2	–	
$(30, 28)$	216	300	30	†	
$(20, 38)$	164	238	30	–	
$(10, 48)$	61	99	100	–	
$(20, 48)$	61	99	300	–	
$(10, 08)$	408	486	1	†	
$(15, 48)$	400	479	3	†	
$(15, 43)$	375	458	1	–	
$(25, 43)$	375	458	1	–	
$(35, 43)$	375	458	2	–	
$(15, 38)$	340	426	2	–	
$(25, 38)$	340	426	5	–	
$(15, 33)$	310	398	1	–	
$(25, 33)$	310	398	2	–	
$(35, 33)$	310	398	3	–	
$(45, 33)$	310	398	5	–	
$(55, 33)$	310	398	10	†	$\oplus$

S_1 (LY564)

(x_i, y_i) [mm,mm]	v_{MIJA} [m/s]	$v_{\widehat{D}}$ [m/s]	N_i	Damage	Notation
$(15, 28)$	280	368	2	–	
$(25, 28)$	280	368	5	–	
$(35, 28)$	280	368	20	†	
$(15, 23)$	250	337	1	–	
$(25, 23)$	250	337	2	–	
$(35, 23)$	250	337	3	–	
$(45, 23)$	250	337	5	–	
$(55, 23)$	250	337	10	†	
$(65, 23)$	250	337	20	†	
$(05, 23)$	250	337	30	†	$\odot$
$(15, 18)$	200	281	3	–	
$(25, 18)$	200	281	5	–	
$(35, 18)$	200	281	20	–	
$(45, 18)$	200	281	50	†	
$(15, 13)$	160	233	20	–	
$(25, 13)$	160	233	50	†	
$(15, 08)$	108	166	20	–	
$(25, 08)$	108	166	30	–	
$(35, 08)$	108	166	50	†	

Table B.1. Impact site locations (x, y), speed of MIJA (v_{MIJA}), equivalent speed of a 2 mm droplet ($v_{\hat{D}}$). Damage is indicated by (†) and no damage by (−). For the notation part: Incipient is denoted by ($\oplus$), gross crack by ($\otimes$) and punctured through hole by ($\odot$).

S_2 (LY564 + 0.5% MWCNT)

(x_i, y_i) [mm,mm]	v_{MIJA} [m/s]	$v_{\widehat{D}}$ [m/s]	N_i	Damage	Notation
(08, 08)	108	166	1	–	
(08, 18)	108	166	10	–	
(08, 28)	108	166	100	†	
(08, 38)	108	166	300	†	
(18, 08)	176	253	1	–	
(18, 18)	176	253	10	–	
(18, 28)	176	253	30	†	
(18, 38)	176	253	100	†	
(28, 08)	251	338	1	–	
(28, 18)	251	338	5	–	
(28, 28)	251	338	10	–	$\oplus$
(28, 38)	251	338	30	†	
(38, 08)	323	410	1	–	
(38, 18)	323	410	2	–	
(38, 28)	323	410	5	–	
(38, 38)	323	410	10	†	
(48, 08)	408	486	1	†	
(48, 18)	408	486	2	†	
(48, 28)	408	486	3	†	
(48, 38)	408	486	5	†	
(13, 23)	350	435	5	†	
(13, 18)	350	435	3	–	
(13, 13)	350	435	2	–	
(13, 08)	350	435	1	–	
(33, 23)	370	453	5	†	
(33, 13)	370	453	2	†	
(33, 08)	370	453	1	–	
(23, 23)	360	444	5	†	
(23, 18)	360	444	3	†	
(23, 13)	360	444	2	–	
(23, 08)	360	444	1	–	
(43, 23)	380	462	5	†	
(43, 18)	380	462	3	†	
(43, 13)	380	462	2	†	

S_2 (LY564 + 0.5% MWCNT)

(x_i, y_i) [mm,mm]	v_{MIJA} [m/s]	$v_{\widehat{D}}$ [m/s]	N_i	Damage	Notation
$(43, 08)$	380	462	1	–	
$(13, 42)$	390	471	5	†	
$(13, 38)$	390	471	3	–	
$(13, 33)$	390	471	2	–	
$(13, 28)$	390	471	1	–	
$(23, 42)$	400	479	5	†	
$(23, 38)$	400	479	3	†	
$(23, 33)$	400	479	2	†	
$(23, 28)$	400	479	1	–	
$(08, 48)$	108	166	30	–	
$(18, 48)$	61	99	100	–	
$(28, 48)$	61	99	300	–	
$(33, 28)$	275	363	2	–	
$(33, 33)$	275	363	3	†	
$(33, 38)$	275	363	5	–	
$(33, 43)$	275	363	10	†	
$(43, 28)$	210	293	2	–	
$(43, 33)$	210	293	3	–	
$(43, 38)$	210	293	5	–	
$(43, 43)$	210	293	10	†	
$(08, 48)$	140	208	20	†	
$(13, 48)$	140	208	30	†	
$(18, 48)$	140	208	50	†	
$(23, 48)$	140	208	100	†	
$(28, 48)$	140	208	10	–	
$(33, 48)$	175	252	20	†	$\oplus$
$(38, 48)$	210	293	20	†	$\oplus$
$(43, 48)$	210	293	5	†	$\oplus$

Table B.2. Impact site locations (x, y), speed of MIJA (v_{MIJA}), equivalent speed of a 2 mm droplet ($v_{\widehat{D}}$). Damage is indicated by (†) and no damage by (−). For the notation part: Incipient is denoted by ($\oplus$), gross crack by ($\otimes$) and punctured through hole by ($\odot$).

S_5 (32_MINAS1_07)

(x_i, y_i) [mm,mm]	v_{MIJA} [m/s]	$v_{\widehat{D}}$ [m/s]	N_i	Damage	Notation
$(20, 08)$	108	166	1	–	
$(20, 18)$	108	166	10	–	
$(20, 28)$	108	166	100	†	$\oplus$
$(20, 38)$	108	166	300	†	
$(60, 08)$	296	384	1	–	
$(60, 18)$	296	384	2	†	
$(60, 28)$	296	384	5	†	
$(60, 38)$	296	384	10	†	
$(30, 08)$	150	221	1	–	
$(30, 18)$	150	221	10	–	
$(30, 28)$	150	221	20	†	
$(30, 38)$	150	221	50	†	
$(30, 48)$	150	221	100	†	
$(40, 08)$	200	281	1	–	
$(40, 18)$	200	281	2	–	$\oplus$
$(40, 38)$	200	281	10	†	
$(40, 48)$	200	281	20	†	
$(50, 08)$	251	338	1	–	
$(50, 18)$	251	338	2	–	
$(50, 28)$	251	338	5	†	
$(50, 38)$	251	338	10	†	
$(10, 08)$	342	428	1	–	
$(10, 18)$	342	428	1	–	
$(10, 28)$	342	428	2	†	
$(10, 38)$	342	428	2	†	
$(10, 48)$	342	428	3	†	
$(15, 08)$	408	486	3	†	
$(15, 18)$	408	486	2	†	
$(15, 28)$	408	486	2	†	
$(15, 38)$	408	486	1	–	
$(15, 48)$	408	486	1	–	
$(25, 08)$	108	166	20	–	
$(25, 18)$	108	166	50	†	
$(25, 28)$	61	99	50	–	

S_5 (32_MINAS1_07)

(x_i, y_i) [mm,mm]	v_{MIJA} [m/s]	$v_{\widehat{D}}$ [m/s]	N_i	Damage	Notation
$(25, 38)$	61	99	100	–	
$(25, 48)$	61	99	300	–	
$(35, 13)$	350	435	1	–	
$(35, 18)$	360	444	1	–	
$(25, 28)$	370	453	1	–	
$(35, 38)$	380	462	1	†	$\oplus$
$(35, 48)$	390	471	1	–	
$(45, 13)$	350	435	1	–	
$(45, 18)$	360	444	1	–	
$(45, 28)$	370	453	1	–	
$(45, 38)$	380	462	1	†	$\oplus$
$(45, 48)$	390	471	1	†	

Table B.3. Impact site locations (x, y), speed of MIJA, (v_{MIJA}), equivalent speed of a 2 mm droplet $(v_{\hat{D}})$. Damage is indicated by (†) and no damage by $(-)$. For the notation part: Incipient is denoted by $(\oplus)$, gross crack by $(\otimes)$ and punctured through hole by $(\odot)$.

S_6 (32_A05_CANBIO1_07)

(x_i, y_i) [mm,mm]	v_{MIJA} [m/s]	$v_{\widehat{D}}$ [m/s]	N_i	Damage	Notation
$(10, 10)$	61	99	50	–	
$(10, 15)$	61	99	100	–	
$(10, 20)$	61	99	300	–	
$(15, 10)$	108	166	10	–	
$(15, 15)$	108	166	20	–	
$(15, 20)$	108	166	50	–	
$(15, 25)$	108	166	100	†	
$(15, 30)$	108	166	300	†	
$(20, 10)$	150	221	10	–	$\oplus$
$(20, 15)$	150	221	20	†	
$(20, 20)$	150	221	50	†	
$(20, 25)$	150	221	100	†	
$(20, 10)$	200	281	1	–	
$(25, 15)$	200	281	2	–	
$(25, 20)$	200	281	5	–	
$(25, 25)$	200	281	10	–	$\oplus$
$(25, 30)$	200	281	20	†	
$(30, 10)$	252	339	1	–	
$(30, 15)$	252	339	2	–	
$(30, 20)$	252	339	5	†	
$(30, 25)$	252	339	10	†	
$(35, 10)$	296	384	1	–	
$(20, 15)$	296	384	2	–	
$(30, 20)$	296	384	5	–	
$(30, 25)$	296	384	10	†	
$(40, 10)$	350	435	1	–	
$(40, 15)$	350	435	2	–	$\oplus$
$(40, 20)$	350	435	3	–	
$(40, 25)$	350	435	5	†	
$(45, 10)$	360	444	1	†	
$(45, 15)$	360	444	2	–	
$(45, 20)$	360	444	3	†	
$(45, 25)$	360	444	5	†	
$(50, 10)$	380	462	1	–	

S_6 (32_A05_CANBIO1_07)

(x_i, y_i) [mm,mm]	v_{MIJA} [m/s]	$v_{\widehat{D}}$ [m/s]	N_i	Damage	Notation
$(50, 15)$	380	462	2	†	
$(15, 20)$	380	462	3	†	
$(15, 25)$	380	462	5	†	
$(55, 10)$	396	476	1	−	
$(55, 15)$	396	476	2	†	
$(55, 20)$	396	476	3	−	
$(60, 10)$	396	476	1	−	
$(60, 15)$	396	476	2	†	
$(60, 20)$	396	476	3	†	
$(70, 15)$	325	412	1	−	
$(70, 20)$	325	412	2	−	
$(70, 25)$	325	412	3	−	
$(70, 30)$	325	412	5	†	
$(70, 35)$	325	412	10	†	

Table B.4. Impact site locations (x, y), speed of MIJA (v_{MIJA}), equivalent speed of a 2 mm droplet ($v_{\widehat{D}}$). Damage is indicated by (†) and no damage by (−). For the notation part: Incipient is denoted by ($\oplus$), gross crack by ($\otimes$) and punctured through hole by ($\odot$).

S_8 (SW404+XB5173)

(x_i, y_i) [mm,mm]	v_{MIJA} [m/s]	$v_{\widehat{D}}$ [m/s]	N_i	Damage	Notation
$(05, 05)$	296	384	1	–	
$(05, 10)$	296	384	2	–	
$(05, 15)$	296	384	3	–	
$(05, 20)$	296	384	5	†	
$(05, 25)$	296	384	10	†	
$(10, 05)$	252	339	1	–	
$(10, 10)$	252	339	2	–	
$(10, 15)$	252	339	3	–	
$(10, 20)$	252	339	5	–	
$(10, 25)$	252	339	10	†	
$(15, 05)$	350	435	1	–	
$(15, 10)$	350	435	2	–	
$(15, 15)$	350	435	3	†	
$(15, 20)$	350	435	5	†	
$(15, 25)$	350	435	10	†	
$(20, 05)$	200	281	1	–	
$(20, 10)$	200	281	5	–	
$(20, 15)$	200	281	10	–	
$(20, 20)$	200	281	20	†	
$(20, 25)$	200	281	30	†	
$(25, 05)$	61	99	50	–	
$(25, 10)$	61	99	100	–	
$(25, 15)$	61	99	300	–	N/A
$(25, 20)$	108	166	10	–	N/A
$(25, 25)$	108	166	20	–	N/A
$(30, 05)$	108	166	50	–	
$(30, 10)$	108	166	100	–	
$(30, 15)$	108	166	300	–	N/A
$(30, 20)$	150	221	10	–	
$(30, 25)$	150	221	20	–	
$(35, 05)$	150	221	50	–	
$(35, 10)$	150	221	100	†	
$(35, 15)$	108	166	300	†	
$(35, 20)$	61	99	300	–	$\oplus$

S_8 (SW404 + XB5173)

(x_i, y_i) [mm,mm]	v_{MIJA} [m/s]	$v_{\widehat{D}}$ [m/s]	N_i	Damage	Notation
$(35, 25)$	375	458	1	–	
$(40, 05)$	375	458	2	–	
$(40, 10)$	375	458	3	†	
$(40, 15)$	375	458	5	†	
$(40, 20)$	408	486	2	†	
$(40, 25)$	408	486	1	–	

Table B.5. Impact site locations (x, y), speed of MIJA (v_{MIJA}), equivalent speed of a 2 mm droplet ($v_{\hat{D}}$). Damage is indicated by (†) and no damage by (−). For the notation part: Incipient is denoted by ($\oplus$), gross crack by ($\otimes$) and punctured through hole by ($\odot$).

Appendix C

Specimen Subdivision

C.1 Large specimens

The subdivision scheme for large specimens areas is shown in Figure C.1 and Table C.1.

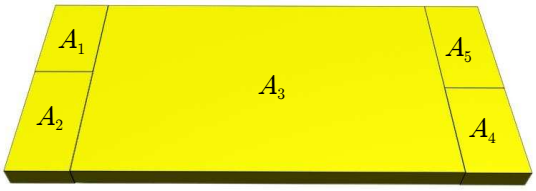

Figure C.1. The schematic subdivision of large specimens.

j	L_j	W_j	A_j
1	βL	δW	$(\beta\delta)LW$
2	βL	$(1-\delta)W$	$\beta(1-\delta)LW$
3	$(1-2\beta)L$	W	$(1-2\beta)LW$
4	βL	δW	$(\beta\delta)LW$
5	βL	$(1-\delta)W$	$\beta(1-\delta)LW$

Table C.1. The subdivision of large experimental specimens in relation to the scaling factors, β, $\delta \in [0, 1]$ and the length ($\rightarrow$) and width direction ($\uparrow$) respectively. From the notations it is obvious that $A_1 = A_4$ and conversely $A_2 = A_5$. Moreover, $A_3 > A_j$ where $j = 1, 2, 4$ and 5.

C.2 Small specimens

The corresponding subdivision for small specimens is shown in Figure C.2 and Table C.2.

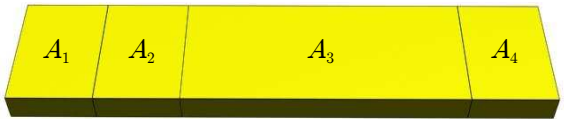

Figure C.2. The schematic subdivision of small specimens.

j	L_j	W_j	A_j
1	βL	W	$(\beta)LW$
2	βL	W	$(\beta)LW$
3	$(1-3\beta)L$	W	$(1-3\beta)LW$
4	βL	W	$(\beta)LW$

Table C.2. The subdivision of small experimental specimens in relation to the scaling factors, $\beta \in [0, 1]$. From the notations it is obvious that $A_1 = A_4$. Further, $A_3 > A_j$ where $j = 1, 2$ and 4.

Appendix D

Ranking

D.1 Density

Specimen name	Density ranking
LY564	9
LY564 + 0.5% MWCNT	10
32_MINAS1_06	6
32_A05_CANBIO1_06	5
32_MINAS1_07	7
32_A05_CANBIO1_07	4
Araldite DBF	8
SW404 + XB5173	1
LAYSA_ICE01	3
SICOMP_NA_ICE1	2

Table D.1. The ranking of density ρ for the given specimens. The lowest number refers to the highest density and the highest number refers to the lowest density.

D.2 Speed of sound

Specimen name	Speed of sound ranking
LY564	10
LY564 + 0.5% MWCNT	9
32_MINAS1_06	2
32_A05_CANBIO1_06	1
32_MINAS1_07	4
32_A05_CANBIO1_07	3
Araldite DBF	7
SW404 + XB5173	5
LAYSA_ICE01	8
SICOMP_NA_ICE1	6

Table D.2. The ranking of speed of sound c in the given specimens. The lowest number refers to the highest speed of sound and the highest number refers to the lowest speed of sound.

D.3 Acoustic impedance

Specimen name	Acoustic impedance ranking
LY564	10
LY564 + 0.5% MWCNT	9
32_MINAS1_06	6
32_A05_CANBIO1_06	4
32_MINAS1_07	7
32_A05_CANBIO1_07	5
Araldite DBF	8
SW404 + XB5173	1
LAYSA_ICE01	3
SICOMP_NA_ICE1	2

Table D.3. The ranking of acoustic impedance Z, for the given specimens. The lowest number refers to the highest acoustic impedance value and the highest number refers to the lowest acoustic impedance value.

D.4 Vickers Hardness

Specimen name	Vickers hardness ranking
LY564	6
LY564 + 0.5% MWCNT	8
32_MINAS1_06	3
32_A05_CANBIO1_06	2
32_MINAS1_07	4
32_A05_CANBIO1_07	5
Araldite DBF	7
SW404 + XB5173	1

Table D.4. The ranking of Vickers hardness HV, for the given specimens. The lowest number refers to the highest Vickers hardness value and the highest number refers to the lowest Vickers hardness value.

D.5 Damage Threshold Velocity

Specimen name	DTV ranking
LY564	1
LY564 + 0.5% MWCNT	3
32_MINAS1_07	4
32_A05_CANBIO1_07	5
SW404 + XB5173	2

Table D.5. The ranking of Damage Threshold Velocity (DTV), for the given specimens. The lowest number refers to the highest DTV and the highest number refers to the lowest DTV value.

D.6 Dynamic wettability

Specimen name	Dynamic wetting ranking
LY564	7
LY564 + 0.5% MWCNT	5
32_A05_CANBIO1_06	2
32_MINAS1_06	3
32_A05_CANBIO1_07	8
32_MINAS1_07	4
Araldite DBF	6
SW404 + XB5173	1

Table D.6. The ranking of dynamic wetting for the given specimens. The lowest number refers to a hydrophobic nature on the specimen and the highest number refers to the hydrophilic nature on the specimen.

Appendix E

Vickers Hardness Indenter Error

The effect of an incorrect apex angle $\beta \neq 136°$, can be investigated by considering a range of deviated apex angles of $\Delta\beta \in [0, -10°]$ resulting in a range of apex angles, $\beta + \Delta\beta$. Utilizing the standard relationship for the Vickers hardness value

$$HV = \frac{2P \sin\left(\frac{\beta}{2}\right)}{d^2} \tag{E.1}$$

where $\beta = 136°$. The percentage error is easily estimated by defining

$$\frac{2P}{d^2} \equiv 1 \tag{E.2}$$

and estimating $HV(\beta)$ in comparison to $HV(\beta + \Delta\beta)$. The percent error for each deviation ε_i can then be written as

$$\varepsilon_i = \left(\frac{|HV(\beta) - HV(\beta + \Delta\beta_i)|}{|HV(\beta)|}\right) \cdot 100 \tag{E.3}$$

where $i \in [0, 10]$. The deviation $|\Delta\beta|$ and its corresponding percentage error ε, are shown in Table E.1.

$\lvert\Delta\beta\rvert$	1°	2°	3°	4°	5°	6°	7°	8°	9°	10°
ε	0.36%	0.72%	1.09%	1.47%	1.86%	2.25%	2.65%	3.06%	3.47%	3.90%

Table E.1. The deviation $|\Delta\beta|$ and its corresponding percentage error ε.

Appendix F

Bead representation

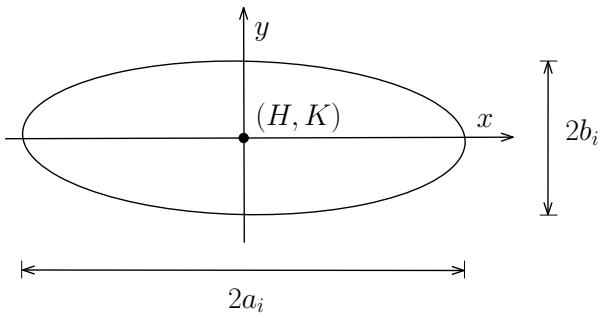

The equation for an ellipse with the coordinates of the origin at (H, K) is given by

$$\frac{(x-H)}{a_i^2} + \frac{(y-K)^2}{b_i^2} = 1 \tag{F.1}$$

From the given figure

$$\begin{cases} a_i = \frac{w_i}{2} \\ b_i = h_i \end{cases} \tag{F.2}$$

Equations (F.1) and (F.2) and $K = 0$ yield that $y(x)$ is given by

$$y(x) = \frac{h_i(-4x^2 + 8xH - 4H^2 + w_i^2)^{\frac{1}{2}}}{w_i} \tag{F.3}$$

In Equation (F.3) only $y > 0$, is considered. The horizontal shift for different $x-$coordinates can further be described by

$$H_n(x) \equiv \begin{cases} \frac{w_1}{2} & , n = 1 \\ w_1 + \frac{w_2}{2} & , n = 2 \\ H_{n-1} + w_{n-1} + w_n & , n > 2 \end{cases} \tag{F.4}$$

Appendix G

Stress Reduction on the Substrate by Usage of A Coating Layer

G.1 LY564 Substrate

Coating Name	σ^* [%]	Coating Protection
S_1	0.0	N/A
S_2	0.09	Yes
S_3	0.65	Yes
S_4	0.68	Yes
S_5	0.55	Yes
S_6	0.68	Yes
S_7	0.45	Yes
S_8	1.70	Yes
S_9	0.81	Yes
S_{10}	1.06	Yes

Table G.1. Coating protection with different materials S_n for the S_1 (LY564) substrate. A negative reduction stress value $\sigma^* < 0$, indicates an increase in stress within the coating, which is unfavorable.

G.2 LY564 + 0.5% MWCNT Substrate

Coating Name	σ^* [%]	Coating Protection
S_1	-0.09	No
S_2	0.0	N/A
S_3	0.53	Yes
S_4	0.56	Yes
S_5	0.43	Yes
S_6	0.55	Yes
S_7	0.33	Yes
S_8	1.50	Yes
S_9	0.66	Yes
S_{10}	0.90	Yes

Table G.2. Coating protection with different materials S_n for S_2 (LY564 +0.5% MWCNT) substrate. A negative reduction stress value $\sigma^* < 0$, indicates an increase in stress within the coating, which is unfavorable.

G.3 32_MINAS1_06 Substrate

Coating Name	σ^* [%]	Coating Protection
S_1	-0.45	No
S_2	-0.38	No
S_3	0.0	N/A
S_4	0.03	Yes
S_5	-0.08	No
S_6	0.01	Yes
S_7	-0.17	No
S_8	0.69	Yes
S_9	0.05	Yes
S_{10}	0.23	Yes

Table G.3. Coating protection with different materials S_n for the S_3 (32_MINAS1_06) substrate. A negative reduction stress value $\sigma^* < 0$, indicates an increase in stress within the coating, which is unfavorable.

G.4 32_A05_CANBIO1_06 Substrate

Coating Name	σ^* [%]	Coating Protection
S_1	-0.47	No
S_2	-0.40	No
S_3	-0.03	No
S_4	0.0	N/A
S_5	-0.11	No
S_6	-0.02	No
S_7	-0.19	No
S_8	0.65	Yes
S_9	0.02	Yes
S_{10}	0.20	Yes

Table G.4. Coating protection with different materials S_n for the S_4 (32_A05_CANBIO1_06) substrate. A negative reduction stress value $\sigma^* < 0$, is indicative of an increase in stress within the coating, which is unfavorable.

G.5 32_MINAS1_07 Substrate

Coating Name	σ^* [%]	Coating Protection
S_1	-0.39	No
S_2	-0.32	No
S_3	0.09	Yes
S_4	0.11	Yes
S_5	0.0	N/A
S_6	0.10	Yes
S_7	-0.09	No
S_8	0.82	Yes
S_8	0.15	Yes
S_8	0.35	Yes

Table G.5. Coating protection with different materials S_n for the S_5 (32_MINAS1_07) substrate. A negative reduction stress value $\sigma^* < 0$, indicates an increase in stress within the coating, which is unfavorable.

G.6 32_A05_CANBIO1_07 Substrate

Coating Name	σ_* [%]	Coating Protection
S_1	-0.46	No
S_2	-0.39	No
S_3	-0.01	No
S_4	0.02	Yes
S_5	-0.09	No
S_6	0.0	N/A
S_7	-0.18	No
S_8	0.68	Yes
S_9	0.04	Yes
S_{10}	0.23	Yes

Table G.6. Coating protection with different materials S_n for the S_6 (32_A05_CANBIO1_07) substrate. A negative reduction stress value $\sigma^* < 0$, indicates an increase in stress within the coating, which is unfavorable.

G.7 Araldite DBF Substrate

Coating Name	σ^* [%]	Coating Protection
S_1	-0.33	No
S_2	-0.25	No
S_3	0.18	Yes
S_4	0.21	Yes
S_5	0.09	Yes
S_6	0.19	Yes
S_7	0.0	N/A
S_8	0.97	Yes
S_9	0.26	Yes
S_{10}	0.46	Yes

Table G.7. Coating protection with different materials S_n for the S_7 (Araldite DBF) substrate. A negative reduction stress value $\sigma^* < 0$, indicates an increase in stress within the coating, which is unfavorable.

G.8 SW404 + XB5173 Substrate

Coating Name	σ^* [%]	Coating Protection
S_1	-0.77	No
S_2	-0.71	No
S_3	-0.45	No
S_4	-0.42	No
S_5	-0.52	No
S_6	-0.46	No
S_7	-0.59	No
S_8	0.0	N/A
S_9	-0.47	No
S_{10}	-0.33	No

Table G.8. Coating protection with different materials S_n for the S_8 (SW404 + XB5173) substrate. A negative reduction stress value $\sigma^* < 0$, indicates an increase in stress within the coating, which is unfavorable.

G.9 LAYSA_ICE01 Substrate

Coating Name	σ^* [%]	Coating Protection
S_1	-0.49	No
S_2	-0.42	No
S_3	-0.04	No
S_4	-0.08	No
S_5	-0.13	No
S_6	-0.04	No
S_7	-0.21	No
S_8	0.62	Yes
S_9	0.0	N/A
S_{10}	0.18	Yes

Table G.9. Coating protection with different materials S_n for the S_9 (LAYSA_ICE01) substrate. A negative reduction stress value $\sigma^* < 0$, indicates an increase in stress within the coating, which is unfavorable.

G.10 SICOMP_NA_ICE1

Coating Name	σ^* [%]	Coating Protection
S_1	-0.58	No
S_2	-0.52	No
S_3	-0.19	No
S_4	-0.16	No
S_5	-0.26	No
S_6	-0.19	No
S_7	-0.34	No
S_8	0.40	Yes
S_9	-0.16	No
S_{10}	0.0	N/A

Table G.10. Coating protection with different materials S_n for the S_{10} (SICOMP_NA_ICE1) substrate. A negative reduction stress value $\sigma^* < 0$, indicates an increase in stress within the coating, which is unfavorable.

Appendix H

Matlab Schemes

H.1 Vickers Hardness Topography

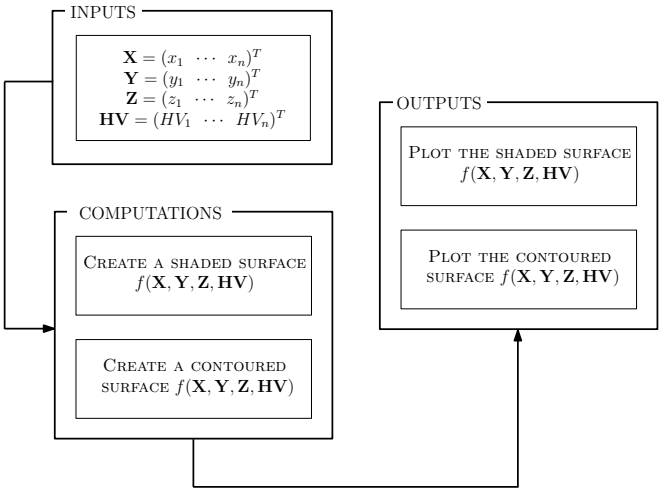

H.2 Coating Stress Computations

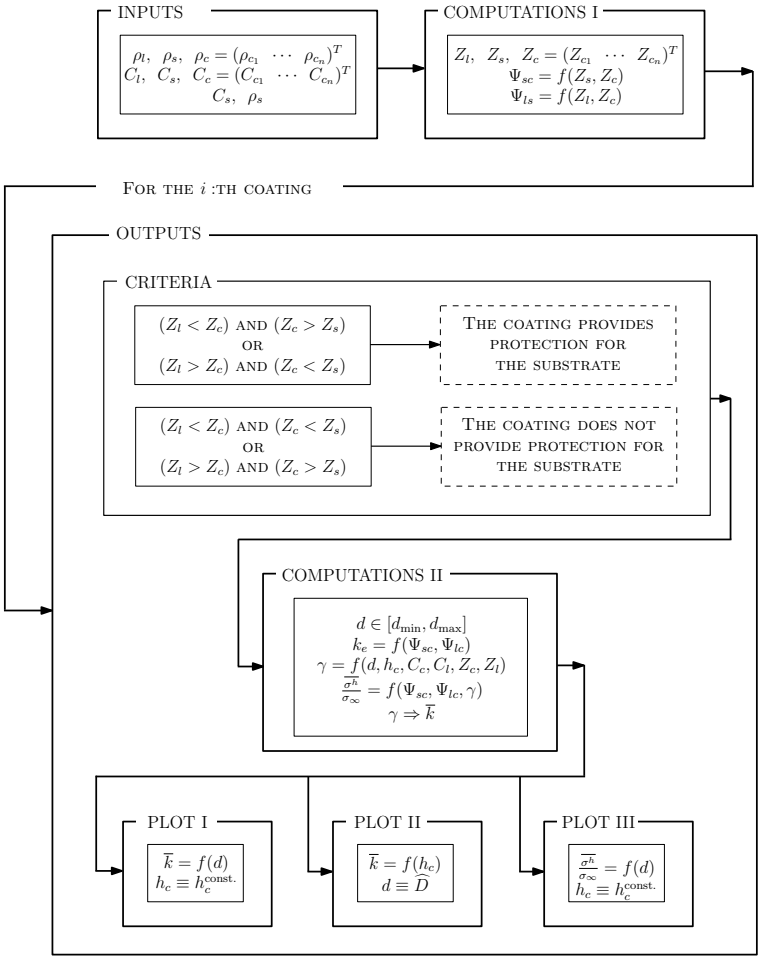

Appendix I

Publications

The findings of this study and related studies have publicly been presented in the following forums:

- O. Gohardani. Impact of erosion testing aspects on current and future flight conditions. *Progress in Aerospace Sciences*, Volume 47, Issue 4, Pages 280−303, ISSN 0376-0421, 2011. doi:10.1016/j.paerosci.2011.04.001.
- O. Gohardani and D.W. Hammond. Droplet interaction and dynamic wettability of advanced materials used in aeronautics. *Presented at the 6th Subrata Chakrabarti International Conference on Fluid Structure Interaction, 9-11 May 2011, Orlando, U.S.A.*
  To be published in: *Advances in Fluid Mechanics IX*. WIT Transactions on Engineering Sciences, 2012. ISBN 9781845646004.
- O. Gohardani, D.H. Williamson, D.W. Hammond. Multiple liquid impacts on polymeric matrix composites reinforced with carbon nanotubes. *Wear*, 2012. (Submitted)
- O. Gohardani and D.W. Hammond. Dynamic and static wettability of advanced materials used in aeronautical applications. *The International Journal of Computational Methods and Experimental Measurements*, 2012. (Submitted)
- O. Gohardani and D.W. Hammond. Ice adhesion to pristine and eroded polymeric matrix composites reinforced with carbon nanotubes. *Cold Regions Science and Technology*, 2012. (To be submitted)
- A.S. Gohardani and O. Gohardani. Ceramic engine considerations for future aerospace propulsion. *Aircraft Engineering and Aerospace Technology*, Volume 84, Issue 2, 2012.

I.1 Progress in Aerospace Sciences

Progress in Aerospace Sciences 47 (2011) 280–303

Contents lists available at ScienceDirect

Progress in Aerospace Sciences

journal homepage: www.elsevier.com/locate/paerosci

Impact of erosion testing aspects on current and future flight conditions

Omid Gohardani *

Cranfield University, Department of Power and Propulsion, School of Engineering, MK43 0AL, United Kingdom

ARTICLE INFO

Keywords:
Solid erosion
Erosion testing
Erosion modeling
Hydrometeors
Volcanic ash

ABSTRACT

High speed of aero vehicles including commercial and military aircraft, missiles, unmanned air vehicles, as well as conceptual aircraft of the future are imposing larger restrictions on the materials of these vehicles and highlight the importance of adequate quantification of material behavior and performance during different flight conditions. Erosion due to weather conditions and other present particles such as hydrometeors; rain, hail and ice, as well as sand, volcanic ash and dust resulting from residues in the atmosphere are eminent as hazardous on the structure of a flying vehicle and may adversely influence the lifecycle of the structure. This study outlines an extensive review of research efforts on erosion in aviation and provides a basis for comparison between different apparatus simulating rain erosion and their usage within the aerospace industry. The significant aspects of erosion testing and future prospects for erosion impact are further addressed for forthcoming generations of flying vehicles.

Contents

* Tel.: +44 1234 750111x5056, fax: +44 1234 758208.
E-mail address: omid.gohardani@cranfield.ac.uk

0376-0421/$ - see front matter © 2011 Elsevier Ltd. All rights reserved.
doi:10.1016/j.paerosci.2011.04.001

Appendix J

COSHH Form

J.1 Example of a COSHH Form

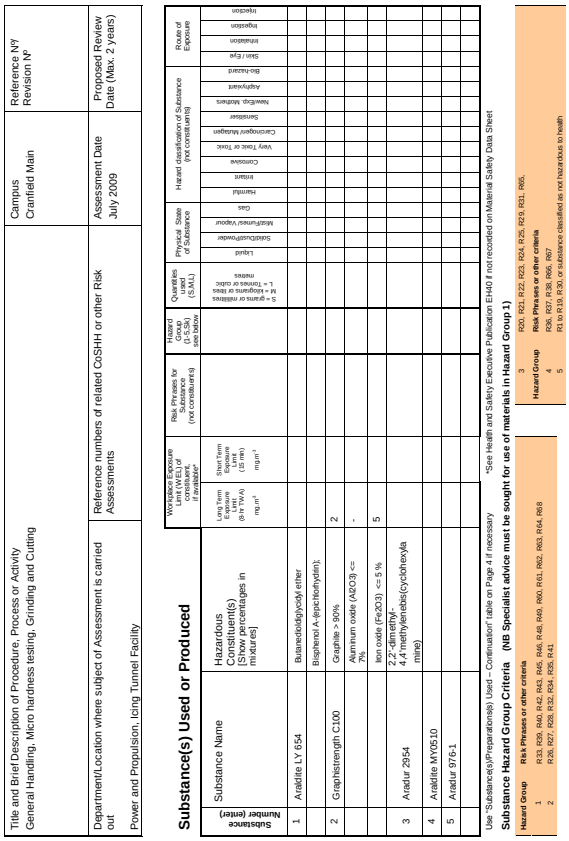

COSHH RISK ASSESSMENT FORM

Title and Brief Description of Procedure, Process or Activity General Handling, Micro hardness testing, Grinding and Cutting	Campus Cranfield Main	Reference N°/ Revision N°
Department/Location where subject of Assessment is carried out Power and Propulsion, Icing Tunnel Facility	Assessment Date July 2009	Proposed Review Date (Max. 2 years)
Reference numbers of related CoSHH or other Risk Assessments		

Substance(s) Used or Produced

Substance Number (enter)	Substance Name	Hazardous Constituent(s) [Show percentages in mixtures]	Workplace Exposure Limit (WEL) of Constituent(s) if available*		Risk Phrases for Substance (not constituents)	Hazard Data (CHIP) (see below)	Quantities used (S/M/L)	Physical State of Substance			Hazard Identification of Substance (not constituents)												Route of Exposure				
			Long Term Exposure (8-hr TWA) mg.m^{-3}	Short Term Exposure Limit (15 min) mg.m^{-3}			S = grams or millilitres M = kilograms or litres L = Tonnes or cubic metres	Liquid	Solid/Dust/Powder	Mist/Fumes/ Vapour	Gas	Harmful	Irritant	Corrosive	Very Toxic or Toxic	Carcinogen/ Mutagen	Sensitiser	New/Exp. substance	Asphyxiant	Bio-hazard	Skin / Eye	Inhalation	Ingestion	Injection
1	Araldite LY 654	Butanedioldiglycidyl ether																									
		Bisphenol A diglycidylether)																									
2	Graphistrength C100	Graphite > 90%	2																								
		Aluminium oxide (Al2O3) <= 7%	-																								
		Iron oxide (Fe2O3) <= 5 %	5																								
3	Aradur 2954	2,2'-dimethyl-4,4'-methylenebis(cyclohexylamine)																									
4	Araldite MY0510																										
5	Aradur 976-1																										

Use 'Substance(s)/Preparation(s) Used – Continuation' table on Page 4 if necessary *See Health and Safety Executive Publication EH40 if not recorded on Material Safety Data Sheet

Substance Hazard Group Criteria (NB Specialist advice must be sought for use of materials in Hazard Group 1)

Hazard Group	Risk Phrases or other criteria
1	R33, R39, R40, R42, R43, R45, R46, R48, R60, R61, R62, R63, R64, R68
2	R26, R27, R28, R32, R34, R35, R41
3	R20, R21, R22, R23, R24, R25, R29, R31, R65,
Hazard Group	Risk Phrases or other criteria
4	R36, R37, R38, R66, R67
5	R1 to R19, R30, or substance classified as not hazardous to health

CU 005 May 2008 Page 1 of 10